Single-Chain Polymeric Nanoparticles for Bioorthogonal Catalysis

Citation for published version (APA):
Sathyan, A. (2023). *Single-Chain Polymeric Nanoparticles for Bioorthogonal Catalysis: Nanoreactors in Action*. [Phd Thesis 1 (Research TU/e / Graduation TU/e), Chemical Engineering and Chemistry]. Eindhoven University of Technology.

Document status and date:
Published: 23/06/2023

Document Version:
Publisher's PDF, also known as Version of Record (includes final page, issue and volume numbers)

Please check the document version of this publication:

• A submitted manuscript is the version of the article upon submission and before peer-review. There can be important differences between the submitted version and the official published version of record. People interested in the research are advised to contact the author for the final version of the publication, or visit the DOI to the publisher's website.
• The final author version and the galley proof are versions of the publication after peer review.
• The final published version features the final layout of the paper including the volume, issue and page numbers.

Link to publication

General rights
Copyright and moral rights for the publications made accessible in the public portal are retained by the authors and/or other copyright owners and it is a condition of accessing publications that users recognise and abide by the legal requirements associated with these rights.

- Users may download and print one copy of any publication from the public portal for the purpose of private study or research.
- You may not further distribute the material or use it for any profit-making activity or commercial gain
- You may freely distribute the URL identifying the publication in the public portal.

If the publication is distributed under the terms of Article 25fa of the Dutch Copyright Act, indicated by the "Taverne" license above, please follow below link for the End User Agreement:

www.tue.nl/taverne

Take down policy
If you believe that this document breaches copyright please contact us at:

openaccess@tue.nl

providing details and we will investigate your claim.

Download date: 16. Nov. 2023

Single-Chain Polymeric Nanoparticles for Bioorthogonal Catalysis

Nanoreactors in Action

THESIS

ter verkrijging van de graad van doctor aan de Technische Universiteit Eindhoven, op gezag van de rector magnificus prof.dr. S.K. Lenaerts, voor een commissie aangewezen door het College voor Promoties, in het openbaar te verdedigen op vrijdag 23 juni 2023 om 11:00 uur

door

Anjana Sathyan

geboren te Kuzhuppilly, India

Dit proefschrift is goedgekeurd door de promotoren en de samenstelling van de promotiecommissie is als volgt:

Voorzitter:	Prof.dr. A.P.H.J. Schenning
Promotor:	Prof.dr.ir. A.R.A. Palmans
Co-promotor:	Prof.dr. A. Unciti-Broceta (University of Edinburgh)
Promotiecommissieleden:	Prof.dr.ir. L. Brunsveld
	Prof.dr. R.P. Sijbesma
	Prof.dr. E.W. Meijer
	Dr. Y. Liu (South China University of Technology)
	Dr. L. Albertazzi

Het onderzoek of ontwerp dat in dit thesis wordt beschreven is uitgevoerd in overeenstemming met de TU/e Gedragscode Wetenschapsbeoefening.

സ്നേഹപൂർവ്വം അമ്മയ്ക്ക്

Single-Chain Polymeric Nanoparticles for Bioorthogonal Catalysis
Nanoreactors in Action

Anjana Sathyan
Eindhoven University of Technology, The Netherlands, 2023

This work is financed by the European Union's Horizon 2020 research and innovation program under the Marie Sklodowska-Curie Grant Agreement no. 765497 (THERACAT).

A catalogue record is available from the Eindhoven University of Technology Library
ISBN: 978-90-386-5767-7

Cover design: Anjana Sathyan, Image generated by Microsoft Designer

Printed by Gilderprint, The Netherlands

Table of contents

Chapter 5 147

Chapter 1

Bioorthogonal catalysis in complex media: Consequences of using polymeric scaffold materials on catalyst stability and activity

Abstract: Bioorthogonal catalysis using transition-metal-based complexes (TMCs) is a promising approach for converting substrates to desired products in complex cellular media. Notably, the *in situ* activation of prodrugs or synthesis of active drugs with the aim to complement existing treatments in diseases such as cancer has received significant attention. Whereas the focus has initially been on optimizing ligands to enhance the activity and stability of the metal complexes, more recently the benign effects of compartmentalization of the catalyst into homogeneous or heterogeneous scaffolds have been unveiled. Such tailor-made carrier materials not only afford active catalysts but also permit to guide the catalyst to the site of interest in *in vivo* applications. Here, we emphasize the potential of synthetic amphiphilic polymers that form compartmentalized nanostructures for TMCs. The use of amphiphilic polymers is well established in the field of nanomedicine for *i.e.* drug delivery purposes, but their application as homogeneous carrier materials for TMCs has been less well explored. Since synthetic polymers are readily functionalised with ligands and targeting moieties, they can act as versatile catalyst carriers. After a short overview of the state-of-the-art in bioorthogonal catalysis using ligand-based TMCs, the advances in using synthetic homogeneous and heterogeneous carrier materials for bioorthogonal catalysis is summarised.

This work has been published as:

A. Sathyan; L. Deng; T. Loman and A. R. A. Palmans; Bio-orthogonal catalysis in complex media: Consequences of using polymeric scaffold materials on catalyst stability and activity. *Catalysis Today,* **2023***, 418,* 114116.

1.1 Introduction

Progress in the field of catalysis has resulted in high selectivity, efficiency and versatility when converting substrates to desired products in different reaction media. Still, few synthetic catalysts can compete with the activity and selectivity of enzymes in water at low concentrations and mild temperatures. In fact, enzymes are unmatched in terms of rate and selectivity at mild conditions, which is a consequence of their folded, tertiary structure. Their perfectly defined three-dimensional structure results from a strictly defined length and amino acid sequence of the polypeptide chain. Directional hydrogen-bonding motifs that induce secondary structure elements via α-helix and β-sheet formation, additional hydrophobic effects and disulfide bonds complete nature's toolset to control the enzyme's three-dimensional structure.[1–3] The three-dimensionally controlled conformation of enzymes ensures a precise spatial positioning of crucial, catalytic amino acid residues, which is optimized for selective substrate binding.[4] These features result not only in unprecedented reactivity and selectivity, but also in compatibility with highly competitive and crowded environments, and complementarity to other types of enzymes. It is therefore no surprise that scientists have long aspired to mimic the catalytic features of these sophisticated systems. Great progress has been achieved to evolve enzymes to initiate nonnatural conversions and accept non-natural substrates.[5] Nevertheless, there remains a need to develop synthetic catalysts that perform well in aqueous media, not only for the further development of green chemical conversions in water, but also to augment the catalytic repertoire of enzymes with the versatility in bond breaking and bond forming reactions that transition metals offer. The latter is especially important in view of the recent developments in bioorthogonal catalysis, a relatively new field where transition metal complexes (TMCs) are applied in complex cellular media with the ultimate aim to activate prodrugs or synthesize drugs *in situ* and *in vivo*.

The importance of performing non-natural chemical reactions in *in vivo* conditions, coined "bioorthogonal chemistry" by Bertozzi and coworkers in 2003, was recently highlighted by awarding the Nobel prize in 2022. Bioorthogonal chemical reactions allow chemical modifications to take place in a selective manner in complex environments without interfering with the biological system.[6] The search for new bioorthogonal reactivities also turned to catalytic conversions and more specifically the use of TMCs.[7–9] This allowed to access new-to-nature reactions such as Suzuki-Miyaura couplings,[10–12] Heck and Sonogashira reactions,[13,14] carbene insertions,[15] and a variety of metal-catalysed bond cleavage reactions[16,17] in complex cellular media. Applying TMCs in biological environments comes with its own challenges. First, the catalysts have to be highly active and reach high turnover numbers to cope with the typical sub-micromolar concentrations in biological systems. Additionally, high catalyst stability is required due to the wide variety of competitive species present in complex biological media, which can interact with the metal. Furthermore, water-solubility, non-toxicity, and activity at physiological pH and temperature are necessary for the TMC to work in biological contexts.[7,18] Finally, when the *in situ* preparation or activation of therapeutical drugs are considered, the TMC has to be present at the site of interest when used *in vivo*.

The importance of the ligand is well-recognized to boost the activity of transition-metal complexes, as well as for enhancing their stability. In addition, compartmentalization of the TMC has been found to enhance catalyst stability as well as provide opportunities to localise the TMC at the site of interest. A number of approaches have been evaluated to compartmentalize the TMC using both synthetic as well as natural carrier materials as shown in Figure 1. Nevertheless, accurately localising the TMCs *in vivo* to specific diseased organs or tumours while maintaining activity in a highly competitive environment remains a challenging endeavor. Well-designed polymeric scaffolds, both natural as well as synthetic, can offer various advantages as they potentially protect the TMC from competitive species and carry the TMC to the desired location. In addition, all progress achieved in polymer-based nanocarriers that have been developed for drug delivery,[19,20] can be included in the polymer scaffold design to target, actively or passively, the TMC to the desired location *in vivo*.

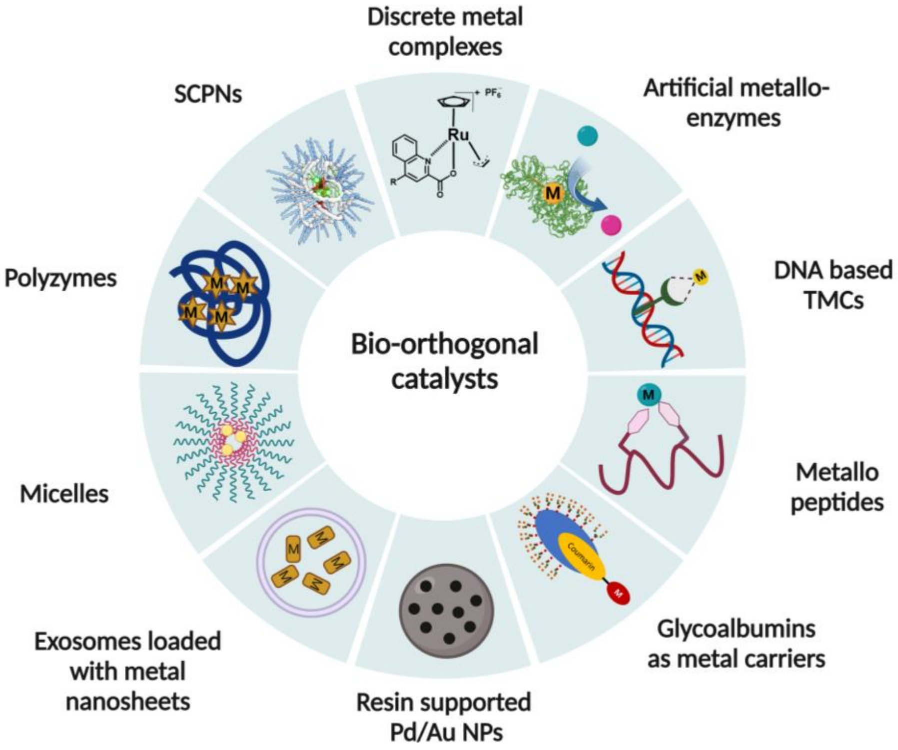

Figure 1: An overview of synthetic or natural ligands and / or carrier materials that have been combined with TMCs to afford bioorthogonal TMC-based catalysts for *in vitro* or *in vivo* applications. Figure created with biorender.com

1.2 TMCs in bioorthogonal reactions: effect of ligand on catalyst stability and activity

While organometallic complexes such as *cis*-platinum have been used as metallodrugs for a long time,[21] the application of TMCs to catalyse non-natural reactions in living cells is of more recent interest. Designing TMCs that are both stable and reactive in living cells is a challenging task, given that the complex sea of functionalities in cells, particularly thiols, can quickly deactivate them. In 2006, Streu and Meggers were the first to demonstrate the use of Ru-based TMCs as a bioorthogonal catalyst for the cleavage of allyl carbamates to their respective amines *in vitro*.[22] It was quickly realized that the nature of the ligands had a profound impact on the efficiency of the reaction as it can help to tune the reactivity and stability of these catalysts *in vitro*. Later studies focused on the ligand's effect on the catalyst's reactivity and stability by varying the ligands for dealkylation reactions (Figure 2A).[8] It was found that the 2-quinoline carboxylate-based Ru complex **2** showed a dramatic increase in the activity reaching up to 90 turnovers under biologically relevant conditions as compared to 4 turnovers by their previously reported [Cp*Ru(COD)Cl] complex **1** (Figure 2A). Further, a significant boost in the activity was achieved reaching up to 270 turnovers with the introduction of π-donating methoxy and dimethylamino group onto the quinoline moiety **3** and **4** (Figure 2A). The most active complex **4** enabled the uncaging of protected rhodamine **6** by cleaving allylcarbamate protected amines inside HeLa cells (Figure 2B).[8,22] In addition, the same Ru complex **4** successfully induced cell apoptosis in HeLa cells by uncaging protected doxorubicin **8**. In subsequent work, Ru complexes were fine-tuned by using 8-hydroxyquinolinate as ligand, which resulted in Ru complex **5** with a higher turnover (>300) in uncaging alloc-protected amines in blood serum (Figure 2A). Thereby, protected doxorubicin **8** was activated using a very low concentration of catalyst in Hela cell culture (Figure 2C). These findings highlight the fact that the reactivity of the Ru-complexes can be tuned by selecting appropriate ligands. However, the effect of ligands on catalyst's activity can differ in complex environments versus organic media as the rate determining step of the reactions can be shifted due to competing nucleophiles present in complex media. In earlier work, reducing the π-backbonding of bidendate ligand using methoxy and dimethylamino group boosted the catalytic activity of the Ru complexes. An opposite trend in reactivity was observed by Kitamura and co-workers in organic solvents, where reduced π-backbonding of bidendate ligands diminished the catalytic activity of analogous Ru complexes.[23]

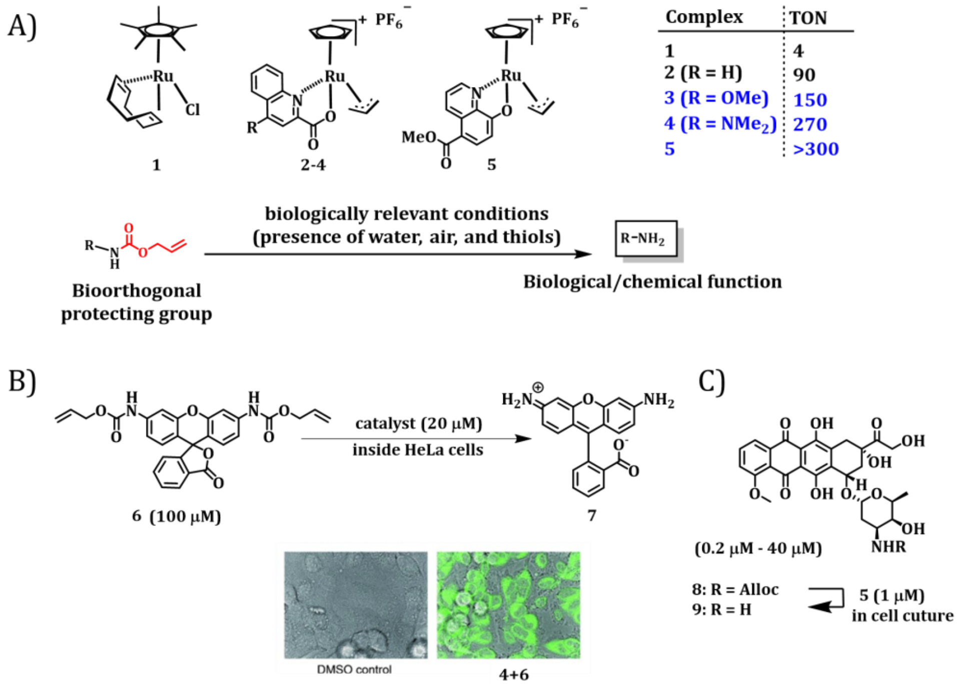

Figure 2: A) Structure of ruthenium complexes for catalytic cleavage of *O*-allyl carbamates with their corresponding turnover number (TON). B) Uncaging of protected rhodamine inside Hela cells using Ru catalyst **4**. Cell image adapted from Ref. [8] with permission. C) Structure of protected doxorubicin uncaged in HeLa cell culture using Ru catalyst **5**.

After the pioneering studies of Meggers and coworkers on introducing Ru-based TMCs as a bioorthogonal tool,[8] the field flourished with the application of new TMCs for a range of organic reactions in cells and even living systems such as Pd(II)/(0),[24–26] Au,[27,28] Cu,[29,30] Ir,[31] Pt,[32] and Fe,[33] which opened up new avenues for *in situ* drug synthesis or prodrug activation. TMCs based on Pd(II)/Pd(0) were studied to catalyse deprotections and Suzuki-Miyaura cross-coupling reactions in biological settings owing to their low toxicity.[34] The oxidation state of Pd was found to have a large impact on the depropargylation reaction rate, which was studied in detail by Chen and co-workers (Figure 3A).[35] They screened heterogeneous Pd(0) nanoparticles (NPs), Pd(0)/Pd(II) and Pd(IV) complexes for their catalytic efficiency in water. The conclusion was that Pd(0) NPs **12** and triphenylphosphine-based Pd(0) complex **14** (Figure 3A) showed the highest reactivity in the deprotection of *N*-

proc-caged coumarin **10** in water. They further performed metabolic incorporation of Neu5Proc **20** onto cell surface glycans and their *in situ* conversion to neuramic acid **21** using Pd-NPs (Figure 3B).

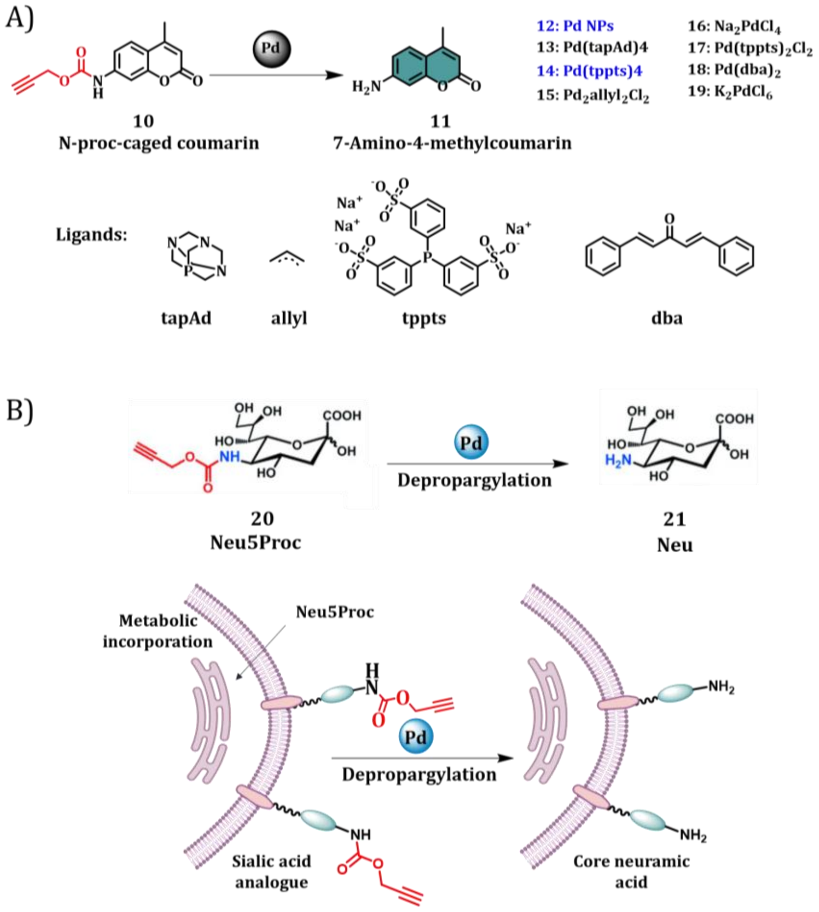

Figure 3: A) Palladium catalysts with different ligands screened for depropargylation of *N*-proc-caged coumarin (stochiometric amount of catalysts were used in water). B) Representation for metabolic incorporation of Neu5Proc and its *in situ* conversion to neuramic acid using Pd-mediated depropargylation.[35] Best-performing catalysts are marked in blue. Figure created with biorender.com.

More research on ligand tuning of Pd(II) complexes for intracellular catalysis was carried out by Mascareñas and co-workers (Figure 4).[25] They modified the solubility, stability and reactivity of the Pd(II) complex and observed that triphenylphosphine based complexes outperformed others in uncaging of protected dye **22** in cell lysates and even in mammalian cells. Moreover, both depropargylation and deallylation reactions were catalysed, albeit with moderate activity. Interestingly, they could target the complex to the mitochondria of HeLa cells by using a phosphine ligand tethered to phosphonium and hydrophobic pyrene groups **32** (Figure 4B).[25] They also used the same targeting group to modify Meggers' ruthenium catalyst **4** to selectively target the catalyst to mitochondria of HeLa cells and locally generate 2,4-dinitrophenol for mitochondrial depolarization. Thereby, they showed that ligand modifications can also allow targeting and preferential accumulation of catalysts to achieve functional alterations in living cells.

Cu-catalysed click chemistry is widely used for a variety of transformations in biological settings such as modification of nucleic acids, proteins or virus particles.[36] Even after the introduction of strain-promoted azide-alkyne cycloaddition reactions, the catalytic nature of Cu click reactions lure chemists to continue to come up with complexes that are highly biocompatible and active.[36] Also here, the ligands played a significant role in balancing reactivity, stability, and toxicity as they aid in preventing the Cu(I) ion from oxidation and disproportionation. However, that balance is delicate: when the ligand-binding is too labile, the redox stability of the metal can be compromised but when the ligand-binding is strong, the catalytic activity of the metal can be suppressed.[37] Pezacki and co-workers studied the cellular consequences of copper complexes commonly used for bioconjugation reactions and found that the ligand environment affected the toxicity, cellular uptake, and lipid metabolism of mammalian cells.[38] The Cu(I)–L–histidine complex was tolerated in cells at millimolar concentrations for 3 days while other copper complexes that employ TBTA (tris(benzyltriazolylmethyl)amine) or BPS (bathophenanthroline disulfonate disodium salt) were toxic on prolonged exposure. The results confirmed that toxicity of the metal species is dependent on ligand environment and variation of the ligand could alter this toxicity by at least 3 orders of magnitude. Ligand specific ligation of copper can not only prevent reactive oxygen species generation, but also helps to give antioxidant properties. Many biocompatible and amino acid based chelating ligands for Cu were developed later for bioconjugation reactions that exhibited efficient catalytic activity with low cytotoxicity.[39]

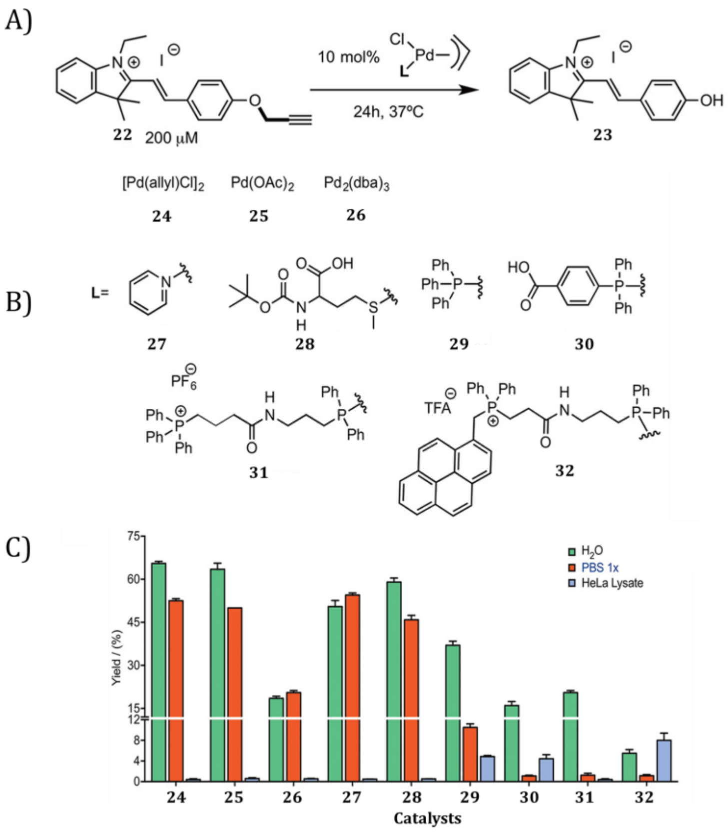

Figure 4: A) Depropargylation reaction catalysed by palladium catalysts. B) Palladium catalysts with ligand modifications. C) Bar diagram representing the yield obtained for each catalyst in water, PBS and Hela Lysate determined using HPLC-MS. Image adapted from Ref. [25] with permission from the American Chemical Society.

So far, Cu has been mainly utilized for click reactions and depropargylation reactions.[17,40] Recently, Mascareñas and co-workers introduced Cu(II)-catalysed carbene insertion reactions to catalyse the *in vitro* synthesis of quinoxaline derivatives.[15] This work highlighted the importance of developing new catalytic reactions that can be performed in biological settings. Here, fluorescent benzoquinoxalines were formed in-situ, of which one compound was a bio-active agent that altered the mitochondrial function of cells. Moreover, by conjugating the copper catalyst to an integrin targeting moiety, it was possible to achieve cell-selective biological effects.

1.3 Synthetic polymers as scaffolds for TMCs

1.3.1 Heterogeneous microspheres based on polystyrene-based beads

The inherent disadvantages of using “naked” transition metal complexes can be overcome by using heterogeneous catalysts that possess improved stability in the presence of deactivating nucleophiles and proteins in complex media. In fact, the very first example of using Pd chemistry in mammalian cells was shown by Bradley and co-workers using heterogeneous catalysts in 2011.[24] Palladium nanoparticles were trapped on 500 nm amino functionalised polystyrene based beads synthesized by dispersion polymerisation from styrene-based monomers,[41] followed by extensive crosslinking of the available amino groups, which allowed permanent entanglement of Pd(0) nanoparticles. This approach increased the biocompatibility of the NPs while retaining the catalytic activity amidst the complex environment in living cells. The heterogeneous microspheres acted as ‘Trojan horses’ to deliver palladium nanoparticles into living cells, stayed in the cytoplasm for several days and performed allyl carbamate cleavage and Suzuki-Miyaura coupling reactions.[10,34] It was proposed that these heterogeneous catalysts can act as an artificial organelle with longer retention in cytoplasm of cells and with minimal leakage of catalysts thereby decreasing their toxicity.[10,34,42] Even though the aforementioned reactions were catalytic in nature in a non-biological environment, it was found that this was not the case in living cells. The possibility of the Pd catalyst deactivating partially over time in the presence of intracellular components was therefore not completely ruled out.[10] Later, Bradley and co-workers developed fluorescent microspheres loaded with Pd nanoparticles and a cyclic peptide cRGD was conjugated to their surface as a targeting ligand (Figure 5A). This allowed rapid and selective uptake in glioblastoma cells as well as dual drug synthesis. They performed simultaneous activation of a pro-drug of 5-fluorouracil (5FU) **33** to 5FU **34** and Suzuki-Miyaura coupling of two benign precursors **35** and **36** to form an anticancer agent PP-121 **37** (Figure 5B).[43]

Unciti-Broceta and co-workers used a similar approach and reported extracellular microdevices using TentaGel® resins (crosslinked polystyrene matrix with grafted PEG chains for additional biocompatibility) that are 150 μm in diameter to trap Pd(0) nanoparticles.[26] They showed for the first time the activation of an anticancer pro-drug, pro-5FU, near cancer cells using Pd catalysts. They also elegantly implanted a single Pd(0) resin into the yolk sac of zebra fish, which displayed excellent bio-compatibility and local catalytic activity by activating a non-fluorescent lipophilic pro-dye based on rhodamine 110.[26] This work paved the way for further developments of bioorthogonally activated pro-drug approach in *in vivo* disease models. In subsequent work, they optimized the size of the resins to obtain the best Pd loading capacity and catalytic efficacy for ultrasound guided intra-tumoral implantation in mouse prostate tumours. The size of 30 μm Pd-devices was found to be optimal for performing this procedure and these NPs did not leak out from the tumours, were not toxic to the animal, and did not affect the tumour growth. By activating a pro-dye based on rhodamine 110, they demonstrated for the first time that a bioorthogonal catalyst can be hosted in a tumour *in vivo* without negatively impacting the turnover rate of the devices over time.[42] They also demonstrated the capacity of these devices to sequester circulating pro-doxorubicin and generate cytotoxic levels of doxorubicin drug in tumour explants. Moreover, they showed that these Pd(0) devices uncage a variety of newly developed pro-drugs based on active metabolite of irinotecan,[44] vorinostat,[45] floxuridine,[46] and gembicitabine.[47] Most recently, Unciti-Broceta and coworkers marked another milestone in the field by developing a novel Pd activable 5FU prodrug that can be administered orally as it can evade anabolic and catabolic drug pathways. This pro-drug was activated by intratumourally implanted Pd resins inside a tumour xenograft in mice.[48] This study highlights the potential of using heterogeneous Pd(0) resins for site specific activation of orally administered pro-drugs for new side-effect-free cancer therapies. The work was recently extended to other bioactive molecules as reported by Kane and co-workers, where Pd-NPs were immobilised on TentaGel® resins to activate a prodrug of resatorvid, an anti-inflammatory agent in *in vitro* conditions.[49] In addition to this, Qu and co-workers reported studies on photo-sensitive Pd loaded silica nanoparticles functionalised with azobenzene units that allow light regulated catalyst activation.[50] Another novel approach was pursued by Gu and co-workers, where a bioorthogonal catalytic patch was developed with Pd-NPs coated on TiO_2 nanosheets that can activate pro-drugs in sub-cutaneous tumours in mice.[51]

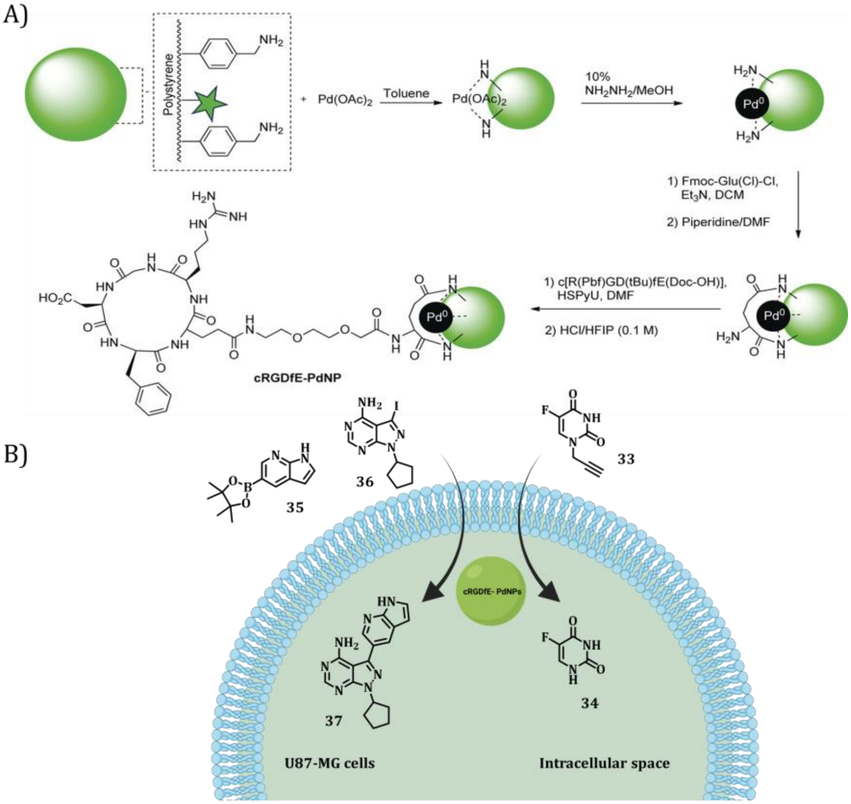

Figure 5: A) Synthesis of RGD functionalised polystyrene Pd-NPs by Clavadetscher *et al.* Image reproduced with permission from Ref.[43] B) Representation of in-cell dual drug synthesis of PP 121 **37** and 5-fluorouracil **34** by these Pd-NPs.[43] Figure created with biorender.com.

A formidable challenge in the field is to bring the catalytic system to the site of interest, which is especially challenging with heterogeneous systems. Santamaria and coworkers together with Unciti-Broceta developed new therapeutic vectors combining the targeting ability of cancer-derived exosomes and catalytic potential of palladium nanosheets for the release of the anti-cancer drug Panobinostat.[52] These heterogeneous vectors not only had the ability to enter cancer cells and remain catalytically active, they also preferentially targeted their progenitor cells from other cells. Further, they perfected the protocol to load Pd-nanosheets inside the exosomes using a mild reduction process using CO without disrupting the membranes thereby protecting surface integrins responsible for targeting.[53]

Gold and copper have also been studied extensively as bioorthogonal catalysts, and the polymer resin-based approach can significantly increase their biocompatibility while lowering toxicity. The first example of heterogeneous gold catalysis in living systems was reported by Unciti-Broceta and co-workers where intracranial activation of a bioorthogonal probe in zebra fish using 75 μm Au-resins was performed.[27] Moreover, they reported an inspiring example of *in vivo* heterogeneous gold catalysis, where localised uncaging of a neuroactive agent, the anxiolytic drug fluoxetine **39**, was demonstrated in the head of zebrafish, which decreased their locomotor activity compared to their normal mode (Figure 6).[28] Also, a novel strategy was developed to increase the number of active metal centers on the outer layer of the polymer scaffold. This was achieved by using an electrostatic loading method to load negatively charged Au-NPs at the positively charged outer amphiphilic layer of NH_2-PEG-grafted polystyrene micro-implants with a diameter of 75 μm (Figure 6A). The study highlights the numerous exciting applications of bioorthogonal chemistry where in this case modification of cognition activity was possible by localised release of a neuroactive agent in the brain of an animal (Figure 6B-E). This is a promising strategy to treat localised neurological disorders such as neuropathic pain if it can be extended to damaged nerves in the future.

The use of copper as a bioorthogonal catalyst was always perceived to be limited due to the inherent toxicity of Cu(I) salts.[54] However, Bradley and co-workers developed non-toxic, biocompatible and implantable heterogeneous copper catalysts for *in vitro* synthesis of a combretastatin analogue, an anticancer agent, using an azide-alkyne cycloaddition. In addition, the *in vivo* synthesis of a fluorophore based on coumarin was achieved in the yolk sac of zebra fish embryos, while no toxicity was observed.[29]

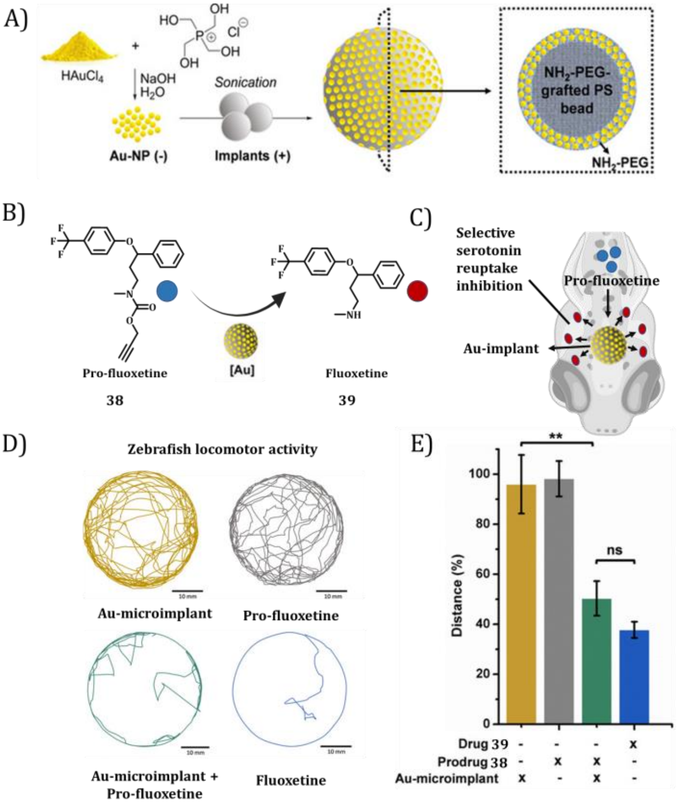

Figure 6: A) Synthesis of polystyrene PEGylated Au-NPs by Ortega-Liebana et al. Image adapted from Ref.[28] B) Generation of anxiolytic drug **39** from inactive precursor **38** by Au-NPs. C) Representation for generation of anxiolytic drug **39** in brain of zebrafish by localised Au-NPs. D) Representative images of the tracked distances of individual zebrafish in a cell culture dish under different treatments. E) Percentage distance swum by zebrafish embryos when treated relative to the DMSO-treated control.[28]

1.3.2 Homogeneous water-compatible polymers as carriers materials for TMCs

While the number of successful examples to catalytically activate prodrugs or make drugs *in vivo* using heterogeneous TMCs is increasing rapidly,[9,55,56] there is an intrinsic challenge to heterogeneous systems, namely that they either need to be implanted at the tumour site using microsurgery or require a delivery vehicle such as exosomes to reach the site of interest. An interesting alternative is the use of nanoparticles based on water-compatible synthetic copolymers. Borrowing from the advances in the field of nanomedicine,[19,57,58] such synthetic polymeric nanoparticles could offer several advantages. For example, polymeric NPs form homogeneous, compartmentalized structures in water that possess hydrophobic interiors, in which apolar TMCs can be physically or covalently trapped and hydrophobic substrates can be sequestered affording high local concentrations. In addition, it is straightforward to attach peripheral targeting groups to help guide the NPs to the tumour sites. Finally, the size and shape of these polymeric NPs is easily controlled by the length and microstructure of the amphiphilic polymers. As a result, amphiphilic block copolymers that from nanoparticles,[13] cationically charged polymers that form micelles, so called polyzymes,[59] and random amphiphilic heterocopolymers that collapse/fold into single-chain polymeric nanoparticles[30,60] have been actively investigated in the last decade .

In 2017, Weissleder and coworkers used poly(lactic-*co*-glycolic acid)-*b*-polyethylene glycol based NPs to encapsulate the hydrophobic bis[tri(2-furyl)phosphine] palladium(II) dichloride (Pd-TFP) catalyst **40** for bioorthogonal prodrug activation (Figure 7A).[13] The NPs were around 60 nm in size and demonstrated good stability in biological solutions. Taking advantage of the enhanced permeability and retention (EPR) effect, the Pd-NPs accumulated at tumour sites in mouse models of cancer. Interestingly, at the tumour site the Pd-NPs activated different model prodrugs, which inhibited tumour growth, and increased the survival of tumour-bearing mice (Figure 7B). Detailed studies showed that the NPs were taken up by cells via an endocytic/macropinocytic process that results predominantly in lysosomal uptake.[61] In addition, their efficacy was further improved by a dual action whereby both the Pd-catalysts as well as the prodrug embedded in NPs were colocalised in the tumour cells via the EPR effect. These detailed studies showed that the use of synthetic polymers, in this case an FDA approved amphiphilic block copolymer, is a viable strategy to simultaneously protect the catalyst from deactivation in complex media as well as deliver the catalytic system to the site of interest *in vivo*.

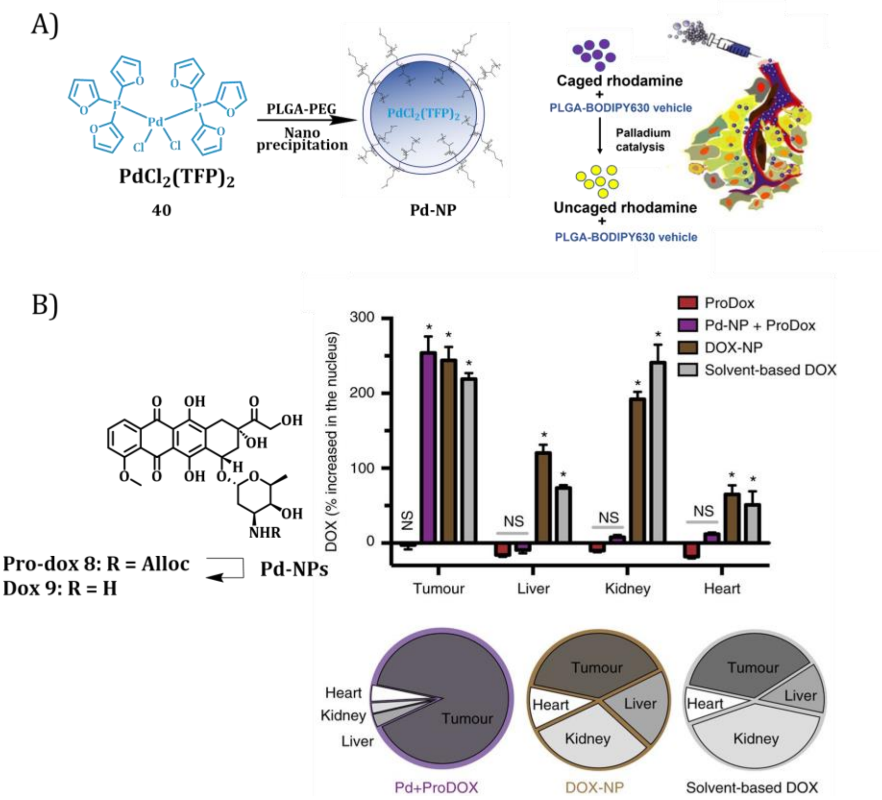

Figure 7: A) Nanoencapsulation of Pd-NPs using PLGA-PEG surfactant, followed by intravenous administration into live xenograft cancer mice models for activation of caged rhodamine and pro-doxorubicin. B) Activation of pro-doxorubicin **8** using Pd-NPs leading to drug accumulation in tumour nuclei of ovarian tumours, but not in the nuclei of key organs related to toxicity. The tumours and organs were excised and imaged for colocalisation between intrinsic doxorubicin fluorescence and DNA after 24 h, pie chart shows the accumulation of nuclear doxorubicin in ovarian tumours and key organs relating to toxicity. Image reproduced with permission from Ref.[13]

In 2020, Rotello and coworkers developed the concept of polyzymes, which are poly(oxanorborneneimides) with pendant cationic tetra-alkylamines that ensure water solubility (Figure 8).[62] In water, these polymers form nanoparticles of around 50 nm in size in which the TMC is non-covalently embedded in the hydrophobic interior (Figure 8B). These systems rely on the hydrophobicity of the TMC to retain the catalyst in the hydrophobic parts of the nanoparticles. Their results showed that the cationic nature of the polyzymes helped to transport a porphyrin-based iron catalyst [Fe(TPP)]Cl **41** across a bacterial biofilm. When adding appropriately protected resorufin, the formation of fluorescent resorufin indicated that the protective group was cleaved, indicating that the Fe-catalyst remained active in the biofilm. Next, appropriately protected prodrugs of the antibacterial agents moxifloxacin and ciprofloxacin, were activated by the polyzyme, and a decreased viability of the biofilms was observed (Figure 8C).

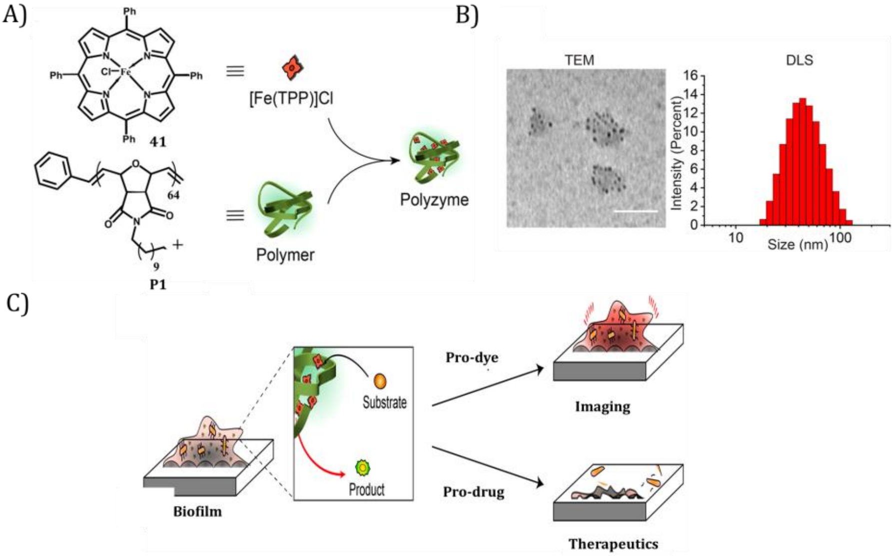

Figure 8: A) Structure of Fe catalyst **41** and poly(oxanorborneneimides) polymer **P1** forming polyzyme. B) Size of polyzymes ~50 nm monitored by transmission electron microscopy and dynamic light scattering. C) Representation of the bioorthogonal activation by polyzymes for imaging and eradication of bacterial biofilms. Image reproduced with permission from Ref.[62]

As the polyzymes showed no acute cytotoxicity for fibroblast cells, which are mammalian cells, the authors continued with bioorthogonally activating prodrugs in the presence of HeLa cells.[59] Here, the Meggers Ru-catalyst[22] was formulated in the hydrophobic compartments of the nanoparticles. Approximately four Ru centers were present per nanoparticle, which showed a size of around 80 nm. The size of the polyzymes remained similar in 10% fetal bovine serum for at least 3 days, highlighting the protective capability of the polymer towards the embedded Ru-TMC. Ru-catalysed deallylation of protected mitoxantrone, a cytotoxic drug, in the presence of HeLa cells showed a reduced cell viability, indicative of the release of the activated drug.

Our group started to explore the use of amphiphilic random heterocopolymers that fold into defined conformations in water as catalyst carriers in 2011 (Figure 9).[63] Engineering the microstructure of the amphiphilic copolymer by balancing the ratio of hydrophilic, hydrophobic and hydrogen-bonding grafts, permitted single polymer chains to spontaneously form particles of nanometer size (5-20 nm), which are referred to as single-chain polymeric nanoparticles (SCPNs).[64] These particles comprise an inner hydrophobic compartment, and a Jeffamine-based hydrophilic periphery. Compared to the previously applied block copolymer NPs,[13] these particles are much smaller and do not have a critical micelle concentration because they are unimolecular. Upon incorporating TMCs[65,66] into the hydrophobic interior of the SCPNs, reactions proceeded at good rates and high lipophiloselectivity for Ru-based transfer hydrogenations and oxidations.[66] Hydrophobic substrates were converted at a much higher rate than hydrophilic substrates in competition reactions, indicating that the logP of the substrate plays an important role in enhancing the local concentration for high logP substrates, and hereby the reaction rate.

As a consequence of these promising early findings, our group started to explore TMC-based SCPNs for bioorthogonal catalysis.[60] In biological environments, both high turnover frequency (TOF) of the TMC as well as high conformational stability of the SCPN are crucial to ensure good catalyst performance over time. Experiments using a covalently attached solvatochromic dye Nile Red indicated that the compartmentalized nature of the SCPNs remained intact in cellular growth media, in the cell’s cytosol and, when an optimized microstructure was used, also inside lysosomal compartments of HeLa cells.[68] In addition, the Jeffamine-based SCPNs showed low toxicity and were taken up by endocytosis only slowly, requiring incubation times of 24 h. By attaching triphenylphosphine-, bipyridine-, or phenantroline-based ligands to the SCPNs, catalytic conversions such as Cu(I)-catalysed click reactions and depropargylations,[67,69] and Pd(II)-catalysed depropargylations, proceeded fast in buffered aqueous media. Interestingly, the use of the dimethylpropargyl group rather than the commonly used propargyl group significantly accelerated the deprotection reactions rate when Cu(I) was used as the catalysts.[67] However, a reduction of activity was observed in the presence of the cell culture medium DMEM with 10% fetal bovine serum. Interestingly, adding HeLa cells did not further reduce activity, suggesting that the hydrophobic proteins in the serum likely represent the most deactivating factor for the Pd(II)- and Cu(I)-based SCPNs. This can be rationalized by two factors (or a combination of the two): (i) the sequestration of hydrophobic substrates by serum protein binding or (ii) the serum proteins inactivate the catalyst. The fact that the catalyst in DMEM reached a plateau before full conversion, indicated that the catalyst loses efficacy over time. Gratifyingly, the results also showed that a pro-rhodamine dye was still successfully converted into a fluorescent product by depropargylation when the SCPN-based catalysts were added to the cultured HeLa cells (Figure 9B,C).

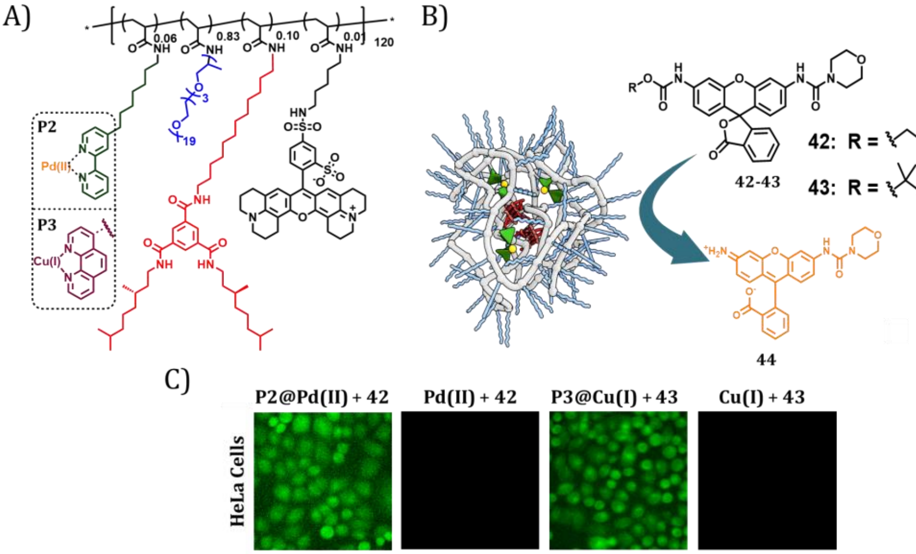

Figure 9: A) Structure of polyacrylamide-based polymers developed by Palmans and co-workers for depropargylation reactions in biological settings.[67] B) Structure of protected rhodamines **42** and **43** for activation. C) Activation of pro-dye **42** and **43** in HeLa cells using Pd(II) and Cu(I) catalysts respectively.

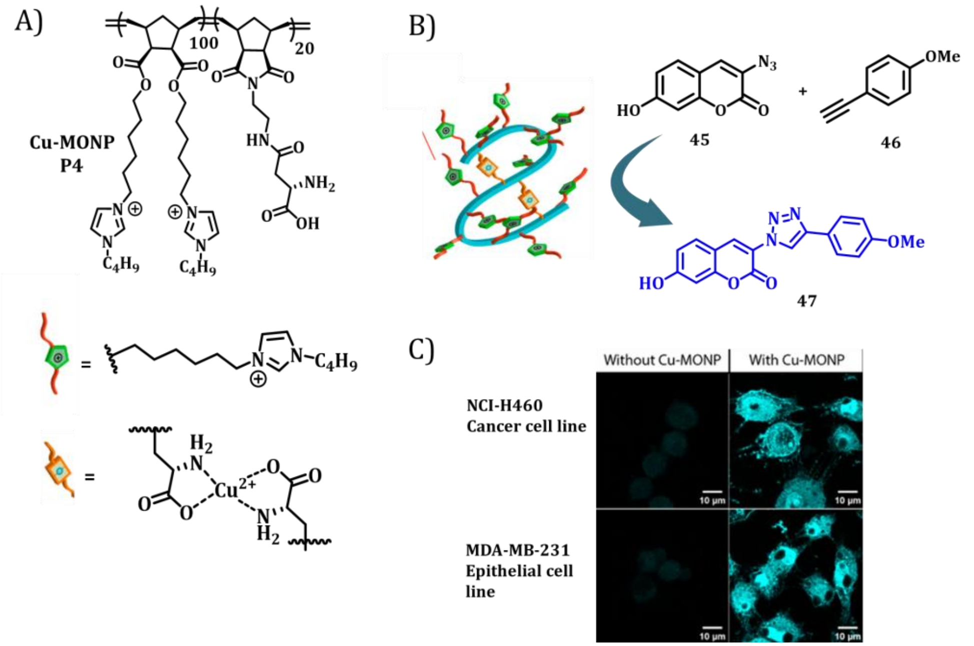

Figure 10: A) Structure of polynorbornene-based polymer **P4** developed by Zimmerman and co-workers for intracellular click reactions. B) Fluorogenic click compounds used for reactions in living cells **45** and **46** C) Confocal microscopy study of intracellular catalysis of the click reaction between **45** and **46** in cancer and epithelial cell lines using Cu-MONP. Image reproduced with permission from Ref. [30]

The previously discussed SCPNs were based on amphiphilic polyacrylamide-based polymers with Jeffamine M-1000 grafts to impart water solubility. In contrast, the group of Zimmerman focused on polynorbornene-based amphiphilic polymers made via Ru-catalysed ring-opening metathesis polymerisation (ROMP) with both water soluble imidazolium groups and aspartate-bearing grafts for copper binding (Figure 10A).[30] After the addition of Cu(II), particles with sizes < 10 nm were formed in water, which were referred to as copper-crosslinked single-chain metal-organic nanoparticles (Cu-MONPs). By *in situ* reduction to Cu(I) using sodium ascorbate (NaAsc), the Cu-MONPs showed very high activities in azide-alkyne click reactions at ppm catalyst concentration, also in the presence of different cell types (Figure 10B,C).[30,70] The rate of reaction was found to have a strong correlation with charge and hydrophobicity of the alkyne substrate, with more hydrophobic substrates and negatively charged substrates reacting faster. Interestingly, the alkyne substrate must enter the particles' interior in order for the reaction to occur, which corroborated that binding of the substrate to the particles interior was crucial for turnover. Recently, Bai and co-workers introduced a polymerisation-crosslinking method to obtain polynorbornene-based dense shell nanoparticle scaffolds with the aim to embed the Cu-containing nanoparticles (NPs) in the membrane of cells.[71] Such embedding was envisaged to reduce catalyst poisoning on the one hand but at the same time allow the synthesis of drug targets of low membrane permeability inside the membrane, hereby facilitating the uptake. A systematic investigation on the nature of the cationic group used for water-compatibility —phosphonium, imidazolium or ammonium— revealed a dramatic effect on the cytotoxicity of the NPs on mammalian NIH/3T3 cells, with the phosphonium-based NPs showing the best biocompatibility. In addition, a balance between water-soluble phosphonium and oligo-ethylene glycol pendants was necessary to retain the NPs in the membrane. Interestingly, different monomolecular and bimolecular reactions at low concentrations were possible, as well as the cell internalization of less-cell-permeable molecules by synthesizing them directly inside the membrane.

Zimmerman and co-workers also investigated intramolecularly crosslinked polyacrylamide-based Cu-SCNPs comprising a tris(triazolylmethyl)amine-based ligand for Cu-binding and cationically charged grafts for water solubility.[72] These particles showed very high activity for click reactions, and were also very efficient for click reactions on modified protein surfaces and cell surface glycans. The catalysis was proposed to occur through an "attach mode" where the SCNPs reversibly bind protein surfaces through multiple hydrophobic and electrostatic contacts. The polyacrylamide-based systems were further functionalised with light-activatable Ru-catalysts (Figure 11A).[73] The co-delivery of these Ru-SCPNs with β-galactosidase (β-gal) was possible via endosomal uptake into HeLa cells (Figure 11B). An azide-containing doxorubicin derivative **49** and a galactose-masked combretastatin A4 **50** were chosen as the prodrugs, able to be activated via light-activated Ru-catalysis and β-gal induced galactose cleavage, respectively (Figure 11C). After intracellular activation, both anticancer agents were released as evidence by the significant reduction in cell viability.

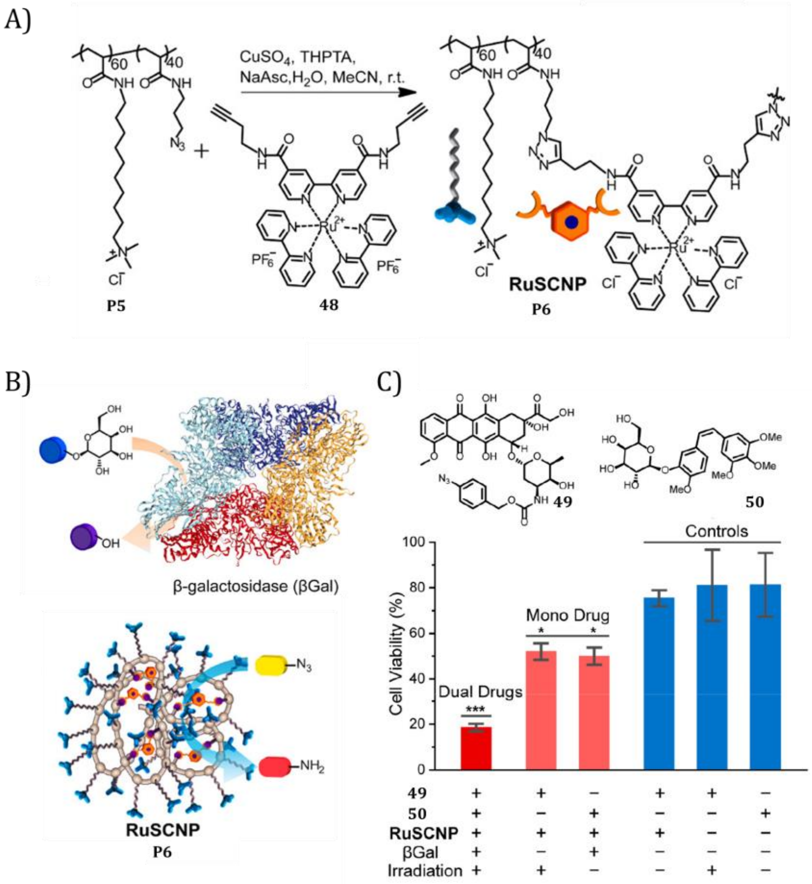

Figure 11: A) Synthesis of RuSCNP using Ru catalyst **48**. B) Illustration of dual catalysis performed by β-galactosidase and RuSCNP. C) Intracellular dual drug activation of drugs **49** and **50** in HeLa cells monitored by cell viability assay by performed by β-galactosidase and RuSCNP. Adapted with permission from ref.[73] Copyright 2020 American Chemical Society.

Further work[74] using neutral rather than cationically charged polymers and replacing Cu by Ru to afford Ru-SCNPs showed that also allylcarbamate cleavage reactions were feasible in biologically relevant conditions using a modified Meggers-type Ru catalyst.[75] In the presence of DMEM and DMEM containing 5 mM glutathione, the Ru-SCNP showed decent conversions. In HeLa cell lysate, in contrast, lower initial rates and lower percent conversions were observed, a consequence of the complex environment of the cell lysate. The lower activity of Ru-SCNP in cell lysate was assigned to a reduced ability to bind substrates and due to unfolding of the polymer chain that results in enhanced interactions of the TMC with specific cellular bio- macromolecules.

1.4 Challenges in developing bioorthogonal catalysts based on homogeneous water-compatible polymers

Despite great progress and the Nobel prize in 2022 underlining the importance of the field of bioorthogonal chemistry, the number of examples of TMC-based catalysts that successfully function in *in vivo* models is still limited. This can be rationalized by the high degree of interdisciplinarity that is required between the fields of catalysis, carrier material development and medicinal chemistry. Progress in this area requires a number of issues to be addressed simultaneously rather than separately. First, the TMC, its carrier material, and the combination of the two should be non-toxic. While *in vitro* cell studies are a good start to establish toxicity effects, there are still only few studies that have been conducted in living systems and that have investigated long-term toxicity effects. Second, the TMC needs to show high activity, which is typically achieved by optimization of the ligand-metal complex. Third, long term stability of the catalyst is needed in the presence of competitive compounds that abound in biological media. As this is a consequence of the metal-ligand interaction, and since higher binding constants result in lower catalyst activity, the effects of ligand-metal binding strength on activity and stability typically require a compromise. Fourth, for *in vivo* prodrug activation or *in situ* drug formation for therapeutic applications, the TMC needs to accumulate or be present at a site of interest. While elegant approaches have been worked out for heterogeneous systems, such as localising the catalysts via microsurgery or the use of exosomes for Pd-nanoparticles, only very few non-invasive targeting approaches have been evaluated till now for homogeneous polymer-based systems.

Amphiphilic polymeric carriers to which suitable ligands are covalently bound, form compartmentalized nanostructures of tunable size, with hydrophobic regions, which comprise the TMC. The hydrophobic regions help sequester hydrophobic substrates, and when these are in the vicinity of the TMC, the high local concentration of both substrates and catalyst will result in an increase of the reaction rates. Stably folded polymeric NPs that mimic the folding of polypeptides into enzymes, can likely also help protect the TMC by shielding it from interactions with competitive compounds, hereby enhancing stability. From the nanomedicine field, a vast knowledge is available on desired sizes and shapes of polymeric carrier materials. In addition, synthetic polymers can be easily functionalised with selective targeting groups that can assist in guiding the TMC-based NPs to the site of interest. Despite the current debate on the EPR effect[76] and the challenges associated with targeted nanoparticle delivery to tumour sites,[77] combined with the vast differences that exist between different types of tumours, advances in the field of nanomedicine will be beneficial to help design suitable carriers for TMCs.[78] All in all, the versatility of synthetic polymers, and the ability to control their microstructure and hereby the superstructures they form, make homogeneous polymer-based TMCs highly complementary to heterogeneous TMC-NP.

1.5 Aim and Outline of this thesis

As outlined in the literature overview, amphiphilic polymer catalyst carriers have great potential to advance the field of bioorthogonal catalysis for applications in biomedicine, albeit that several challenges need to be addressed. Although ambitious, the development of catalytic single-chain polymeric nanoparticles as bioorthogonal catalysts with an efficiency that can match the level metalloenzymes is highly desirable to push the boundaries of the field. The aim of this thesis is to understand how catalytic efficiency of SCPNs can be improved to perform desired functions in the presence of living cells. A systematic and detailed approach was used to achieve this, with catalysis studies performed in aqueous solutions gradually increasing medium complexity, and finally in the presence of living cells, to understand all of the contributing factors that affect catalyst performance. Further, a first step was taken in the direction of understanding their function at single-particle level, which in future can help to elucidate the structure-activity relationships, the key to achieve enzyme-like efficiency. The insights gained from this thesis can be helpful for the rational design of efficient catalytic SCPNs for bio-orthogonal catalysis in future.

In Chapter 2, we looked at different aspects of the Pd(II)-SCPN based catalytic system that can affect its performance in complex media. For this, we developed amphiphilic polymers with polyacrylamide backbone and functionalised them with the Pd(II)-binding ligands triphenylphosphine and bipyridine. We evaluated the effect of polymer microstructure, ligand–metal complex, and substrate hydrophobicity on the catalytic activity of the nanoparticles for depropargylation reactions in water, PBS and DMEM. Triphenylphosphine-based polymeric nanoparticles was then used to activate anti-cancer pro-drugs based on 5FU, paclitaxel, and doxorubicin in complex media. The results showed that structure of pro-drugs also have a strong influence on how efficiently it gets activated by SCPNs.

In Chapter 3, the above triphenylphosphine based Pd(II) amphiphilic polymeric nanoparticles were reduced to Pd(0) nanoparticles using CO, a mild reductant. This helped to achieve fast kinetics in depropargylation reaction even in complex media that allowed us to evaluate their performance in the presence of living cells. Activation of a protected rhodamine and pro-drug of 5FU in presence of living cells revealed that the performance of these nanoparticles is impacted by the differences in polymer microstructure, size of the formed Pd(0) NPs and amount of stabilizing ligand on the backbone.

In Chapter 4, we explored the capability of SCPNs to non-covalently encapsulate hydrophobic rhodium-based catalysts, thereby allowing to export the functions of highly active and stable metal complexes to complex media. For this, we looked at NH insertion reactions that can form fluorescent and bioactive benzoquinoxaline products catalysed by dirhodium(II) catalysts encapsulated inside SCPNs. The reactions were truly catalytic in nature and could be exported to complex media without any loss in catalytic efficiency thus expanding the possibilities of catalytic SCPNs to perform efficient and diverse reactions *in vitro*.

In Chapter 5, we took a first step to look at the heterogeneity in the catalytic function of polymeric nanoparticles at the single-particle level. Towards this, highly efficient Cu-SCPNs were developed that showed enzyme-like Michaelis–Menten behavior at ensemble-level towards depropargylation reactions in water. We observed an intraparticle turnover dispersity within same batch of polymeric nanoparticles, which revealed the heterogeneity in the function of catalytic SCPNs for the first time. Although preliminary, this study paves the way for studying the structure-activity relationships of diverse catalytic SCPNs in future.

1.6 References

(1) Dobson, C. M. Protein Folding and Misfolding. *Nature* **2003**, *426* (6968), 884–890. https://doi.org/10.1038/nature02261.

(2) Dill, K. A.; MacCallum, J. L. The Protein-Folding Problem, 50 Years On. *Science* **2012**, *338* (6110), 1042–1046. https://doi.org/10.1126/science.1219021.

(3) Baker, D. What Has de Novo Protein Design Taught Us about Protein Folding and Biophysics? *Protein Sci.* **2019**, *28* (4), 678–683. https://doi.org/10.1002/pro.3588.

(4) Martí, S.; Roca, M.; Andrés, J.; Moliner, V.; Silla, E.; Tuñón, I.; Bertrán, J. Theoretical Insights in Enzyme Catalysis. *Chem Soc Rev* **2004**, *33* (2), 98–107. https://doi.org/10.1039/B301875J.

(5) Chen, K.; Arnold, F. H. Engineering New Catalytic Activities in Enzymes. *Nat. Catal.* **2020**, 1–11. https://doi.org/10.1038/s41929-019-0385-5.

(6) Scinto, S. L.; Bilodeau, D. A.; Hincapie, R.; Lee, W.; Nguyen, S. S.; Xu, M.; am Ende, C. W.; Finn, M. G.; Lang, K.; Lin, Q.; Pezacki, J. P.; Prescher, J. A.; Robillard, M. S.; Fox, J. M. Bioorthogonal Chemistry. *Nat. Rev. Methods Primer* **2021**, *1* (1), 30. https://doi.org/10.1038/s43586-021-00028-z.

(7) Bai, Y.; Chen, J.; Zimmerman, S. C. Designed Transition Metal Catalysts for Intracellular Organic Synthesis. *Chem. Soc. Rev.* **2018**, *47* (5), 1811–1821. https://doi.org/10.1039/C7CS00447H.

(8) Völker, T.; Dempwolff, F.; Graumann, P. L.; Meggers, E. Progress towards Bioorthogonal Catalysis with Organometallic Compounds. *Angew. Chem. Int. Ed Engl.* **2014**, *53* (39), 10536–10540. https://doi.org/10.1002/anie.201404547.

(9) van de L'Isle, M. O. N.; Ortega-Liebana, M. C.; Unciti-Broceta, A. Transition Metal Catalysts for the Bioorthogonal Synthesis of Bioactive Agents. *Curr. Opin. Chem. Biol.* **2021**, *61*, 32–42. https://doi.org/10.1016/j.cbpa.2020.10.001.

(10) Unciti-Broceta, A.; Johansson, E. M. V; Yusop, R. M.; Sánchez-Martín, R. M.; Bradley, M. Synthesis of Polystyrene Microspheres and Functionalization with Pd0 Nanoparticles to Perform Bioorthogonal Organometallic Chemistry in Living Cells. *Nat. Protoc.* **2012**, *7* (6), 1207–1218. https://doi.org/10.1038/nprot.2012.052.

(11) Dumas, A.; Spicer, C. D.; Gao, Z.; Takehana, T.; Lin, Y. A.; Yasukohchi, T.; Davis, B. G. Self-Liganded Suzuki-Miyaura Coupling for Site-Selective Protein PEGylation. *Angew Chem Int Ed* **2013**, *52* (14), 3916–3921. https://doi.org/10.1002/anie.201208626.

(12) Spicer, C. D.; Triemer, T.; Davis, B. G. Palladium-Mediated Cell-Surface Labeling. *J. Am. Chem. Soc.* **2012**, *134* (2), 800–803. https://doi.org/10.1021/ja209352s.

(13) Miller, M. A.; Askevold, B.; Mikula, H.; Kohler, R. H.; Pirovich, D.; Weissleder, R. Nano-Palladium Is a Cellular Catalyst for *in vivo* Chemistry. *Nat. Commun.* **2017**, *8* (May), 15906. https://doi.org/10.1038/ncomms15906.

(14) Li, N.; Lim, R. K. V; Edwardraja, S.; Lin, Q. Copper-Free Sonogashira Cross-Coupling for Functionalization of Alkyne-Encoded Proteins in Aqueous Medium and in Bacterial Cells. *J. Am. Chem. Soc.* **2011**, *133* (39), 15316–15319. https://doi.org/10.1021/ja2066913.

(15) Gutiérrez, S.; Tomás-Gamasa, M.; Mascareñas, J. L.; Tomás-gamasa, M.; Mascareñas, J. L. Exporting Metal-Carbene Chemistry to Live Mammalian Cells: Copper-Catalyzed Intracellular Synthesis of Quinoxalines Enabled by N−H Carbene Insertions. *Angew. Chem. Int. Ed.* **2021**, *60* (40), 22017–22025. https://doi.org/10.1002/anie.202108899.

(16) Coelho, S. E.; Schneider, F. S. S.; de Oliveira, D. C.; Tripodi, G. L.; Eberlin, M. N.; Caramori, G. F.; de Souza, B.; Domingos, J. B. Mechanism of Palladium(II)-Mediated Uncaging Reactions of Propargylic Substrates. *ACS Catal.* **2019**, *9* (5), 3792–3799. https://doi.org/10.1021/acscatal.9b00210.

(17) Latocheski, E.; Dal Forno, G. M.; Ferreira, T. M.; Oliveira, B. L.; Bernardes, G. J. L.; Domingos, J. B. Mechanistic Insights into Transition Metal-Mediated Bioorthogonal Uncaging Reactions. *Chem. Soc. Rev.* **2020**, *49* (21), 7710–7729. https://doi.org/10.1039/D0CS00630K.

(18) Devaraj, N. K. The Future of Bioorthogonal Chemistry. *ACS Cent. Sci.* **2018**, *4* (8), 952–959. https://doi.org/10.1021/acscentsci.8b00251.

(19) Sun, T.; Zhang, Y. S.; Pang, B.; Hyun, D. C.; Yang, M.; Xia, Y. Engineered Nanoparticles for Drug Delivery

in Cancer Therapy. *Angew Chem Int Ed* **2014**, *53* (46), 12320–12364. https://doi.org/10.1002/anie.201403036.

(20) Blanco, E.; Shen, H.; Ferrari, M. Principles of Nanoparticle Design for Overcoming Biological Barriers to Drug Delivery. *Nat. Biotechnol.* **2015**, *33* (9), 941–951. https://doi.org/10.1038/nbt.3330.

(21) Anthony, E. J.; Bolitho, E. M.; Bridgewater, H. E.; Carter, O. W. L.; Donnelly, J. M.; Imberti, C.; Lant, E. C.; Lermyte, F.; Needham, R. J.; Palau, M.; Sadler, P. J.; Shi, H.; Wang, F.-X.; Zhang, W.-Y.; Zhang, Z. Metallodrugs Are Unique: Opportunities and Challenges of Discovery and Development. *Chem. Sci.* **2020**, *11* (48), 12888–12917. https://doi.org/10.1039/D0SC04082G.

(22) Streu, C.; Meggers, E. Ruthenium-Induced Allylcarbamate Cleavage in Living Cells. *Angew Chem Int Ed* **2006**, *45* (34), 5645–5648. https://doi.org/10.1002/anie.200601752.

(23) Tanaka, S.; Saburi, H.; Hirakawa, T.; Seki, T.; Kitamura, M. Dehydrative Allylation of Alcohols and Deallylation of Allyl Ethers Catalyzed by [CpRu(CH 3 CN) 3]PF 6 and 2-Pyridinecarboxylic Acid Derivatives. Effect of π-Accepting Ability and COOH Acidity of Ligand on Reactivity. *Chem. Lett.* **2009**, *38* (2), 188–189. https://doi.org/10.1246/cl.2009.188.

(24) Yusop, R. M.; Unciti-Broceta, A.; Johansson, E. M. V.; Sánchez-Martín, R. M.; Bradley, M. Palladium-Mediated Intracellular Chemistry. *Nat. Chem.* **2011**, *3* (3), 239–243. https://doi.org/10.1038/nchem.981.

(25) Martínez-Calvo, M.; Couceiro, J. R.; Destito, P.; Rodríguez, J.; Mosquera, J.; Mascareñas, J. L. Intracellular Deprotection Reactions Mediated by Palladium Complexes Equipped with Designed Phosphine Ligands. *ACS Catal.* **2018**, *8* (7), 6055–6061. https://doi.org/10.1021/acscatal.8b01606.

(26) Weiss, J. T.; Dawson, J. C.; Macleod, K. G.; Rybski, W.; Fraser, C.; Torres-Sánchez, C.; Patton, E. E.; Bradley, M.; Carragher, N. O.; Unciti-Broceta, A. Extracellular Palladium-Catalysed Dealkylation of 5-Fluoro-1-Propargyl-Uracil as a Bioorthogonally Activated Prodrug Approach. *Nat. Commun.* **2014**, *5* (1), 3277. https://doi.org/10.1038/ncomms4277.

(27) Pérez-López, A. M.; Rubio-Ruiz, B.; Sebastián, V.; Hamilton, L.; Adam, C.; Bray, T. L.; Irusta, S.; Brennan, P. M.; Lloyd-Jones, G. C.; Sieger, D.; Santamaría, J.; Unciti-Broceta, A. Gold-Triggered Uncaging Chemistry in Living Systems. *Angew. Chem. Int. Ed.* **2017**, *56* (41), 12548–12552. https://doi.org/10.1002/anie.201705609.

(28) Ortega-Liebana, M. C.; Porter, N. J.; Adam, C.; Valero, T.; Hamilton, L.; Sieger, D.; Becker, C. G.; Unciti-Broceta, A. Truly-Biocompatible Gold Catalysis Enables Vivo-Orthogonal Intra-CNS Release of Anxiolytics. *Angew. Chem. Int. Ed.* **2022**, *61* (1), 1–5. https://doi.org/10.1002/anie.202111461.

(29) Clavadetscher, J.; Hoffmann, S.; Lilienkampf, A.; Mackay, L.; Yusop, R. M.; Rider, S. A.; Mullins, J. J.; Bradley, M. Copper Catalysis in Living Systems and *In situ* Drug Synthesis. *Angew. Chem. Int. Ed.* **2016**, *55* (50), 15662–15666. https://doi.org/10.1002/anie.201609837.

(30) Bai, Y.; Feng, X.; Xing, H.; Xu, Y.; Kim, B. K.; Baig, N.; Zhou, T.; Gewirth, A. A.; Lu, Y.; Oldfield, E.; Zimmerman, S. C. A Highly Efficient Single-Chain Metal–Organic Nanoparticle Catalyst for Alkyne–Azide “Click” Reactions in Water and in Cells. *J. Am. Chem. Soc.* **2016**, *138* (35), 11077–11080. https://doi.org/10.1021/jacs.6b04477.

(31) Bose, S.; Ngo, A. H.; Do, L. H. Intracellular Transfer Hydrogenation Mediated by Unprotected Organoiridium Catalysts. *J. Am. Chem. Soc.* **2017**, *139* (26), 8792–8795. https://doi.org/10.1021/jacs.7b03872.

(32) Oliveira, B. L.; Stenton, B. J.; Unnikrishnan, V. B.; de Almeida, C. R.; Conde, J.; Negrão, M.; Schneider, F. S. S.; Cordeiro, C.; Ferreira, M. G.; Caramori, G. F.; Domingos, J. B.; Fior, R.; Bernardes, G. J. L. Platinum-Triggered Bond-Cleavage of Pentynoyl Amide and N -Propargyl Handles for Drug-Activation. *J. Am. Chem. Soc.* **2020**, *142* (24), 10869–10880. https://doi.org/10.1021/jacs.0c01622.

(33) Sasmal, P. K.; Carregal-Romero, S.; Han, A. A.; Streu, C. N.; Lin, Z.; Namikawa, K.; Elliott, S. L.; Köster, R. W.; Parak, W. J.; Meggers, E. Catalytic Azide Reduction in Biological Environments. *ChemBioChem* **2012**, *13* (8), 1116–1120. https://doi.org/10.1002/cbic.201100719.

(34) Chankeshwara, S. V; Indrigo, E.; Bradley, M. Palladium-Mediated Chemistry in Living Cells. *Curr. Opin. Chem. Biol.* **2014**, *21*, 128–135. https://doi.org/10.1016/j.cbpa.2014.07.007.

(35) Wang, J.; Cheng, B.; Li, J.; Zhang, Z.; Hong, W.; Chen, X.; Chen, P. R. Chemical Remodeling of Cell-Surface Sialic Acids through a Palladium-Triggered Bioorthogonal Elimination Reaction. *Angew. Chem. Int. Ed.* **2015**, *54* (18), 5364–5368. https://doi.org/10.1002/anie.201409145.

(36) Agard, N. J.; Prescher, J. A.; Bertozzi, C. R. A Strain-Promoted [3 + 2] Azide−Alkyne Cycloaddition for Covalent Modification of Biomolecules in Living Systems. *J. Am. Chem. Soc.* **2004**, *126* (46), 15046–15047. https://doi.org/10.1021/ja044996f.

(37) Chan, T. R.; Hilgraf, R.; Sharpless, K. B.; Fokin, V. V. Polytriazoles as Copper(I)-Stabilizing Ligands in Catalysis. *Org. Lett.* **2004**, *6* (17), 2853–2855. https://doi.org/10.1021/ol0493094.

(38) Kennedy, D. C.; McKay, C. S.; Legault, M. C. B.; Danielson, D. C.; Blake, J. A.; Pegoraro, A. F.; Stolow, A.; Mester, Z.; Pezacki, J. P. Cellular Consequences of Copper Complexes Used To Catalyze Bioorthogonal Click Reactions. *J. Am. Chem. Soc.* **2011**, *133* (44), 17993–18001. https://doi.org/10.1021/ja2083027.

(39) Guo, Y.-Y.; Zhang, B.; Wang, L.; Huang, S.; Wang, S.; You, Y.; Zhu, G.; Zhu, A.; Geng, M.; Li, L. An Efficient and Easily-Accessible Ligand for Cu(I)-Catalyzed Azide–Alkyne Cycloaddition Bioconjugation. *Chem. Commun.* **2020**, *56* (92), 14401–14403. https://doi.org/10.1039/D0CC06348G.

(40) McKay, C. S.; Finn, M. G. Click Chemistry in Complex Mixtures: Bioorthogonal Bioconjugation. *Chem. Biol.* **2014**, *21* (9), 1075–1101. https://doi.org/10.1016/j.chembiol.2014.09.002.

(41) Cho, J. K.; Najman, R.; Dean, T. W.; Ichihara, O.; Muller, C.; Bradley, M. Captured and Cross-Linked Palladium Nanoparticles. *J. Am. Chem. Soc.* **2006**, *128* (19), 6276–6277. https://doi.org/10.1021/ja057480k.

(42) Bray, T. L.; Salji, M.; Brombin, A.; Pérez-López, A. M.; Rubio-Ruiz, B.; Galbraith, L. C. A.; Patton, E. E.; Leung, H. Y.; Unciti-Broceta, A. Bright Insights into Palladium-Triggered Local Chemotherapy. *Chem. Sci.* **2018**, *9* (37), 7354–7361. https://doi.org/10.1039/C8SC02291G.

(43) Clavadetscher, J.; Indrigo, E.; Chankeshwara, S. V.; Lilienkampf, A.; Bradley, M. In-Cell Dual Drug Synthesis by Cancer-Targeting Palladium Catalysts. *Angew Chem Int Ed* **2017**, *56* (24), 6864–6868. https://doi.org/10.1002/anie.201702404.

(44) Adam, C.; Pérez-López, A. M.; Hamilton, L.; Rubio-Ruiz, B.; Bray, T. L.; Sieger, D.; Brennan, P. M.; Unciti-Broceta, A. Bioorthogonal Uncaging of the Active Metabolite of Irinotecan by Palladium-Functionalized Microdevices. *Chem Eur J* **2018**, *24* (63), 16783–16790. https://doi.org/10.1002/chem.201803725.

(45) Rubio-Ruiz, B.; Weiss, J. T.; Unciti-Broceta, A. Efficient Palladium-Triggered Release of Vorinostat from a Bioorthogonal Precursor. *J. Med. Chem.* **2016**, *59* (21), 9974–9980. https://doi.org/10.1021/acs.jmedchem.6b01426.

(46) Weiss, J. T.; Carragher, N. O.; Unciti-Broceta, A. Palladium-Mediated Dealkylation of N-Propargyl-Floxuridine as a Bioorthogonal Oxygen-Independent Prodrug Strategy. *Sci. Rep.* **2015**, *5* (1), 9329. https://doi.org/10.1038/srep09329.

(47) Weiss, J. T.; Dawson, J. C.; Fraser, C.; Rybski, W.; Torres-Sánchez, C.; Bradley, M.; Patton, E. E.; Carragher, N. O.; Unciti-Broceta, A. Development and Bioorthogonal Activation of Palladium-Labile Prodrugs of Gemcitabine. *J. Med. Chem.* **2014**, *57* (12), 5395–5404. https://doi.org/10.1021/jm500531z.

(48) Adam, C.; Bray, T. L.; Pérez-López, A. M.; Tan, E. H.; Rubio-Ruiz, B.; Baillache, D. J.; Houston, D. R.; Salji, M. J.; Leung, H. Y.; Unciti-Broceta, A. A 5FU Precursor Designed to Evade Anabolic and Catabolic Drug Pathways and Activated by Pd Chemistry *In vitro* and *In vivo*. *J. Med. Chem.* **2022**, *65* (1), 552–561. https://doi.org/10.1021/acs.jmedchem.1c01733.

(49) Plunk, M. A.; Alaniz, A.; Olademehin, O. P.; Ellington, T. L.; Shuford, K. L.; Kane, R. R. Design and Catalyzed Activation of Tak-242 Prodrugs for Localised Inhibition of TLR4-Induced Inflammation. *ACS Med. Chem. Lett.* **2020**, *11* (2), 141–146. https://doi.org/10.1021/acsmedchemlett.9b00518.

(50) Wang, F.; Zhang, Y.; Du, Z.; Ren, J.; Qu, X. Designed Heterogeneous Palladium Catalysts for Reversible Light-Controlled Bioorthogonal Catalysis in Living Cells. *Nat. Commun.* **2018**, *9* (1), 1209. https://doi.org/10.1038/s41467-018-03617-x.

(51) Chen, Z.; Li, H.; Bian, Y.; Wang, Z.; Chen, G.; Zhang, X.; Miao, Y.; Wen, D.; Wang, J.; Wan, G.; Zeng, Y.; Abdou, P.; Fang, J.; Li, S.; Sun, C.-J.; Gu, Z. Bioorthogonal Catalytic Patch. *Nat. Nanotechnol.* **2021**, *16* (8), 933–941. https://doi.org/10.1038/s41565-021-00910-7.

(52) Sancho-Albero, M.; Rubio-Ruiz, B.; Pérez-López, A. M.; Sebastián, V.; Martín-Duque, P.; Arruebo, M.; Santamaría, J.; Unciti-Broceta, A. Cancer-Derived Exosomes Loaded with Ultrathin Palladium Nanosheets for Targeted Bioorthogonal Catalysis. *Nat. Catal.* **2019**, *2* (10), 864–872. https://doi.org/10.1038/s41929-019-0333-4.

(53) Sebastian, V.; Sancho-Albero, M.; Arruebo, M.; Pérez-López, A. M.; Rubio-Ruiz, B.; Martin-Duque, P.; Unciti-Broceta, A.; Santamaría, J. Nondestructive Production of Exosomes Loaded with Ultrathin Palladium Nanosheets for Targeted Bio-Orthogonal Catalysis. *Nat. Protoc.* **2021**, *16* (1), 131–163. https://doi.org/10.1038/s41596-020-00406-z.

(54) Macomber, L.; Imlay, J. A. The Iron-Sulfur Clusters of Dehydratases Are Primary Intracellular Targets of Copper Toxicity. *Proc. Natl. Acad. Sci.* **2009**, *106* (20), 8344–8349. https://doi.org/10.1073/pnas.0812808106.

(55) Wang, W.; Zhang, X.; Huang, R.; Hirschbiegel, C.-M.; Wang, H.; Ding, Y.; Rotello, V. M. *In situ* Activation of

Therapeutics through Bioorthogonal Catalysis. *Adv. Drug Deliv. Rev.* **2021**, *176*, 113893. https://doi.org/10.1016/j.addr.2021.113893.

(56) Lozhkin, B.; Ward, T. R. Bioorthogonal Strategies for the *in vivo* Synthesis or Release of Drugs. *Bioorg. Med. Chem.* **2021**, *45*, 116310. https://doi.org/10.1016/J.BMC.2021.116310.

(57) Bobo, D.; Robinson, K. J.; Islam, J.; Thurecht, K. J.; Corrie, S. R. Nanoparticle-Based Medicines: A Review of FDA-Approved Materials and Clinical Trials to Date. *Pharm. Res.* **2016**, *33* (10), 2373–2387. https://doi.org/10.1007/s11095-016-1958-5.

(58) Barua, S.; Mitragotri, S. Challenges Associated with Penetration of Nanoparticles across Cell and Tissue Barriers: A Review of Current Status and Future Prospects. *Nano Today* **2014**, *9* (2), 223–243. https://doi.org/10.1016/j.nantod.2014.04.008.

(59) Zhang, X.; Landis, R. F.; Keshri, P.; Cao-Milán, R.; Luther, D. C.; Gopalakrishnan, S.; Liu, Y.; Huang, R.; Li, G.; Malassiné, M.; Uddin, I.; Rondon, B.; Rotello, V. M. Intracellular Activation of Anticancer Therapeutics Using Polymeric Bioorthogonal Nanocatalysts. *Adv. Healthc. Mater.* **2021**, *10* (5), 2001627. https://doi.org/10.1002/adhm.202001627.

(60) Liu, Y.; Pauloehrl, T.; Presolski, S. I.; Albertazzi, L.; Palmans, A. R. A.; Meijer, E. W. Modular Synthetic Platform for the Construction of Functional Single-Chain Polymeric Nanoparticles: From Aqueous Catalysis to Photosensitization. *J. Am. Chem. Soc.* **2015**, *137* (40), 13096–13106. https://doi.org/10.1021/jacs.5b08299.

(61) Kronister, S.; Luthria, G.; Mikula, H.; Mitchison, T.; Li, R.; Kohler, R. H.; Weissleder, R.; Miller, M. A.; Prytyskach, M. Modular Nanoparticulate Prodrug Design Enables Efficient Treatment of Solid Tumors Using Bioorthogonal Activation. *ACS Nano* **2018**, *12* (12), 12814–12826. https://doi.org/10.1021/acsnano.8b07954.

(62) Huang, R.; Li, C.-H.; Cao-Milán, R.; He, L. D.; Makabenta, J. M.; Zhang, X.; Yu, E.; Rotello, V. M. Polymer-Based Bioorthogonal Nanocatalysts for the Treatment of Bacterial Biofilms. *J. Am. Chem. Soc.* **2020**, *142* (24), 10723–10729. https://doi.org/10.1021/jacs.0c01758.

(63) Terashima, T.; Mes, T.; de Greef, T. F. A.; Gillissen, M. A. J.; Besenius, P.; Palmans, A. R. A.; Meijer, E. W. Single-Chain Folding of Polymers for Catalytic Systems in Water. *J. Am. Chem. Soc.* **2011**, *133* (13), 4742–4745. https://doi.org/10.1021/ja2004494.

(64) ter Huurne, G. M.; de Windt, L. N. J.; Liu, Y.; Meijer, E. W.; Voets, I. K.; Palmans, A. R. A. A. Improving the Folding of Supramolecular Copolymers by Controlling the Assembly Pathway Complexity. *Macromolecules* **2017**, *50* (21), 8562–8569. https://doi.org/10.1021/acs.macromol.7b01769.

(65) Artar, M.; Terashima, T.; Sawamoto, M.; Meijer, E. W.; Palmans, A. R. A. Understanding the Catalytic Activity of Single-Chain Polymeric Nanoparticles in Water. *J. Polym. Sci. Part Polym. Chem.* **2014**, *52* (1), 12–20. https://doi.org/10.1002/POLA.26970.

(66) Artar, M.; Souren, E. R. J.; Terashima, T.; Meijer, E. W.; Palmans, A. R. A. Single Chain Polymeric Nanoparticles as Selective Hydrophobic Reaction Spaces in Water. *ACS Macro Lett.* **2015**, *4* (10), 1099–1103. https://doi.org/10.1021/acsmacrolett.5b00652.

(67) Liu, Y.; Pujals, S.; Stals, P. J. M.; Paulöhrl, T.; Presolski, S. I.; Meijer, E. W.; Albertazzi, L.; Palmans, A. R. A. Catalytically Active Single-Chain Polymeric Nanoparticles: Exploring Their Functions in Complex Biological Media. *J. Am. Chem. Soc.* **2018**, *140* (9), 3423–3433. https://doi.org/10.1021/jacs.8b00122.

(68) Deng, L.; Albertazzi, L.; Palmans, A. R. A. Elucidating the Stability of Single-Chain Polymeric Nanoparticles in Biological Media and Living Cells. *Biomacromolecules* **2021**, acs.biomac.1c01291. https://doi.org/10.1021/acs.biomac.1c01291.

(69) Liu, Y.; Turunen, P.; de Waal, B. F. M. M.; Blank, K. G.; Rowan, A. E.; Palmans, A. R. A.; Meijer, E. W. Catalytic Single-Chain Polymeric Nanoparticles at Work: From Ensemble towards Single-Particle Kinetics. *Mol. Syst. Des. Eng.* **2018**, *3* (4), 609–618. https://doi.org/10.1039/C8ME00017D.

(70) Chen, J.; Wang, J.; Bai, Y.; Li, K.; Garcia, E. S.; Ferguson, A. L.; Zimmerman, S. C. Enzyme-like Click Catalysis by a Copper-Containing Single-Chain Nanoparticle. *J. Am. Chem. Soc.* **2018**, *140* (42), 13695–13702. https://doi.org/10.1021/jacs.8b06875.

(71) Deng, Y.; Wu, T.; Chen, X.; Chen, Y.; Fei, Y.; Liu, Y.; Chen, Z.; Xing, H.; Bai, Y. A Membrane-Embedded Macromolecular Catalyst with Substrate Selectivity in Live Cells. *J. Am. Chem. Soc.* **2022**. https://doi.org/10.1021/jacs.2c11168.

(72) Chen, J.; Wang, J.; Li, K.; Wang, Y.; Gruebele, M.; Ferguson, A. L.; Zimmerman, S. C. Polymeric “Clickase” Accelerates the Copper Click Reaction of Small Molecules, Proteins, and Cells. *J. Am. Chem. Soc.* **2019**, *141* (24), 9693–9700. https://doi.org/10.1021/jacs.9b04181.

(73) Chen, J.; Li, K.; Shon, J. S.; Zimmerman, S. C. Single-Chain Nanoparticle Delivers a Partner Enzyme for

Concurrent and Tandem Catalysis in Cells. *J. Am. Chem. Soc.* **2020**, *142* (10), 4565–4569. https://doi.org/10.1021/jacs.9b13997.

(74) Garcia, E. S.; Xiong, T. M.; Lifschitz, A.; Zimmerman, S. C. Tandem Catalysis Using an Enzyme and a Polymeric Ruthenium-Based Artificial Metalloenzyme. *Polym. Chem.* **2021**, *12* (46), 6755–6760. https://doi.org/10.1039/D1PY01255J.

(75) Völker, T.; Meggers, E. Chemical Activation in Blood Serum and Human Cell Culture: Improved Ruthenium Complex for Catalytic Uncaging of Alloc-Protected Amines. *ChemBioChem* **2017**, *18* (12), 1083–1086. https://doi.org/10.1002/cbic.201700168.

(76) Danhier, F. To Exploit the Tumor Microenvironment: Since the EPR Effect Fails in the Clinic, What Is the Future of Nanomedicine? *J. Controlled Release* **2016**, *244*, 108–121. https://doi.org/10.1016/j.jconrel.2016.11.015.

(77) Wilhelm, S.; Tavares, A. J.; Dai, Q.; Ohta, S.; Audet, J.; Dvorak, H. F.; Chan, W. C. W. Analysis of Nanoparticle Delivery to Tumours. *Nat. Rev. Mater.* **2016**, *1* (5), 16014. https://doi.org/10.1038/natrevmats.2016.14.

(78) Torrice, M. Does Nanomedicine Have a Delivery Problem? *ACS Cent. Sci.* **2016**, *2* (7), 434–437. https://doi.org/10.1021/acscentsci.6b00190.

Chapter 2

Pd(II) based amphiphilic polymeric nanoparticles for pro-drug activation in complex media

Abstract: We investigated the factors that can affect the efficiency of Pd(II) based amphiphilic polymeric nanoparticles to perform bioorthogonal reactions in complex media. Herein, we functionalised amphiphilic polymers with the Pd(II)-binding ligands triphenylphosphine and bipyridine. The resulting polymers collapsed into small-sized nanoparticles (5-6 nm) with an inner hydrophobic domain that comprises the Pd(II) catalyst. We systematically evaluated the effect of polymer microstructure, ligand-metal complex, and substrate hydrophobicity on the catalytic activity of the nanoparticles for depropargylation reactions in water, PBS or DMEM. The results showed that the catalytic activity of nanoparticles is primarily impacted by the ligand-metal complex while polymer microstructure has only a minor influence. Careful deconstruction of the catalytic system revealed that covalent attachment of the ligand to the polymer backbone is necessary to retain its catalytic activity in cell culture medium while this is not required in water. Finally, we activated anti-cancer pro-drugs based on 5-fluorouracil, paclitaxel, and doxorubicin using the best-performing catalytic SCPNs. We found that the rate of pro-drug activation in water was accelerated efficiently by catalytic SCPNs, whereas in cell culture medium the results depended on the type of protecting group and hydrophobicity of the prodrug.

This work has been published as:

Developing Pd(II) based amphiphilic polymeric nanoparticles for pro-drug activation in complex media. A. Sathyan, S. Croke, A.M. Pérez-López, B.F.M. de Waal, A. Unciti-Broceta and A.R.A Palmans, *Mol. Syst. Des. Eng.*, **2022**, *7*, 1736-1748.

2.1 Introduction

With the advances in bioorthogonal chemistry, reactions using various transition metal catalysts such as Pd (II)/(0), Ru, Au, or Cu in living cells became promising for biomedical applications.[1–10] Among them, Pd is known for both cross-coupling and bond cleavage reactions in cellular media,[11–13] and has been explored for protein modification or activation[14,15], cell surface remodeling [16,17], DNA modification[18] and pro-drug activation.[19,20] Pd(0)/Pd(II) can perform C-O bond cleavage reactions of propargylic or allylic carbamates, ethers, amines, or carbonates in cellular media.[3,4,21–27] Hence, it displays therapeutic potential exemplified by its ability to activate pro-drugs or pro-dyes in a controlled manner with minimal toxicity and high specificity. Bradley and co-workers first reported intracellular de-allylation and Suzuki-Miyaura coupling reactions using Pd(0) entrapped polystyrene microspheres of 0.5 μm in diameter.[4] Later, Pd-mediated depropargylation reactions were reported by Chen and coworkers using discrete Pd(II) complexes for protein activation which proved to function better than deallylation reactions[14] Parallel studies performed by Unciti-Broceta and coworkers with extracellular Pd(0) resins found equivalent results, i.e. Pd-mediated depropargylation reactions are faster than deallylations, enabling the activation of the propargyl-protected anticancer drug 5-fluorouracil[28] and propargyloxycarbonyl-protected gemcitabine[29] in cell cultures. They also highlighted the compatibility of these catalysts in-vivo by locally activating a pro-dye in zebrafish.[28] Weissleder and coworkers reported in-vivo pro-drug activation of doxorubicin and monomethyl auristatin E by Pd-based nanoparticles thereby inhibiting the growth of solid tumours in mice models opening exciting opportunities to expand in-vivo palladium chemistry for developing new cancer therapies.[1,27] Further developments from Unciti-Broceta and co-workers on Pd-activable non-toxic pro-drugs from chemotherapeutics such as doxorubicin, 5-fluorouracil, paclitaxel, etc., widened the scope of new therapies exploiting Pd catalysed pro-drug activation.[3,28–32]

The use of heterogeneous Pd catalysts proved to be advantageous and promising over discrete palladium complexes for in-vivo pro-drug activation, as it helps overcome the issues of biocompatibility, stability, deactivation, or their sequestration by proteins.[33] However, they are often employed as implants near the tumour tissue which may need to be surgically removed after treatment.[3] To cope with this issue, metal complexes can be loaded into the hydrophobic domain of polymeric scaffolds to form homogeneous systems such as micelles[34–36] dendrimers[37], polymerosomes,[38] star polymers[39] ,or polymeric nanoparticles.[40–43] They offer the possibility of systemic administration and can be localised to tumour tissues by EPR-mediated passive and RGD or NGR-based active targeting.[44]

In our group, Liu *et al.* previously evaluated the potential of a first-generation Pd(II)-based SCPN in the depropargylation of a protected rhodamine dye in the cytosol and lysosomal compartments of Hela cells. The work revealed that while deprotection was feasible, a boost in the activity and enhancement of the stability of the catalytic system is required to make the system amenable for *in vivo* pro-drug activation.[45] In addition, ter Huurne *et al.* found that the polymer's microstructure affected the size and shape of the formed SCPNs and optimised the hydrophobic/hydrophilic balance to attain well-defined, compartmentalised systems with a structured hydrophobic interior.[46] Using the optimised polymer design, Deng *et al.* recently observed that the biocompatibility of SCPNs without metals incorporated is excellent and that SCPNs retain their folded, compartmentalised structure in complex media and in the cytoplasm of a variety of cell types.[47] Thus, a profound understanding on how different aspects of the catalytic system affect its efficiency when increasing the complexity of the medium is required to make the step to *in vivo* applications.

We present here our systematic approach to increase the efficiency of Pd(II)-based polymeric nanoparticles for catalysing depropargylation reactions in cellular media by tuning the different aspects of the catalytic system. We focus on depropargylation reactions as they are reported to be faster than deallylation reactions[28] and various propargyl-protected pro-drugs of clinically used chemotherapeutics are already reported to be non-toxic to cells.[3,28–32] Moreover, depropargylation is cleaner and activates the pro-drug/dye without any toxic side products.[24] Hereto, we use our optimised polymer microstructure and investigate (1) the effect of the metal-ligand combination, (2) the effect of the hydrophobicity of the substrate, (3) the effect of the polymer's microstructure on catalyst's activity and (4) the effect of medium complexity. The best design was then applied in the prodrug activation of the well-established cancer chemotherapeutics paclitaxel (pac), doxorubicin (doc) and 5–fluorouracil (5FU) in the cell culture medium DMEM. The results indicate that while some prodrugs are activated even in DMEM, a careful balance is required between the substrate and product hydrophobicity. Our bottom-up approach highlights not only the challenges associated with pro-drug activation in complex cellular media but also that a fundamental understanding of all aspects of the applied system is crucial for progress.

2.2 Design, synthesis and characterization of amphiphilic polymers

2.2.1 Synthesis of amphiphilic polymers with Pd(II) binding ligands

The design of the catalytic polymeric nanoparticle system (Scheme 1) is based on our previously studied amphiphilic polymers with a polyacrylamide backbone, grafted with Jeffamine M-1000 to ensure water solubility, n-dodecyl groups to induce a hydrophobic collapse, and benzene-1,3,5-tricarboxamide groups for imparting a secondary structure formation in the nanoparticle's interior via hydrogen bonding.[46] In addition, selected ligands are covalently attached to the polymer backbone capable of binding Pd(II). Following the work of Mascareñas, we select triphenylphosphine as this affords active, discrete Pd(II) complexes, also inside HeLa cells.[48] Incorporating phosphine ligands into amphiphilic polymers improves their compatibility with aqueous media, while extending the substrate scope to more hydrophobic molecules. In addition, bipyridine-based ligands were attached to the polymer backbone for reference as we have observed in previous work that these are capable of pro-dye activation in the presence of HeLa cells, albeit with low activity. [45] To obtain an efficient catalytic system, the Pd(II) complex should be well protected inside the hydrophobic pocket and should not leak out into the complex biological environment.

Table 1 summarises the details of the composition of the different polymers **P1-P6**. Amine-functionalised triphenylphosphine (TPP) ligand was synthesized starting from 4-(diphenylphosphaneyl) benzoic acid in two steps, and amine-functionalised bipyridine ligand was synthesised following a reported procedure.[49] To prepare the polymer backbone, pentafluorophenyl acrylate **3** was synthesized and subsequently, polymerised using reversible addition-fragmentation chain-transfer (RAFT) polymerisation (Scheme 1). The RAFT-end group was removed to afford poly(pentafluorophenylacrylate) homopolymer *p*-**PFPA** (DP = 214, *Đ* = 1.23, Scheme 1, Table 1). All polymers were synthesised starting from the same poly(pentafluorophenylacrylate) homopolymer *p*-**PFPA** by a post-functionalisation approach, using previously developed procedures (Scheme 1).[40] This post-functionalisation approach allows easy functionalisation and ensures a random distribution of the side groups of interest while keeping the same average degree of polymerisation and molar mass dispersity of the polymer backbone.[40,46,50]

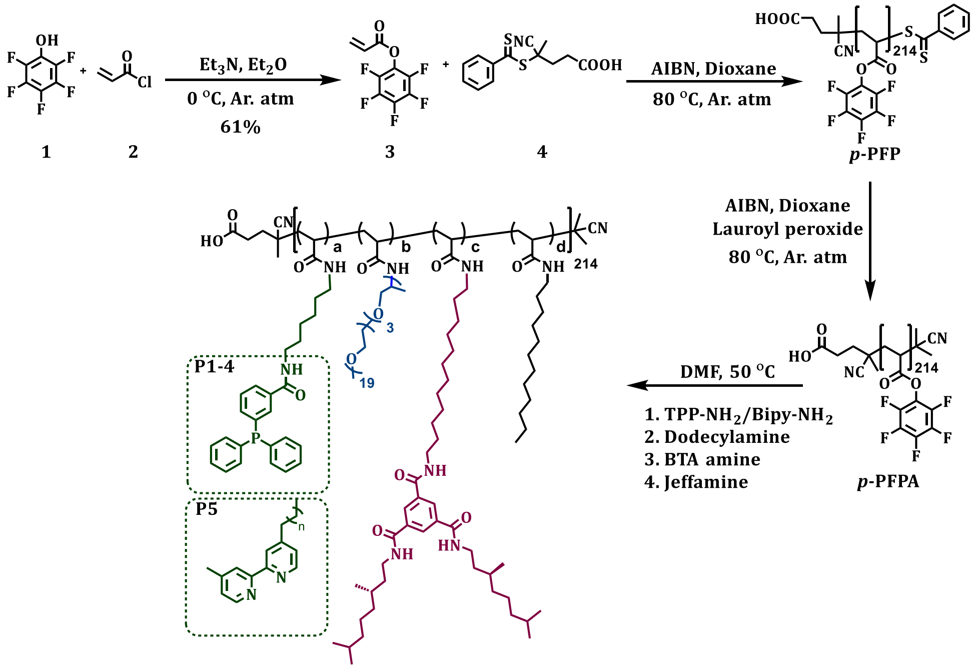

Scheme 1: Synthesis and subsequent RAFT polymerisation of pentafluorophenylacrylate and the sequential post-functionalisation of **p-PFPA** by addition of amines to synthesise **P1**-**P5.**

Polymers **P1-P4** comprised TPP ligands (~10% in **P1-P3**, ~20% in **P4**), variable amounts of hydrophobic and supramolecular BTA units, and hydrophilic Jeffamine M-1000 (Scheme 1, Table 1) to vary the microstructure of polymers. **P1** contains ~10% BTAs. BTAs attached to a polymer backbone assemble via threefold hydrogen-bonding interactions forming *M*-helical stacks.[46] These stacks provide a structured, hydrophobic interior inside the nanoparticles, which is known to enhance the nanoparticle's stability.[47] **P2** contains ~5% BTA and ~20% dodecyl chains on the backbone, which affords both a structured as well as a compact interior while preventing multichain aggregates due to BTA stacking.[46] **P3** contains ~15% dodecyl chains, while **P4** has just the hydrophobicity of the ligand to form a hydrophobic domain inside the particles. The simple chemical structures of **P3** and **P4** highlight the potential of developing easily accessible catalytic polymers for bioorthogonal catalysis using this approach.

Table 1: Overview of the copolymer composition a-d, number-average molecular weight (M_n), and molar mass dispersity ($Đ$) of **pPFP_{214}** and **P1-P6**.

Polymer	a	b	c	d	$Đ$	$\boldsymbol{M}_{\mathbf{n},\mathrm{SEC}}$ (kD)	$\boldsymbol{M}_{\mathbf{n},\mathrm{theoretical}}$ **(kD)**
***p*PFPA$_{214}$**					1.23^{a}	36.7^{a}	51
P1	9	80	11	-	1.43^{b}	46.8^{b}	183
P2	8	68	4	20	1.18^{b}	42.2^{b}	163
P3	9	76	-	15	1.28^{b}	62.0^{b}	158
P4	18	82	-	-	1.34^{b}	55.4^{b}	178
P5	10	66	5	19	1.42^{b}	46.9^{b}	179
P6	-	76	-	24	1.41^{b}	57.6^{b}	164

a-d were determined by ^{19}F NMR. $\boldsymbol{M}_{\mathbf{n}}$ and $\boldsymbol{Đ}$ were measured by SEC in ^{a}THF, relative to poly(styrene) standards and in ^{b}DMF with 10 mM LiBr, relative to poly(ethylene oxide) standards.

P5 is equipped with ~10% bipyridine ligand, ~5% BTA, ~20% dodecyl, and Jeffamine M-1000, similar to the polymer reported previously.[45] A control polymer **P6** without ligands was also prepared to breakdown the complex catalytic system into a simple system which permits physical encapsulation of a Pd(II) complex and study its effect on activity with increasing medium complexity. Since **P1-P4** are susceptible to oxidation of the TPP ligand, workup and dialysis were performed in degassed solvents. The covalent attachment of the TPP ligands to polymers **P1-P4** was indicated by a resonance peak at –5 ppm in the ^{31}P NMR spectrum (Figure 1B). Next, TPP functionalised polymers were complexed with **Pd(II)** using **$PdCODCl_2$** as the palladium source in degassed chloroform under argon atmosphere and highly diluted conditions to minimise intermolecular crosslinking of the particles (see experimental section).[51] We refer to polymer nanoparticles comprising **Pd(II)** as **P@Pd(II)**. ^{31}P NMR showed that the signal of triphenylphosphine at −5 ppm disappeared, and a new signal downfield between 23-27 ppm formed, confirming the complexation of **Pd(II)** to TPP (Figure 1). We observed minor oxidation of triphenylphosphine in all polymers during complexation as indicated by a small peak at 28 ppm, characteristic of triphenylphosphine oxide.[52] **P1-P4@Pd(II)** were dialysed in chloroform to remove most of the unbound Pd(II) salt. Next, the complexed polymers were formulated into nanoparticles in water.

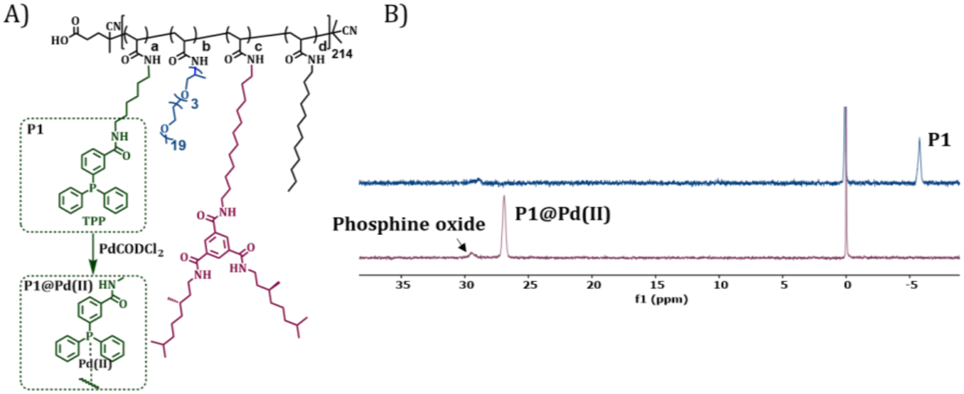

Figure 1: A) Polymer structure depicting the complexation of TPP-based polymer **P1** with **Pd(II)** using **PdCODCl$_2$** as precursor in CHCl$_3$ B) ^{31}P NMR spectra of **P1** and **P1@Pd(II)** in CDCl$_3$ using 85% H$_3$PO$_4$ (in D$_2$O) as external standard (reference standard added as coaxial insert).

In contrast, bipyridine-based polymer **P5** does not suffer from sensitivity to oxygen and was first formulated to nanoparticles in water by dissolution, followed by complexation of **Pd(II)** using the water-soluble **Pd(II)** precursor **Na$_2$PdCl$_4$**. The complexation of **P5** to **Pd(II)** was followed by UV-Vis spectroscopy, where the characteristic absorption of bipyridine was red-shifted after complexation with **Pd (II)** (Figure 2).[45]

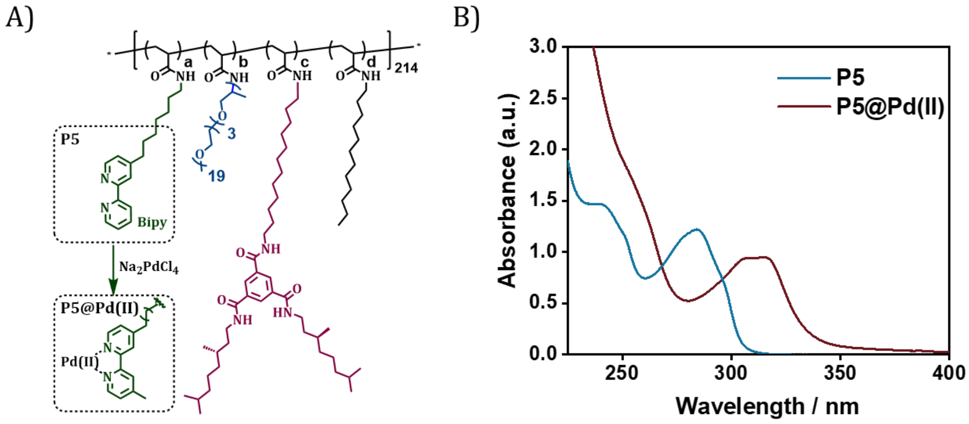

Figure 2: A) Polymer structure depicting the complexation of bipy-based polymer **P5** with **Pd(II)** using **Na_2PdCl_4** as precursor in H_2O. B) UV-Vis spectra of **P5** and **P5@Pd(II)** in H_2O, [**P5**]=1 mg/mL, [**Pd(II)**] = 100 µM, T = 20 °C).

2.2.2 Characterization of amphiphilic polymers

The size of formulated nanoparticles **P1-P5** and **P1-P5@Pd(II)** was monitored using dynamic light scattering (DLS) studies. **P1-P4@Pd(II)** in water showed hydrodynamic radii (R_H) of 5 - 6 nm, well in line with previously reported SCPN systems.[45] **P5@Pd(II)** also showed a R_H of 6 nm (Table 2). The sizes of **P1-P5** nanoparticles did not change significantly before and after complexation (Table 2). Due to the presence of a small fraction of aggregates after complexation as observed in DLS, we adopted the name polymeric nanoparticles instead of SCPNs in this study (Figure 14).

The negative Cotton effect with a minimum at λ = 225 nm in the circular dichroism (CD) spectra of polymers **P1**, **P2**, and **P5** indicated the presence of *M*-helical BTA aggregates that form threefold hydrogen bonding between the pendant BTA units (Figure 3).[53,54] In the case of TPP-based polymers with BTA **P1** and **P2**, complexation of TPP ligands with Pd(II) in $CHCl_3$ affected self-assembly of BTAs when they were formulated into nanoparticles in water (Figure 3A).

Table 2: Hydrodynamic radii (R_H) of **P1-P5** and **P1-P5@Pd(II)**, **Pd(II)** content of **P1-P5@Pd(II)** in H_2O

P	R_H [a] (nm)	**P@Pd(II)** (1 mg/mL)	R_H [a] (nm)	Pd(II) [b] concentration (mg/L)	Pd(II) [c] ions per particle (~)
P1	5.2	**P1@Pd(II)**	5.7	2.6	25
P2	4.6	**P2@Pd(II)**	6.4	4.6	43
P3	3.7	**P3@Pd(II)**	5.4	5.4	48
P4	5.9	**P4@Pd(II)**	5.6	7.6	76
P5	5.7	**P5@Pd(II)**	5.8	n.d.[d]	20[e]

[a] monitored by dynamic light scattering, in all cases the measurements were done at [**P**] = [**P1@Pd(II)** = 1 mg/mL. [b] determined from MP-AES measurement ([**P1@Pd(II)** = 0.2 mg/mL). [c] determined from molar ratio of polymer to Pd(II) ion. [d] required amount of **Pd(II)** is added after the formulation of nanoparticles as desired. [e] determined from the amount of **Pd(II)** added to **P5** for complexation. All samples were prepared in H_2O.

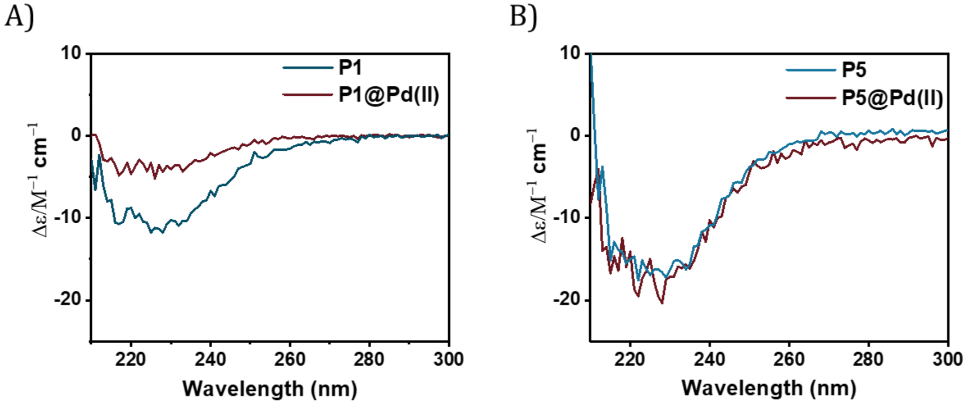

Figure 3: Molar circular dichroism spectra before and after complexation A) **P1** and **P1@Pd(II)** B) **P5** and **P5@Pd(II)**. [**P1**] = 0.4 mg/mL, [**P1@Pd(II)**] = 0.4 mg/mL, [**P5**] = 1 mg/mL, [**P5@Pd(II)**] = 0.5 mg/mL, T = 20 °C.

In the case of **P5**, as **Pd(II)** complexation was performed after the formulation of nanoparticles, BTA aggregates formed were unaffected (Figure 3B). The palladium concentration in all nanoparticles was analysed by MP-AES spectroscopy prior to catalysis studies and the results indicated the presence of

~ 30-80 Pd(II) ions per particle, meaning that an excess of palladium is trapped in the polymeric nanoparticles, which are not able to diffuse out during dialysis (Table 2). For all catalytic studies, the total concentration of Pd(II) in the reaction mixture was kept constant taking this into consideration.

2.3 Propargyl-protected pro-dyes for activation – model for pro-drugs

Pro-dyes act as models for pro-drugs making it easier to progress the reaction progress or catalyst efficiency using spectroscopic techniques. This will help in the optimization of the catalytic system before they are used to activate pro-drugs, which is more challenging to track and quantify. The hydrophobicity of the substrates and protecting group plays an essential role during their deprotection by catalytic polymeric nanoparticles, especially in complex media in the presence of competing molecules. The greater the hydrophobicity, the higher the tendency of substrates to accumulate in hydrophobic reaction space inside the nanoparticles.[55] Therefore, we designed and synthesized a set of propargyl-protected, palladium-activatable pro-dyes based on *o*-dinitrophenol (pro-DNP **5**), 7-amino-4-methyl coumarin (pro-cou **7**), morpholinecarbonyl rhodamine 110 (pro-rho, **9**) and benzothiazole derivative **12** (pro-ben **11**) that have different hydrophobicities (Figure 4), following reported procedures.[16,24,44,56] During the depropargylation reactions mediated by Pd(II), the acidity of the hydroxyl group (leaving group) also play a role in their reactivity. In the case of *N*-propargyloxycarbonyl group on pro-dyes **7** and **9**, pK_a reflects the acidity of carboxylic acid making it very sensitive to palladium-mediated depropargylation at physiological pH (7.4) (Figure 4B). But, in the case of *O*-propargyl protection, pK_a of the hydroxyl group (after deprotection) is dependent on the substituents as in dyes **6** and **12** (Figure 4), which can affect the reactivity of their corresponding pro-dyes **5** and **11** towards depropargylation. DNP **6** being an electron-deficient phenol, has a pK_a of 4.5 that favours deprotection. While benzothiazole derivative **12** has pK_a of 7.6, decreasing its reactivity at pH 7.4. Weiss *et al.* have already reported that depropargylation kinetics may vary from the prediction based on theoretical pK_a, as it can also be influenced by steric and conformational effects. They also observed that the pH of the solution affects the rate of Pd(0)-promoted depropargylation.[57] Therefore, experimental investigations of depropargylation kinetics of the selected pro-dyes is important to help us choose the right substrate or pro-drugs to export to complex media or living cells.

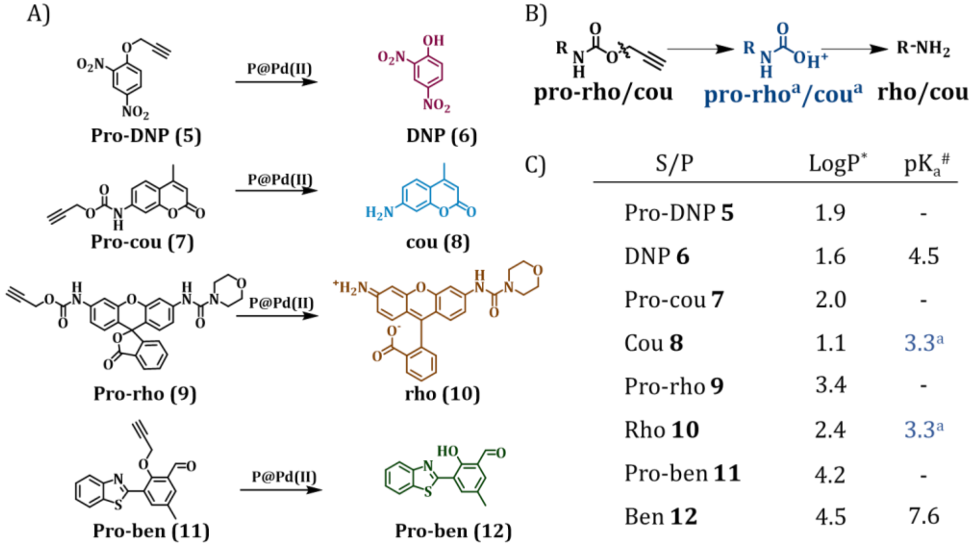

S/P	LogP*	pK$_a$$^\#$
Pro-DNP **5**	1.9	-
DNP **6**	1.6	4.5
Pro-cou **7**	2.0	-
Cou **8**	1.1	3.3^a
Pro-rho **9**	3.4	-
Rho **10**	2.4	3.3^a
Pro-ben **11**	4.2	-
Ben **12**	4.5	7.6

Figure 4: A) Structure of propargyl-protected pro-dyes for **Pd(II)** based activation and their corresponding activated dyes B) Cleavage of N-propargyloxycarbonyl group of pro-cou **7** and pro-rho **9** by release of CO_2 to form corresponding amines C) Log P values of substrates and products, pK$_a$ of the hydroxyl group on the product after depropargylation. *# calculated using ChemAxon MarvinSketch 22.16. ^{a} pK$_a$ of carbamic acid of corresponding amines – pro-cou^a and pro-rho^a (blue) in part B.

The rate of the deprotection reaction was monitored using UV-Vis spectroscopy for pro-DNP **6** and fluorescence spectroscopy for **7**, **9** and **11**. The conversion from substrates to products was then confirmed and quantified using HPLC-UV/MS. The presence of polymeric nanoparticles in the reaction mixture hindered the accurate determination of conversion. We tried to filter out polymeric nanoparticles from reaction mixtures using centrifugal filters, but some amount of hydrophobic substrates or products remained with the polymer, affecting reliable quantification. Therefore, aliquots from the reaction mixture were diluted with acetonitrile (50% v/v) and were directly injected into HPLC. The conversion was quantified from calibration curves of pure products. Therefore, spectroscopic and chromatographic techniques were used parallelly to monitor the reaction progress.

2.4 Activation of pro-dyes in aqueous solution

2.4.1 Catalytic activity and influence of polymer microstructure

We first checked the catalytic performance of newly developed Pd(II) loaded TPP-based polymeric nanoparticles in the depropargylation of *O*-propargyl protected dye pro-DNP **5**. Given these are model reactions toward pro-drug activation in cells, the reaction parameters were chosen to fit with the biological environment. Therefore, reactions were performed in aqueous solutions at physiological temperature (37 °C) and at micromolar concentration of substrates, concentrations used for pro-drug administration *in vivo*.[27] The rate of the reaction was first studied in water and PBS. **P1-P4@Pd(II)** nanoparticles were prepared in water or PBS to reach a concentration of 30 μM **Pd(II)**. To this, a substrate stock solution in DMSO (0.2% v/v in water) was added ([Pro-DNP **5**] = 100 μM). The *in situ* formation of product DNP **6** was monitored using UV-Vis spectroscopy over time. The kinetic curves in water (Figure 5A) showed saturation after 210 min for **P1@Pd(II)** and around 700 min for **P2-P4@Pd(II)**. For the free catalyst, **PdCODCl$_2$**, no saturation is observed, even after 1200 min. In PBS, **P1-P3@Pd(II)** and **PdCODCl$_2$** showed faster formation of DNP **6**, whereas **P4@Pd(II)** showed a similar kinetic profile as in water (Figure 5B). The results indicate that catalytically active nanoparticles, both in water and PBS, show significantly faster rates compared to free palladium salt **PdCODCl$_2$**. The kinetic data also implied that the exact microstructure of the polymers **P1-P4** does not have a major influence on catalytic activity in water and PBS (Figure 5).

The free palladium salt **PdCODCl$_2$** showed different behaviour in water and in PBS. In PBS two rate regimes, one fast and one slow, can be observed (Figure 5B). This is similar to what was reported previously for depropargylations by Pd(II) salts in PBS, where it was studied that depropargylation proceeds via two phases, one fast and the other slow.[24] The fast phase ends within two turnovers due to product inhibition by the propargylic hydrolytic product, which is followed by a slower reaction phase promoted by Pd(0) nanoparticles formed from Pd(II) in the mixture.[24,58] In contrast, **P1-P4@Pd(II)** nanoparticles catalysed the reaction faster without a slow phase. This could be due to two reasons, a) products formed, which are more hydrophilic than the starting substrate, will have a higher tendency to partition into the aqueous phase, decreasing the chances of product inhibition or b) Pd(0) formed during the cycle is stabilised within the nanoparticles which further allows the continuation of the reaction.[59] The conversion of pro-DNP **5** after 24 h was between 80 – 90% in the case of the **P1-P4@Pd(II)**, outperforming the **PdCODCl$_2$** salt where the conversion was only 55%.

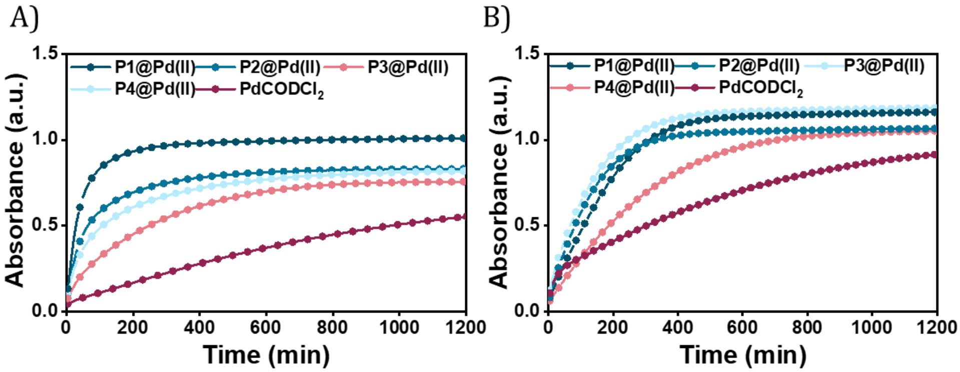

Figure 5: Activation of pro-DNP **5** (100 μM) to DNP **6** monitored by UV-Vis spectroscopy overtime at λ = 400 nm A) in water B) in PBS, all reactions were performed at 37 °C using **P1-P4@Pd(II)** and **PdCODCl$_2$**, in all cases [Pd(II)] = 30 μM.

2.4.2 Influence of substrate hydrophobicity and reactivity

The new polymers were further tested on *N*-propargyloxycarbonyl protected dyes pro-cou **7** (hydrophilic) and pro-rho **9** (hydrophobic) to assess the effect of substrate hydrophobicity on the rate of the reaction, as both substrates have the same protecting group. The deprotection of pro-cou **7** in water (Figure 6A) proceeds very slow, reaching only 50% even after 24 h. There is no clear trend between the activity of **P1-P4@Pd(II)** and the free **PdCODCl$_2$** salt (Figure 6A), albeit that **P1@Pd(II)** seems to be the faster catalyst system. On the other hand, deprotection of pro-rho **9** proceeds very fast, with saturation of the fluorescence increase already after 10 min in the case of **P1-P3@Pd(II)**.

The kinetic curves also show that **P4@Pd(II)**, the most hydrophilic nanoparticle with the least hydrophobic content, performed slower compared to others (Figure 6B), which is also seen for the free $PdCODCl_2$ salt. However, it is important to note that **P4@Pd(II)** has a twice higher ligand incorporation compared to **P1-P3@Pd(II)** resulting in higher Pd(II) loading (Section 2.2.2, Table 2). As a consequence of keeping the Pd(II) concentration constant, the concentration of nanoparticles **P4@Pd(II)** in the solution is lower, resulting in an overall lower hydrophobicity to accommodate hydrophobic substrate pro-rho **9**.

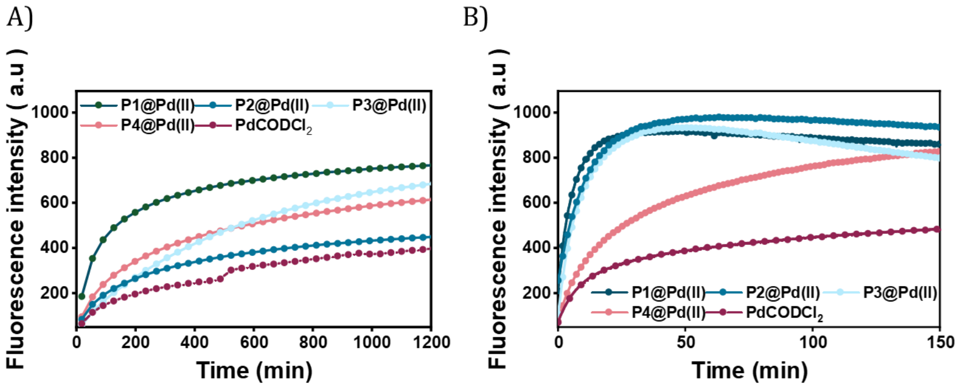

Figure 6: A) Activation of pro-cou **7** (100 μM) to cou **8** monitored by fluorescence spectroscopy over time λ_{ex}= 370 nm and λ_{em} = 420 nm in water B) Activation of pro-rho **9** (100 μM) to rho **10** monitored by fluorescence spectroscopy over time λ_{ex}= 485 nm and λ_{em} = 520 nm in water; all reactions were performed at 37 °C using **P1-P4@Pd(II)** and **$PdCODCl_2$**, in all cases [Pd(II)] = 30 μM.

Quantification of the conversion with HPLC-UV showed quantitative conversion of pro-rho **9** to rho **10** after 3.3 h using **P1-P3@Pd(II)** (Figure 16A). The faster conversion of pro-rho **9** by the more hydrophobic nanoparticles **P1-P3@Pd(II)** suggests that the rate of the deprotection correlates with the hydrophobicity of the substrate, since the rates are significantly slower in the case of pro-DNP **5** and pro-cou **7**. The results also show that **P1@Pd(II)** comprising 10% BTA units outperforms the other nanoparticles in some cases in water. However, the differences between **P1-P3@Pd(II)** are rather small, indicating that as long as the interior of the nanoparticle is sufficiently hydrophobic to accommodate the substrates, the rate of the reaction is similar. We also observed that the product formed tends to aggregate inside the hydrophobic interior, which was inferred from the quenching of the fluorescence over time.

Pro-ben **11**, which has similar hydrophobicity as that of pro-rho **9**, was also tested as a substrate in water using **P1@Pd(II)** (Figure 18A). The reaction progress was monitored using fluorescence spectroscopy over time, and product **12** formation was not observed. However, upon increasing the pH of the solution with the addition of triethylamine, a rapid increase in fluorescence was observed which plateaued within 10 min, indicating the formation of product **12** (Figure 18A). For a bioorthogonal catalyst to efficiently function in biological media, it should perform its best at physiological pH (7.4) or even lower (tumour cells). So substrates that are less reactive at lower pH like pro-dye **11** will not be suitable for Pd(II) based depropargylation. Therefore, we can confirm that it is important to carefully select the substrates with the right hydrophobicity and reactivity to achieve the optimum catalytic activity of nanoparticles in aqueous solutions. Especially when the complexity of the medium is increased as in DMEM, substrate accumulation near catalyst site in polymeric nanoparticles can be achieved by selecting hydrophobic substrates as compared to hydrophilic ones. Owing to the fast kinetics of activation of pro-rho substrate **9**, we selected this substrate for subsequent experiments.

2.5 Role of ligand-metal complex in the catalytic activity of polymeric nanoparticles

The choice of ligands attached to the polymer backbone to bind Pd(II) plays an important role in the catalytic system design. The ligands should be labile to allow substrate binding but if they are too labile, nucleophiles in the complex media can deactivate the catalyst faster. Therefore, a fine balance on the lability of ligands is necessary to achieve a high turnover in complex media.[58] Here, we compare two ligands, TPP and bipyridine, where TPP is a more labile ligand compared to bipyridine in binding with Pd(II). The labile TPP-Pd(II) complex will allow facile substrate binding and thereby can be more reactive than the stable bipy-Pd(II) complex in water. However, their reactivity in competing environments like in cell culture medium such as DMEM may vary. DMEM medium contains different amino acids such as histidine, cysteine, methionine etc. that are known to complex with Pd(II), with a higher affinity to sulphur-containing amino acids.[60] Therefore, these amino acids can interact with Pd(II) displacing the ligands, hence deactivating the catalyst. Here, we studied the effect of TPP and bipyridine on the catalytic activity of polymer nanoparticles in the depropargylation of pro-rho **9** in both water and DMEM. **P1@Pd(II)** and **P5@Pd(II)** were compared, as well as their Pd(II) precursors **$PdCODCl_2$** and **Na_2PdCl_4**.

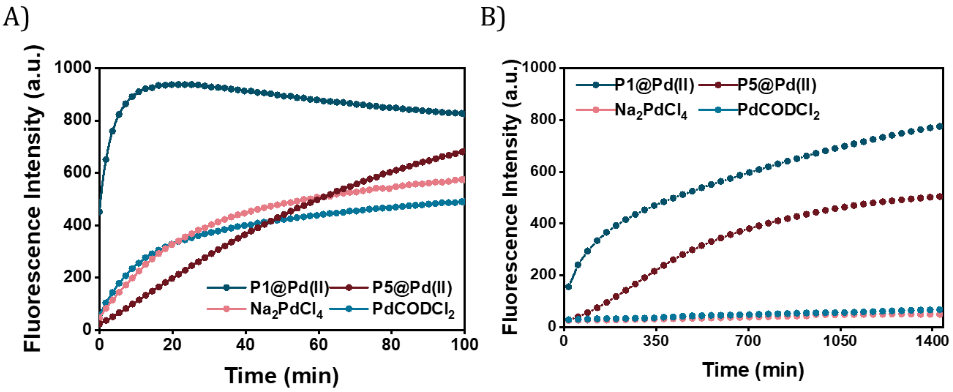

Figure 7: Activation of pro-rho **9** (100 μM) monitored by fluorescence spectroscopy over time λ_{ex}= 485 nm and λ_{em} = 520 nm A) in water, B) in DMEM all reactions were performed at 37 °C by **P1@Pd(II), P5@Pd(II), Na_2PdCl_4** and **$PdCODCl_2$,** [Pd(II)] = 30 μM in water and [Pd(II)] = 100 μM in DMEM.

In water, TPP-based **P1@Pd(II)** performed the depropargylation faster, reaching full conversion in 3.3 h, compared to bipy-based **P5@Pd(II)** which was slower and did not reach full conversion even after 16 h (Figure 7A, Table 3). This suggests that the **TPP-Pd(II)** complex accelerates the depropargylation more efficiently than the bipy-Pd(II) complex. Also in DMEM, TPP-based **P1@Pd(II)** performed slightly better than bipy-based **P5@Pd(II)** (Figure 7B, Table 3). Interestingly the free Pd salts **$PdCODCl_2$** and **Na_2PdCl_4** showed a decent activity in water (Figure 7A) but were fully deactivated in the presence of DMEM (Figure 7B). This result suggests that TPP and bipy ligands when bound to Pd(II) prevent fast deactivation, and the presence of ligands is essential to retain the catalytic activity of Pd(II) catalysts. However, there is a significant rate decrease when the reactions are conducted in DMEM compared to water.

Table 3: Conversion of pro-rho **9** (100 µM) to rho **10** monitored by HPLC-UV

Catalyst	Medium*	Pd(II)* mol%	Conversion
P1@Pd(II)	Water	30	100%[a]
	DMEM	100	29[b], 72% ± 5%[c]
P5@Pd(II)	Water	30	51% ± 4%[a], 80% ± 5%[b]
	DMEM	100	22% ± 4%[c], 46% ± 8%[d]
$PdCODCl_2$	Water	30	37% ± 9%[a], 64% ± 2%[b]
	DMEM	100	n.d.[c], n.d.[d]
Na_2PdCl_4	Water	30	55% ± 1%[a], 75% ± 5%[b]
	DMEM	100	n.d.[c], n.d.[d]

[a] 3.3 h [b] 16 h [c] 24 h [d] 48 h. n.d.= not determined as no conversion was observed in DMEM during fluorescence kinetic experiments. Reactions performed at T = 37 °C. *Concentration of Pd(II) and medium of reaction as specified.

2.6 Catalytic activity of nanoparticles in the presence of additives

The best-performing catalyst **P1@Pd(II)** was further utilized to study the effect of possible deactivating components on catalytic activity independently, as a significant decrease in reaction rate was observed when the medium's complexity was increased from water to DMEM (section 1.4). But before that, we investigated if catalyst suffers from any deactivation during the reaction in the water itself. Gratifyingly, **P1@Pd(II)** did not show any deactivation after one cycle, as the addition of more substrate pro-rho **9** resulted in the continuation of the reaction to reach full conversion in water (Figure 8A).

The tumour environment is highly reducing with millimolar concentration of glutathione (GSH) and DMEM is composed of high concentration of salt buffers and thiol containing amino acids. **P1@Pd(II)** did not show any difference in its catalytic activity when the reaction medium was changed from water to phosphate-buffered saline solution (Figure 8B). This was also the case in a highly reducing environment, in the presence of 2 mM sodium ascorbate (NaAsc). In this case, ascorbate may have caused the reduction of Pd(II) to Pd(0) which can also promote depropargylations.[25] But, in the presence of 0.4 mM GSH, catalytic activity was significantly decreased, meaning that the catalyst has been deactivated by the thiol nucleophile (Figure 8B). It is also important to note that DMEM does not mimic the extracellular environment but it is necessary for catalytic nanoparticles to retain their activity in this medium to test their efficiency *in vitro*.

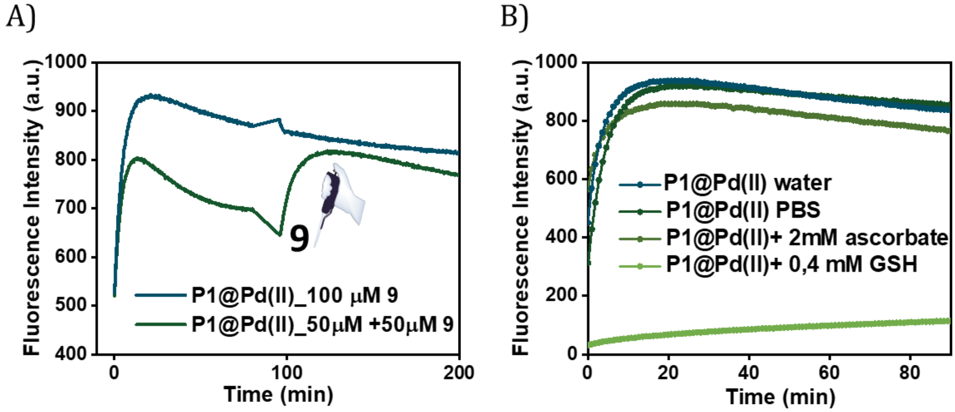

Figure 8: Fluorescence kinetics of pro-rho **9** activation using **P1@Pd(II)** A) blue curve: **9** added at once (100 μM), green curve: **9** added equal portion wise (t = 0 min and t = 95 min) to reach 100 μM. T = 37 °C, [Pd(II)] = 30 μM, reaction medium = H_2O B) Reaction medium = water, PBS, PBS + 2 mM ascorbate and 0.4 mM GSH, T = 37 °C, [Pd(II)] = 30 μM, λ_{ex}= 485 nm and λ_{em} = 520 nm.

2.7 Pd(II) leaching tests

In order to export bioorthogonal catalytic nanoparticles to living cells or *in vivo*, it is extremely important to understand if the Pd(II) catalysts remain stable in the hydrophobic pocket of polymeric nanoparticles. If they are leached out, it will affect the catalytic efficiency and can cause off-target toxicity. Therefore, we designed an experiment to test the leaching of Pd(II) catalysts from the nanoparticles. **P1@Pd(II)** and **P5@Pd(II)** in water ([Pd(II)] = 30 μM,[**P1**]=**P2**] = 0.25 mg/mL) were centrifuged with centrifugal filters with a molecular weight cutoff of 50 kD, to separate the polymers from the solution. The solution was then tested for the presence of leached-out Pd(II) using an imidazole derivative-based dye **13**, which exhibits fluorescence quenching in the presence of Pd(II) (Figure 9A).[61] The concentration of **13** was fixed at 10 μM while mixing with the filtrate solution (final [Pd(II)] = 25 μM, if there is complete leaching of Pd(II)). Total quenching of **13** fluorescence will be observed if 100% Pd(II) is leached out. In the case of **P5@Pd(II)**, there was no significant reduction in the emission of **13** and the result was similar to the control polymer **P5** without Pd(II) (Figure 9B). This indicates that there is no significant leaching of Pd(II) and that the ligand-Pd(II) complex is very stable in **P5@Pd(II)**. However, for **P1@Pd(II)** there was a slight reduction in fluorescence intensity, which corresponded to ~4-8% of Pd(II) leaching out. Still, the overall loss of Pd(II) is rather low. We conclude from the leaching experiment that our design of ligand-based nanoparticles ensures good catalyst encapsulation while limiting its deactivation compared to free Pd(II) catalysts.

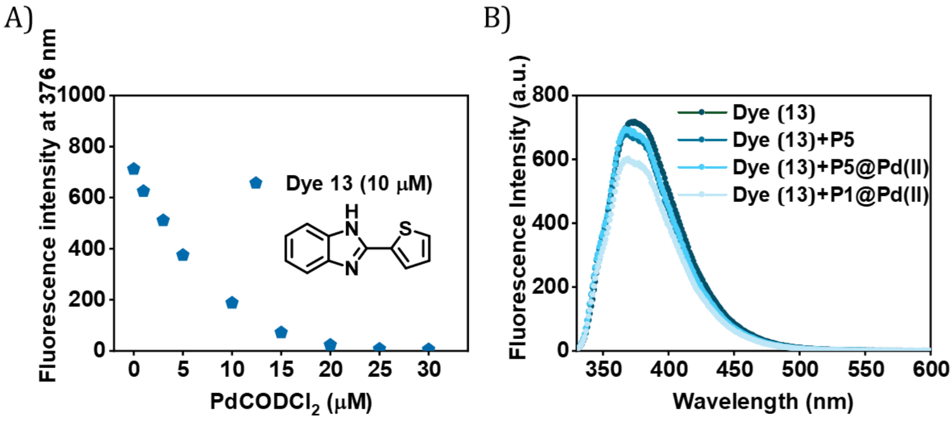

Figure 9: A) Fluorescence quenching of dye **13** (10 μM) with increasing PdCODCl$_2$ concentration (1–30 μM), λ_{ex} = 320 nm, λ_{ex} = 376 nm B) Pd(II) leaching test, emission spectra of **13** at λ_{ex} = 320 nm in the presence of **P1&P5@Pd(II)** filtrate solutions [**13**] = 10 μM, [**P**] = 0.25 mg/mL, [Pd(II)] = 30 μM (before filtration), T = 20 °C, in H_2O.

2.8 Complexity of the system vs catalytic activity in different media

Polymeric nanoparticles perform functions utilising the hydrophobic compartment where both hydrophobic substrates and catalysts can accumulate, accelerating reactions in the aqueous medium. If the catalysts are sufficiently hydrophobic, the catalytic system can be simplified by encapsulation of the catalyst in a simple and easily accessible amphiphilic polymer, which can perform the same function. If such a system remains active in a complex medium, many synthesis steps can potentially be avoided, making the applicability of such nanoparticles more versatile. In order to test this, we designed, evaluated, and compared four systems: a) a simple Pd(II) salt encapsulated in amphiphilic polymers (**P6@PdCODCl$_2$**); b) phosphine-Pd(II) complex encapsulated in amphiphilic polymers (**P6@TPPPd$_2$Cl$_2$**); c) phosphine-Pd(II) complex covalently attached to polymer (**P1@Pd(II)**); and d) the free **PdCODCl$_2$** as a reference.

The four catalytic systems were compared for their efficiency to catalyse the depropargylation reaction of pro-rho **9** in water and DMEM medium (Figure 10). In water, a steep increase in fluorescence intensity is observed for all systems except for free **PdCODCl$_2$** (Figure 10A). Although **P1@Pd(II)** is by far the fastest catalyst, covalent attachment of the catalyst to the polymer backbone is not necessary to achieve conversion in a reasonable time scale. This indicates that the free catalysts either accumulate in the hydrophobic pocket or get trapped inside the polymer microstructure, which then aids in the solubilisation of substrates converting them to products.

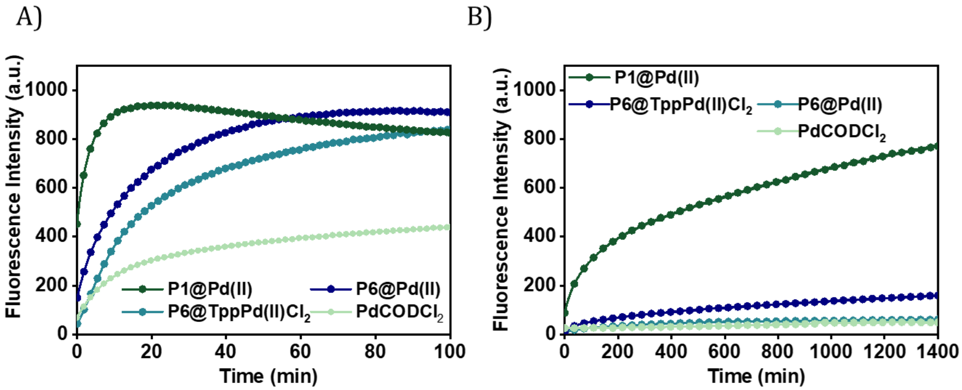

Figure 10: Activation of pro-rho **9** (100 μM) by **P1@Pd(II)**, **P6@PdCODCl$_2$**, **P6@TppPd(II)Cl$_2$** and **PdCODCl$_2$** in A) water B) DMEM monitored by fluorescence spectroscopy over time λ_{ex} = 485 nm and λ_{em} = 520 nm; T = 37 °C, [Pd(II)] = 30 μM in water and [Pd(II)] = 100 μM in DMEM.

Remarkably, in DMEM, the covalent attachment of the Pd(II) ligand to the polymer backbone as in **P1@Pd(II)** is crucial to retain catalytic activity (Figure 10B). In all other catalyst systems, activity is strongly decreased as in

P6@TPPPd$_2$Cl$_2$ or almost completely lost (free **PdCODCl$_2$** and **P6@PdCODCl$_2$**). Thus, encapsulation of the Pd(II) salt does not provide sufficient protection to the catalysts as it is likely not hydrophobic enough to remain inside the hydrophobic reaction pocket. The TPP-Pd(II) complex is more hydrophobic, due to which the encapsulated complex performs slightly better than Pd(II) salts in DMEM (Figure 10B). All in all, our results show that an increase in the complexity of the system, aids the catalyst activity when the reaction is performed in competitive media such as DMEM (Figure 11).

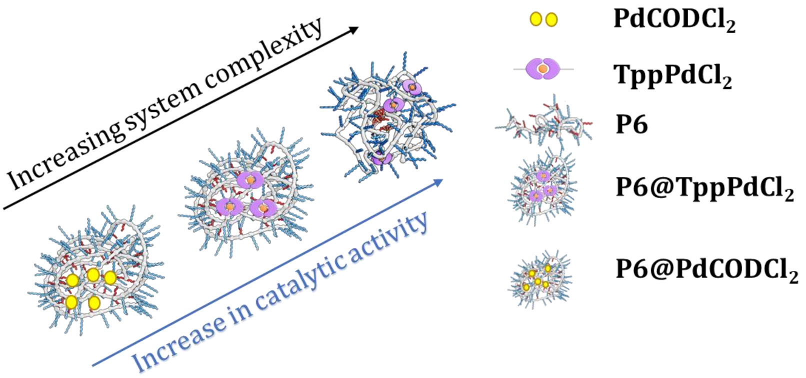

Figure 11: Representation of the four catalytic systems with increasing system complexity and their catalytic activity with increasing medium complexity.

2.9 Activation of anti-cancer pro-drugs

TPP-based **P1@Pd(II)** shows promising activity in complex media. Therefore, we selected **P1@Pd(II)** for evaluating the ability to activate anticancer pro-drugs. Pro-drugs based on 5-fluorouracil, paclitaxel, and doxorubicin (Scheme 2) with different hydrophobicities and protecting groups were chosen as substrates for the activation to find the best substrate suitable for the nanoparticle-based catalytic system. The pro-drugs were synthesized by Stephen Croke and Ana Pérez at University of Edinburgh. Masking of these drugs with Pd labile protecting groups reduces their cytotoxicity but on activation converts to the active drugs that induce cell death. The activation pathway of all four pro-drugs (Scheme 2) starts with depropargylation mediated by Pd(II). Catalytic reactions were performed with **P1@Pd(II)** and the results were compared to those obtained by free **PdCODCl₂** salt. The qualitative conversion was monitored using HPLC-UV/MS.

Pro-5FU **14** is a very hydrophilic pro-drug (Log P = 0.4) of the widely used therapeutic drug 5FU **15** and is of interest to test if it is compatible with the nanoparticle-based catalytic system. Pro-5FU activation was tested in water, PBS, and DMEM. In water, **P1@Pd(II)** activates pro-5FU **14** in 16 h when equimolar concentrations of Pd(II) were used. This is significantly faster than when free **PdCODCl₂** is applied, where no full conversion is observed after 16 h. The same trend was observed when using PBS (Figure 12A). When the amount of Pd(II) was reduced to 30 mol% in PBS, the reaction progressed slower, and no significant difference between free **PdCODCl₂** and **P1@Pd(II)** was observed (Figure 12B).

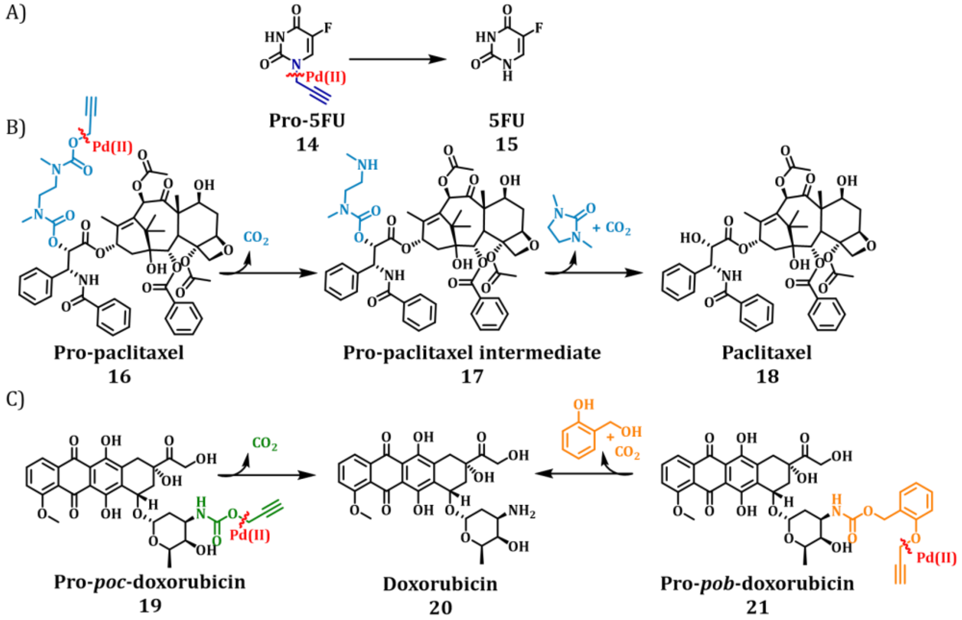

Scheme 2: Scheme for pro-drug activation catalysed by **Pd(II)** catalyst on 4 different anti-cancer pro-drugs (A) Pro-5FU **14** to 5FU **15** (B) Pro-paclitaxel **16** to paclitaxel **18** (C) Pro-poc-doxorubicin **19** and pro-pob-doxorubicin **21** to doxorubicin **20**.

In DMEM, the trend was difficult to observe by UV/MS detection due to the presence of its components that influence detection. However, pro-5FU **14** activation proceeded at a slow rate, and full conversion was not achieved, not even at an equimolar concentration of Pd(II) (Figure 19). These findings suggest that hydrophilic pro-drugs are indeed suitable for nanoparticle-based catalytic systems where the reaction proceeds, even if slowly, at catalytic amounts of Pd(II). But if the rate of pro-drug activation is slower than rate of cancer cell proliferation, our system may cannot generate cytotoxic levels of 5FU.

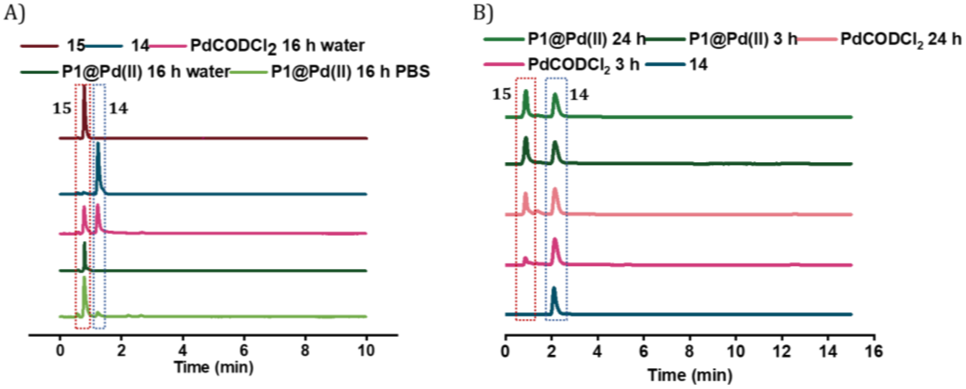

Figure 12: Pro-5FU **14** activation A) in water and PBS [**Pd(II)**] = 100 μM, [**14**] = 100 μM (HPLC-UV detection 265 nm) B) in PBS using HPLC-MS, [**Pd(II)**] = 30 μM, [**14**] = 100 μM, T = 37 °C, time as specified.

In contrast to pro-5FU, pro-paclitaxel **16** is a very large and hydrophobic drug (Log P = 4.1) and therefore an interesting substrate to be tested. Due to its high hydrophobicity, the parent drug paclitaxel is usually delivered using nanoplatforms such as micelles, or liposomes for clinical therapy.[62] During activation, depropargylation of the terminal propargyl group of pro-paclitaxel can be followed by the disappearance of pro-paclitaxel **16**, resulting in an intermediate **17** which should undergo intramolecular cyclisation to form paclitaxel **18**. In PBS, complete disappearance of **16** was observed within 9 h in case of reaction catalysed by **P1@Pd(II)** (30 mol% Pd (II) with respect to substrate) while this was not the case for the **PdCODCl$_2$** salt (Figure 13A, B). This shows that substrate and catalyst accumulation indeed result in good kinetics in the case of **P1@Pd(II)**. However, in both cases, the formed intermediate **17** was stable, eluted earlier, and did not further convert to paclitaxel **18**, not even after 48 h. In DMEM, the **$PdCODCl_2$** salt did not activate pro-paclitaxel **16** both at 30 mol% and 100 mol% catalyst concentrations (Figure 13A, D). In the case of the **P1@Pd(II)**, **17** and **18** were formed in trace amounts within 50 min although full conversion was not achieved even after 48 h (Figure 13C). The HPLC trace indicates two peaks corresponding to paclitaxel (confirmed by MS) in the presence of polymers which is more obvious in DMEM medium. We hypothesise that the paclitaxel present in the hydrophobic cavity of the nanoparticles and paclitaxel in solution elute at different time points. These results indicate that pro-drugs/activated drugs with high hydrophobicity are stabilised in the hydrophobic pocket and are likely less suitable for designing nanoparticle-based pro-drug activation in cells.

We also tested pro-*poc*-doxorubicin **19** (Log P = 1.2) and pro-*pob*-doxorubicin **21** (Log P = 2.8) in water. Both **$PdCODCl_2$** salt and **P1@Pd(II)** activated these pro-drugs but only in case of free catalyst **$PdCODCl_2$** full disappearance of substrate was observed in 16 h (Figure 20). Even though the peaks are not clearly resolved in HPLC chromatogram for the reaction catalysed by **P1@Pd(II)**, minute amounts of substrates **19** and **21** can be detected together with product **20** which took up to 36 h to completely disappear (Figure 20A). Easily cleavable propargyl carbamate protecting group and hydrophilicity together makes these prodrugs more prone to activation even without the presence of nanoparticles. This shows that our nanoparticle-based catalytic system does not improve the activation of dox-based pro-drugs dramatically. Therefore, careful selection of new pro-drugs with optimum hydrophobicity and stable protecting groups is necessary to further develop a polymeric nanoparticle-based pro-drug activation strategy. A good balance of pro-drug and drug hydrophobicity is required for this system for efficient efflux of drugs to induce cell death.

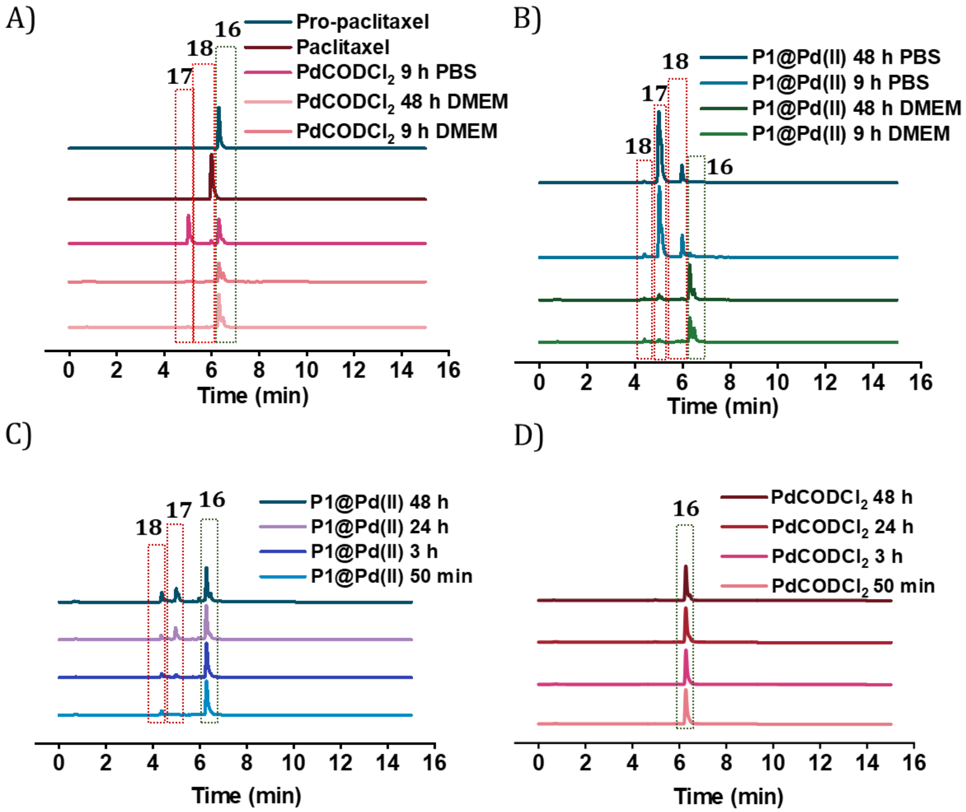

Figure 13: HPLC-MS chromatogram of pro-paclitaxel **16** activation using A) **PdCODCl$_2$** in PBS and DMEM, [Pd(II)] = 30 µM, [**16**] = 100 µM B) **P1@Pd(II)** in PBS and DMEM, [Pd(II)] = 30 µM, [**16**] = 100 µM C) using **P1@Pd(II)** in DMEM, [Pd(II)] = 100 µM, [**16**] = 100 µM D) using **PdCODCl$_2$** in DMEM, [Pd(II)] = 100 µM, [**16**] = 100 µM, T = 37 °C, reaction time as specified.

2.10 Conclusions

In conclusion, we have evaluated different aspects of the SCPN-based catalytic system to improve its performance in complex cellular media. Our findings confirmed that the polymer microstructure has only a minor influence on the catalytic activity of nanoparticles when there is enough hydrophobicity in the pocket to accommodate substrates. The most crucial aspect of the design is the selection of the ligand-metal complex, where an optimal balance of stability and activity is required. TPP-based **P1@Pd(II)** nanoparticles were the most efficient and activated pro-rho to reach full conversion in 3.3 h at 30 mol%

catalyst loading in water. Notably, unlike free Pd(II) catalysts, both bipy-based and TPP-based catalytic systems retained their activity in the cell culture medium DMEM, and **P1@Pd(II)** activated pro-rho reaching 72% conversion in 48 h at 100 mol% catalyst loading. The catalyst loadings used in this work are lower compared to other reports in the field, highlighting the efficiency of our system to perform at low Pd(II) concentrations in complex media.[16,25,28,30,31] In addition, Pd(II) leaching studies revealed that 4-8% of Pd(II) is lost from the hydrophobic interior in the case of TPP-based system **P1@Pd(II)**, while no leaching was observed in the case of bipy-based **P5@Pd(II)**. This confirmed that our designed nanoparticles are efficient in preventing the leaching of Pd(II), which is critical for *in vivo* applications as free Pd(II) ions can cause off-target toxicity and decrease the efficiency of catalysts. Careful deconstruction of the catalytic system revealed that the design can be modified to be more synthetically accessible depending on the medium complexity. Physical encapsulation of catalysts in an amphiphilic polymer proved to be sufficient for activity in less complex media such as water and PBS.

TPP-based nanoparticles proved to be the best in terms of activity, which was further evaluated for pro-drug activation of pro-5FU, pro-paclitaxel, and pro-doxorubicin in relevant media. The rate of pro-drug activation in water is accelerated efficiently by nanoparticles, but the conversion in complex media was more sensitive to the protection group and the substrate polarity. The activation of pro-5FU and pro-paclitaxel in PBS by our designed system is as efficient as Pd(0) resins and Pd-nanosheets, respectively, that are already reported to work efficiently near tumour tissue, which highlights the possibility of translating our system for *in vivo* applications.[29,31] The catalytic efficiency of TPP-based nanoparticles in complex media could not be directly compared to other studies, as often these are performed directly in cells instead of cell culture media. However, hydrophobic drugs such as paclitaxel tend to accumulate in the hydrophobic pocket of nanoparticles, which can affect catalyst performance by product inhibition while also limiting its bioactivity. Overall, our results indicated that hydrophobic substrates in combination with nanoparticles accelerated reaction rates, but a good balance of substrate and product hydrophobicity is required for further improvements and new designs. The ligand-based approach is essential to retain the catalytic activity in a complex medium while screening of new ligand-metal complexes that can withstand nucleophiles in complex media is necessary to further improve the efficiency of nanoparticles. As the rate of pro-drug activation is required to be superior to the rate of cancer cell proliferation to control tumour growth[57], more active catalysts are required to translate the system *in vitro*. However, our findings can aid in the development of more efficient synthetically accessible, stable, and active catalytic nanoparticles, which, when combined with improved substrate design, can greatly increase the potential for *in vivo* pro-drug activation.

2.11 Experimental section

Materials and methods

Pentafluorophenol was purchased from ABCR GmbH und Co. KG. 4-Cyano-4-(phenylcarbonothioylthio)pentanoic acid and lauryl peroxide was purchased from Merck Life Science NV. Jeffamine M-1000® was provided by Huntsman Holland BV. Commercially available AIBN was recrystallized from methanol. Rhodamine 110 hydrochloride was purchased from Fisher scientific. 4,4'-Dimethyl-2,2'-dipyridyl was obtained from Merck Life Science NV. All other chemicals were purchased either from Merck or TCI chemicals. Deuterated solvents were purchased from Cambridge isotope laboratories. The dialysis membrane was regenerated cellulose tubing purchased from Spectra/Por® with a molecular weight cut-off of 6-8 kDa. All solvents were purchased from Biosolve. Gibco DMEM (glucose concentration 1 g/L, with sodium pyruvate, without L-glutamine, without phenol red) and MEM medium were purchased from Fischer scientific. Dialysis of triphenylphosphine (TPP) functionalised polymers was done in degassed solvents in a wide screw-capped 1 L container, keeping it tightly closed. Dialysis solvents were refreshed regularly with new degassed solvents to prevent oxidation of phosphines. Chloroform used for triphenylphosphine polymers' complexation was dried using Mbraun solvent purification system (MB-SPS 800) and was degassed thoroughly by six freeze-pump thaw cycles. All the flasks and needles used for TPP complexation were pre-dried in the oven at 135 °C overnight, and experiments were performed under an argon atmosphere. Automated column chromatography was performed on Grace Reveleris X2 Flash Chromatography System using Flashpure BUCHI prepacked silica columns. BTA amine was previously synthesized in our lab according to the reported protocol.46 All pro-dyes and pro-drugs were synthesized following the previously reported protocol.[3,16,24,30,45,63]

Characterisation methods

^1H, ^{13}C, and ^{31}P NMR measurements were recorded on Bruker 400 MHz spectrometer at ambient temperature, and chemical shifts were recorded concerning TMS as the internal standard for ^1H and ^{13}C spectra and 85% H_3PO_4 in D_2O as an external standard for ^{31}P NMR spectra. Fluorescence measurements were performed on an Agilent Cary Eclipse fluorescence spectrophotometer using 1 cm × 1 cm pathlength quartz cuvettes. UV- Vis measurements were performed on JASCO V-750 spectrometer using 1 cm pathlength quartz cuvettes, and CD measurements were performed on Jasco J-815 spectropolarimeter using 0.5 cm pathlength quartz cuvettes. Liquid chromatography - UV was performed using Shimadzu UFLC-XR with PDA detector with water + 0.1% formic acid and ACN + 0.1% formic acid as eluents on Kinetex column C18 5 mm EVO 100 Å. HPLC Method 1 for pro-dyes **1** - **3**: eluent A: water (0.1% formic acid); eluent B: acetonitrile (0.1% formic acid); and A/B = 90:10 isocratic 2 min, 90:10 to 0:100 in 2 min, isocratic 2 min, 0:100 to 90:0 in 2 min, and isocratic 2.0 min (flow = 0.2 mL/min). Method 2 for pro-5FU: A/B = 95:5 isocratic 15 min. Method 3 for pro-paclitaxel: A/B = 80:20 isocratic 0.5 min, A/B = 80:20 to 0:100 in 10 min, isocratic 2 min, and 0:100 to 80:20 in 5 min, isocratic 1.5 min (flow = 0.2 mL/min). Method 4 for pro-dox: A/B = 95:5 isocratic 3 min, A/B = 95:5 to 20:80 in 8 min, isocratic 1 min, and 20:80 to 95:5 in 3 min, isocratic 4 min (flow = 0.2 mL/min).

Size exclusion chromatography (SEC) measurements of poly(pentafluorophenyl)acrylate were recorded using Shimadzu LC-2030C 3D with RID-20 refractive index detector and PDA detector at a flow rate of 1 mL min^{-1} with THF as eluent with Agilent mixed-C and mixed-D column in series at 40 °C. Exclusion limit = 2.000.000 g mol^{-1}, 7.5 mm i.d. × 300 mm. Calibration was performed using polystyrene standards from polymer laboratories. DMF-SEC measurements of functionalised polymers were performed using PL-GPC-50 plus (Varian Inc. Company) equipped with a refractive index detector. DMF with 10 mM LiBr was used as eluent at a flow rate of 1 mL min^{-1} on the Shodex GPC-KD-804 column at 50 °C. Exclusion limit = 100.000 Da, 0.8 cm i.d. × 300 mm calibrated using poly (ethylene oxide) from polymer laboratories. Palladium quantification was performed on Agilent MP-AES 4200 (Microwave plasma atomic emission spectrometer) elemental analyser calibrated using Palladium Standard for ICP. Dynamic light scattering experiments were performed using Malvern Zetasizer with 830 nm laser and an angle of scattering 90°.

Synthesis

Pentafluorophenylacrylate[46]

Acryloyl chloride **2** (4.4 mL, 1 eq, 54 mmol) was dissolved in dry diethyl ether (50 mL) and was added slowly via a dropping funnel to a combined mixture of pentafluorophenol **1** (10 g, 1 eq, 54 mmol) and triethylamine (8.3 mL, 1.1 eq, 60 mmol) dissolved in 150 mL of dry diethyl ether cooled under ice bath. After 3 h, the reaction was brought to room temperature and was stirred overnight. After confirming the completion of the reaction via TLC, the white precipitate formed was filtered off and the filtrate was collected. The solvent was removed using rotary evaporator to obtain crude product as pale-yellow liquid. The crude product was purified by column chromatography (100 g FlashPure irregular silica column, n-heptane) and **3** was obtained as colourless liquid. Yield: 8 g, 61% ^{1}H NMR (400 MHz, $CDCl_3$) δ 6.72 (dd, *J* = 17.3, 1.0 Hz, 1H), 6.37 (dd, *J* = 17.3, 10.5 Hz, 1H), 6.18 (dd, *J* = 10.5, 1.0 Hz, 1H), ^{19}F NMR (376 MHz, $CDCl_3$): δ -152.28 – -153.07 (m), -158.04 (t, *J* = 21.7 Hz), -162.08 – -162.96 (m).

tert-Butyl (6-(4-(diphenylphosphaneyl)benzamido)hexyl)carbamate

4-Diphenylphosphinobenzoic acid (800 mg, 1 eq, 2.6 mmol) was dissolved in dry and degassed DMF (20 mL) followed by the addition of DIPEA (500 µL, 1.1 eq, 2.8 mmol) and TBTU (840 mg, 1 eq, 2.6 mmol). After stirring the reaction mixture for 15 min, *N*- boc-1,6 hexadiamine (583 µL, 1 eq, 2.6 mmol) was added. The reaction mixture was then stirred overnight at room temperature under argon atmosphere. Completion of the reaction was monitored by TLC by mini work up in Eppendorf using ethyl acetate. After completion of the reaction, 40 mL degassed water was added to the reaction mixture and water phase was extracted using degassed ethyl acetate (40 mL × 3) and dried over Na_2SO_4. The solvent was removed using rotary evaporator and residue was purified using column chromatography (12 g, FlashPure HP silica column, MeOH/CH_2Cl_2: 0/100 - 10/90) to obtain white solid. Yield: 680 mg, 52%. ^1H NMR (400 MHz, $CDCl_3$) δ 7.73 (d, *J* = 7.8 Hz, 2H), 7.38 – 7.27 (m, 12H), 6.34 (b, 1H), 4.53 (b, 1H), 3.44 (q, *J* = 6.7 Hz, 2H), 3.12 (q, *J* = 6.7 Hz, 2H), 1.62 (m, 4H), 1.53 (m, 2H), 1.42 (s, 9H), 1.40 (m, 2H). ^{13}C NMR (100 MHz, $CDCl_3$) δ 167.31, 156.26, 141.94, 141.81, 136.56, 136.46, 134.93, 134.09, 133.90, 133.77, 133.58, 129.18, 128.81, 128.74, 126.97, 126.90, 40.16, 39.69, 36.62, 30.20, 29.60, 28.56, 26.22, 26.02. ^{31}P NMR (162 MHz, $CDCl_3$) δ -5.56.

N-(6-Aminohexyl)-4-(diphenylphosphaneyl) benzamide

tert-Butyl (6-(4-(diphenylphosphaneyl)benzamido)hexyl)carbamate (50 mg, 1 eq, 0.099 mmol) was dissolved in degassed DCM (1 mL) followed by the addition of TFA (1 mL) and was stirred at 0 °C for 6 h. After completion of the reaction determined by TLC, the reaction mixture was concentrated in vacuum. Excess of TFA was removed by co-evaporation with DCM (6 times). Further, the product was redissolved in DCM (10 mL) and washed with sat. $NaHCO_3$ (15 mL × 2), brine (10 mL) and was dried over $MgSO_4$. The solvent was evaporated using rotary evaporator and dried under vacuum to get sticky white solid which was stored under argon at -19 °C. Yield: quantitative, 36 mg. Some phosphine oxidation was observed from ^{31}P NMR. ^1H NMR (400 MHz, $CDCl_3$) δ 7.69 (d, *J* = 7.7 Hz, 2H), 7.38 – 7.27 (m, 12H), 6.11 (b, 1H), 3.45 (q, *J* = 6.7 Hz, 2H), 2.69 (t, *J* = 6.7 Hz, 2H), 1.66 – 1.57 (m, 2H), 1.51 (2H), 1.45 (m, 2H), 1.41 – 1.29 (m, 4H). ^{13}C NMR (100 MHz, $CDCl_3$) δ 167.31, 141.79, 141.65, 136.40, 136.30, 134.86, 133.95, 133.75, 133.57, 133.38, 129.07, 128.69, 128.62, 126.89, 126.82, 41.94, 39.98, 33.30, 29.60, 26.76, 26.49. ^{31}P NMR (162 MHz, $CDCl_3$) δ -5.61. MALDI-TOF-MS: m/z calc: 404.2; found: 405.2 $[M+H]^+$, 421.2 (oxidized TPP), 443.2 $[oxidized+Na]^+$ Phosphine oxidation was negligible as observed from ^{31}P NMR, MALDI-TOF-MS data showed oxidized peaks because samples were not handled under argon atmosphere.

2,4-Dinitro-1-(prop-2-yn-1-yloxy) benzene[24]

2,4-Dinitrophenol **6** (460 mg, 1 eq, 2.5 mmol) was dissolved in DMF (5 mL) together with propargyl bromide (354 mg, 1.2 eq, 3 mmol) and K_2CO_3 (414 mg,1.2 eq, 3 mmol). The reaction mixture was stirred overnight at 50 °C. After confirming the completion of reaction by TLC, water

(10 mL) was added to reaction mixture and was extracted with diethyl ether (10 mL ×3) and dried over $MgSO_4$, followed by concentration using rotary evaporator. The product was purified by flash column chromatography (10 g FlashPure irregular Silica column, Heptane/DCM: 80/20) to afford a pale-yellow solid. Yield: 399 mg, 72% ^1H NMR (400 MHz, $CDCl_3$): δ 8.77 (d, *J* = 2.8 Hz, 1H), 8.46 (dd, *J* = 9.2, 2.8 Hz, 1H), 7.41 (d, *J* = 9.3 Hz, 1H), 4.99 (d, *J* = 2.4 Hz, 2H), 2.67 (t, *J* = 2.4 Hz, 1H).

Prop-2-yn-1-yl (4-methyl-2-oxo-2H-chromen-7-yl) carbamate[16]

7-Amino-4-methyl coumarin **8** (100 mg, 1 eq, 0.57 mmol) was dissolved in 4 mL dry DCM under ice bath followed by the addition of pyridine (61 µL, 1.3 eq, 0.75 mmol). Propargyl carbonyl chloride (85 mg, 1.2 eq, 0.72 mmol) was added to this reaction mixture resulting in a yellow suspension. The reaction mixture was stirred at 0 °C for 3 h and was brought to room temperature and stirred overnight under argon atmosphere. After completion of the reaction monitored by TLC, 1 N HCl (30 mL) was added to the reaction mixture, the pale-yellow precipitate formed was filtered, and washed with diethyl ether until the yellow colour was faded. The product was purified by column chromatography to afford white powder. (Silica, MeOH/ DCM: 10/90) Yield: 117 mg, 80 % ^1H NMR (400 MHz, DMSO-d_6): δ 10.37 (s, 1H), 7.71 (d, *J* = 8.7 Hz, 1H), 7.53 (d, *J* = 2.1 Hz, 1H), 7.41 (dd, *J* = 8.7, 2.1 Hz, 1H), 6.25 (d, *J* = 1.4 Hz, 1H), 4.81 (d, *J* = 2.5 Hz, 2H), 3.61 (t, *J* = 2.4 Hz, 1H), 2.39 (d, *J* = 1.2 Hz, 3H).

2-(3-Iminio-6-(morpholine-4-carboxamido)-3H-xanthen-9-yl)benzoate[64]

A pre-dried three-neck round bottom flask was purged under argon, allowed to cool down and dry DMF (50 mL) was added to the flask followed by the addition of rhodamine 110 chloride (500 mg, 1 eq, 1.3 mmol). The reaction was performed under argon atmosphere and covered with aluminium foil throughout. To this solution, NaH 60% dispersion in mineral oil (119 mg, 2.2 eq, 2.9 mmol) was added portion wise over 10 min and was stirred for 1 h. After, 4-morpholinecarbonyl chloride (160 µL, 1 eq, 1.3 mmol) was added dropwise over 7 min. The color of the reaction turned fluorescent brown and was stirred overnight. The color changed to purple after 24 h and the reaction mixture was concentrated using rotary evaporator. The crude product was purified using column chromatography (Flashpure BUCHI 12 g 40 µm irregular silica column, $CHCl_3$: MeOH: CH_3COOH = 100:7:1). After column, product was redissolved in Toluene/Methanol/DMF: 100/5/0.5 (30 mL×3) and co-evaporated using rotary evaporator to remove CH_3COOH. The presence of acetic acid can result in unwanted side products in the next step that can reduce the yield drastically. The product was dried under vacuum to afford red powder. ^1H NMR showed presence of toluene which will not interfere with the next step while was necessary to get rid of CH_3COOH. Yield: 200 mg, 35% ^1H NMR (400 MHz, DMSO-d_6) δ 8.79 (s, 1H), 7.97 (d, *J* = 7.6 Hz, 1H), 7.74 (dt, *J* = 32.9, 7.4 Hz, 2H), 7.62 (d, *J* = 2.1 Hz, 1H), 7.09 (dd, *J* = 8.7, 2.1 Hz, 1H), 6.57 (d, *J* = 8.7 Hz, 1H), 6.43 (d, *J* = 1.9 Hz, 1H), 6.40 – 6.27 (m, 2H), 5.64 (s, 2H), 3.61 (t, *J* = 4.7 Hz, 4H), 3.43 (t, *J* = 4.8 Hz, 4H).

Prop-2-yn-1-yl (3'-(morpholine-4-carboxamido)-3-oxo-3H-spiro[isobenzofuran-1,9'-xanthen]-6'-yl) carbamate[64]

2-(3-Iminio-6-(morpholine-4-carboxamido)-3H-xanthen-9-yl) benzoate (200 mg, 1 eq, 0.45 mmol) was dissolved in dry DMF (6 mL) followed by the addition of pyridine (2 mL, 53 eq, 24 mmol) under argon atmosphere at 0 °C and covered with aluminum foil. Then, propargyl chloroformate (0.5 mL, 10 eq, 5 mmol) was added dropwise through a syringe. The reaction mixture was brought to room temperature and stirred overnight, and solvent was removed using rotary evaporator. The crude product was redissolved in 15 mL chloroform and washed with 1 N HCl (20 mL × 1), water (20 mL × 1), saturated brine (10 mL × 1) solution and dried over $MgSO_4$. The crude mixture was then purified by column chromatography (Flashpure BUCHI 12 g 40 µm irregular silica column, EtOAc) to afford pale yellow powder. Yield = 140 mg, 60%. ^1H NMR (400 MHz, $CDCl_3$) δ 8.01 (d, *J* = 7.5 Hz, 1H), 7.63 (dt, *J* = 19.4, 7.3 Hz, 2H), 7.48 (d, *J* = 14.2 Hz, 2H), 7.13 (d, *J* = 7.5 Hz, 1H), 6.94 (d, *J* = 7.2 Hz, 2H), 6.84 (s, 1H), 6.71 (dd, *J* = 12.9, 8.6 Hz, 2H), 6.45 (s, 1H), 4.83 – 4.74 (m, 2H), 3.76 (t, *J* = 4.9 Hz, 4H), 3.50 (t, *J* = 4.9 Hz, 4H), 2.53 (s, 1H).

4-(7-Bromoheptyl)-4'-methyl-2,2'-bipyridine[49]

4,4' -Dimethylbipyridine (1 g, 1 eq, 5.4 mmol) was dissolved in dry THF (30 mL) and cooled under ice bath in a Schenk flask. In another Schlenk flask cooled in ice-bath, dry THF (5 mL) was added, followed by the addition of diisopropylamine (909 µL, 1.2 eq, 6.5 mmol) under argon atmosphere. To this mixture *n*-butyllithium (2.2 mL of 2.5 M solution in hexane, 1 eq, 5.4 mmol) was added via syringe. Finally, precooled 4,4' -dimethylbipyridine in THF was added to the former solution and was stirred for 1 h. After this, 1,6-dibromohexane (1.7 mL, 2 eq, 10.8 mmol) dissolved in dry THF (3 mL) was added to the reaction mixture and was stirred for 3 h. The reaction was quenched by the addition of water (20 mL) and after stirring for 30 min, pH was adjusted to ~5 by addition of 1 N HCl. Then, this mixture was stirred overnight. Diethyl ether (20 mL) was added to the mixture and product was extracted using dichloromethane (30 mL × 5), dried over $MgSO_4$, and concentrated under vacuum at room temperature. The crude product was purified by column chromatography (Silica, Dichloromethane) Yield: 840 mg, 45 %. ^1H NMR (400 MHz, $CDCl_3$) δ 8.55 (t, *J* = 5.5 Hz, 2H), 8.27 – 8.19 (m, 2H), 7.13 (dd, *J* = 4.8, 2.1 Hz, 2H), 3.40 (t, *J* = 6.8 Hz, 2H), 2.69 (t, *J* = 8.8, 6.8 Hz, 2H), 2.44 (s, 3H), 1.85 (p, *J* = 6.9 Hz, 2H), 1.74 – 1.65 (m, 2H), 1.47 – 1.32 (m, 6H).

2-(7-(4'-Methyl-[2,2'-bipyridin]-4-yl)heptyl)isoindoline-1,3-dione[49]

4-(7-Bromoheptyl)-4'-methyl-2,2'-bipyridine (340 mg, 1 eq, 1 mmol) was dissolved in dry DMF (20 mL), followed by the addition of potassium phthalimide (222 mg, 1 eq, 1.2 mmol). The reaction mixture was stirred for 90 h. Water was added (20 mL) to this mixture and product was extracted using chloroform (20 mL× 3). Organic layer was washed with 0.2 M sodium hydroxide (20 mL × 1), brine (20 mL × 1) and dried over $MgSO_4$. The crude product was purified by column chromatography (Silica, DCM) to obtain white solid. Yield: 351 mg, 85% ^1H NMR (400 MHz,

$CDCl_3$) δ 8.53 (m, 2H), 8.20 (m, 2H), 7.82 (m, 2H), 7.68 (m, 2H), 7.11 (m, 2H), 3.66 (t, *J* = 7.3 Hz, 2H), 2.66 (t, *J* = 7.8 Hz, 2H), 2.42 (s, 3H), 1.67 (m, 4H), 1.34 (m, 6H).

7-(4'-Methyl-[2,2'-bipyridin]-4-yl)heptan-1-amine[49]

2-(7-(4'-Methyl-[2,2'-bipyridin]-4-yl)heptyl) isoindoline-1,3-dione (200 mg, 1 eq, 0.48 mmol) was dissolved in methanol (10 mL) and was heated to reflux in oil bath at 70 °C followed by the addition of hydrazine hydrate (60 mg, 2.5 eq, 1.2 mmol) and was stirred for 24 h. The solvent was removed using rotary evaporator and residue was redissolved in chloroform (15 mL). This solution was washed with 6 M hydrochloric acid (10 mL × 1), water (10 mL × 1), brine (10 mL × 1) and dried over $MgSO_4$. The combined aqueous layers was basified using 5 M sodium hydroxide till pH~8 and was extracted again using chloroform (10 mL × 2). Finally, chloroform was removed using rotary evaporator and dried under vacuum to obtain product as white solid. Yield: 76 mg, 56% ^{1}H NMR (400 MHz, $CDCl_3$) δ 8.55 (t, *J* = 5.0 Hz, 2H), 8.23 (dd, *J* = 3.9, 1.8 Hz, 2H), 7.13 (dd, *J* = 4.9, 1.8 Hz, 2H), 2.68 (q, *J* = 7.1, 6.6 Hz, 4H), 2.44 (s, 3H), 1.70 (p, *J* = 7.6 Hz, 2H), 1.56 – 1.21 (m, 12H).

2-(Thiophen-2-yl)-1H-benzo[d]imidazole[61]

o-Phenylenediamine (0.50 g, 1 eq, 5 mmol) was dissolved in 10 mL absolute ethanol. To this solution, 2-thiophene carboxaldehyde (0.57 g, 1 eq, 5 mmol) dissolved in absolute ethanol (20 mL) was added slowly. The reaction mixture was stirred at room temperature overnight. Completion of reaction was monitored by TLC. The crude yellow precipitate that formed was recrystallized from absolute ethanol. Yield = 500 mg, 51%. ^{1}H NMR (400 MHz, DMSO-d_6) δ 12.92 (s, 1H), 7.83 (dd, *J* = 3.6, 1.2 Hz, 1H), 7.72 (dd, *J* = 5.0, 1.2 Hz, 1H), 7.60 (d, *J* = 7.8 Hz, 1H), 7.50 (d, *J* = 7.1 Hz, 1H), 7.25 – 7.14 (m, 3H).

2-(2’- Hydroxyphenyl -5’-methyl)benzothiazole[56]

2-Hydroxy-5-methylbenzaldehyde (2.5 g, 18.36 mmol), 2-aminothiophenol (2.3 g, 18.37 mmol) and sodium metabisulfite (3 g, 15.78 mmol) were dissolved in N, N-dimethylformamide (DMF) (50 mL) in a 100 mL round bottom flask. Followingly, the reaction mixture was refluxed at 110 °C for 5 h and the progress of reaction was monitored by TLC. After completion of reaction overnight, reactant solution was cooled to room temperature. To this 50 mL deionized water was added which resulted in precipitation of product, which was filtered, washed with deionized water 7 times or until product turned completely white. Then it was dried under vacuum to afford white product. Yield = 3.4 g, 80%.^{1}H NMR (400 MHz, $CDCl_3$) δ 12.30 (s, 1H), 7.99 (d, *J* = 8.2 Hz, 1H), 7.91 (d, *J* = 8.0 Hz, 1H), 7.56 – 7.45 (m, 2H), 7.41 (t, *J* = 7.6 Hz, 1H), 7.20 (dd, *J* = 8.4, 2.1 Hz, 1H), 7.01 (d, *J* = 8.4 Hz, 1H), 2.36 (s, 3H).

2-(2’- Hydroxyphenyl -3’-aldehyde-5’-methyl) benzothiazole[56]

2-(2’-Hydroxyphenyl -5’-methyl)benzothiazole (1.2 g, 5 mmol) and hexamethylenetetramine (HMT) (2.4 g, 17 mmol) were dissolved in trifluoroacetic acid (7 mL) in a 50 mL round bottom flask. The reaction mixture was refluxed at 100 °C for 6 h and the reaction was monitored by TLC. After completion of the reaction it was cooled to room temperature. HCl (100 mL, 4 M) was added to this and the reaction mixture was extracted with dichloromethane (50 mL × 3). Combined organic phase was washed with brine (25 mL × 1) and the solvent was evaporated under reduced pressure. The crude mixture was purified by manual column chromatography (silica, DCM) to afford faint yellow flaky solid. Yield = 1 g, 70 %. ^{1}H NMR (400 MHz, $CDCl_3$) δ 13.02 (s, 1H), 10.50 (s, 1H), 8.11 – 7.84 (m, 3H), 7.72 (s, 1H), 7.63 – 7.39 (m, 2H), 2.42 (s, 3H).

2-(2’-(Propargyl ether) phenyl -3’-aldehyde-5-methyl)benzothiazole[56]

2-(2-Hydroxyphenyl -3-aldehyde-5-methyl) benzothiazole (0.5 g, 1.86 mmol) was dissolved in dry DMF (50 mL) in a 100 mL round bottom flask, followed by addition of K_2CO_3 (0.616 g, 4.46 mmol). The reaction mixture was then stirred at room temperature for 20 min. Further, 3-bromopropyne (0.531 g, 4.46 mmol) was added to the reaction mixture and was stirred for 24 h at room temperature. The completion of reaction was monitored by TLC. After completion, deionized water (50 mL) was added to this mixture which was extracted with ethyl acetate (50 mL × 3), washed with brine (25 mL × 1) and dried under vacuum. The crude product obtained was purified by manual column chromatography (silica, DCM:hexane = 2:3 v/v) to afford white flaky solid. Yield = 0.39 g, 70%.^{1}H NMR (400 MHz, $CDCl_3$) δ 10.51 (s, 1H), 8.47 – 8.35 (m, 1H), 8.13 (m, *J* = 8.1, 0.8 Hz, 1H), 8.02 – 7.91 (m, 1H), 7.83 (m, *J* = 2.4, 0.9 Hz, 1H), 7.54 (ddd, *J* = 8.3, 7.2, 1.3 Hz, 1H), 7.45 (ddd, *J* = 8.2, 7.2, 1.2 Hz, 1H), 4.75 (d, *J* = 2.4 Hz, 2H), 2.52 (t, *J* = 2.4 Hz, 1H), 2.50 – 2.47 (m, 3H).

*Poly(pentafluorophenyl) acrylate **p-PFP***[46]

Cyano-4-(phenyl-carbonothioylthio)pentanoic acid **4** (16.9 mg, 0.0035 eq, 0.06 mmol) and azobisisobutyronitrile (0.99 mg, 0.00035 eq, 0.006 mmol) was dissolved in 4 mL dry dioxane and was transferred to a oven dried Schlenk tube containing pentafluorophenylacrylate **3** (4.1 g, 1 eq, 17.3 mmol) under argon atmosphere. The mixture was thoroughly degassed for 1 h and was placed into a pre-heated oil bath at 80 °C. After 3.5 h, monomer conversion was determined by ^{19}F NMR spectroscopy from an aliquot of reaction mixture and conversion was 75%. The reaction mixture was immediately quenched by placing the flask in liquid nitrogen. Later, flask was brought to room temperature and highly viscous mixture was dissolved in 5 mL DCM and precipitated into 800 mL ice-cold pentane (3 times). The precipitate was filtrated out and dried in the oven under vacuum overnight at 40 °C. After drying, 2.6 g of polymer ***p*-PFP** was obtained. Yield: 2.6 g, 86%. ^{19}F NMR (376 MHz, $CDCl_3$) δ -153.25, -156.80, -162.25. ^{1}H NMR (400 MHz, $CDCl_3$): δ 3.08 (br), 2.49 (br) 2.15 (br).

*End group modification - **p-PFPA***[46]

***p*-PFP** (1.1 g, 21 µmol, 1 eq), azobisisobutyronitrile (68 mg, 420 µmol, 20 eq) and lauryl peroxide (16 mg, 42 µmol, 2 eq) were dissolved in dry dioxane (15 mL) and degassed for 1 h. Then the reaction mixture was heated to 80 °C under argon atmosphere for 3 h when the solution turned colourless from pink. Later, the solvent was removed, and the residue was re-dissolved in 5 mL chloroform and was precipitated in 800 mL ice-cold pentane (× 3) and dried overnight under vacuum at 40 °C. Yield: 1 g, 91%. ^{1}H NMR (400 MHz, $CDCl_3$) δ 3.08 (br), 2.49 (br), 2.14 (br). ^{19}F NMR (376 MHz, $CDCl_3$) δ -153.23, -156.75, -162.17.

*Post functionalisation of p-PFPA to **P1-P6***

P1: ***p*-PFPA** (200 mg, 1 eq, 0,0039 mmol) was dissolved in dry and degassed DMF in a Schlenk flask kept in preheated oil bath at 50 °C. To this solution, TPP ligand N-(6-Aminohexyl)-4-(diphenylphosphaneyl) benzamide (31 mg, 20 eq, 0,078 mmol) was added and stirred for 2 h. Incorporation was followed by ^{19}F NMR by comparing the peaks of free pentafluorophenol with those in the polymer backbone. Afterwards, BTA amine (51 mg, 20 eq, 0.078 eq) was added to the mixture and stirred for 2 h, and incorporation was monitored. Finally, Jeffamine M-1000 (624 mg, 160 eq, 0.62 mmol) was added. The reaction mixture was then left overnight under argon and completion of reaction was again monitored using ^{19}F NMR. Then, the reaction mixture was purified by dialysis (1 x 1 L methanol, 2 x 1 L THF) for 3 days in a tightly closed screw capped container. Degassed solvents were used for dialysis which was refreshed as frequently as possible (> 6 h time gap) to prevent oxidation of triphenylphosphine. After dialysis, THF was reduced to ~ 3 mL using rotary evaporator and polymer was precipitated into ice cold pentane (800 mL). The polymer was dried under vacuum overnight at 50 °C to yield a pale-yellow solid and was stored at -19 °C. Yield: 426 mg, $M_{\text{theoretical}}$ = 183 kD, $M_{\text{n, SEC-DMF}}$ = 46.8 kD. ^{1}H NMR (400 MHz, $CDCl_3$) δ 8.47 (s), 7.76 (br), 7.34 (br), 6.91 – 6.10 (br), 3.89 – 3.07 (m), 1.70 – 0.71 (m). ^{31}P NMR (162 MHz, $CDCl_3$) δ -5.80.

Same protocol was followed for all polymers with varying ligands as specified below:

P2:***p*-PFPA** (100 mg, 1 eq, 0,0019 mmol), TPP ligand N-(6-Aminohexyl)-4-(diphenylphosphaneyl) benzamide (15 mg, 20 eq, 0,038 mmol) , BTA amine (12 mg, 10 eq, 0.019 eq), dodecyl amine (10 mg, 30 eq, 0.057 mmol) , Jeffamine M-1000 (266 mg, 140 eq, 0.26 mmol) The polymer was dried under vacuum overnight at 50 °C to yield a pale-yellow solid and was stored at -19 °C. Yield: 231 mg, $M_{\text{theoretical}}$ = 163 kD, $M_{\text{n, SEC-DMF}}$ = 42.2 kD. ^{1}H NMR (400 MHz, $CDCl_3$) δ 8.45 (s), 7.77 (br), 7.60 (br), 7.31 (s), 7.08-6.50 (br), 4.17 – 2.41 (m), 1.86 – 0.72 (m). ^{31}P NMR (162 MHz, $CDCl_3$) δ -5.99.

P3:***p*-PFP** (150 mg, 1 eq, 0,0029 mmol), TPP ligand N-(6-Aminohexyl)-4-(diphenylphosphaneyl) benzamide (23 mg, 20 eq, 0,058 mmol) , dodecyl amine (21 mg, 40 eq, 0.116 eq), Jeffamine M-1000 (400 mg, 140 eq, 0.40 mmol). The polymer was dried under vacuum overnight at 50 °C to yield a colourless solid and was stored at -19 °C. Yield: 316 mg, $M_{\text{theoretical}}$ = 158 kD, $M_{\text{n, SEC-DMF}}$ = 62 kD. ^{1}H NMR (400 MHz, $CDCl_3$) δ 7.76 (br), 7.34 (br), 6.98-5.93 (br), 4.22 – 3.04 (m), 1.62 – 0.79 (m). ^{31}P NMR (162 MHz, $CDCl_3$) δ -5.84.

P4:***p*-PFP** (100 mg, 1 eq, 0,0019 mmol), TPP ligand N-(6-Aminohexyl)-4-(diphenylphosphaneyl) benzamide (30 mg, 40 eq, 0,076 mmol), Jeffamine M-1000 (300 mg, 160 eq, 0.30 mmol). The polymer was dried under vacuum overnight at 50 °C to yield a colourless solid and was stored at -19 °C. Yield: 223 mg, $M_{\text{theoretical}}$ = 178 kD, $M_{\text{n, SEC-DMF}}$ = 55.4 kD. ^{1}H NMR (400 MHz, $CDCl_3$) δ 7.78 (br), 7.31 (br), 6.94-6.04 (br), 4.17 – 3.02 (m), 2.42 – 0.90 (m). ^{31}P NMR (162 MHz, $CDCl_3$) δ -5.97.

P5: *p*-PFP (100 mg, 1 eq, 0,0019 mmol), bipy ligand 7-(4'-Methyl-[2,2'-bipyridin]-4-yl)heptan-1-amine (10 mg, 20 eq, 0,038 mmol), BTA amine (12 mg, 10 eq, 0.019 eq), dodecyl amine (10 mg, 30 eq, 0.057 mmol), Jeffamine M-1000 (266 mg, 140 eq, 0.26 mmol). Dialysis was performed same as **P1** but degassing was not performed. The polymer was dried under vacuum overnight at 50 °C to yield a colourless solid and was stored at -19 °C. Yield: 170 mg, $M_{\text{theoretical}}$ = 179 kD, $M_{\text{n, SEC-DMF}}$ = 46.9 kD. ^{1}H NMR (400 MHz, $CDCl_3$) δ 8.52 (s), 8.20 (br), 7.12 (br), 6.90-6.07 (br), 4.70-2.75 (m), 2.29 – 0.67 (m).

P6: *p*-PFP (100 mg, 1 eq, 0,0019 mmol), dodecyl amine (21 mg, 40 eq, 0.116 eq, Jeffamine M-1000 (300 mg, 160 eq, 0.30 mmol. Dialysis was performed same as **P1** but degassing was not performed. The polymer was dried under vacuum overnight at 50 °C to yield a pale-yellow solid and was stored at -19 °C. Yield: 186 mg, $M_{\text{theoretical}}$ = 172 kD, $M_{\text{n, SEC-DMF}}$ = 49.8 kD. ^{1}H NMR (400 MHz, D_2O) 6.87 – 6.08 (br), 3.99 – 2.97 (m), 1.67 – 0.64 (m).

Complexation of polymers with Pd(II)

*Complexation of polymers **P1-P4** with Pd(II)* [51]

Dry chloroform was thoroughly degassed by 6 freeze-pump thaw cycles to remove any trace of oxygen in the solvent and all additions were performed under argon using cannula without atmospheric contamination. Degassed solvent (25 mL) was transferred to 50 mg TPP-functionalised polymers **P1-P4** kept in an oven-dried Schlenk tube via cannula (dried in oven overnight). Degassed solvent (25 mL) was also transferred in the same way into another flask containing 3 mg of **$PdCODCl_2$** (3 eq. with respect to TPP ligand). After that, the polymer solution was transferred dropwise into the **$PdCODCl_2$** solution over 20 min while stirring. This reaction mixture was stirred overnight under argon and concentrated in vacuum and dialyzed for 3 days (3 × 1 L $CHCl_3$) to remove most of the unbound **$PdCODCl_2$**. Complexation was also performed at 2:1 ratio of TPP ligand: Pd(II), however, it resulted in the oxidation of TPP due to highly diluted conditions. Therefore, this protocol was followed to obtain **P1-P4@Pd(II)** that form nanoparticles with small size when dissolved in water with minimal aggregates. MP-AES was performed to obtain the final concentration of Pd(II) in the sample which revealed the presence of unbound **PdCODCl$_2$** which was not removed during dialysis as they are trapped inside polymers. This was also taken into consideration during catalysis studies.

*Complexation with Pd(II) of polymer **P5***[45]

1 mg of **P5** was dissolved in 1 mL Milli-Q water followed by sonication for 30 min and was allowed to equilibrate for 1 h. To this 10 µL of 10 mM Na_2PdCl_4 solution was added and was stirred for 15 min. Complexation was monitored by UV-Vis Spectroscopy.

Dynamic light scattering (DLS) measurements

All polymers **P1-P5** and **P1-P5@Pd(II)** were dissolved in Milli-Q water at 1 mg/mL concentrations in water by sonication for 30 min followed by equilibration of 1 h. Then samples were taken to perform DLS studies.

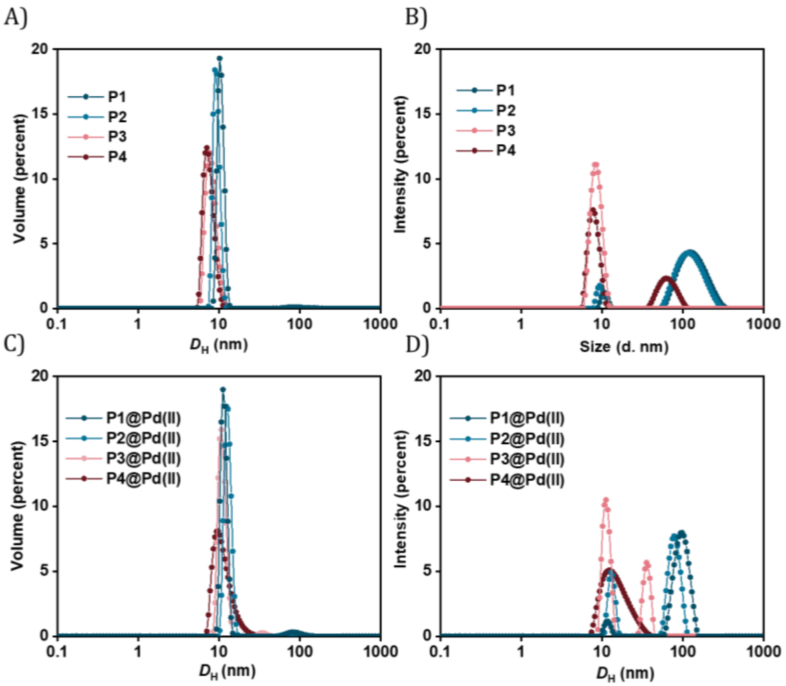

Figure 14: Dynamic light scattering studies of **P1-P4** before and after complexation [**P1-P4**] = 1 mg/mL, [**P1-P5@Pd(II)**] = 1 mg/mL in H_2O, T = 20 °C.

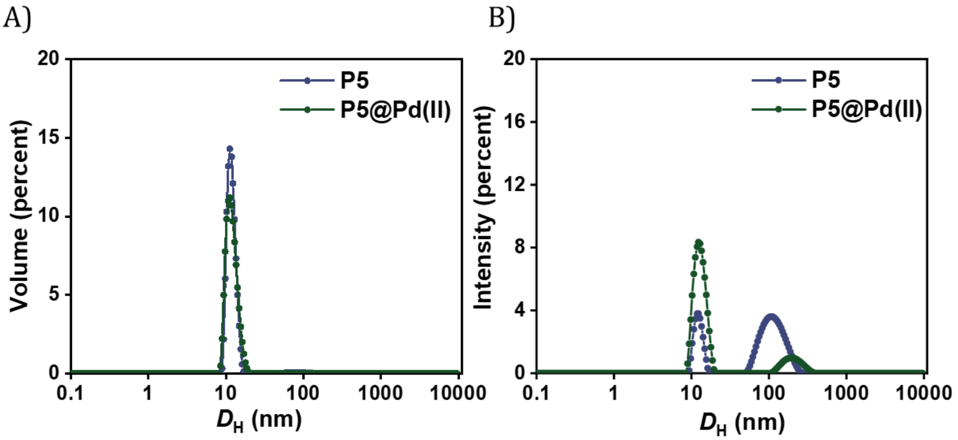

Figure 15: Dynamic light scattering studies of **P5** before and after complexation [**P5**] = 1 mg/mL, [**P5@Pd(II)**] = 1 mg/mL in H_2O, *T* = 20 °C.

Catalysis measurements

Pro-dye activation general procedure :

Pro-dye activation **5-11** in water/PBS/DMEM:

P1-P4@Pd(II) stock solutions were prepared in water by dissolving 10 mg polymer in 1 mL (10 mg/mL) water by sonication for 30 min. **P5@Pd(II)** stock solution was prepared by dissolving 10 mg **P5** in 900 µL water by sonication for 30 min followed by the addition of 100 µL **Na_2PdCl_4** stock solution (10 mM in water). This solution (10 mg/mL) was stirred for 15 min before use. Pro-dye stock solutions (**5-11**) were prepared in DMSO at 50 mM concentration. Stock solution of control **$PdCODCl_2$** was prepared in DMSO at 30/50 mM concentration. Depending on each experiment, all stock solutions were diluted in 3 mL water/PBS in 10 mm fluorescence ((pro-cou (**7**)),(pro-rho (**9**), pro-ben (**11**))/absorbance cuvette (pro-DNP (**5**)) to a reach final concentration of Pd(II) = 30 µM; [**5-11**] = 100 µM. Final concentration of DMSO in aqueous solution is 0.2-0.3 v/v%. Cuvettes were then transferred to UV-Vis/Fluorescence spectrophotometer at 37 °C with stirring and the reaction progress was monitored in real-time. Aliquots from the sample were taken at specified intervals and diluted with 50% ACN by volume which was then analysed using HPLC-UV/MS.

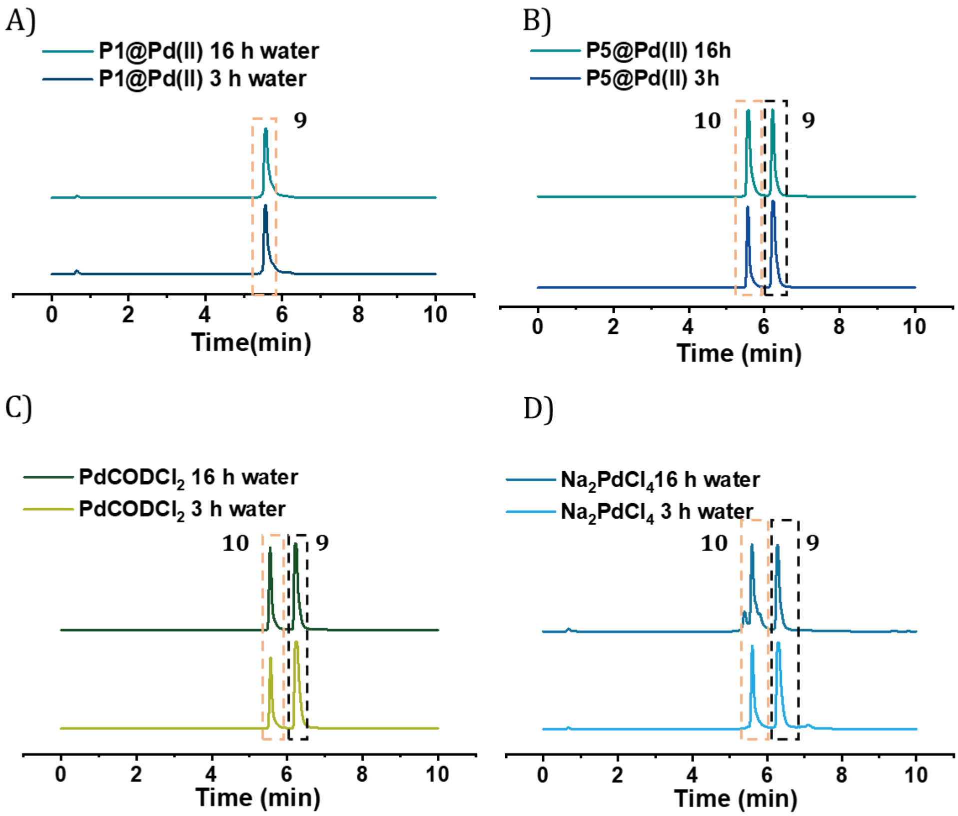

Figure 16: Activation of pro-rho **9** (100 μM) to rho **10** monitored by HPLC-MS. The reaction was performed using A) **P1@Pd(II)** B) **P5@Pd(II)** C) **Na_2PdCl_4** D) **$PdCODCl_2$**, [Pd(II)] = 30 μM in H_2O, T = 37 °C, t = 3h, 16 h.

For DMEM, all additions were done as mentioned above except that 30 mg/mL polymer stock solution in water was prepared. Depending on each experiment, all stock solutions were diluted in 2900 μL DMEM in 10 mm fluorescence cuvette to reach a final concentration of Pd(II) = 100 μM, [**9**] = 100 μM. The amount of water added from stock solutions was compensated to 100 μL in all samples. Cuvettes were then transferred to UV-Vis/Fluorescence spectrophotometer at 37 °C with stirring and the reaction progress was monitored in real-time. Aliquots from the sample were taken at specified intervals and diluted with 50% ACN by volume which was then analysed using HPLC-UV/MS.

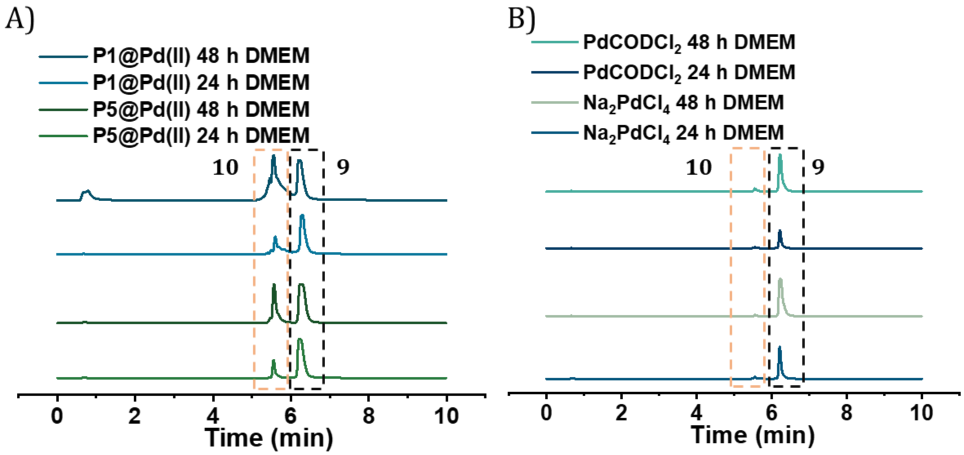

Figure 17: Activation of pro-rho **9** (100 μM) to rho **10** monitored by HPLC-MS. The reaction was performed using A) **P1@Pd(II)** and **P5@Pd(II)** B) **Na_2PdCl_4** and **$PdCODCl_2$**, [Pd(II)] = 100 μM in DMEM, T = 37 °C, t = 24h, 48 h.

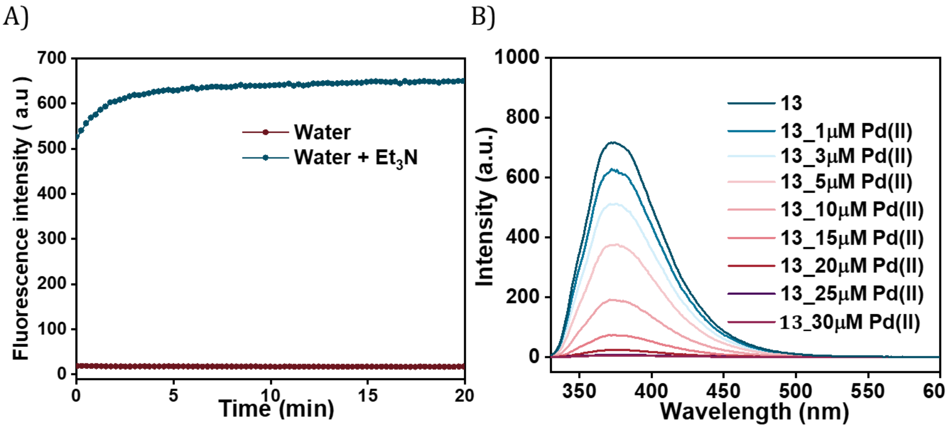

Figure 18: A) Fluorescence kinetic profile of activation of pro-ben **11** (100 μM) to ben **12** using **P1@Pd(II)** in water with and without Et_3N (500 μM), [Pd(II)] = 30 μM, λ_{ex} = 460 nm, λ_{em} = 535 nm, T = 37 °C B) Fluorescence emission spectra of dye **13** with increasing amount of **$PdCODCl_2$** in H_2O, T = 20 °C, λ_{ex} = 320 nm, amount of DMSO (from $PdCODCl_2$ stock solution) was kept constant (0.13 v/v%) throughout the measurements.

Pro-drug activation

P1@Pd(II) stock solutions were prepared in water by dissolving 10 mg of polymer **P1@Pd(II)** in 1 mL (10 mg/mL) water by sonication for 30 min. Pro-drug stock solutions (**14,16,19** and **21**) were prepared in DMSO at 50 mM concentration. The stock solution of control **PdCODCl₂** was prepared in DMSO at 30/50 mM concentration. Depending on each experiment, all stock solutions were diluted in 3 mL water/PBS in glass vials to reach a final concentration of Pd(II) = 30 µM; [pro-drugs] = 100 µM. Final concentration of DMSO in aqueous solution is 0.2-0.3 v/v%. For DMEM, all additions were done as mentioned above except that 30 mg/mL polymer stock solution in water was prepared. Depending on each experiment, all stock solutions were diluted in 2900 µL DMEM in glass vial to reach a final concentration of Pd(II) = 30 µM/ Pd(II) = 100 µM (as specified); [pro-drugs] = 100 µM. The amount of water added from stock solutions was compensated to 100 µL in all samples. Then the reaction mixture was stirred at 37 °C. Aliquots from the sample were taken at specified intervals and diluted with ACN (50% v/v) for pro-paclitaxel **16** and with water (50% v/v) for pro-5FU **14** and pro-dox **19, 20** which was then analysed using HPLC-MS.

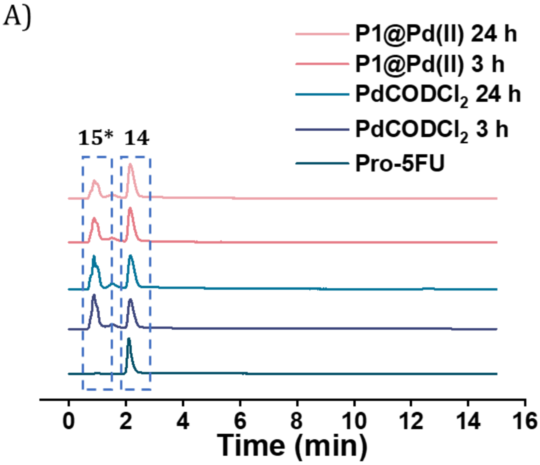

Figure 19: HPLC-MS chromatogram of pro-5FU **14** activation (100 µM) using **PdCODCl₂** and **P1@Pd(II)** in DMEM, [Pd(II)] = 100 µM, T = 37 °C, t = 3h, 24h.*5FU may be detected together with methionine in DMEM.

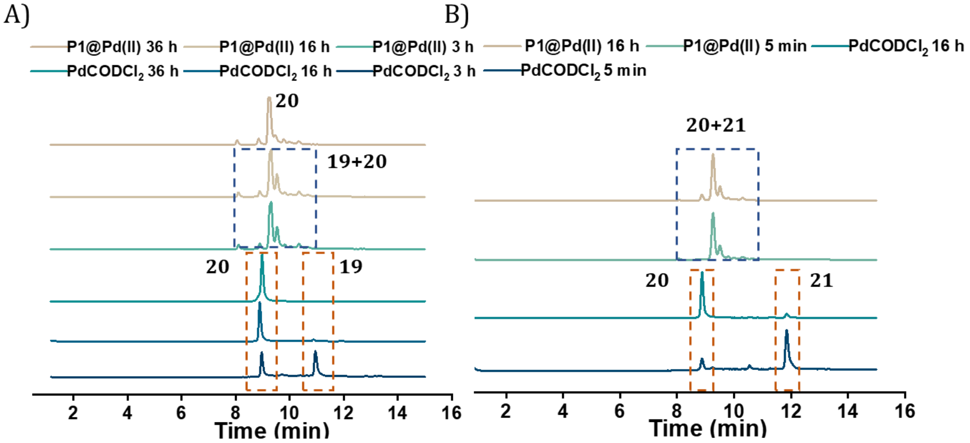

Figure 20: HPLC-MS chromatogram of pro-doxorubicin activation. A) Activation of pro-poc-doxorubicin **19** (100 µM) using **PdCODCl₂** and **P1@Pd(II)** in water, [Pd(II)] = 30 µM, T = 37 °C, t = 3h, 16h, 36 h B) Activation of pro-pob-doxorubicin **21** (100 µM) using **PdCODCl₂** and **P1@Pd(II)** in water, [Pd(II)] = 30 µM, T = 37 °C, t = 5 min, 16h.

2.12 References

(1) Miller, M. A.; Mikula, H.; Luthria, G.; Li, R.; Kronister, S.; Prytyskach, M.; Kohler, R. H.; Mitchison, T.; Weissleder, R. Modular Nanoparticulate Prodrug Design Enables Efficient Treatment of Solid Tumors Using Bioorthogonal Activation. *ACS Nano* **2018**, *12* (12), 12814–12826. https://doi.org/10.1021/acsnano.8b07954.

(2) Pérez-López, A. M.; Rubio-Ruiz, B.; Sebastián, V.; Hamilton, L.; Adam, C.; Bray, T. L.; Irusta, S.; Brennan, P. M.; Lloyd-Jones, G. C.; Sieger, D.; Santamaría, J.; Unciti-Broceta, A. Gold-Triggered Uncaging Chemistry in Living Systems. *Angew. Chem.* **2017**, *129* (41), 12722–12726. https://doi.org/10.1002/ange.201705609.

(3) Bray, T. L.; Salji, M.; Brombin, A.; Pérez-López, A. M.; Rubio-Ruiz, B.; Galbraith, L. C. A.; Patton, E. E.; Leung, H. Y.; Unciti-Broceta, A. Bright Insights into Palladium-Triggered Local Chemotherapy. *Chem. Sci.* **2018**, *9* (37), 7354–7361. https://doi.org/10.1039/C8SC02291G.

(4) Yusop, R. M.; Unciti-Broceta, A.; Johansson, E. M. V.; Sánchez-Martín, R. M.; Bradley, M. Palladium-Mediated Intracellular Chemistry. *Nat. Chem.* **2011**, *3* (3), 239–243. https://doi.org/10.1038/nchem.981.

(5) Völker, T.; Dempwolff, F.; Graumann, P. L.; Meggers, E. Progress towards Bioorthogonal Catalysis with Organometallic Compounds. *Angew. Chem. Int. Ed.* **2014**, *53* (39), 10536–10540. https://doi.org/10.1002/anie.201404547.

(6) Vidal, C.; Tomás-Gamasa, M.; Gutiérrez-González, A.; Mascareñas, J. L. Ruthenium-Catalyzed Redox Isomerizations inside Living Cells. *J. Am. Chem. Soc.* **2019**, *141* (13), 5125–5129. https://doi.org/10.1021/jacs.9b00837.

(7) Völker, T.; Meggers, E. Transition-Metal-Mediated Uncaging in Living Human Cells — an Emerging Alternative to Photolabile Protecting Groups. *Curr. Opin. Chem. Biol.* **2015**, *25*, 48–54. https://doi.org/10.1016/j.cbpa.2014.12.021.

(8) Martínez-Calvo, M.; Mascareñas, J. L. Organometallic Catalysis in Biological Media and Living Settings. *Coord. Chem. Rev.* **2018**, *359*, 57–79. https://doi.org/10.1016/j.ccr.2018.01.011.

(9) Vidal, C.; Tomás-Gamasa, M.; Destito, P.; López, F.; Mascareñas, J. L. Concurrent and Orthogonal Gold(I) and Ruthenium(II) Catalysis inside Living Cells. *Nat. Commun.* **2018**, *9* (1), 1913.

https://doi.org/10.1038/s41467-018-04314-5.

(10) Tomás-Gamasa, M.; Martínez-Calvo, M.; Couceiro, J. R.; Mascareñas, J. L. Transition Metal Catalysis in the Mitochondria of Living Cells. *Nat. Commun.* **2016**, *7* (1), 12538. https://doi.org/10.1038/ncomms12538.

(11) Li, J.; Chen, P. R. Moving Pd-Mediated Protein Cross Coupling to Living Systems. *ChemBioChem* **2012**, *13* (12), 1728–1731. https://doi.org/10.1002/cbic.201200353.

(12) Ramil, C. P.; Lin, Q. Bioorthogonal Chemistry: Strategies and Recent Developments. *Chem. Commun.* **2013**, *49* (94), 11007. https://doi.org/10.1039/c3cc44272a.

(13) Sasmal, P. K.; Streu, C. N.; Meggers, E. Metal Complex Catalysis in Living Biological Systems. *Chem Commun* **2013**, *49* (16), 1581–1587. https://doi.org/10.1039/C2CC37832A.

(14) Li, J.; Yu, J.; Zhao, J.; Wang, J.; Zheng, S.; Lin, S.; Chen, L.; Yang, M.; Jia, S.; Zhang, X.; Chen, P. R. Palladium-Triggered Deprotection Chemistry for Protein Activation in Living Cells. *Nat. Chem.* **2014**, *6* (4), 352–361. https://doi.org/10.1038/nchem.1887.

(15) Chalker, J. M.; Bernardes, G. J. L.; Davis, B. G. A "Tag-and-Modify" Approach to Site-Selective Protein Modification. *Acc. Chem. Res.* **2011**, *44* (9), 730–741. https://doi.org/10.1021/ar200056q.

(16) Wang, J.; Cheng, B.; Li, J.; Zhang, Z.; Hong, W.; Chen, X.; Chen, P. R. Chemical Remodeling of Cell-Surface Sialic Acids through a Palladium-Triggered Bioorthogonal Elimination Reaction. *Angew. Chem. Int. Ed.* **2015**, *54* (18), 5364–5368. https://doi.org/10.1002/anie.201409145.

(17) Spicer, C. D.; Triemer, T.; Davis, B. G. Palladium-Mediated Cell-Surface Labeling. *J. Am. Chem. Soc.* **2012**, *134* (2), 800–803. https://doi.org/10.1021/ja209352s.

(18) Lercher, L.; McGouran, J. F.; Kessler, B. M.; Schofield, C. J.; Davis, B. G. DNA Modification under Mild Conditions by Suzuki-Miyaura Cross-Coupling for the Generation of Functional Probes. *Angew. Chem. Int. Ed.* **2013**, *52* (40), 10553–10558. https://doi.org/10.1002/anie.201304038.

(19) Li, J.; Chen, P. R. Development and Application of Bond Cleavage Reactions in Bioorthogonal Chemistry. *Nat. Chem. Biol.* **2016**, *12* (3), 129–137. https://doi.org/10.1038/nchembio.2024.

(20) Wang, W.; Zhang, X.; Huang, R.; Hirschbiegel, C.-M.; Wang, H.; Ding, Y.; Rotello, V. M. *In situ* Activation of Therapeutics through Bioorthogonal Catalysis. *Adv. Drug Deliv. Rev.* **2021**, *176*, 113893. https://doi.org/10.1016/j.addr.2021.113893.

(21) Bai, Y.; Chen, J.; Zimmerman, S. C. Designed Transition Metal Catalysts for Intracellular Organic Synthesis. *Chem. Soc. Rev.* **2018**, *47* (5), 1811–1821. https://doi.org/10.1039/C7CS00447H.

(22) Chen, Z.; Li, H.; Bian, Y.; Wang, Z.; Chen, G.; Zhang, X.; Miao, Y.; Wen, D.; Wang, J.; Wan, G.; Zeng, Y.; Abdou, P.; Fang, J.; Li, S.; Sun, C.-J.; Gu, Z. Bioorthogonal Catalytic Patch. *Nat. Nanotechnol.* **2021**, *16* (8), 933–941. https://doi.org/10.1038/s41565-021-00910-7.

(23) Chankeshwara, S. V.; Indrigo, E.; Bradley, M. Palladium-Mediated Chemistry in Living Cells. *Curr. Opin. Chem. Biol.* **2014**, *21*, 128–135. https://doi.org/10.1016/j.cbpa.2014.07.007.

(24) Coelho, S. E.; Schneider, F. S. S.; de Oliveira, D. C.; Tripodi, G. L.; Eberlin, M. N.; Caramori, G. F.; de Souza, B.; Domingos, J. B. Mechanism of Palladium(II)-Mediated Uncaging Reactions of Propargylic Substrates. *ACS Catal.* **2019**, *9* (5), 3792–3799. https://doi.org/10.1021/acscatal.9b00210.

(25) Konč, J.; Sabatino, V.; Jiménez-Moreno, E.; Latocheski, E.; Pérez, L. R.; Day, J.; Domingos, J. B.; Bernardes, G. J. L. Controlled In-Cell Generation of Active Palladium(0) Species for Bioorthogonal Decaging. *Angew. Chem. Int. Ed.* **2022**, *61* (8). https://doi.org/10.1002/anie.202113519.

(26) Brewster, R. C.; Klemencic, E.; Jarvis, A. G. Palladium in Biological Media: Can the Synthetic Chemist's Most Versatile Transition Metal Become a Powerful Biological Tool? *J. Inorg. Biochem.* **2021**, *215*, 111317. https://doi.org/10.1016/j.jinorgbio.2020.111317.

(27) Miller, M. A.; Askevold, B.; Mikula, H.; Kohler, R. H.; Pirovich, D.; Weissleder, R. Nano-Palladium Is a Cellular Catalyst for *in vivo* Chemistry. *Nat. Commun.* **2017**, *8* (1), 15906. https://doi.org/10.1038/ncomms15906.

(28) Weiss, J. T.; Dawson, J. C.; Macleod, K. G.; Rybski, W.; Fraser, C.; Torres-Sánchez, C.; Patton, E. E.; Bradley, M.; Carragher, N. O.; Unciti-Broceta, A. Extracellular Palladium-Catalysed Dealkylation of 5-Fluoro-1-Propargyl-Uracil as a Bioorthogonally Activated Prodrug Approach. *Nat. Commun.* **2014**, *5* (1), 3277. https://doi.org/10.1038/ncomms4277.

(29) Weiss, J. T.; Dawson, J. C.; Fraser, C.; Rybski, W.; Torres-Sánchez, C.; Bradley, M.; Patton, E. E.; Carragher, N. O.; Unciti-Broceta, A. Development and Bioorthogonal Activation of Palladium-Labile Prodrugs of Gemcitabine. *J. Med. Chem.* **2014**, *57* (12), 5395–5404. https://doi.org/10.1021/jm500531z.

(30) Pérez-López, A. M.; Rubio-Ruiz, B.; Valero, T.; Contreras-Montoya, R.; Álvarez de Cienfuegos, L.; Sebastián, V.; Santamaría, J.; Unciti-Broceta, A. Bioorthogonal Uncaging of Cytotoxic Paclitaxel through

Pd Nanosheet–Hydrogel Frameworks. *J. Med. Chem.* **2020**, *63* (17), 9650–9659. https://doi.org/10.1021/acs.jmedchem.0c00781.

(31) Adam, C.; Pérez-López, A. M.; Hamilton, L.; Rubio-Ruiz, B.; Bray, T. L.; Sieger, D.; Brennan, P. M.; Unciti-Broceta, A. Bioorthogonal Uncaging of the Active Metabolite of Irinotecan by Palladium-Functionalized Microdevices. *Chem. – Eur. J.* **2018**, *24* (63), 16783–16790. https://doi.org/10.1002/chem.201803725.

(32) Weiss, J. T.; Carragher, N. O.; Unciti-Broceta, A. Palladium-Mediated Dealkylation of N-Propargyl-Floxuridine as a Bioorthogonal Oxygen-Independent Prodrug Strategy. *Sci. Rep.* **2015**, *5* (1), 9329. https://doi.org/10.1038/srep09329.

(33) Tonga, G. Y.; Jeong, Y.; Duncan, B.; Mizuhara, T.; Mout, R.; Das, R.; Kim, S. T.; Yeh, Y.-C.; Yan, B.; Hou, S.; Rotello, V. M. Supramolecular Regulation of Bioorthogonal Catalysis in Cells Using Nanoparticle-Embedded Transition Metal Catalysts. *Nat. Chem.* **2015**, *7* (7), 597–603. https://doi.org/10.1038/nchem.2284.

(34) Tevet, S.; Wagle, S. S.; Slor, G.; Amir, R. J. Tuning the Reactivity of Micellar Nanoreactors by Precise Adjustments of the Amphiphile and Substrate Hydrophobicity. *Macromolecules* **2021**, *54* (24), 11419–11426. https://doi.org/10.1021/acs.macromol.1c01755.

(35) Wallace, S.; Balskus, E. P. Designer Micelles Accelerate Flux Through Engineered Metabolism in *E. Coli* and Support Biocompatible Chemistry. *Angew. Chem. Int. Ed.* **2016**, *55* (20), 6023–6027. https://doi.org/10.1002/anie.201600966.

(36) Cortes-Clerget, M.; Akporji, N.; Zhou, J.; Gao, F.; Guo, P.; Parmentier, M.; Gallou, F.; Berthon, J.-Y.; Lipshutz, B. H. Bridging the Gap between Transition Metal- and Bio-Catalysis via Aqueous Micellar Catalysis. *Nat. Commun.* **2019**, *10* (1), 2169. https://doi.org/10.1038/s41467-019-09751-4.

(37) Deraedt, C.; Pinaud, N.; Astruc, D. Recyclable Catalytic Dendrimer Nanoreactor for Part-Per-Million Cu ^{I} Catalysis of “Click” Chemistry in Water. *J. Am. Chem. Soc.* **2014**, *136* (34), 12092–12098. https://doi.org/10.1021/ja5061388.

(38) Kim, K. T.; Cornelissen, J. J. L. M.; Nolte, R. J. M.; van Hest, J. C. M. A Polymersome Nanoreactor with Controllable Permeability Induced by Stimuli-Responsive Block Copolymers. *Adv. Mater.* **2009**, *21* (27), 2787–2791. https://doi.org/10.1002/adma.200900300.

(39) Lu, Q.; Bai, S.; Chen, Z.; Zheng, N.; Feng, X.; Bai, Y. A Dense-Shell Macromolecular Scaffold for Catalyst- or Substrate-Guided Catalysis in a Cellular Environment. *ACS Mater. Lett.* **2020**, *2* (1), 89–94. https://doi.org/10.1021/acsmaterialslett.9b00400.

(40) Liu, Y.; Pauloehrl, T.; Presolski, S. I.; Albertazzi, L.; Palmans, A. R. A.; Meijer, E. W. Modular Synthetic Platform for the Construction of Functional Single-Chain Polymeric Nanoparticles: From Aqueous Catalysis to Photosensitization. *J. Am. Chem. Soc.* **2015**, *137* (40), 13096–13105. https://doi.org/10.1021/jacs.5b08299.

(41) Artar, M.; Terashima, T.; Sawamoto, M.; Meijer, E. W.; Palmans, A. R. A. Understanding the Catalytic Activity of Single-Chain Polymeric Nanoparticles in Water. *J. Polym. Sci. Part Polym. Chem.* **2014**, *52* (1), 12–20. https://doi.org/10.1002/pola.26970.

(42) Chen, J.; Wang, J.; Bai, Y.; Li, K.; Garcia, E. S.; Ferguson, A. L.; Zimmerman, S. C. Enzyme-like Click Catalysis by a Copper-Containing Single-Chain Nanoparticle. *J. Am. Chem. Soc.* **2018**, *140* (42), 13695–13702. https://doi.org/10.1021/jacs.8b06875.

(43) Chen, J.; Wang, J.; Li, K.; Wang, Y.; Gruebele, M.; Ferguson, A. L.; Zimmerman, S. C. Polymeric “Clickase” Accelerates the Copper Click Reaction of Small Molecules, Proteins, and Cells. *J. Am. Chem. Soc.* **2019**, *141* (24), 9693–9700. https://doi.org/10.1021/jacs.9b04181.

(44) Kunjachan, S.; Pola, R.; Gremse, F.; Theek, B.; Ehling, J.; Moeckel, D.; Hermanns-Sachweh, B.; Pechar, M.; Ulbrich, K.; Hennink, W. E.; Storm, G.; Lederle, W.; Kiessling, F.; Lammers, T. Passive versus Active Tumor Targeting Using RGD- and NGR-Modified Polymeric Nanomedicines. *Nano Lett.* **2014**, *14* (2), 972–981. https://doi.org/10.1021/nl404391r.

(45) Liu, Y.; Pujals, S.; Stals, P. J. M.; Paulöhrl, T.; Presolski, S. I.; Meijer, E. W.; Albertazzi, L.; Palmans, A. R. A. Catalytically Active Single-Chain Polymeric Nanoparticles: Exploring Their Functions in Complex Biological Media. *J. Am. Chem. Soc.* **2018**, *140* (9), 3423–3433. https://doi.org/10.1021/jacs.8b00122.

(46) ter Huurne, G. M.; de Windt, L. N. J.; Liu, Y.; Meijer, E. W.; Voets, I. K.; Palmans, A. R. A. Improving the Folding of Supramolecular Copolymers by Controlling the Assembly Pathway Complexity. *Macromolecules* **2017**, *50* (21), 8562–8569. https://doi.org/10.1021/acs.macromol.7b01769.

(47) Deng, L.; Albertazzi, L.; Palmans, A. R. A. Elucidating the Stability of Single-Chain Polymeric Nanoparticles in Biological Media and Living Cells. *Biomacromolecules* **2022**, *23* (1), 326–338. https://doi.org/10.1021/acs.biomac.1c01291.

(48) Martínez-Calvo, M.; Couceiro, J. R.; Destito, P.; Rodríguez, J.; Mosquera, J.; Mascareñas, J. L. Intracellular Deprotection Reactions Mediated by Palladium Complexes Equipped with Designed Phosphine Ligands. *ACS Catal.* **2018**, *8* (7), 6055–6061. https://doi.org/10.1021/acscatal.8b01606.

(49) Schatzschneider, U.; Barton, J. K. Bifunctional Rhodium Intercalator Conjugates as Mismatch-Directing DNA Alkylating Agents. *J. Am. Chem. Soc.* **2004**, *126* (28), 8630–8631. https://doi.org/10.1021/ja048543m.

(50) Eberhardt, M.; Mruk, R.; Zentel, R.; Théato, P. Synthesis of Pentafluorophenyl(Meth)Acrylate Polymers: New Precursor Polymers for the Synthesis of Multifunctional Materials. *Eur. Polym. J.* **2005**, *41* (7), 1569–1575. https://doi.org/10.1016/j.eurpolymj.2005.01.025.

(51) Willenbacher, J.; Altintas, O.; Trouillet, V.; Knöfel, N.; Monteiro, M. J.; Roesky, P. W.; Barner-Kowollik, C. Pd-Complex Driven Formation of Single-Chain Nanoparticles. *Polym. Chem.* **2015**, *6* (24), 4358–4365. https://doi.org/10.1039/C5PY00389J.

(52) Shriver, D. F.; Atkins, P. W.; Langford, C. H. *Inorganic Chemistry. Hauptbd.*, 3. ed., repr.; Oxford University Press: Oxford, 2002.

(53) Gillissen, M. A. J.; Terashima, T.; Meijer, E. W.; Palmans, A. R. A.; Voets, I. K. Sticky Supramolecular Grafts Stretch Single Polymer Chains. *Macromolecules* **2013**, *46* (10), 4120–4125. https://doi.org/10.1021/ma4006846.

(54) Huerta, E.; Stals, P. J. M.; Meijer, E. W.; Palmans, A. R. A. Consequences of Folding a Water-Soluble Polymer Around an Organocatalyst. *Angew. Chem.* **2013**, *125* (10), 2978–2982. https://doi.org/10.1002/ange.201207123.

(55) Artar, M.; Souren, E. R. J.; Terashima, T.; Meijer, E. W.; Palmans, A. R. A. Single Chain Polymeric Nanoparticles as Selective Hydrophobic Reaction Spaces in Water. *ACS Macro Lett.* **2015**, *4* (10), 1099–1103. https://doi.org/10.1021/acsmacrolett.5b00652.

(56) Chen, T.; Wei, T.; Zhang, Z.; Chen, Y.; Qiang, J.; Wang, F.; Chen, X. Highly Sensitive and Selective ESIPT-Based Fluorescent Probes for Detection of Pd2+ with Large Stocks Shifts. *Dyes Pigments* **2017**, *140*, 392–398. https://doi.org/10.1016/j.dyepig.2017.01.063.

(57) Weiss, J. T.; Fraser, C.; Rubio-Ruiz, B.; Myers, S. H.; Crispin, R.; Dawson, J. C.; Brunton, V. G.; Patton, E. E.; Carragher, N. O.; Unciti-Broceta, A. N-Alkynyl Derivatives of 5-Fluorouracil: Susceptibility to Palladium-Mediated Dealkylation and Toxigenicity in Cancer Cell Culture. *Front. Chem.* **2014**, *2*. https://doi.org/10.3389/fchem.2014.00056.

(58) Latocheski, E.; Dal Forno, G. M.; Ferreira, T. M.; Oliveira, B. L.; Bernardes, G. J. L.; Domingos, J. B. Mechanistic Insights into Transition Metal-Mediated Bioorthogonal Uncaging Reactions. *Chem. Soc. Rev.* **2020**, *49* (21), 7710–7729. https://doi.org/10.1039/D0CS00630K.

(59) Son, S. U.; Jang, Y.; Yoon, K. Y.; Kang, E.; Hyeon, T. Facile Synthesis of Various Phosphine-Stabilized Monodisperse Palladium Nanoparticles through the Understanding of Coordination Chemistry of the Nanoparticles. *Nano Lett.* **2004**, *4* (6), 1147–1151. https://doi.org/10.1021/nl049519+.

(60) Hobart, D. B.; Berg, M. A. G.; Rogers, H. M.; Merola, J. S. Synthesis, Characterization, and Non-Covalent Interactions of Palladium(II)-Amino Acid Complexes. *Molecules* **2021**, *26* (14), 4331. https://doi.org/10.3390/molecules26144331.

(61) Suresh, S.; Bhuvanesh, N.; Raman, A.; Sugumar, P.; Padmanabhan, D.; Easwaramoorthi, S.; Ponnuswamy, M. N.; Kavitha, S.; Nandhakumar, R. Experimental and Theoretical Studies of Imidazole Based Chemosensor for Palladium and Their Biological Applications. *J. Photochem. Photobiol. Chem.* **2019**, *385*, 112092. https://doi.org/10.1016/j.jphotochem.2019.112092.

(62) Ma, P.; Mumper, R. J. Paclitaxel Nano-Delivery Systems: A Comprehensive Review. *J. Nanomedicine Nanotechnol.* **2013**, *4* (2), 1000164. https://doi.org/10.4172/2157-7439.1000164.

(63) Weiss, J. T.; Dawson, J. C.; Macleod, K. G.; Rybski, W.; Fraser, C.; Torres-Sánchez, C.; Patton, E. E.; Bradley, M.; Carragher, N. O.; Unciti-Broceta, A. Extracellular Palladium-Catalysed Dealkylation of 5-Fluoro-1-Propargyl-Uracil as a Bioorthogonally Activated Prodrug Approach. *Nat. Commun.* **2014**, *5* (1), 3277. https://doi.org/10.1038/ncomms4277.

(64) Liu, Y.; Turunen, P.; de Waal, B. F. M.; Blank, K. G.; Rowan, A. E.; Palmans, A. R. A.; Meijer, E. W. Catalytic Single-Chain Polymeric Nanoparticles at Work: From Ensemble towards Single-Particle Kinetics. *Mol. Syst. Des. Eng.* **2018**, *3* (4), 609–618. https://doi.org/10.1039/C8ME00017D.

Chapter 3

Pd(0) based amphiphilic polymeric nanoparticles for pro-drug activation in living cells

Abstract: In this work, Pd(II) based amphiphilic polymers developed in Chapter 2 were reduced using CO, a mild reductant to form Pd(0) polymeric nanoparticles and were characterized by high-angle annular dark-field scanning transmission electron microscopy (STEM-HAADF). We investigated the potential of these nanoparticles to perform versatile reactions such as Heck coupling, Suzuki-Miyaura coupling and depropargylation reactions on hydrophobic substrates in aqueous solutions. The rate of deprotection reactions was not affected when the medium complexity was increased and near quantitative conversion was obtained even in the presence of serum proteins. All polymer designs showed excellent biocompatibility to HepG2 cells and successfully activated pro-rhodamine to rhodamine. The trend in catalytic efficiency of the different polymer designs as observed for the solution studies did not correlate to that found in the cell studies. The results suggested that the size, charged groups, and amount of triphenylphosphine ligands of nanoparticles could be contributing factors to their stability and permanence in extracellular media hence their activity. An orally bioavailable pro-drug of 5-fluorouracil (5FU) was activated by the nanoparticles inducing a cytotoxic effect in HepG2 cells indicating that the fast kinetics of the deprotection reaction prevents the proliferation of cancer cells. The simplest polymer design with only triphenylphosphine ligand and Jeffamine M-1000 was found to be the most efficient for pro-5FU activation highlighting its potential to be developed as a bioorthogonal catalyst for *in vivo* studies.

This work has been performed in close collaboration with Prof. Victor Sebastian (Pd(II) reduction and characterization), Linlin Deng (cell experiments), and Catherine Adam (pro-drug synthesis).

3.1 Introduction

Bioorthogonal strategies for *in situ* synthesis of drugs in living systems using transition metal catalysts (TMCs) have gained interest in the past decade because of their potential for the development of new side-effect-free cancer therapies. These strategies allow selective and controlled synthesis of drugs either by decaging a masked prodrug or coupling two inert precursors. Although there were significant advances in the field, only a few are reported to be successful *in vivo,* where Au or Pd-based heterogeneous or homogeneous nanoparticles were used as bioorthogonal catalysts in mouse models.[1–4] This suggests that there is a significant gap between *in vitro* and *in vivo* experiments, and many factors need to be addressed before these strategies can be translated into clinical applications. Most important is the need for catalysts that show fast kinetics, where the rate of *in situ* formation of the drugs has to be faster than cancer cell proliferation to induce cell death.[5] In addition, the stability and durability of these transition metal catalysts have to be maintained over time, because biological nucleophiles like glutathione can deactivate the catalyst in a complex physiological environment.[6F] And finally, the catalysts need to be targeted specifically to the tumour site.

Unciti-Broceta and co-workers have recently developed a Pd activable orally available pro-drug based on 5-fluorouracil (5FU) that can evade anabolic activation and catabolic processing. This has improved the drug metabolism and pharmacokinetic properties compared to 5FU.[2] Their work marked a milestone in the field by administering the drug orally in mice models and activating it inside a tumour xenograft by intratumorally implanted Pd catalysts. Histological examination of the tumour samples revealed that Pd-implanted tumours had large central necrotic areas in the vicinity of the resins, while tumours without Pd resins in the same animal only showed a minimal amount of necrosis. Although no differences in the measured mass volume were observed between the control and Pd-implanted tumours at the endpoint, it was clear that 5FU had been generated inside the tumour near the resin implanted site creating an intratumoural cytotoxic effect. However, there is still a need for improvement in terms of catalysts' efficiency and delivery for the complete removal of tumours.[2] It is possible that Pd catalysts with more efficiency while having the ability to penetrate deeply into tumours can control tumour growth better.

We envisaged that SCPNs can be more promising in combination with this orally available pro-drug, as they offer the possibility of systemic administration, targeted delivery and better penetration into the tumour microenvironment. Further, the hydrophobic interior of SCPNs can allow high local concentrations of pro-drug, which can result in fast kinetics of pro-drug activation.

In the previous work in Chapter 2, we looked at the efficiency of Pd(II) based amphiphilic polymeric nanoparticles for activation of anticancer pro-drugs. We found that the reaction rates became considerably slower when the complexity of the medium was increased. A way to enhance reaction rates, would be by the reduction of these catalysts from Pd(II) to Pd(0). Such an approach can be highly beneficial because of a number of reasons. Firstly, Pd(0) is already reported to perform depropargylations faster than Pd(II), which is hypothesized to be caused by differences in their cleavage mechanism.[7] Pd(0) is hypothesized to follow an allenylpalladium-mediated mechanism, which goes faster compared to the hydration mechanism followed by Pd(II).[7] Secondly, triphenylphosphine ligands grafted to the amphiphilic polymer backbone can stabilize the formed Pd(0) nanoparticles inside the hydrophobic compartment.[8] Thirdly, Pd(0) catalysts are highly versatile, and catalyze a diverse range of reactions that can be performed in presence of cells. This allows the synthesis of multiple drugs in parallel from inactive counterparts, which are particularly useful for combination therapy in case of drug resistance.[9,10]

In this work, we reduced four different Pd(II) based polymeric nanoparticles (NPs) to Pd(0) using CO which is a mild reductant and capping agent.[11,12] This reduction method has already been successfully utilized for the controlled synthesis of ultrathin Pd nanosheets in exosomes and agarose or alginate hydrogel, used for uncaging anticancer prodrugs in tumour cells.[13,14] The reduction of Pd(II) based amphiphilic polymers with Jeffamine M-1000 as the hydrophilic graft to Pd(0) in water afforded small Pd(0) NPs ~ 5 nm along with some fraction of larger aggregates. The addition of anionic carboxylate groups as grafts resulted in less-defined polydisperse Pd(0) NPs. In order to understand the potential of these catalysts to perform versatile transformations, reactions such as Heck coupling, Suzuki-Miyaura coupling, and depropargylation reactions were performed in water. The fast kinetics of the deprotection reaction exhibited by these nanoparticles even in presence of serum proteins made it possible to export the reaction to living cells. A propargyl-protected pro-dye of rhodamine and pro-drug of 5FU was activated in presence of HepG2 cells. The Pd(0) NPs where amphiphilic polymer contained only dodecyl and Jeffamine M-1000 as side graft exhibited strong cytotoxic effects in HepG2 cells during activation of pro-5FU. Thereby, we have shown that Pd(0) based polymeric nanoparticles are compatible with the activation of an orally bioavailable pro-drug of anticancer drug. With further control of particle size and improvement of catalytic performance, we may get one step closer to taking them to *in vivo* studies.

3.2 Reduction of Pd(II) amphiphilic polymers to Pd(0) NPs and their characterization

The triphenylphosphine (TPP) functionalised Pd(II) amphiphilic polymers **P1**-**P2** as described in Chapter 2 were used for reduction to Pd(0) nanoparticles. **P1** comprises ~5% BTA grafts, ~10% TPP ligands, ~20% dodecyl and the rest Jeffamine M-1000. This is the optimal microstructure that was found to retain its folded structure even inside the cell's cytoplasm or lysosomes.[15] **P2** contains ~20% TPP ligands and the rest Jeffamine M-1000, which may better stabilize the Pd(0) nanoparticles due to the higher ratio of triphenylphosphine ligands but the hydrophobicity of the interior is overall less. **P3** comprises ~1% Nile red, ~20% TPP ligands, ~35% carboxylic acid group and the rest Jeffamine M-1000, and was used to assess the effects of charged groups on the catalytic activity of polymeric nanoparticles during pro-drug activation in the presence of cells. **P4** is the control polymer comprising only dodecyl and Jeffamine M-1000 grafts, and intended to compare the effect of TPP ligand in stabilization of Pd nanoparticles. The chemical structures of the amphiphilic polymers used in this work are as shown in Scheme 1.

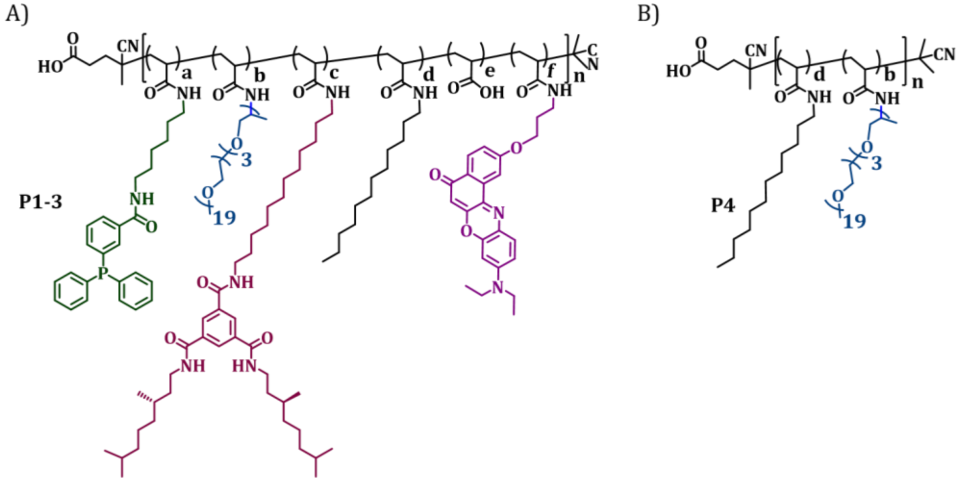

Scheme 1: Chemical structures of amphiphilic polymers **P1-P4**, an overview of the polymer composition can be found in Table 1.

Table 1: Overview of the copolymer composition (a-f), degree of polymerisation (n), molecular weight ($M_{n,SEC}$) and molar mass dispersity ($Đ$) of **P1-P4** before complexation to Pd(II). Dynamic light scattering results of the polymers complexed to Pd(II) and after CO reduction to Pd(0) in H_2O.

Polymer	a	b	c	d	e	f	n	$Đ$	$M_{n,SEC}$ (kD)	R_H (nm) **P@Pd(II)**	R_H (nm) **P@Pd(0)**
P1	8	68	4	20	-	-	214	1.18	46.8	6.6 ± 0.6	8.1 ± 0.9 (43±24)^a
P2	18	82	-	-	-	-	214	1.34	55.4	5.7 ±1.7	6.2 ± 0.3 (15 ± 1)^b
P3	20	44	-	-	35	1	180	1.26	36.5	6.6 ± 1.5	4.6 ± 1.0 (13 ± 2)^c
P4	-	70	-	30	-	-	200	1.16	24.4	5.9 ± 0.9	8.8 ± 0.7 (67 ± 7)^d

a-f were determined by ^{19}F NMR. $\boldsymbol{M_n}$ and $\boldsymbol{Đ}$ were measured by SEC in DMF with 10 mM LiBr, relative to poly(ethylene oxide) standards for polymers before complexation to Pd(II). $\boldsymbol{R_H}$ was determined by dynamic light scattering experiments [P] = 1 mg/mL, [Pd(II)] = [Pd(0)] = 210 µM in H_2O. In all cases, $\boldsymbol{R_H}$ was determined after the filtration of particles using a 100 nm PVDF filter. The $\boldsymbol{R_H}$ was determined from the volume plot of the DLS results, the values in the bracket correspond to a small fraction present as follows ^{a}3%, ^{b}4%, ^{c} 2%, ^{d}3%.

As a first step, **P1-P4** were complexed to Pd(II) following the procedure outlined in Chapter 2.2.1, affording **P1-P4@Pd(II)**. These polymers were formulated into nanoparticles in water, and characterized with dynamic light scattering (DLS). The hydrodynamic radius R_H of the NPs was around 6-7 nm, well in line with previous results. Next, **P1-P4@Pd(II)** nanoparticles in milliQ water ([P] = 1 mg/mL, [Pd(II) = 210 µM] were subjected to a mild reduction by CO treatment for 60 min at 30 °C. Hereby, Pd(II) is reduced to Pd(0), forming **P1-P4@Pd(0)**, using a protocol earlier reported for the reduction of Pd(II) inside exosomes.[13] The Pd(0) nanoparticles formed can be additionally stabilized by the TPP ligand present in the case of polymer **P1-P3**. As a control, Pd(II) precursor PdCODCl$_2$ (210 µM in H_2O, 0.2% DMSO v/v) was also reduced using the same procedure.

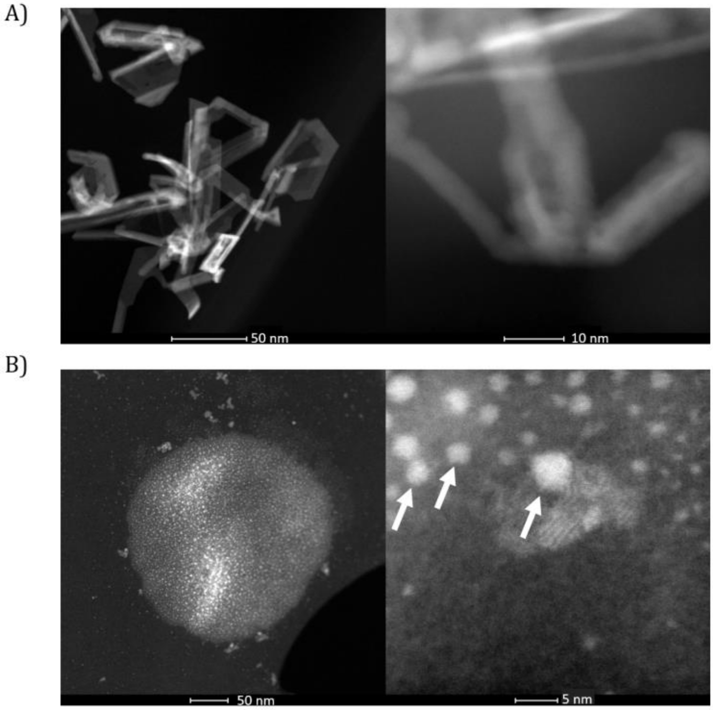

Figure 1: STEM-HAADF images of Pd(0) NPs reduced from A) **PdCODCl$_2$** ([Pd(II)] = 210 µM in H_2O, 0.2% DMSO v/v), B) **P1@Pd(II)** ([Pd(II)] = 210 µM, [**P**] = 1 mg/mL in H_2O. Pd(0) NPs indicated by white arrows.

The Pd(0) NPs formed inside polymeric nanoparticles **P1-P4@Pd(0)** and Pd(0) formed from Pd(II) precursor $PdCODCl_2$ were analysed using high-angle annular dark-field scanning transmission electron microscopy (HAADF-STEM) measurements. This technique is particularly suited to obtain high resolution images of samples containing high atomic weight elements as the HAADF image intensity is proportional to the atomic number of the element.[16] The lighter atoms are difficult to observe. Therefore, in our case a sharp contrast can be obtained between polymeric nanoparticles and Pd(0) NPs. In the absence of amphiphilic polymers, Pd(0) NPs show a trigonal sheet-like structure, which could be due to the presence of CO as a capping ligand that controls the growth of nanoparticles (Figure 1A). However, over a time period of 2 weeks, these particles agglomerated and precipitated (Figure 15A) indicating that they are not well stabilized in the absence of amphiphilic polymers.

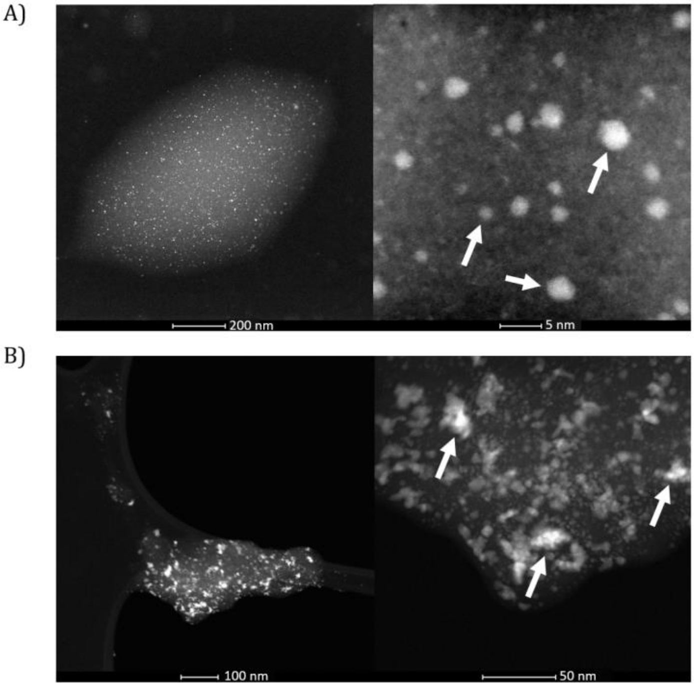

Figure 2: STEM-HAADF images of Pd(0) NPs reduced from A) **P2@Pd(II)**, B) **P3@Pd(II)** ([Pd(II)] = 210 μM, [**P**] = 1 mg/mL in H_2O. Pd(0) NPs indicated by white arrows.

STEM-HAADF images of **P1@Pd(0)** show bright spherical structures (indicated by white arrows Figure 1B) with a size of ~ 5 nm in diameter. This is indicative of the formation of nearly monodisperse Pd(0) NPs that were formed in this case. **P2@Pd(0)** also showed the presence of Pd(0) NPs with ~ 5 nm size, but in this case, there was a higher fraction of particles with variable sizes (Figure 2A). **P3@Pd(0)** showed highly disperse and less defined Pd(0) NPs as observed from aggregated bright spots (Figure 2B). This could be due to negatively charged carboxylate groups that strongly bind to positively charged Pd(II) precursor across the polymer backbone, which when reduced result in large aggregated, non-spherical Pd(0) NPs. Control polymer **P4@Pd(0)** also exhibited spherical Pd(0) NPs with slight dispersity of the size ~ 5-10 nm. The formed Pd(0) NPs in water did not show any sign of precipitation and were stable in water for over two months. They all appear as homogeneous dark brown solutions, indicating that the Pd(0) NPs are stabilized inside the polymers (Figure 15B).

The size of polymeric nanoparticles after CO reduction was also evaluated using DLS. Due to dispersity in the size of the nanoparticles, an accurate evaluation was difficult. All **P1-P4@Pd(0)** were found to have a hydrodynamic radius (R_H) of 100 nm before filtration because of the presence of large aggregated particles. After filtering the samples with a PVDF filter with a pore size of 100 nm, smaller particles were observed as shown in Table 1. The majority (90-98%) of the particles showed an R_H of 4-8 nm and a minority with sizes between 10-70 nm. Compared to **P1-P4@Pd(II)**, which are rather monodisperse with an $R_{H\ of}$ around 5-6 nm, we conclude that larger particles are formed as a result of the formation of Pd(0) NPs. Elemental analysis was performed using Energy-Dispersive X-ray Spectroscopy (EDS) experiments in combination with STEM-HAADF for all samples **P1-P4@Pd(0)** and the results confirmed the presence of palladium in all of them (Figure 15C).

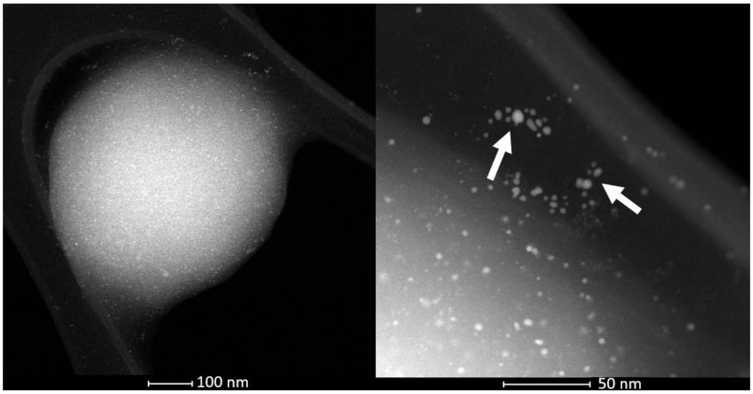

Figure 3: STEM-HAADF images of Pd(0) NPs reduced from **P4@Pd(II)** ([Pd(II)] = 210 µM, [**P**] = 1 mg/mL in H_2O. Pd(0) NPs indicated by white arrows.

3.3 Exploring the catalytic potential of Pd(0) amphiphilic polymeric nanoparticles

3.3.1 Heck reaction in water

An intramolecular Heck coupling reaction was performed on a coumarin precursor substrate **1** (5-diethylamino-2-iodophenyl ester) to form fluorescent product 7-diethylaminocoumarin **2** in water (Figure 4A). The formation of the product was monitored using fluorescence spectroscopy over time. In the case of the reaction promoted by **P1@Pd(0)**, fast formation of **2** was observed, as evidenced by the formation of a fluorescent product, and the fluorescence intensity plateaued within 1 h. In the case of Pd(0), the reaction proceeded significantly slower (Figure 4B). HPLC-UV chromatogram of the reaction mixture indicated full conversion of substrate **1** to product **2** by **P1@Pd(0)**, while in the case of Pd(0) only a negligible amount of product **2** was formed in 3 h. Out of all the different palladium cross-coupling reactions, the Heck reaction is considered the most difficult to perform in an aqueous environment and it is evident that Pd(0) based polymeric catalytic system is highly efficient towards it, outperforming the control Pd(0) NPs.[17]

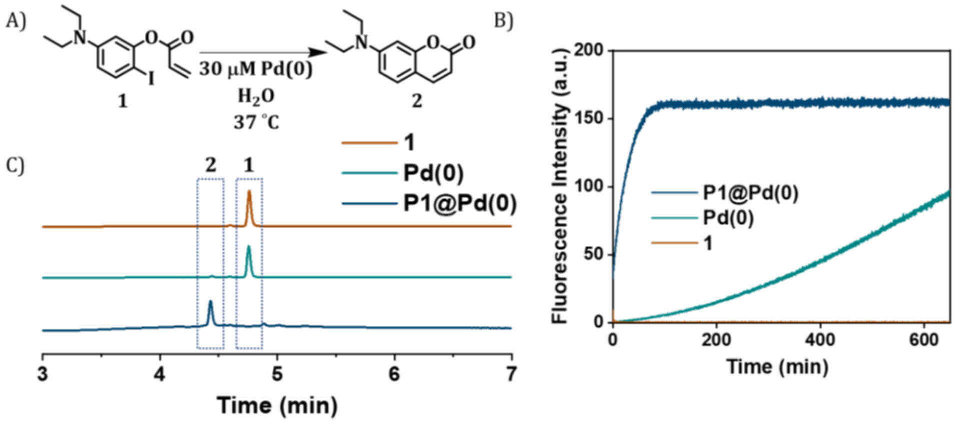

Figure 4: A) Formation of 7-diethylaminocoumarin **2** from non-fluorescent precursor **1** via intramolecular Heck reaction B) Fluorescence kinetic profile of Heck reaction promoted by **P1@Pd(0)** and **Pd(0)**, 7-diethylaminocoumarin **2** monitored at λ_{ex} = 375 nm and λ_{em} = 500 nm. [**1**] = 30 μM, [Pd(0)] = 30 μM, [**P**] ~ 0.1 mg/mL, T = 37 °C, in H_2O. C) HPLC-UV chromatogram from aliquots of the reaction mixture after 180 min.

3.3.2 Suzuki-Miyaura coupling reaction in water

The efficiency of the system was also assessed towards promoting Suzuki-Miyaura cross-coupling reactions on lipophilic substrates in water. The naphthalene boronic acid **3** was reacted with iodobenzaldehyde **4** to form carbon-carbon cross-coupled biaryl product **5** (Figure 5A) under basic conditions (K_2CO_3). HPLC-UV chromatogram of the reaction mixture taken after 24 h indicated complete consumption of iodobenzaldehyde **4** leading to the formation of two new peaks (major and minor, Figure 5B). The reaction mixture was then analysed by MS, which confirmed the major peak as cross-coupled product **5**, while the minor peak did not appear in the MS spectrum (Figure 5C). We hypothesize that the second peak is the homo-coupled product of naphthalene boronic acid **6** because it has a longer retention time than the product due to its high hydrophobicity and is not detected in MS as it is difficult to be ionized. Pd(0) did not promote the coupling reaction in this case because of the insolubility of reactants in water which can only be solubilized in the presence of polymeric nanoparticles.

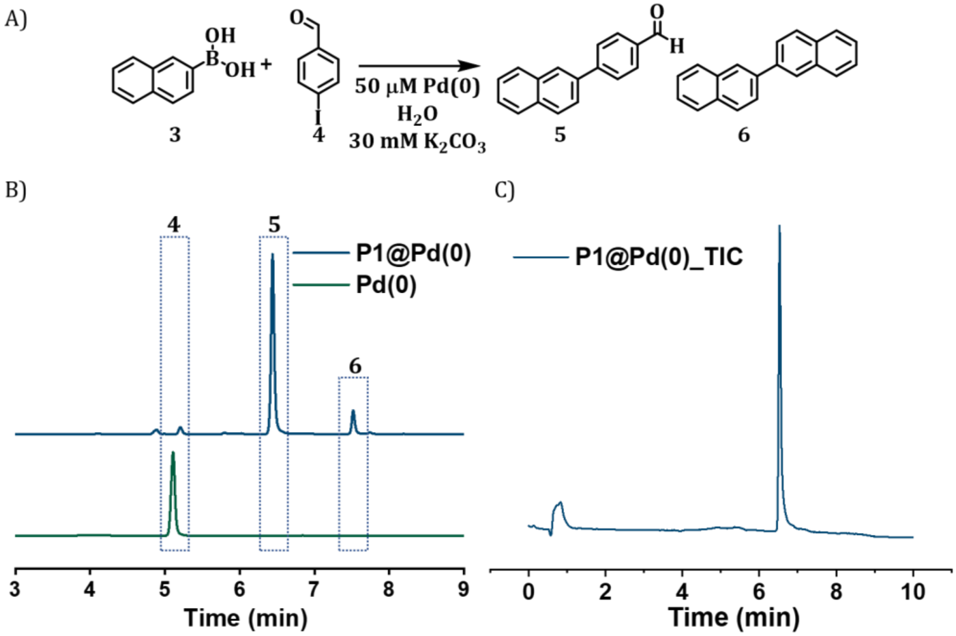

Figure 5: A) Suzuki-Miyaura coupling of naphthalene boronic acid **3** and iodobenzaldehyde **4** to form C-C coupled products B) HPLC-UV chromatogram of the reaction mixture after 24 h C) HPLC-MS chromatogram of the same aliquot, from total ion current (TIC) channel showing mass $[M+H]^+$ = 233, corresponding to product **5** (m/z = 232). Reaction conditions: [**3**] = 100 μM, [**4**] = 50 μM, [Pd(0)] = 50 μM, [**P**] ~ 0.2 mg/mL, T = 37 °C, in H_2O.

3.3.3 Depropargylation reaction in water

The potential of **P1@Pd(0)** to perform depropargylation reactions in water was tested by the activation of pro-rhodamine (pro-rho) substrate **7** in water. **P1@Pd(0)** promoted deprotection of pro-rho **7** to rho **8**, which was monitored using fluorescence spectroscopy over time. The fluorescent intensity plateaued at 200 min and the reaction mixture was analysed using HPLC-UV which confirmed the formation of product **8** (Figure 6). Near full conversion of substrate to the product was observed even at low substrate concentrations (30 μM). The depropargylation reaction on pro-rho **7** was selected as a model reaction to export to complex media and living cells to further test the efficiency of Pd(0) based polymeric catalytic system before the activation of propargyl-protected drug of 5FU.

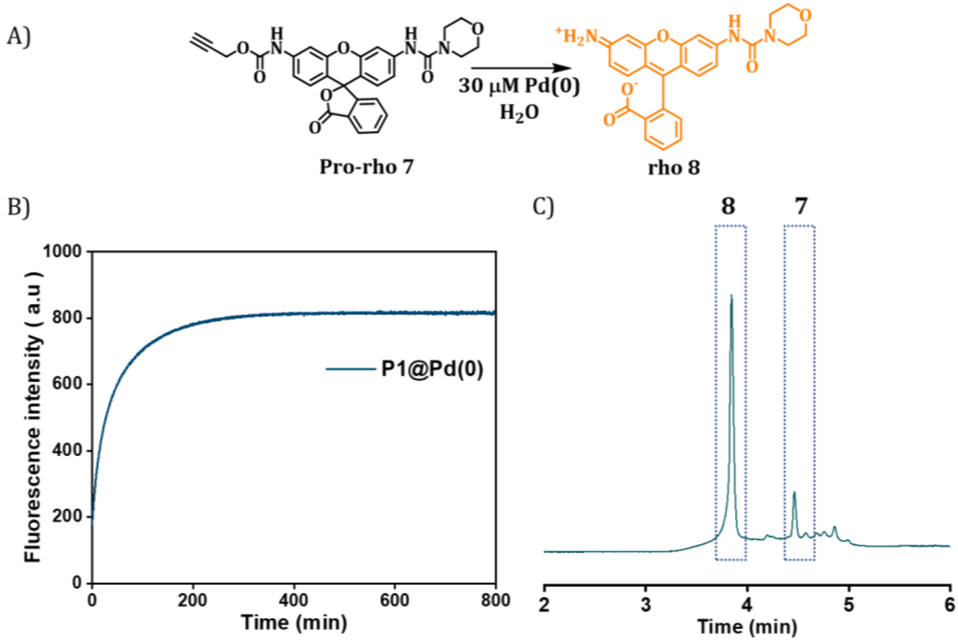

Figure 6: A) Activation of pro-rho **7** to rho **8** by depropargylation promoted by **P1@Pd(0)** in H_2O. B) Fluorescence kinetic profile of pro-rho **7** activation using **P1@Pd(0)** in H_2O where formation of rho **8** was monitored at λ_{ex} = 485 nm and λ_{em} = 520 nm, reaction conditions: [**7**] = 30 μM, [Pd(0)] = 30 μM, [**P**] ~ 0.1 mg/mL, T = 37 °C, in H_2O. C) HPLC-UV chromatogram of the reaction mixture after 24 h monitored at λ = 265 nm.

3.4 Exporting Pd(0) NPs to complex biological media

The efficiency of **P1@Pd(0)** was evaluated in media of varying complexity such as water, PBS, PBS + 10% fetal bovine serum (FBS), and Dulbecco's Modified Eagle Medium (DMEM). FBS has bovine serum albumin (BSA), a globular protein as its major component and variety of other proteins. This together with DMEM and buffered salts mimic the environment of the extracellular milieu like the interstitial fluid to help the growth of *in vitro* cell culture. **P1@Pd(0)** exhibited fast kinetics in activation of pro-rho **7**, where fluorescent intensity saturated within 300 min in all media (Figure 7A). The formation of product **8** was monitored by analysing the reaction mixture using HPLC-UV. The HPLC-UV chromatogram confirmed near quantitative conversion in all cases, with only a negligible amount of substrate pro-rho **7** remaining in water, DMEM, and PBS supplemented with serum (Figure 7B). Most importantly, no significant decrease in reaction rate was observed when the complexity of the medium was increased. This is in sharp contrast to the Pd(II) based polymeric catalytic system discussed in Chapter 2. This highlights that Pd(0) based polymeric nanoparticles are highly efficient catalysts to export to living cells.

The incomplete consumption of substrate in water can be attributed to the dilute conditions, where hydrophobic products have a tendency to remain sequestered within the hydrophobic pockets reducing further substrate diffusion upon the decrease in concentration. However, in PBS full consumption of substrate was observed as it may have prevented product aggregation in the hydrophobic domain. In the case of reaction performed in PBS supplemented with serum proteins, minor fraction of substrates can also end up inside the hydrophobic domains of proteins. This can hinder complete conversion as the substrates are not in proximity to catalytic active sites.

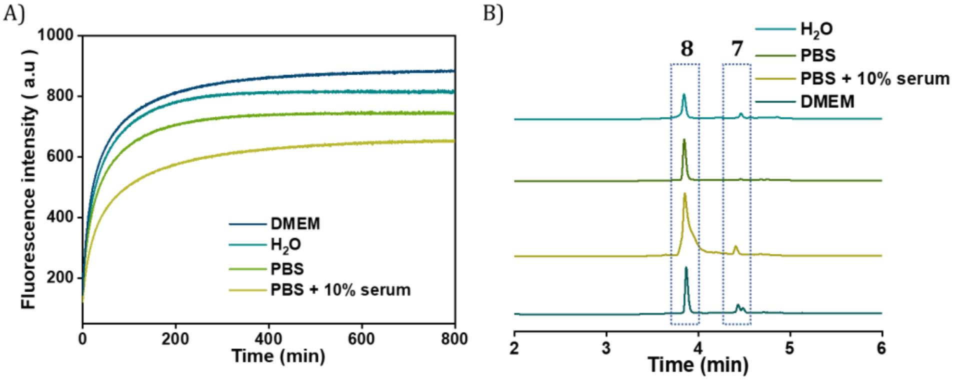

Figure 7: Fluorescence kinetic profiles of pro-rho **7** activation using **P1@Pd(0)** in H_2O, PBS, DMEM, and PBS supplemented with 10% fetal bovine serum, where the formation of rho **8** was monitored at λ_{ex} = 485 nm and λ_{em} = 520 nm, reaction conditions: [**7**] = 30 µM, [Pd(0)] = 30 µM, [**P**] ~ 0.1 mg/mL, T = 37 °C. B) HPLC-UV chromatogram of the corresponding reaction mixture after 24 h monitored at λ = 265 nm.

3.5 Comparison of catalytic efficiency of Pd(0) NPs based on different polymer design in complex media

Having established that **P1@Pd(0)** is a superior catalyst for depropargylations in more complex media compared to its precursor **P1@Pd(II)**, we wondered how the polymer's microstructure would affect the catalytic activity. Therefore, we investigate the efficiency of the different Pd(0) based polymeric nanoparticles **P1-P4@Pd(0)** and Pd(0) as described in section 3.2, towards depropargylation reaction of pro-rho **7** in DMEM medium. **P1-P2@Pd(0)** showed a superior catalytic activity, where the fluorescence intensity plateaued within 300 min (Figure 8). In both cases, the well-defined spherical Pd(0) NPs with small sizes offer a larger surface area for efficient substrate binding and catalysis which is advantageous as it results in fast kinetics. **P3@Pd(0)** equipped with carboxylate groups, however, exhibited significantly slower kinetics with respect to **P1-P2@Pd(0)** (Figure 8). This could be attributed to the dispersity of nanoparticle size and structure. In this case, the Pd(0) NPs were not well-defined as observed in **P1-P2@Pd(0)** and had large fraction of larger aggregates. **P4@Pd(0)** showed slow kinetics, which was as expected as it lacks the TPP ligands for stabilization of the Pd(0) catalysts during the reaction (Figure 8). Pd(0) did not promote the reaction at all and this could be due to two reasons: (1) Pd(0) NPs can be deactivated by nucleophiles present in DMEM or (2) the solubility of pro-rho **7** is compromised in the absence of amphiphilic polymers.

In order to compare the activity of polymeric nanoparticles before and after reduction, **P1@Pd(II)** was used to activate pro-rho **7** under the same reaction conditions. **P1@Pd(II)** exhibited very slow reaction kinetics similar to the observation in previous work in Chapter 2 where pro-rho **7** concentration was higher (Figure 8). The rate of reaction is even slower than **P4@Pd(0)** (without TPP ligands) confirming that Pd(0) catalysts are more efficient for depropargylation reactions. Overall, **P1@Pd(0)** and **P2@Pd(0)** performed the best. This indicates that microstructure of polymers that form well-defined hydrophobic pockets contribute to catalytic efficiency similar to observation in Chapter 2. Further, it suggests that the amount of triphenyl phosphine ligand in the polymer backbone also play a significant role in their overall catalytic efficiency.

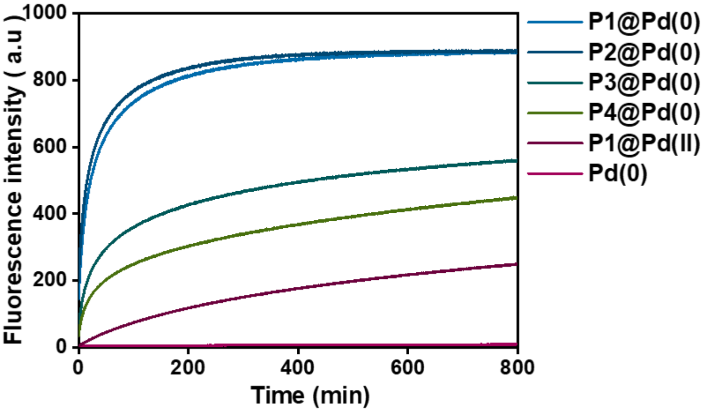

Figure 8: Fluorescence kinetic profiles of pro-rho **7** activation using **P1-P4@Pd(0)**, **P1@Pd(II)**, and **Pd(0)** in DMEM, where the formation of rho **8** was monitored at λ_{ex} = 485 nm and λ_{em} = 520 nm, reaction conditions: [**7**] = 30 µM, [Pd(0)] = 30 µM, [**P**] ~ 0.1 mg/mL, T = 37 °C.

3.6 Pd(0) based pro-drug activation in water

The orally bioavailable pro-drug **9** developed by Unciti-Broceta and co-workers was further evaluated for activation by Pd(0) NPs.[2] The *O,O'*-dipropargylation of 5FU **11** to form pro-5FU **9**, lock the molecule in a lactim form which, when activated by Pd(0), forms 5FU **11** via a monopropargylated intermediate **10** (Figure 9A).

The pro-drug activation in water was performed using catalytic amounts of Pd(0), 50 µM pro-5FU **9** and 5 µM Pd(0). The polymer concentration was kept extremely low (0.02 mg/mL) for the reaction in water to understand the catalytic nature of pro-drug activation. The progress of the reaction was monitored by analysing the reaction mixture by combining the positive and negative modes of ionization in HPLC-MS. This is because of differences in detection sensitivity of **9**, **10,** and **11** by both modes of ionization in single quadrupole HPLC-MS. 5FU **11** could only be detected in negative ionization mode and pro-5FU **9** and **10** in positive ionization mode. Therefore, two modes were used subsequently to detect them from the reaction mixture over time. As the focus of the experiment was to monitor the progress of the reaction rather than the accurate quantification of 5FU formed, more sensitive analytical techniques such as LC-MS/MS (triple quadrupole) were not used for analysis.

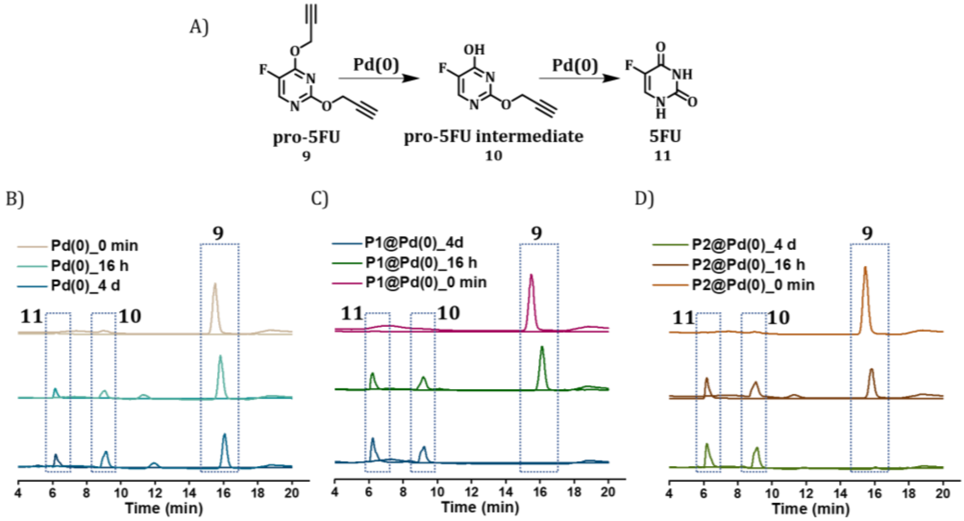

Figure 9: A) Activation of pro-5FU **9** by depropargylation promoted by Pd(0) to form 5FU **11** via pro-5FU intermediate **10**. HPLC-UV chromatogram of pro-5FU activation from aliquots of the reaction mixture at specified time intervals using B) Pd(0) C) **P1@Pd(0)** D) **P2@Pd(0)**, reaction conditions: [**9**] = 50 μM, [Pd(0)] = 5 μM, [**P**] ~ 0.02 mg/mL, T = 37 °C.

In the case of pro-drug activation catalysed by Pd(0), the formation of intermediate **10** and 5FU **11** was observed over time, albeit that full conversion of pro-5FU **9** to 5FU **11** was not observed even after 4 days (Figure 9B). In the case of **P1-P2@Pd(0)**, complete consumption of the substrate **9** was observed leading to 5FU **11** and intermediate **10** in 4 days (Figure 9C, D). There was no complete consumption of intermediate **10**. Further, the concentration of **P1-P2@Pd(0)** was increased to 0.2 mg/mL in water ([Pd(0) = 50 μM], in order to investigate the conversion of intermediate **10** to 5FU **11**. In the case of **P1@Pd(0)**, the complete disappearance of pro-5FU **9** was observed within 4 h, but the intermediate **10** did not convert to 5FU even after 16 h (Figure 10A). In the case of **P2@Pd(0)**, pro-5FU **9** was completely converted to intermediate and 5FU within 4 h, and also significant conversion of intermediate **10** to 5FU **11** was observed after 16 h when compared to **P1@Pd(0)** (Figure 10B). The hydrophobic domains in **P1@Pd(0)** may stabilize the intermediate **10** formed from further activation. While, more open catalytic binding sites that may be available in **P2@Pd(0)** facilitates further transformation of intermediate **10** to 5FU **11**. This result also confirms the hypothesis that microstructure of the polymers will need to be optimized according to the substrates and indicates there is no one polymer structure that works best for all substrates.

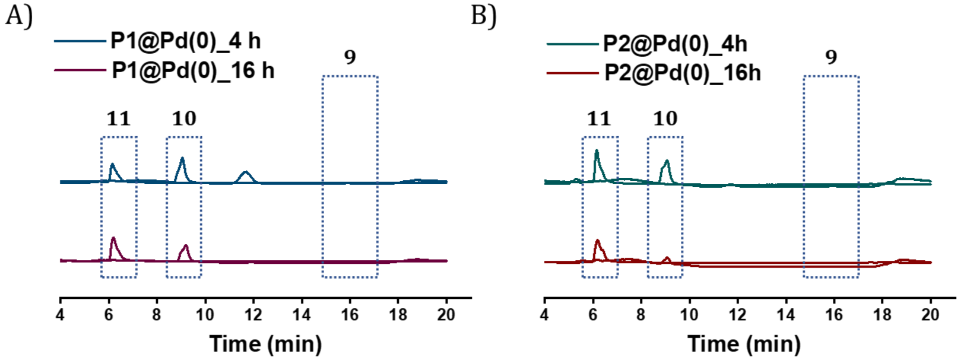

Figure 10: HPLC-UV chromatogram of pro-5FU activation from aliquots of the reaction mixture at specified time intervals using A) **P1@Pd(0)** B) **P2@Pd(0)**, reaction conditions: [**9**] = 50 μM, [Pd(0)] = 50 μM, [**P**] ~ 0.2 mg/mL, T = 37 °C.

3.7 Pro-dye activation in living cells

P1-P4@Pd(0) proved to be efficient in promoting depropargylation reaction even in the presence of complex biological media including serum proteins. Therefore, they were further evaluated for depropargylation reactions in the presence of living cells, in this case, human liver cancer cell line, HepG2 cells. However, the biocompatibility of the Pd(0) comprising polymers is an important issue. Therefore, we first performed a cytotoxicity assay by incubating the cultured HepG2 cells with **P1-P4@Pd(0)** at different Pd(0) concentrations from 0 μM to 100 μM for 48 h. The CCK-8 cell viability assay after 48 h indicated that none of the polymers **P1-P4@Pd(0)** showed cytotoxicity since at all concentrations, the cell viability remained above 90% (Figure 11). This indicated that developed Pd(0) based polymeric nanoparticles have excellent biocompatibility.

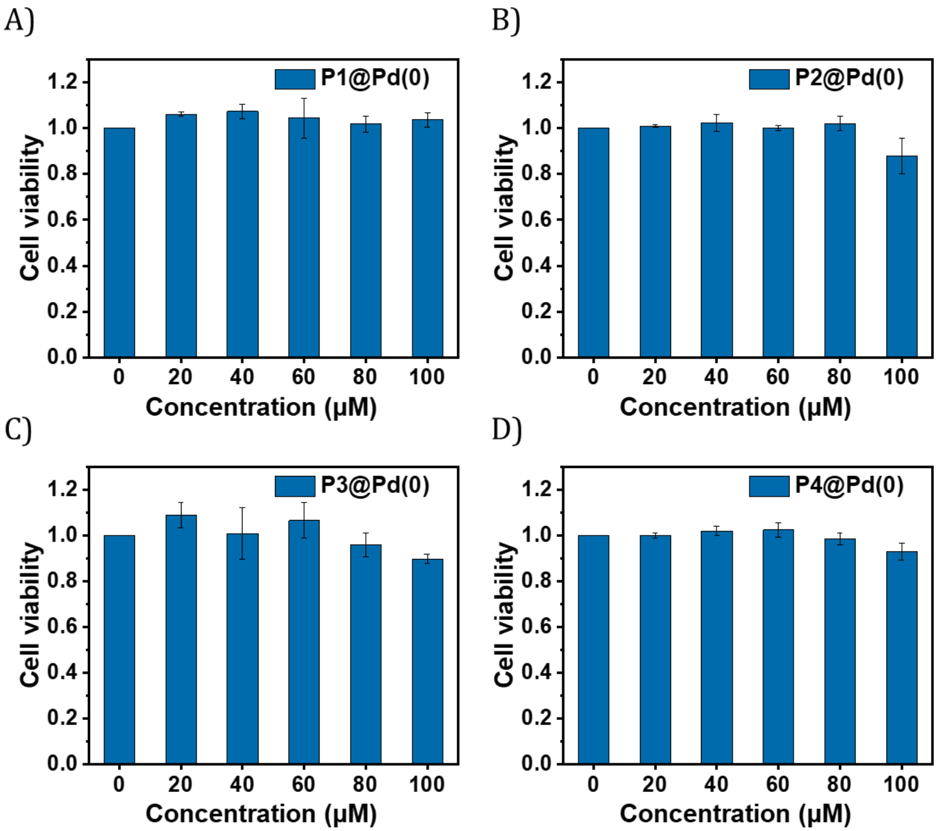

Figure 11: CCK-8 cell viability assay of HepG2 cells after incubating with A) **P1@Pd(0)** B) **P2@Pd(0)** C) **P3@Pd(0)** and D) **P4@Pd(0)** for 48 h, results are average of 3 wells. X-axis corresponds to Pd(0) concentration varied from 0 -100 μM.

We aimed to perform the pro-rho activation in the extracellular space where the dye formed can permeate the cell membrane to the cytoplasm of cells. The presence of oligo(ethylene-oxide)-based side chains in the amphiphilic polymers limits the interaction of these polymers with the cell membrane allowing these particles to remain in extracellular space for several hours.[18] However, over time endocytic internalization of nanoparticles will happen where **P3@Pd(0)** will be internalized faster due to the presence of charged groups.[18] The nanoparticles' size also affects the internalization time where the small nanoparticles are internalized faster.[19]

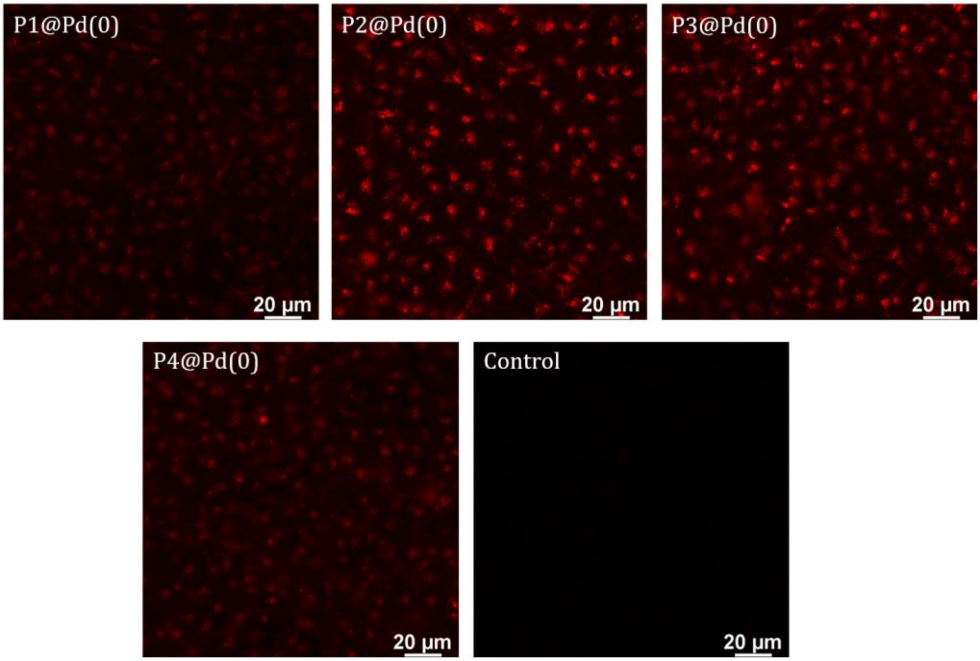

Figure 12: Confocal imaging of HepG2 cells after pro-rho **7** activation using **P1-P4@Pd(0)**. The red colour indicates the fluorescence of rho **8**. [pro-rho **7**] = 25 μM, [Pd(0)] = 60 μM, [P] = 0.2 mg/mL. Incubation time = 36 h, T = 37 °C. λ_{ex} = 485 nm. Control has only pro-rho **7** (25 μM).

HepG2 cells were incubated with **P1-P4@Pd(0)** ([Pd(0)] = 60 μM, [P] ~ 0.28 mg/mL) together with pro-rho **7** (25 μM) for 36 h. As a control, cells were only incubated with pro-rho **7** without Pd(0) NPs. Afterwards, cells were observed under a confocal microscope at an excitation wavelength of 485 nm. In all cases, except for the control, the confocal images of the cells show intracellular fluorescence build up, indicating the formation of rho **8** (Figure 12). The confocal images of the cells incubated with **P2-P3@Pd(0)** showed higher fluorescence buildup from rho **8**. Interestingly, the TPP ligand-functionalised **P1@Pd(0)** and control **P4@Pd(0)** showed similar results. This is in sharp contrast to the results obtained in the solution catalysis studies in DMEM medium (Section 3.5, Figure 8), where **P1@Pd(0)** performed significantly better than **P4@Pd(0)**. **P1@Pd(0)** and **P2@Pd(0)** exhibited similar reaction kinetics in DMEM, but in presence of cells **P2@Pd(0)** is found to outperform the former. While **P3@Pd(0)** only showed reasonable activity in solution, it was also found to outperform **P1@Pd(0)** in the presence of cells. Although not completely understood at this point in time, these results may indicate that the higher percentage of TPP ligands (20%) in **P2&P4@Pd(0)** plays a role in retaining the catalytical activity of Pd(0) nanoparticles. Also, the higher fraction of large aggregated particles (Section 3.2) in these two systems could explain the higher activity. The catalysis studies in DMEM solution showed remarkably different results than the *in vitro* studies, indicating that the catalytic efficiency is not the only limiting factor of their performance in the presence of cells. Catalyst performance can also be significantly impacted by differences in size and structure of both Pd(0) NPs and polymeric nanoparticles or the presence of charged groups on polymers. This is because these factors directly affect their stability or the amount of time needed for internalization by the cells. The *in vitro* studies confirmed that Pd(0) based polymeric nanoparticle systems are biocompatible and retain their activity in the presence of living cells.

3.8 Pro-drug activation in living cells

Given that **P1-P4@Pd(0)** remain active in the presence of living cells and can also activate pro-5FU **9** in aqueous solution (Section 3.6-3.7), we further investigated their potential to generate 5FU to induce cell death in HepG2 cancer cell cultures. Many cancer cell lines have increased resistance to 5FU while pancreatic cancer cells are the most sensitive to 5FU treatment.[5] In the case of cell lines that are very sensitive to 5FU, only a low concentration of the drug is required to induce a strong antiproliferative effect.[5] In order to test the cytotoxic effect of 5FU on HepG2 cell lines, they were incubated with 100 μM of 5FU for 48 h. This was also done by encapsulating 5FU in presence of amphiphilic polymer **P1** to see if its presence negatively impacts the bioavailability of the drug. The CCK-8 cell viability assay was performed after incubation of both for 48 h; the results showed that 5FU alone reduced the cell viability to 30% and **5FU@P1** reduced the cell viability to 40%. As the difference in cell viability is not significant, we can confirm that after pro-5FU activation, generated 5FU can easily diffuse out of polymers to induce the cytotoxic effect. As complete cell death was not observed even in the presence of 100 μM 5FU, we inferred that the HepG2 cell line is not very sensitive to 5FU. Therefore, a high rate of pro-drug activation by the Pd(0) NPs will be crucial as this rate has to be higher than the cell proliferation rate to see any cytotoxic effect on this cell line.[5] On the other hand, this is beneficial to observe the differences in the efficiency of different polymer designs to activate pro-5FU, as otherwise complete cell-death will be observed in all cases.

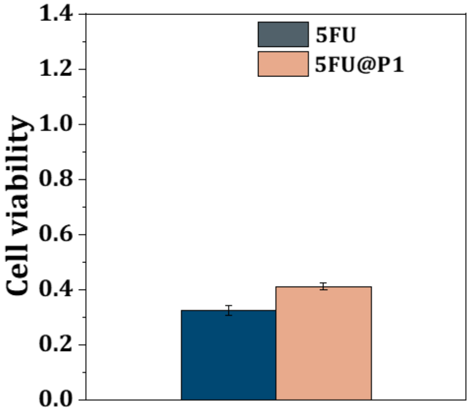

Figure 13: CCK-8 cell viability assay after incubation of HepG2 cell line with 100 µM 5FU and **5FU@P1** for 48 h.

For pro-drug activation studies, new batches of Pd(II)-containing polymers **P1-P4** were prepared and the Pd(II) was reduced to the corresponding Pd(0). The new batches are named as **P1-P4@Pd(0)*** from here on. The reproducibility in the cytotoxicity of the new polymers was found to be good with HepG2 cells, but some deviations were observed in case of **P2@Pd(0)*** (Figure 14 &11). For pro-5FU **9** activation, HepG2 cells were incubated with **P1-P4@Pd(0)*** with increasing Pd(0) concentrations (20 µM – 100 µM) together with 100 µM pro-5FU in each case for 48 h. To confirm that cytotoxicity arises from the activation of 5FU, cells were also separately incubated with **P1-P4@Pd(0)*** and pro-5FU at the same concentrations for 48 h. The CCK-8 cell viability assay was performed after 48 h in all cases (Figure 14). In the case of **P1@Pd(0)***, the cell viability was decreased to 60% at 100 µM Pd(0) indicating a reasonable antiproliferative effect as direct incubation of **5FU@P1** only decreased cell viability to 40% (Figure 13 & 14A).

P2@Pd(0)* showed a promising cytotoxic effect at 80 µM Pd(0) concentration, decreasing cell viability to 25% same as when cells were treated with 5FU (Figure 13 and 14B). However, with a further increase of Pd(0) concentration to 100 µM, **P2@Pd(0)*** showed a slight cytotoxicity by itself. **P3&P4@Pd(0)*** behaved similarly, where cytotoxicity was reduced to 40-50% at 100 µM Pd(0) concentration, also showing a reasonable antiproliferative effect. In the case of pro-dye activation, both **P2&P3@Pd(0)*** outperformed other nanoparticles, while in the case of pro-drug activation only **P2@Pd(0)*** showed the best results. The higher efficiency of **P2@Pd(0)*** when compared to the other catalysts can be attributed to the fact that it was more efficient in activating pro-5FU intermediate **10** to 5FU, whereas in the case of **P1@Pd(0)*** intermediate **10** did not fully convert to 5FU. All in all, the results again confirm that polymer microstructure plays an important role in the catalyst performance. Interestingly, even small differences in the polymer design can have higher impact on their function in cellular environment.

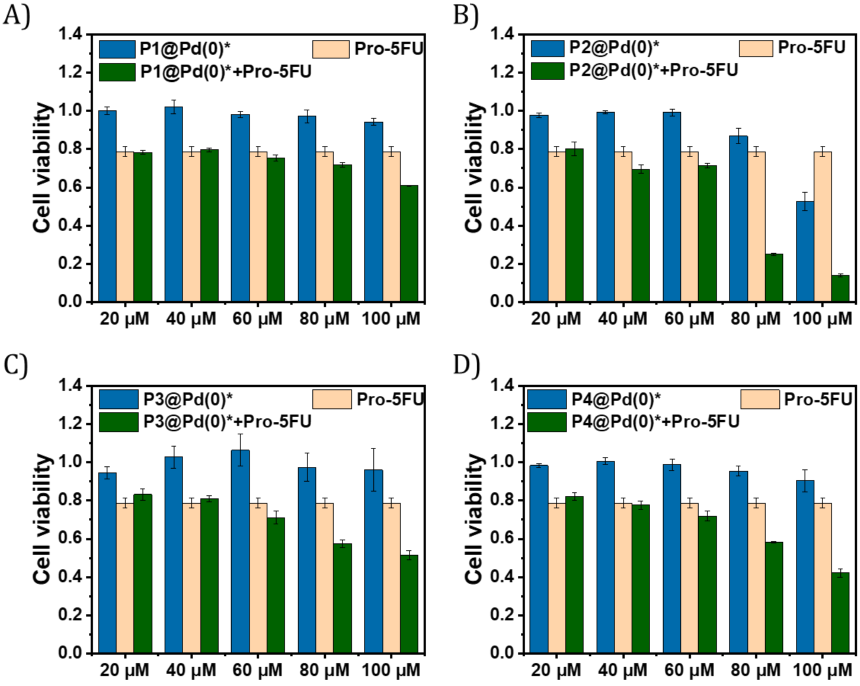

Figure 14: CCK-8 cell viability assay after incubation of HepG2 cells with A) **P1@Pd(0)***, pro-5FU and **P1@Pd(0)*** + pro-5FU, B) **P2@Pd(0)***, pro-5FU and **P2@Pd(0)*** + pro-5FU, C) **P3@Pd(0)***, pro-5FU and **P3@Pd(0)*** + pro-5FU, D) **P4@Pd(0)***, pro-5FU and **P4@Pd(0)*** + pro-5FU. [Pd(0)] = 20 – 100 µM, [pro-5FU] = 100 µM, T = 37 °C. The results are average of 3 wells.

3.9 Conclusion and Outlook

In conclusion, we have developed highly efficient and versatile amphiphilic polymeric nanoparticle-based Pd(0) NPs by reducing Pd(II) in the presence of amphiphilic polymers using CO as a mild reductant. Both TPP functionalised and control amphiphilic polymer stabilized Pd(0) NPs, where **P1, P2&P4@Pd(0)** formed spherical Pd(0) NPs of size ~ 5 nm as observed from STEM-HAADF measurements along with larger aggregates. **P3@Pd(0)** with carboxylate ligand formed predominantly non-spherical aggregated Pd(0) NPs.

The formed Pd(0) based polymeric nanoparticles were found to be versatile catalysts that promote Heck coupling, Suzuki-Miyaura coupling and depropargylation reactions in water. The rate of the depropargylation reaction did not change significantly in the presence of buffered saline medium or complex media such as DMEM and serum proteins. Near quantitative conversion of pro-rhodamine to rhodamine dye was observed in all cases. This is a remarkable improvement in comparison to Pd(II) based amphiphilic polymers, where the rate of depropargylation was significantly reduced when the complexity of the medium was increased.

During the pro-dye activation in DMEM, **P1&P2@Pd(0)** outperformed the other catalysts as fast kinetics for the depropargylation were observed. The control polymer without TPP ligands **P4@Pd(0)** and negatively charged **P3@Pd(0)**, also activated pro-dye but exhibited slower kinetics. The activation of pro-5FU was possible using catalytic amounts of Pd(0) in water, with complete substrate consumption observed within 4 days. In this case, the intermediate prodrug was found to be stable without further transformation to 5FU. On increasing Pd(0) concentrations, pro-drug activation was faster and full consumption of the pro-drug was observed within 16 h. However, the 5FU intermediate was completely transformed to 5FU only in the case of the reaction promoted by **P2@Pd(0)**.

All nanoparticles **P1-P4@Pd(0)** were found to be non-toxic to the HepG2 cell line, up to an incubation time of 48 h as monitored by the CCK-8 cell viability assay. The *in vitro* pro-dye activation studies showed very different results compared to solution studies in DMEM. In presence of HepG2 cells,

P2&P3@Pd(0) outperformed **P1@Pd(0)**. In the case of pro-drug activation, **P2@Pd(0)** was found to exhibit a strong cytotoxic effect by the activation of pro-5FU, while other nanoparticles behaved the same with only a moderate effect. Although the exact reasons of the deviation of activity of these nanoparticles in DMEM and cell culture are not clear yet, it can be inferred that the size of Pd(0) NPs and amount of phosphine ligand seems to play a significant role here. The overall results indicate that the efficiency of the system in presence of cells can be the combined effect of the size of Pd(0) NPs, microstructure of amphiphilic polymers and also structure of pro-drugs or substrates. The optimization of polymer microstructure depending on pro-drug's structure and hydrophobicity will be one way of approach to get a better cytotoxic effect in the tumour cells.

In order to further improve the catalytic performance of these nanoparticles, further studies are required to attribute the differences in activity to the size of the Pd(0) NPs. In order to achieve this, precise control over the size and structure of Pd(0) based polymeric nanoparticles is required which could be done by varying the amount of Pd incorporated into the polymer backbone in future studies. A thorough understanding to further improve the catalytic performance of Pd(0) based amphiphilic polymeric nanoparticles is necessary to translate this system to *in vivo* studies. However, we believe the ability of this Pd(0) based catalytic system to activate orally bioavailable pro-drug of 5FU is promising and can be further extended to activate pro-drugs of more cytotoxic anticancer drugs such as doxorubicin. Further, they can also be utilized to synthesize multiple drugs in case of drug resistance by combining depropargylation and cross-coupling reactions on inactive substrates.

3.10 Experimental Section

Materials and characterisation methods

Pd(II) complexed amphiphilic polymers synthesized in Chapter 2 were used for reduction to Pd(0) nanoparticles. Control polymer **P4** is the same as described in Chapter 5. Reduction of Pd(II) to Pd(0) NPs and characterization by STEM-HAADF was performed by Prof. Victor Sebastian. The substrate for the Heck coupling reaction was obtained from Roy Oerlemans which was synthesized according to a previously reported protocol.[3] The substrates for Suzuki-Miyaura coupling reactions were commercially available. Pro-rhodamine **7** was synthesized as reported in Chapter 2. Pro-5FU was obtained from Catherine Adam, University of Edinburgh, and synthesized according to a previously reported protocol.[2] Nile red amine was obtained from Linlin Deng which was synthesized according to previously reported protocol.[15] The cell experiments were performed by Linlin Deng. Fluorescence measurements were performed on an Agilent Cary Eclipse fluorescence spectrophotometer using 1 cm × 1 cm pathlength quartz cuvettes. Liquid chromatography - UV was performed using Shimadzu UFLC-XR with PDA detector with water + 0.1% formic acid and ACN + 0.1% formic acid as eluents on Kinetex column C18 5 mm EVO 100 Å. HPLC Method 1 for Heck coupling, Suzuki-Miyayura coupling and depropargylation reactions: eluent A: water (0.1% formic acid); eluent B: acetonitrile (0.1% formic acid); and A/B = 90:10 isocratic 2 min, 90:10 to 0:100 in 2 min, isocratic 2 min, 0:100 to 90:0 in 2 min, and isocratic 2.0 min (flow = 0.2 mL/min). High-Performance Liquid Chromatography – HPLC-UV/MS was performed on a SHIMADZU Nexera-I LC-2040C 3D coupled with LC-MS 2020 for detection. Method 2 for pro-5FU: A/B = 95:5 isocratic 15 min on Hypercarb column.

DMF-SEC measurements of functionalised polymers were performed using PL-GPC-50 plus (Varian Inc. Company) equipped with a refractive index detector. DMF with 10 mM LiBr was used as eluent at a flow rate of 1 mL min^{-1} on the Shodex GPC-KD-804 column at 50 °C. Exclusion limit = 100.000 Da, 0.8 cm i.d. × 300 mm calibrated using poly (ethylene oxide) from polymer laboratories. Dynamic light scattering experiments were performed using Malvern Zetasizer with 830 nm laser and an angle of scattering 90°. For cell experiments, analysis of the microplate was performed using a Tecan MC-SPARK. Confocal microscopy images of HeLa cells were obtained with a Leica SP5 confocal microscope with a HyD2 detector. Identical conditions were followed throughout all measurements. ImageJ was used for processing images.

Experimental procedures

Synthesis of **P3**: ***p*-PFPA$_{180}$** (100 mg, 1 eq, 0,0023 mmol) was dissolved in dry and degassed DMF in a Schlenk flask kept in a preheated oil bath at 50 °C. To this solution Nile red amine[15] (3 mg, 3 eq, 0.0069) was added and stirred overnight, the reaction was monitored using ^{19}F NMR by comparing the peaks of free pentafluorophenol with those in the polymer backbone. The incorporation of Nile red amine was found to be 1% after overnight stirring. To this solution, TPP ligand *N*-(6-aminohexyl)-4-(diphenylphosphaneyl) benzamide (33 mg, 36 eq, 0,082 mmol) was added and stirred overnight. Followingly, 100 µL triethylamine (not dried) was added to the reaction mixture to trigger hydrolysis of the poly-(pentafluorophenol acrylate) backbone. After monitoring the amount of displaced pentafluorophenol using ^{19}F NMR, Jeffamine@1000 (414 mg, 180 eq, 0.41 mmol) was added. The reaction mixture was then left overnight under argon and the completion of the reaction was again monitored using ^{19}F NMR. Then, the reaction mixture was purified by dialysis (1 x 1 L methanol, 2 x 1 L THF) for 3 days in a tightly closed screw-capped container. Degassed solvents were used for dialysis which was refreshed as frequently as possible (> 6 h time gap) to prevent oxidation of triphenylphosphine. After dialysis, THF was reduced to ~ 3 mL using a rotary evaporator and the polymer was precipitated into ice-cold pentane (800 mL). The polymer was dried under vacuum overnight at 50 °C to yield a bright pink solid and was stored at -19 °C wrapped with aluminium foil. Yield: 42 mg. $M_{n,\,SEC\text{-}DMF}$ = 36.5 kD. $Đ$ = 1.26. ^{1}H NMR (400 MHz, $CDCl_3$) δ 8.05 – 7.89 (br), 7.86 – 7.71 (br), 7.69 – 7.40 (m), 7.38 – 7.29 (br), 7.02 – 6.97 (m), 4.21 – 2.64 (m), 1.67 – 0.80 (m). ^{31}P NMR (162 MHz, $CDCl_3$) δ -5.79 (triphenylphosphine peak, major), 29.24 (triphenylphosphine oxide peak, minor).

Reduction of Pd(II) to Pd(0)

The concentration of polymer and Pd(II) before reduction: 100 mg of TPP functionalised amphiphilic polymer was mixed with 6 mg of $PdCODCl_2$ solution under an argon atmosphere in dry chloroform under dilute conditions as described in Chapter 2 (Complexation of TPP polymers in the experimental section). After complete drying of the polymer under vacuum overnight, they were formulated into nanoparticles by sonication for 30 min to form **P1-P4@Pd(II)**.

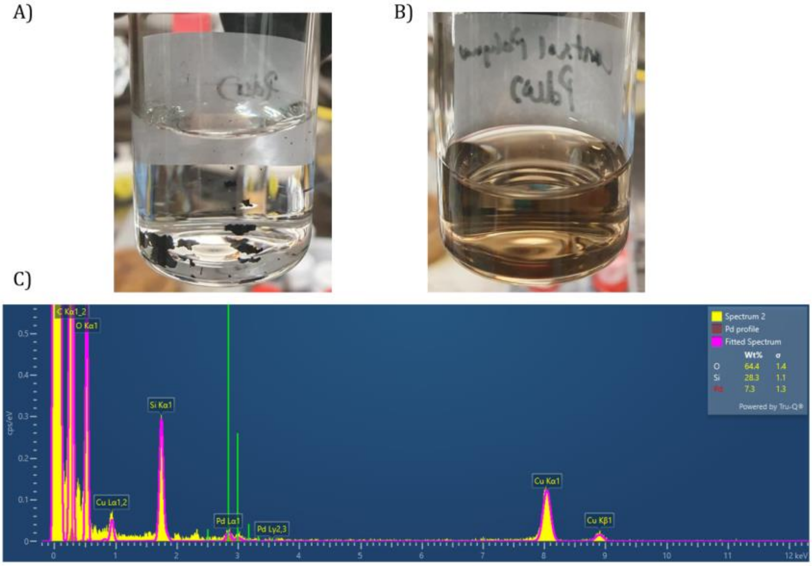

Figure 15: A) Images of solution of Pd(0) NPs reduced A) from $\mathbf{PdCODCl_2}$ ([Pd(II)] = 210 μM in H_2O, 0.2% DMSO v/v), B) **P4@Pd(II)** ([Pd(II)] = 210 μM, [**P**] = 1 mg/mL in H_2O, both after 1 month. C) Elemental mapping using Energy Dispersive X-Ray Spectroscopy measurements on a mapped area of STEM-HAADF showing Pd wt% in the area of the sample **P1@Pd(0)** measured, Pd wt% = 7.3%.

Reduction of Pd(II) to Pd(0) was performed at 1 mg/mL concentration of polymers with a corresponding concentration of Pd(II) = 210 μM. A sample volume of 10 mL was used for reduction every time. Samples were reduced at the University of Zaragoza, Spain and the samples sent back after reduction were immediately kept in a glove box under a nitrogen atmosphere. Samples when kept under atmospheric conditions were found to have decreased reactivity overtime.

General procedure for reactions in water :

Heck coupling reaction: Substrate stock solution (**1**) was prepared in DMSO at 30 mM concentration. P1@Pd(0) and Pd(0) stock solutions were at 210 µM concentration. Depending on each experiment, all stock solutions were diluted in 3 mL water in 10 mm fluorescence cuvette to a reach final concentration of Pd(0) = 30 µM; [**1**] = 30 µM. Cuvettes were then transferred to fluorescence spectrophotometer at 37 °C with stirring and the reaction progress was monitored in real-time. Aliquots from the sample were taken at specified intervals and diluted with 50% ACN by volume which was then analysed using HPLC-UV.

Suzuki-Miyaura coupling reaction: Substrate stock solution **3** was prepared in DMSO at 100 mM concentration, **4** at 50 mM concentration, K_2CO_3 at 200 mM concentration. **P1@Pd(0)** and Pd(0) stock solutions were at 210 µM concentration. Depending on each experiment, all stock solutions were diluted in 3 mL water into a glass vial to a reach a final concentration of Pd(0) = 50 µM; [**3**] = 100 µM; [**4**] = 50 µM ;[K_2CO_3] = 30 mM in water. The glass vial was then transferred to an oil bath at 37 °C with stirring and the reaction progress was monitored over time using HPLC-UV and MS. Aliquots from the sample were taken at specified intervals and diluted with 50% ACN by volume which was then analysed using HPLC-UV.

Depropargylation reaction: Substrate stock solution (**7**) was prepared in DMSO at 30 mM concentration. **P1@Pd(0)** and Pd(0) stock solutions were at 210 µM concentration. Depending on each experiment, all stock solutions were diluted in 3 mL water in 10 mm fluorescence cuvette to a reach a final concentration of Pd(0) = 30 µM; [**7**] = 30 µM. Cuvettes were then transferred to fluorescence spectrophotometer at 37 °C with stirring and the reaction progress was monitored in real-time. Aliquots from the sample were taken at specified intervals and diluted with 50% ACN by volume which was then analysed using HPLC-UV.

General procedure for reactions in complex media:

Pro-rho **7** activation in different media: Substrate stock solution (**7**) was prepared in DMSO at 30 mM concentration. **P1 @Pd(0)** stock solutions was at 210 µM concentration. Depending on each experiment, all stock solutions were diluted in 3 mL water, PBS, DMEM or PBS supplemented with 10% FBS serum, in 10 mm fluorescence cuvette to a reach a final concentration of Pd(0) = 30 µM; [**7**] = 30 µM. Cuvettes were then transferred to fluorescence spectrophotometer at 37 °C with stirring and the reaction progress was monitored in real-time. Aliquots from the sample were taken at specified intervals and diluted with 50% ACN by volume which was then analysed using HPLC-UV.

Depropargylation reaction in DMEM of all polymeric nanoparticles: Substrate stock solution (**7**) was prepared in DMSO at 30 mM concentration. **P1-P4@Pd(0)** and Pd(0) stock solutions were at 210 µM concentration. P1@Pd(II) was also prepared at same concentration. Depending on each experiment, all stock solutions were diluted in 3 mL DMEM in 10 mm fluorescence to a reach a final concentration of Pd(0) = 30 µM; [**7**] = 30 µM. Cuvettes were then transferred to

Fluorescence spectrophotometer at 37 °C with stirring and the reaction progress was monitored in real-time. Aliquots from the sample were taken at specified intervals and diluted with 50% ACN by volume which was then analysed using HPLC-UV.

Pro-5FU activation in water: same procedure as for pro-dye but was performed in glass vial and reaction monitored using HPLC-MS, at specified concentration of substrate and Pd(0) in water.

Cell experiments

Assessment of cell viability: HepG2 cells were cultured and seeded in Dulbecco's modified Eagle's medium (DMEM) supplemented with 10% fetal bovine serum (FBS) and phenol red. Cytotoxicity of P1-P4@Pd(0) was studied using the cell counting kit-8 (CCK-8) assay. A 96-well plate was used seed HepG2 cells. Wells were filled with 100 μL of cell suspension containing 8000 cells. The plate was then placed in an oven at 37 °C with 5% CO_2 flow for 24 h. Then, the P1-P4@Pd(0) to be tested was added to the cells by varying Pd(0) from 20 – 100 μM. The amount of stock solution volume to be added was first removed from the well to keep concentrations constant. Followingly, the plate was placed in the oven. After 24 h, the medium was removed and 100 μL DMEM with 10% CCK8 were added to each well. The plate was then placed back in the oven at 37 °C for 2 to 4 h. The absorbance of each well containing cells was measured at 450 nm at the microplate reader. Cell viability was determined as a fold change of the absorbance with respect to untreated cells. Error bars represent the standard deviation of 3 different wells incubated with same sample.

Procedure for pro-rhodamine activation in HepG2 cells: Cultured HepG2 cells were seeded in a μ-Slide 18 well from Ibidi. Wells were filled with 100 μL of cell suspension containing 8000 cells. Cells were incubated with **P1-P4@Pd(0)** and **7** for the incubation time as mentioned from the corresponding stock solutions. Later, the μ-Slide was placed back in the oven. The cells were then monitored in a confocal microscope at an excitation wavelength of 485 nm. For the control experiment, only pro-rho **7** was incubated.

Procedure for pro-drug activation in HepG2 cells: The procedure was followed as explained above for pro-5FU as substrate. New set of reduced Pd(0) samples **P1-P4@Pd(0)*** was used for experiments. After the indicated reaction times the compound containing medium was removed and 100 μL DMEM with 10% CCK-8 was added to each well. The plate was then placed back in the oven at 37 °C for 2 to 4 h. The absorbance of each well containing the cells was measured at 450 nm at the microplate reader. Cell viability was determined as explained before.

3.11 References

(1) Miller, M. A.; Mikula, H.; Luthria, G.; Li, R.; Kronister, S.; Prytyskach, M.; Kohler, R. H.; Mitchison, T.; Weissleder, R. Modular Nanoparticulate Prodrug Design Enables Efficient Treatment of Solid Tumors Using Bioorthogonal Activation. *ACS Nano* **2018**, 12 (12), 12814–12826. https://doi.org/10.1021/ACSNANO.8B07954/SUPPL_FILE/NN8B07954_SI_002.PDF.

(2) Adam, C.; Bray, T. L.; Pérez-López, A. M.; Tan, E. H.; Rubio-Ruiz, B.; Baillache, D. J.; Houston, D. R.; Salji, M. J.; Leung, H. Y.; Unciti-Broceta, A. A 5-FU Precursor Designed to Evade Anabolic and Catabolic Drug Pathways and Activated by Pd Chemistry in Vitro and *in vivo. J Med Chem* **2022**, 65 (1), 552–561. https://doi.org/10.1021/ACS.JMEDCHEM.1C01733/SUPPL_FILE/JM1C01733_SI_005.PDB.

(3) Miller, M. A.; Askevold, B.; Mikula, H.; Kohler, R. H.; Pirovich, D.; Weissleder, R. Nano-Palladium Is a Cellular Catalyst for *in vivo* Chemistry. *Nat Commun* **2017**, 8 (1), 1–13. https://doi.org/10.1038/ncomms15906.

(4) Ortega-Liebana, M. C.; Porter, N. J.; Adam, C.; Valero, T.; Hamilton, L.; Sieger, D.; Becker, C. G.; Unciti-Broceta, A. Truly-Biocompatible Gold Catalysis Enables Vivo-Orthogonal Intra-CNS Release of Anxiolytics. *Angewandte Chemie International Edition* **2022**, 61 (1), e202111461. https://doi.org/10.1002/ANIE.202111461.

(5) Weiss, J. T.; Fraser, C.; Rubio-Ruiz, B.; Myers, S. H.; Crispin, R.; Dawson, J. C.; Brunton, V. G.; Patton, E. E.; Carragher, N. O.; Unciti-Broceta, A. N-Alkynyl Derivatives of 5-Fluorouracil: Susceptibility to Palladium-Mediated Dealkylation and Toxigenicity in Cancer Cell Culture. *Front Chem* **2014**, 2 (JUL). https://doi.org/10.3389/fchem.2014.00056.

(6) Du, Z.; Qu, X. Exosomes for Cell-Targeted Bioorthogonal Catalysis. *Nature Catalysis* **2019** 2:10 2019, 2 (10), 837–838. https://doi.org/10.1038/s41929-019-0350-3.

(7) Li, J.; Yu, J.; Zhao, J.; Wang, J.; Zheng, S.; Lin, S.; Chen, L.; Yang, M.; Jia, S.; Zhang, X.; Chen, P. R. Palladium-Triggered Deprotection Chemistry for Protein Activation in Living Cells. *Nat Chem* **2014**, 6 (4), 352–361. https://doi.org/10.1038/nchem.1887.

(8) Uk Son, S.; Jang, Y.; Youl Yoon, K.; Kang, E.; Hyeon, T. Facile Synthesis of Various Phosphine-Stabilized Monodisperse Palladium Nanoparticles through the Understanding of Coordination Chemistry of the Nanoparticles. *Nano Letters* **2004**, 4, 6, 1147-1151 https://doi.org/10.1021/nl049519+.

(9) Pérez-López, A. M.; Belsom, A.; Fiedler, L.; Xin, X.; Rappsilber, J. Dual-Bioorthogonal Catalysis by a Palladium Peptide Complex. *J Med Chem* **2022**, 66, 16. https://doi.org/10.1021/ACS.JMEDCHEM.2C01689/ASSET/IMAGES/LARGE/JM2C01689_0005.JPEG.

(10) Clavadetscher, J.; Indrigo, E.; Chankeshwara, S. V.; Lilienkampf, A.; Bradley, M. In-Cell Dual Drug Synthesis by Cancer-Targeting Palladium Catalysts. *Angewandte Chemie International Edition* **2017**, 56 (24), 6864–6868. https://doi.org/10.1002/ANIE.201702404.

(11) Sebastian, V.; Smith, C. D.; Jensen, K. F. Shape-Controlled Continuous Synthesis of Metal Nanostructures. Nanoscale **2016**, 8 (14), 7534–7543. https://doi.org/10.1039/C5NR08531D.

(12) Herrer, L.; Sebastian, V.; Martín, S.; González-Orive, A.; Pérez-Murano, F.; Low, P. J.; Serrano, J. L.; Santamaría, J.; Cea, P. High Surface Coverage of a Self-Assembled Monolayer by *in situ* Synthesis of Palladium Nanodeposits. *Nanoscale* **2017**, 9 (35), 13281–13290. https://doi.org/10.1039/C7NR03365F.

(13) Sancho-Albero, M.; Rubio-Ruiz, B.; Pérez-López, A. M.; Sebastián, V.; Martín-Duque, P.; Arruebo, M.; Santamaría, J.; Unciti-Broceta, A. Cancer-Derived Exosomes Loaded with Ultrathin Palladium Nanosheets for Targeted Bioorthogonal Catalysis. *Nature Catalysis* **2019**, 2 (10), 864–872. https://doi.org/10.1038/s41929-019-0333-4.

(14) Pérez-López, A. M.; Rubio-Ruiz, B.; Valero, T.; Contreras-Montoya, R.; Álvarez De Cienfuegos, L.; Sebastián, V.; Santamaría, J.; Unciti-Broceta, A. Bioorthogonal Uncaging of Cytotoxic Paclitaxel through Pd Nanosheet-Hydrogel Frameworks. *J Med Chem* **2020**, 63 (17), 9650–9659. https://doi.org/10.1021/acs.jmedchem.0c00781.

(15) Deng, L.; Albertazzi, L.; Palmans, A. R. A. Elucidating the Stability of Single-Chain Polymeric Nanoparticles in Biological Media and Living Cells. *Biomacromolecules* **2022**, 23 (1), 326–338. https://doi.org/10.1021/acs.biomac.1c01291.

(16) Otten, M. T. High-Angle Annular Dark-Field Imaging on a Tem/Stem System. *J Electron Microsc Tech* **1991**, 17 (2), 221–230. https://doi.org/10.1002/JEMT.1060170209.

(17) Christoffel, F.; Ward, T. R. Palladium-Catalyzed Heck Cross-Coupling Reactions in Water: A Comprehensive Review. *Catalysis Letters* **2017**, 148 (2), 489–511. https://doi.org/10.1007/S10562-017-2285-0.

(18) Liu, Y.; Pujals, S.; Stals, P. J. M.; Paulöhrl, T.; Presolski, S. I.; Meijer, E. W.; Albertazzi, L.; Palmans, A. R. A. Catalytically Active Single-Chain Polymeric Nanoparticles: Exploring Their Functions in Complex Biological Media. *J Am Chem Soc* **2018**, 140 (9), 3423–3433.

(19) Shang, L.; Nienhaus, K.; Nienhaus, G. U. Engineered Nanoparticles Interacting with Cells: Size Matters. *J Nanobiotechnology* **2014**, 12 (1), 1–11. https://doi.org/10.1186/1477-3155-12-5/FIGURES/1.

Chapter 4

Exporting Rh-catalysed NH carbene insertion reactions to living cells

---

Abstract: Rh-catalysed NH carbene insertion reactions were exported to living cells with the help of amphiphilic polymeric nanoparticles. Hereto, hydrophobic dirhodium carboxylate catalysts were efficiently encapsulated in amphiphilic polymeric nanoparticles comprising dodecyl and Jeffamine M-1000 as side grafts. The developed catalytic nanoparticles promoted NH carbene insertions between alpha-keto diazocarbenes and 2,3-diaminonapthalene, followed by intramolecular cyclisation to form fluorescent or biologically active benzoquinoxalines. These reactions were studied in different reaction mediums of varying complexity. The best performing catalyst was exported to HeLa cells, where photophysically and biologically active products were synthesized *in situ* at low catalyst loading within a short time. Most of the developed bioorthogonal transition metal catalysts reported to date are easily deactivated by the reactive biomolecules in living cells, limiting their applications. The high catalytic efficiency of the Rh-based polymeric nanoparticles reported here opens the door to expanding the repertoire of bioorthogonal reactions and is therefore promising for biomedical applications.

This work has been performed in close collaboration with Tessa Loman (synthesis and catalysis) and Linlin Deng (cell studies).

4.1 Introduction

Performing bioorthogonal, new-to-nature reactions in the presence of living cells is an approach towards *in situ* synthesis of bio-active agents that can help develop innovative therapies in future.[1] Many heterogeneous and homogeneous bioorthogonal catalysts were developed in the past decade, incorporating the transition metal catalysts (TMCs) in synthetic or natural scaffolds enabling them to remain in a biological environment and perform reactions.[2–11] However, the term 'catalysis' is often misused over these years while developing chemistries that work in living cells. Often stochiometric amounts of TMCs or even more are required to synthesize bioactive agents in living cells or to activate pro-drugs.[7,9,12–14] There are only very few examples where real catalytic amounts of TMCs were reported to induce a biological activity *in vitro*.[2,11,15,16] Also, so far the focus was mainly on coupling and cleavage reactions catalysed by commonly used TMCs such as Pd, Cu, Ru and Au in biological milieu.[2,6,15,17–19] In order to push the boundaries of the field for meaningful applications, it is of utmost importance to expand the bioorthogonal toolbox both in terms of developing new and efficient catalysts and thereby new bioorthogonal reactions.

In this regard, metal carbenes are an interesting class of molecules that can possibly generate novel bioorthogonal reactions, however, less explored in mammalian cell environments.[20–22] Metal carbenes are formed from diazo compounds and TMCs under mild conditions by the release of nitrogen gas, making it possible to translate to water or complex media. Also, diazo compounds have been known to endure cell metabolism and were utilized for bioorthogonal reactions in cellulo.[23,24] Recently, Mascareñas and co-workers exported Cu-catalysed NH carbene insertions to generate bioactive agents *in situ* in HeLa cells.[25] Even though copper-catalysed reactions are important from a proof-of-concept point of view when it comes to biomedical applications copper catalysts will be a no-go due to their potential toxicity.[26] Other less toxic and exogenous metals such as iron, ruthenium, iridium and rhodium also can catalyse NH insertion reactions. [27–32]

From an exploratory point of view, rhodium catalysts will be an excellent choice for NH carbene insertion reactions in the biological milieu, especially as they have inherently low toxicity and high stability, where both can be tuned by proper ligand choice.[33] Rhodium catalysts have already been explored to study biological systems exploiting carbene chemistry. Francis and co-workers showed that Rh(II)acetate can catalyse NH insertions to modify tryptophan residues while Gillingham and co-workers showed that it is possible to modify nucleic acids in the same way.[34–36] Moreover, these rhodium catalysts have proven to be very reactive towards a wide range of synthetic transformations such as cyclopropanation, C-H and X-H insertion, aromatic substitution and ylide formation reactions.[37] Many hydrophobic chiral dirhodium carboxylate catalysts were developed in an effort to develop enantioselective and diastereoselective reactions, but with limited success.[38–41] As they are highly stable and active, they can be utilized for bioorthogonal reactions, especially for carbene NH insertion reactions if they can be solubilized in an aqueous environment.[33] This can be executed with the help of amphiphilic polymeric nanoparticles, which can sequestrate highly hydrophobic catalysts in their hydrophobic domain in aqueous solutions. [16]

In this chapter, we investigated the possibility of using Rh carbene chemistry in living cells for the *in situ* synthesis of imaging or bioactive agents with the help of nanomaterial scaffolds, namely single-chain polymeric nanoparticles and micelles. Towards this, hydrophobic dirhodium(II) carboxylate catalysts were encapsulated in amphiphilic polymeric nanoparticles. After selection of the most active catalyst, we performed the annulation of alpha-keto diazocarbenes with 2,3-diaminonapthalene to form benzoquinoxaline products, a catalytic reaction initiated by an N-H carbene insertion by Rh catalysts in the presence of cells. The results showed that quinoxalines readily formed using catalytic amounts of Rh embedded in amphiphilic polymeric nanoparticles or micelles in aqueous solutions of varying complexity and most importantly, in the presence of HeLa cells.

4.2 Development of Rh-based polymeric nanoparticles for carbene insertion reactions in water

Exporting reactions to living cells is a step by step process, which requires careful optimization of catalytic system. For this, the best performing hydrophobic catalysts need to be selected and encapsulated in polymeric nanoparticles. Further, the encapsulation efficiency of nanoparticles has to be determined. The substrate selection also should be done in such a way that product formation can be monitored at micromolar level concentrations, as it is necessary to investigate the efficiency of catalysts before the system can be exported to biological environments.

4.2.1 Dirhodium(II) carboxylates as catalysts for NH carbene insertion reactions

Dirhodium(II) carboxylates are an important class of rhodium catalysts, constituting a paddle wheel like structure formed by the bridging carboxylate ligands and a unique di-rhodium bridge that offers exceptional stability to these catalysts.[42] Notably, they have two vacant axial positions that allows substrate binding for carbene formation in this case.[42,43] The utilisation of $Rh_2(OAC)_4$ in the Merck synthesis of the antibiotic thienamycin via intramolecular N-H insertion of a diazoacetoacetate early in 1980 itself exemplifies the benefits of these complexes for metal carbene transformations.[44] However, the hydrophobicity of the catalysts is an important factor to consider when they have to be efficiently encapsulated inside amphiphilic polymeric nanoparticles. Therefore, we chose three highly hydrophobic dirhodium carboxylate catalysts, **C1-C3**, with Log P values > 10 (Figure 1).

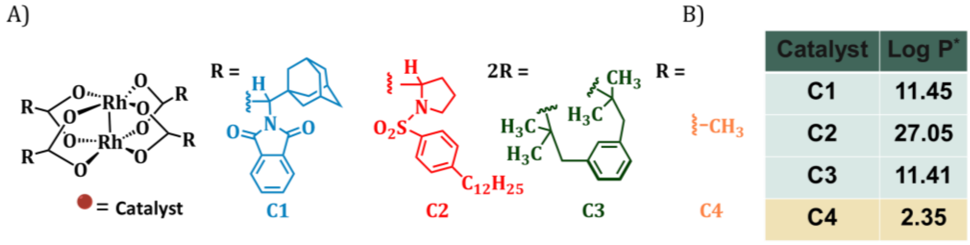

Catalyst	Log P*
C1	11.45
C2	27.05
C3	11.41
C4	2.35

Figure 1: A) Chemical structures of dirhodium(II) carboxylates-based catalysts, B) Log P values of the catalysts calculated using MarvinSketch 22.16.

$Rh_2(OAC)_4$, **C4**, has low hydrophobicity and was used as a reference. It helps to compare the performance of catalytic nanoparticles with dirhodium catalyst **C4** that can be homogeneously dissolved in aqueous solution at very low concentrations (Figure 1). Even though **C1-C2** are well studied chiral catalysts, we are only interested in their hydrophobicity, stability and reactivity.

4.2.2 Encapsulation of dirhodium(II) carboxylate catalysts in amphiphilic polymeric nanoparticles

The selected dirhodium carboxylate catalysts **C1-C4** were encapsulated in the hydrophobic pocket of a polyacrylamide based amphiphilic polymer **P1** (Figure 2A,B), which contained pendant groups of 20% dodecyl for hydrophobicity and 80% Jeffamine M-1000 for hydrophilicity (DP = 100). Encapsulation of the catalysts was performed using a modification of a previously reported protocol as described in experimental section.[45]

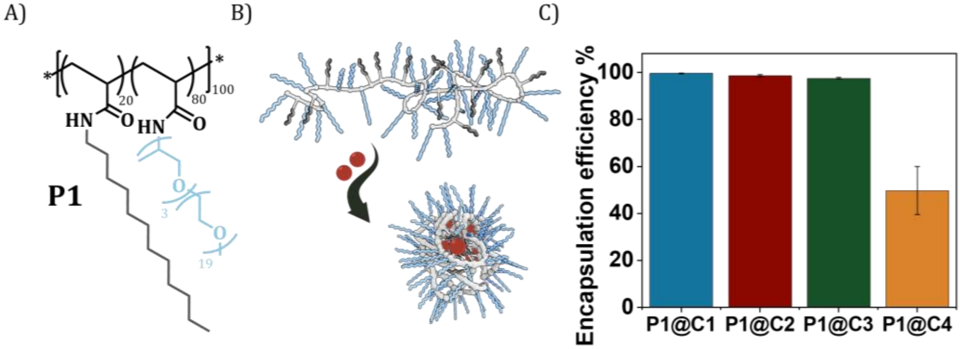

Figure 2: A) Chemical structure amphiphilic random copolymer **P1**; B) Representation of the encapsulation of catalysts (red spheres) **C1-C4** in the hydrophobic pocket of polymeric nanoparticles; C) Encapsulation efficiency of the dirhodium carboxylate catalysts **C1-C4** in polymeric nanoparticles calculated from the leached out rhodium using ICP-OES. [**P1**] = 1 mg/mL, **P1:C** = 1:5 (molar ratio), [Rh] = 10 mg/L before filtration. The results for the encapsulation efficiency are the average of three independent measurements.

In order to check the efficiency of **P1** to encapsulate the catalysts, the amount of rhodium leached out from the hydrophobic pocket was monitored using ICP-OES (Inductively Coupled Plasma Optical Emission Spectroscopy). The solution of **P1@C1-C4** in water (10 mg/L rhodium) were filtered using centrifugal filters with a molecular weight cutoff of 50 kD, to ensure separation of polymeric nanoparticles (MW_{cal} ~ 98 kD) from the aqueous solution. Therefore, any leached out Rh catalysts (*MW* = 400-1800 g/mol) will remain in the filtered solution and the Rh concentration can be monitored using ICP-OES. In case of 100% leaching, the Rh concentration in the filtered solution should be 10 mg/L rhodium. ICP-OES measurements revealed that for hydrophobic catalysts **C1-C3**, only 0.03 – 0.2 mg/L rhodium leached out while in case of hydrophilic catalyst **C4** it was 5 mg/L. This clearly indicated that the hydrophobic catalysts **C1-C3** were encapsulated with 97-99% efficiency in the hydrophobic pocket of **P1** in contrast to hydrophilic catalyst **C4** (50% efficiency) as hypothesized (Figure 2C).

4.2.3 Optimization of catalyst incorporation ratio

Catalyst **C1** was encapsulated in **P1** to form polymeric nanoparticles ([**P**] = 1 mg/mL) with incorporation ratio (molar) of 1:1, 1:5, 1:10 (**P1:C1**) and was compared with **P1**. The size distribution of the nanoparticles was monitored by dynamic light scattering (DLS) measurements (Figure 3). **P1@C1** with 1:1 ratio formed nanoparticles with hydrodynamic radius of 7 nm (R_H), similar to the one found for pure **P1**. Upon increasing the incorporation ratio to 1:5 and 1:10, R_H slightly increased to 10 and 12 nm, respectively (Figure 3A).

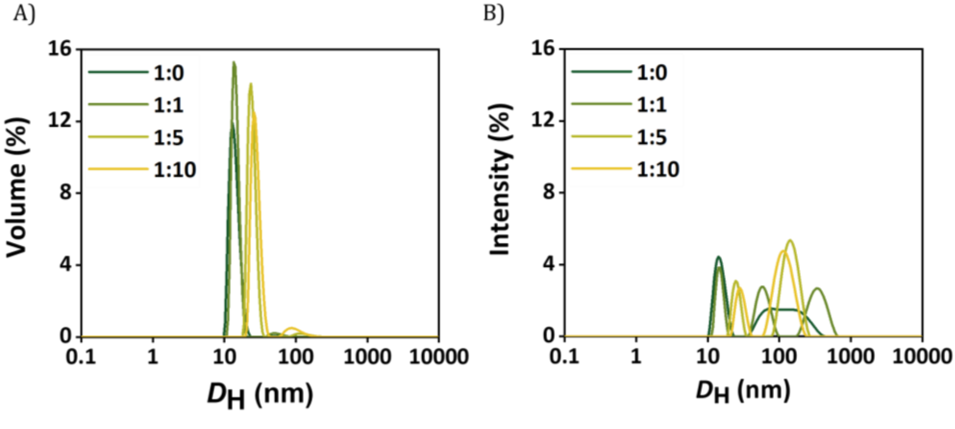

Figure 3: A) Volume distribution of the hydrodynamic diameter D_H of **P1@C1** nanoparticles at various catalyst incorporation ratios; B) Intensity distribution of the hydrodynamic diameter D_H of **P1@C1** nanoparticles at various catalyst incorporation ratios ([P] = 1.0 mg/mL, T = 20 °C) monitored by DLS measurements.

The intensity plot of the DLS measurements revealed that all particles, regardless of catalyst incorporation, have some amount of aggregates, but aggregation increases with higher catalyst incorporation (Figure 3B). From these results, the optimum incorporation was selected to be 1:5 (**P1:C**) to minimize the aggregation as well as to have higher probability of having catalysts inside the nanoparticles compared to the 1:1 **P**:**C** ratio. Due to the presence of aggregates, we refer to the formed particles as amphiphilic polymeric nanoparticles rather than single-chain polymeric nanoparticles.

4.3 Rh-catalysed NH insertions – towards the synthesis of bioactive agents

Substrates for the NH insertion reactions were selected as reported earlier by Mascareñas and co-workers as shown in Figure 4.[25] The diazo substrates **2a-c** was synthesized according to previously reported protocol.[25] The reaction of 2,3-diaminonapthalene **1** with various diazo substrates **2a-c** affords benzoquinoxalines **3a-c**, by a process initiated by NH insertion reaction followed by intramolecular imine condensation and oxidative aromatization (Figure 4B).[46] The products formed are fluorescent (**3a**) or biologically relevant (**3c**). Fluorescent benzoquinoxaline **3a** allows visualisation of product formation in living cells while **3c** induces cytotoxic effects by promoting mitochondrial fragmentation and depolarization.[47] The *in situ* reactions kinetics can also be monitored using fluorescence spectroscopy over time given that both 2,3-diaminonapthalene **1** and benzoquinoxaline products are fluorescent at different excitation wavelengths. An important factor to consider here is that the hydrophobicity of the products is higher than the substrates, which can lead to product aggregation or crystallization after the reaction in aqueous solutions. Therefore, accurate conversions can only be determined by using HPLC-UV/MS by taking aliquots of reaction mixture and dissolving these in acetonitrile (50% v/v). Before exporting the reactions to living cells, the efficiency will be determined by performing reactions in media of increasing complexity, *i.e* water, phosphate buffered saline solution (PBS), and the cell culture medium DMEM (Dulbecco Dulbecco's Modified Eagle Medium).

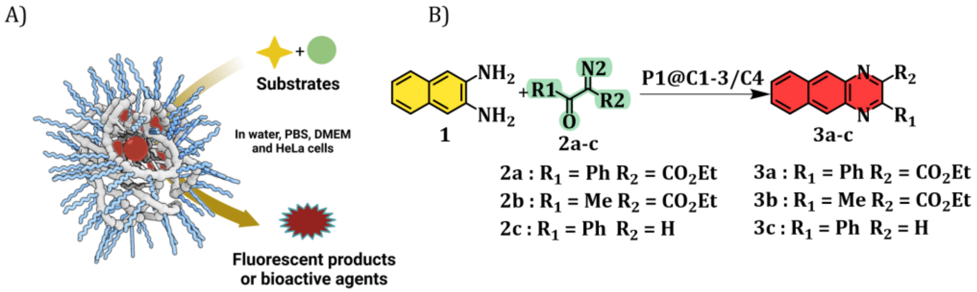

Figure 4: A) Representation of reaction involving two substrates using catalytic polymeric nanoparticles, B) Formation of benzoquinoxalines **3a-c** initiated by NH insertion followed by intramolecular cyclisation.

4.4 Rh-based polymeric nanoparticles – screening catalysts

Dirhodium carboxylates catalysts encapsulated in amphiphilic polymeric nanoparticles **P1@C1-C3** were tested for their efficiency to catalyse the NH insertion reactions. We select 2,3-diaminonaphthalene **1** and diazo substrate **2a** as substrates as the fluorescent benzoquinoxaline **3a** is formed, and follow the reaction in water, PBS and DMEM (increasing medium complexity). For comparison, hydrophilic catalyst **C4** was used by directly dissolving in water. Reactions were performed at 500 µM concentration of substrates **1** and **2a**, and 10 mol% of catalyst in the appropriate medium at physiological temperature 37 °C. The polymer to catalyst molar ratio was fixed at 1:5 and the concentration of polymer in the reaction mixture was ~ 1 mg/mL.

Aliquots from the reaction mixtures were taken and diluted with acetonitrile, followed by analysis with HPLC-UV (H_20/ACN + 0.1 % formic acid) after 24 h to quantify the conversion of reactants to products. The HPLC method was optimized using pure substrates and products, which were injected separately as described in experimental section. 2,3-Diaminonaphthalene **1** get protonated due to the presence of formic acid present in eluent, as a result it could not be retained in column. Substrate **2a** and product **3a** were easily separated, which helped to monitor the reaction progress. The consumption of 2,3-diaminonaphthalene **1** in the reaction was monitored using fluorescence spectroscopy over time, which also gave insight into *in situ* reaction kinetics.

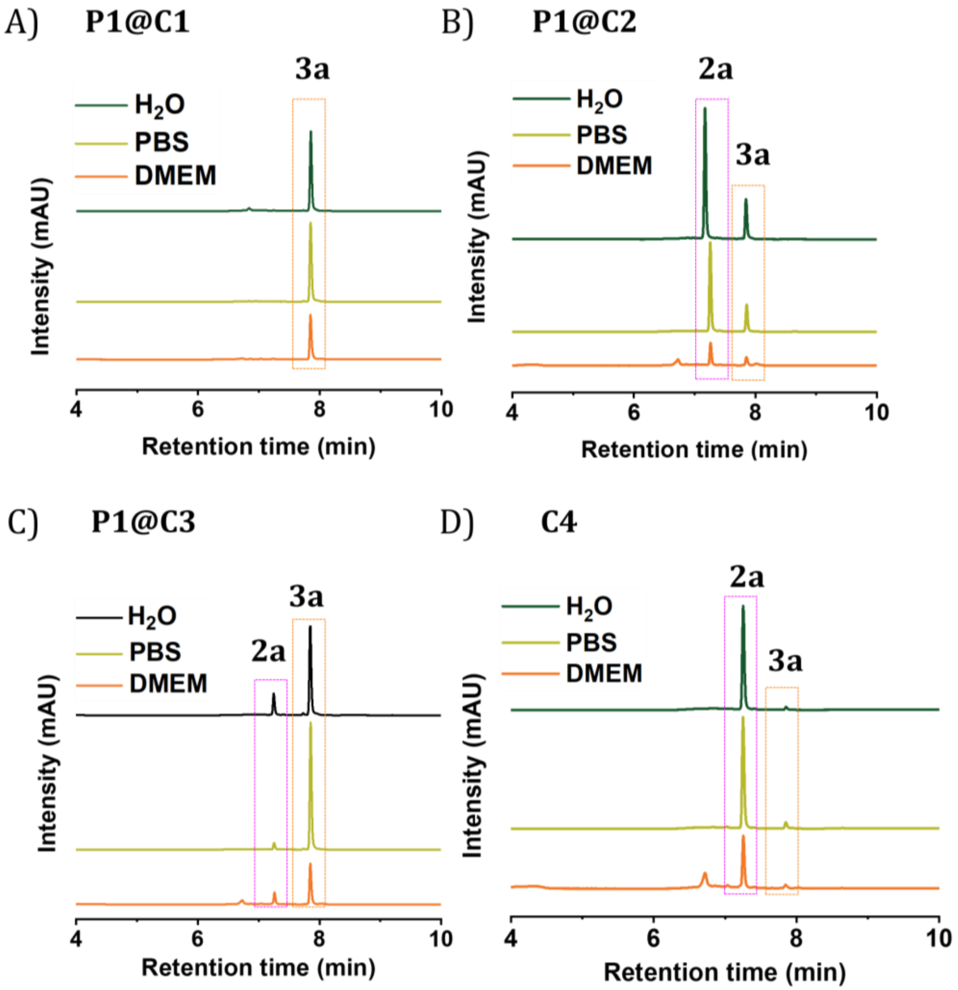

Figure 5: HPLC-UV chromatogram of the reaction progress of **1** and **2a** after 24 h. The reaction was catalysed by A) **P1@C1**; B) **P1@C2**; C) **P1@C3**; D) **C4**. The reaction was monitored at 279 nm. Reaction conditions: [**1**] = [**2a**] = 500 μM, [**C**] = 50 μM, [**P**] = 1 mg/mL, **P1**:**C1-C3** = 1:5, at 37 °C in water, PBS or DMEM medium.

The HPLC-UV chromatogram of the reaction mixture after 24 h indicated that **P1@C1** is an efficient catalyst in water, PBS and DMEM: in all cases diazo substrate **2a** is completely consumed leading to the formation of product **3a** (Figure 5A). The consumption of 2,3-diaminonaphthalene **1** was confirmed from the decrease in the fluorescence intensity over time (Figure 6 A). **P1@C2** did not efficiently catalyse the reaction as the majority of the substrate **2a** remained in the reaction mixture with approximately 24% conversion after 24 h in water (Figure 5B). A similar activity was observed both in PBS and DMEM. **P1@C3** performed better than **P1@C2** (Figure 5B,C), with significant amount of **3a** formed (approximately 83% conversion in water). However, it was not as efficient as **P1@C1** as full consumption of diazo substrate **2a** was not observed in any medium (Figure 5A,C). With the hydrophilic catalyst **C4**, a large amount of diazo substrate **2a** remained in the catalytic mixture, and only a negligible amount of product **3a** was formed (Figure 5D). Fluorescence kinetics measurements confirmed the presence of unconsumed diamine **1** over time (Figure 6A).

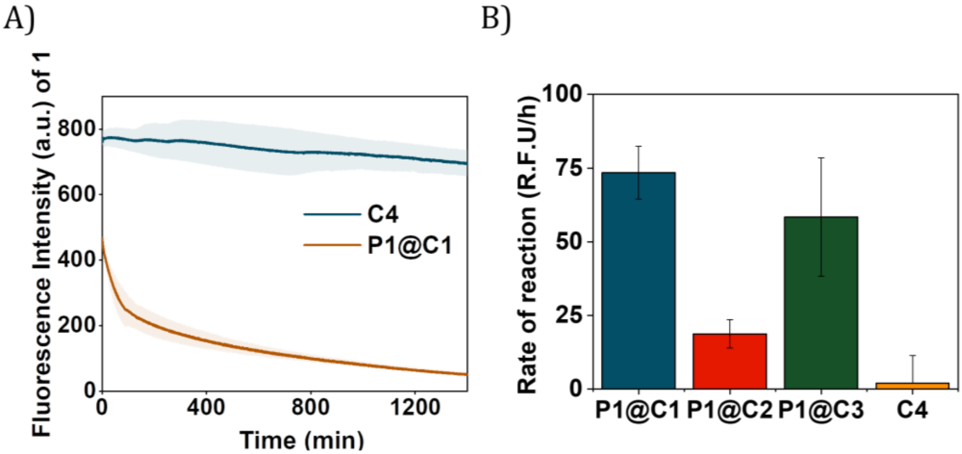

Figure 6: A) Fluorescence kinetic profile of reaction progress of **1** and **2a** catalysed by **P1@C1** and **C4** over time, wavy shadows depict the range of error in the kinetic curves. B) Comparison of the rate of the same reaction catalysed by **P1@C1**, **P1@C2**, **P1@C3** and **C4** (t_0 = 10 min and t_F = 180 min). Reaction conditions, [**1**] = [**2a**] = 500 µM, [**C**] = 50 µM, [**P**] = 1 mg/mL, **P1**:**C1-C3** = 1:5, T = 37 °C in deionised water. The results for the encapsulation efficiency are the average of three independent measurements.

The percentage conversion towards the product at different time intervals was calculated from the calibration curve of product at a wavelength of 279 nm in HPLC-UV. Unfortunately, the fluctuations in the peak area of the product due to the interference from polymeric nanoparticles made accurate quantification of catalytic efficiency difficult. Therefore, the rate of the reaction was calculated from the decrease in fluorescence intensity in the first 180 min (omitting the first 10 min to allow sample equilibration) for **P1@C1-C3** and **C4** (Figure 6B). The catalytic efficiency followed the order **P1@C1**>**P1@C3**>**P1@C2**>**C4**, the same trend as observed from product formation in the HPLC chromatograms (Figure 5 and 6B).

To get a better understanding of the role of polymeric nanoparticles in the catalytic reactions, all hydrophobic catalysts were compared by adding directly water/PBS/DMEM from stock solution in DMSO. The reactions were performed at the same conditions and concentrations as before, but now without polymeric nanoparticles. Due to the high hydrophobicity of the catalysts, the reaction mixtures were highly inhomogeneous, with catalyst and substrates sticking to the vial or magnetic stirrer. This clearly indicated that the presence of polymeric nanoparticles is important to aid catalyst and substrate solubilization. Due to inhomogeneities in the reaction mixtures, the reaction kinetics could not be followed by fluorescence spectroscopy over time. The progress of the reaction was therefore followed by HPLC-UV by taking aliquots and dissolving these in acetonitrile before analysis. From the HPLC chromatogram, we observed that the catalysts **C1** and **C3** performed worse than the corresponding encapsulated catalysts **P1@C1** and **P1@C3** (Figure 7A,C). The substrate **2a** remained without reaching full conversion to products even after 24 h in water, PBS or DMEM (Figure 7A,C). Surprisingly, **C2** performed much better than **P1@C2**, leading to significant consumption of **2a** to form product **3a** after 24 h both in PBS and DMEM (Figure 7B). This could be due to the very high hydrophobicity of the catalyst itself (Log P = 27.05) with 4 long aliphatic C_{12} chains present in the catalyst **C2**, resulting in their aggregation in water creating hydrophobic pockets for the reaction to proceed.

The reason that the **C2** catalyst performed poorly when encapsulated in polymeric nanoparticles could be due to the increase in overall hydrophobicity from dodecyl groups from amphiphilic polymers preventing the proper diffusion of substrates and products. Monitoring the reactions by complete dissolution of the reaction mixture with acetonitrile instead of just aliquots, showed slight differences in the peak areas (Figure 7D), highlighting that taking aliquots is not representative of the entire reaction mixture due to the inhomogeneities. To conclude, **P1@C1** formed the most efficient catalytic nanoparticles and proved to be promising for further studies as it retained catalytic activity even in highly complex DMEM medium.

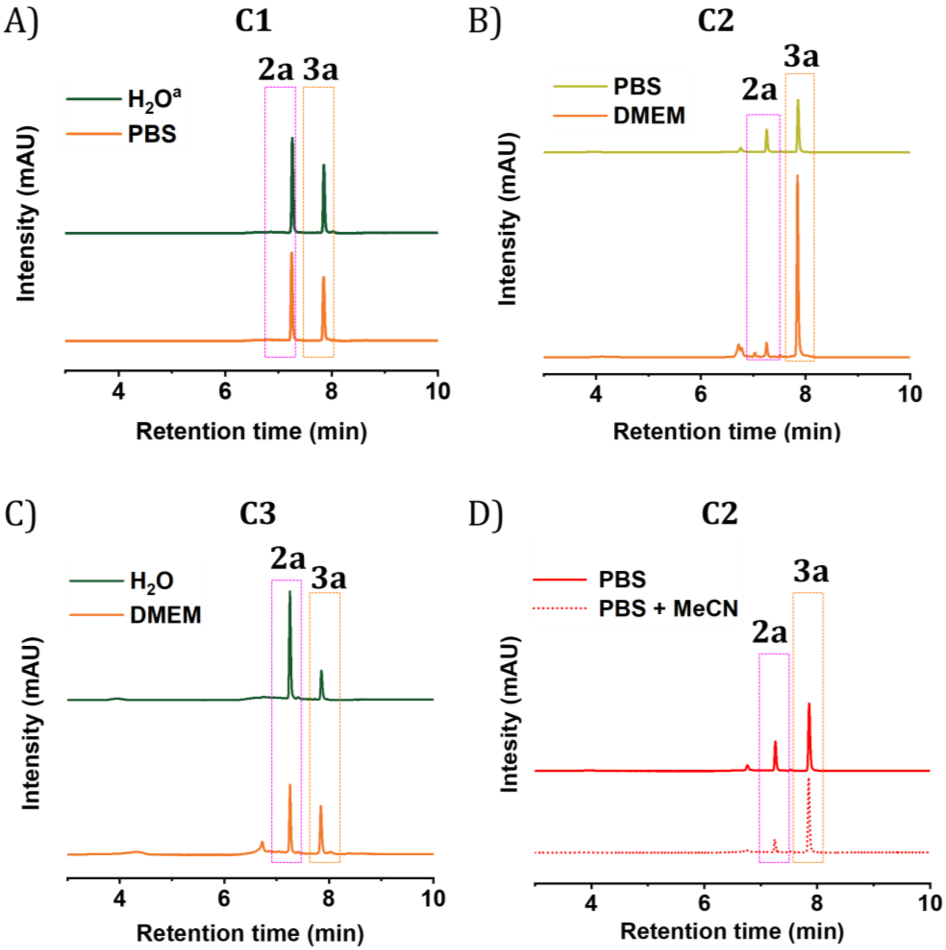

Figure 7: HPLC-UV chromatogram of reaction progress of **1** and **2a** nm after 24 h catalysed by A) **C1**; B) **C2**; C) **C3**; and D) **C2** from aliquot and after completely dissolving the reaction mixture in 50% v/v ACN, monitored at 279 nm wavelength. Reaction conditions, [**1**] = [**2a**] = 500 µM, [**C**] = 50 µM, at 37 °C in water, PBS or DMEM medium. ^{a} measured after 22 h.

4.5 The best catalyst – testing the limits of catalytic efficiency

P1@C1 was the best performing catalysts after screening, therefore its efficiency was tested by further pushing the limits of reaction conditions. Reactions of **1** and **2a** were performed in dilute conditions by lowering the concentration of substrate to 100 µM and 50 µM, while keeping the amount of catalyst constant at 10 mol% in water. In both cases, the reaction was monitored at different time intervals using HPLC-UV. Product formation was seen within 3 h, leading to almost full conversion of **2a** to **3a** within 24 h (Figure 8 A,B). Further, the reaction was also performed at 5 mol% of catalyst concentration, which also resulted in significant product formation within 6 h and reaching almost full conversion within 24 h (Figure 8C). Given that the product **3a** was formed with decreased substrate and catalyst concentrations, **P1@C1** proved promising to work under harsh conditions and in dilute concentrations similar to the environment of living cells.

The next step was to further increase the medium complexity and test the efficiency of catalyst in the presence of serum proteins. For this, the same reaction was performed in cell culture media DMEM supplemented with 10% FBS (Fetal Bovine Serum proteins) with 10 mol% catalyst at 500 µM substrate concentration. The HPLC chromatogram indicated the complete consumption of **2a** and the formation of **3a**, in addition to the peaks due to the presence of FBS. The HPLC chromatogram was compared to a control experiment were **C4** was used as catalyst, which showed no peaks for the product after 24 h (Figure 8D).

Despite numerous studies and reports on the development of bioorthogonal catalysts, most of the reported catalysts suffer deactivation from the nucleophile attack or get sequestrated by proteins present in complex biological media. This leads to the requirement of high catalyst concentration for reasonable product formation in the presence of cells. In our case, **P1@C1** showed excellent catalytic activity even in the presence of cell culture media and serum proteins at only 10 mol% catalyst concentration and the reaction proceeded to full conversion even at demanding conditions (Figure 9A). The rate of the reaction catalysed by **P1@C1** did not diminish significantly when the medium complexity was increased which is not often the case for widely used bioorthogonal catalysts (Figure 9B).

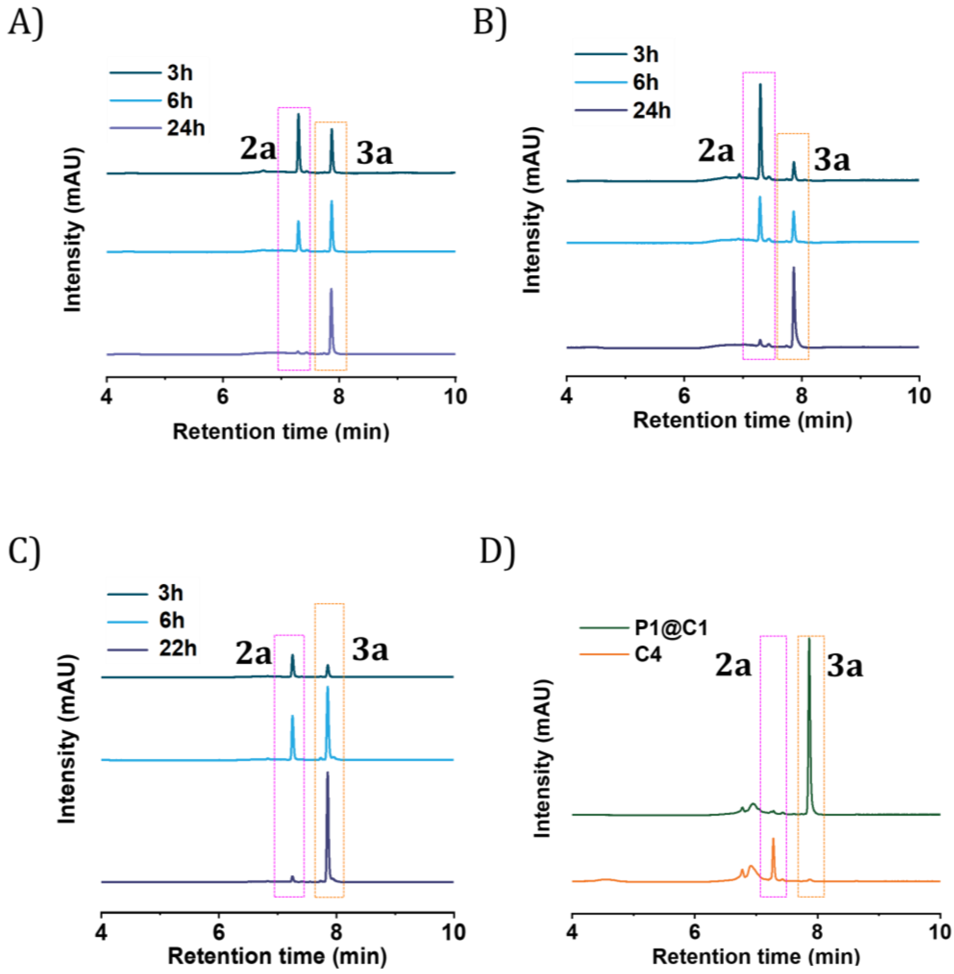

Figure 8: HPLC-UV chromatogram of the reaction progress of **1** and **2a** over time catalysed by **P1@C1**, monitored at 279 nm. A) [**1**] = [**2a**] = 100 µM, [**C1**] = 10 µM in water; B) [**1**] = [**2a**] = 50 µM, [**C1**] = 5 µM in water; C) [**1**] = [**2a**] = 500 µM in water [**C1**] = 25 µM; D) [**1**] = [**2a**] = 500 µM in water [**C1**] = 50 µM in DMEM+10%FBS. All reactions are performed at 37 °C, with [**P1**]:[**C1**] = 1:5.

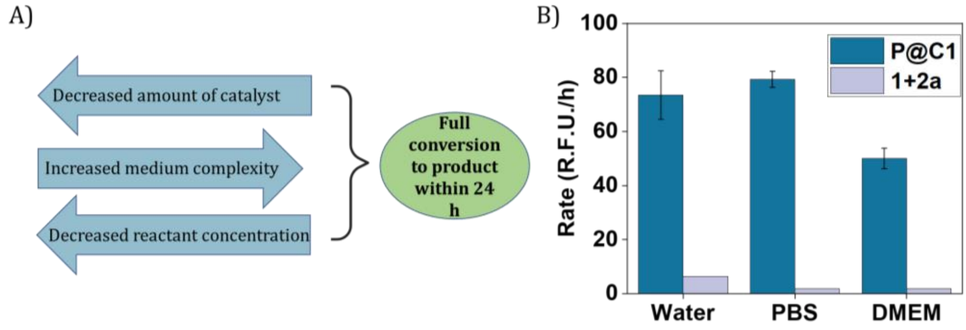

Figure 9: A) Summary of demanding reaction conditions necessary for bioorthogonal catalysis *in vitro*, where the reaction between **1**+**2a** catalysed by **P1@C1** reached full conversion to product **3a**; B) Comparison of the rate of the same reaction catalysed by **P1@C1** and uncatalysed reaction in water, PBS and DMEM (t_0 = 10 min and t_F = 180 min). Reaction conditions, [**1**] = [**2a**] = 500 µM, [**C1**] = 50 µM, [**P**] = 1 mg/mL, **P1**:**C1** = 1:5, T = 37 °C. The results for the encapsulation efficiency are the average of three independent measurements.

4.6 Substrate scope of NH insertion reaction catalysed by polymeric nanoparticles – *en route* to the synthesis of bioactive agents

Given that **P1@C1** proved to be a very efficient catalyst, we examined the substrate scope of these reactions in aqueous media and thereby investigate the possibility to synthesize bioactive molecules in the presence of living cells. We started looking at NH insertion reaction with a very hydrophilic diazo substrate **2b** (log P = -2.59) and diamine **1** (log P = 1.4) **,** which can form benzoquinoxaline **3b** (Figure 10 A). The reaction conditions were as before, 500 µM substrate with 10 mol% catalyst **C4** or **P1@C1** in water, PBS and DMEM. The reactions were monitored by HPLC-UV/MS after 24 h. The HPLC method was optimized by analysing pure substrate and product by HPLC. In PBS, **P1@C1** showed complete consumption of **2b** and formation of **3b** in 24 h (Figure 10C). In contrast, in case of **C4** the reaction did not go to completion even though a significant amount of product was formed (Figure 10B).

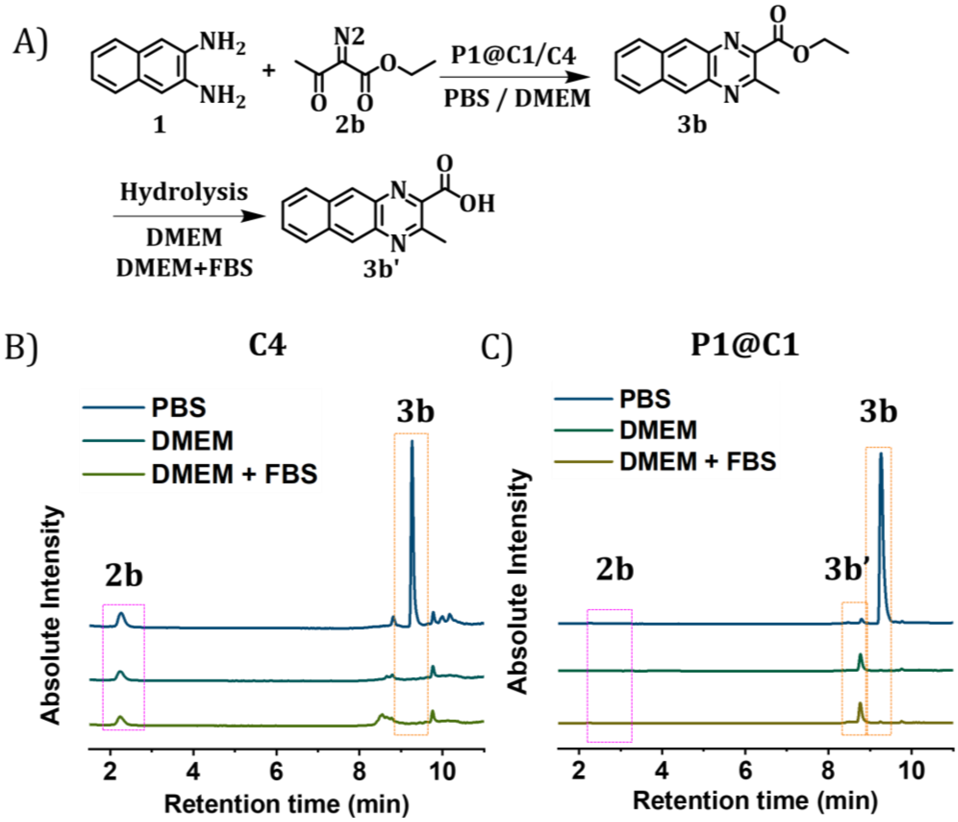

Figure 10: A) Formation of benzoquinoxaline **3b** and corresponding hydrolysed product **3b'** when **1** and **2b** was reacted with **P1@C1**, B) HPLC chromatogram of the same reaction catalysed by **C4**, C) by **P1@C1** after 24 h, monitored at 279 nm wavelength. [**1**] = [**2b**] = 500 µM in PBS, DMEM and DMEM+10% FBS, [**C1**] = 50 µM, all reactions performed at 37 °C, [**P1**]:[**C1**] = 1:5, [P] = ~ 1 mg/mL.

When increasing the medium complexity to DMEM and DMEM+FBS, **C4** did not catalyse the reaction, substrate **2b** remained in the reaction mixture and no product formation was observed (Figure 10B). Surprisingly, in case of **P1@C1**, there was complete consumption of **2b** but the major product peak **3b** was missing (Figure 10C). An additional small peak **3b'** was observed with slightly shorter retention time indicating that the formed compound is slightly hydrophilic and absorbs less at 279 nm (Figure 10C). In order to investigate this further, we utilized HPLC-MS coupled with UV for analysis of the product formed. As **3b'** was observed only in DMEM or DMEM+FBS, reaction was performed with the latter as reaction medium. Aliquots of the reaction mixture were taken at different time points to monitor the process of formation of **3b** and **3b’** overtime. From the chromatograms at different time points it is clear that product **3b** was formed with consumption of substrate **2a** within 3 h. This peak disappeared over time leading to the formation of **3b’**.(Figure 11A). It was deduced that the peak corresponded to 239, $[M+H]^+$ of **3b’** which is the hydrolysed product of **3b** (Figure 10A, 11)**.** We hypothesize that spontaneous hydrolysis of the ester may be brought forward due to the presence of charged groups or serum esterases present in complex media.[48]

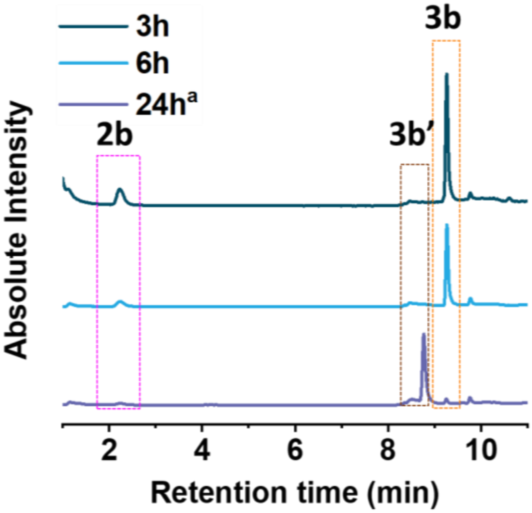

Figure 11: HPLC-MS chromatogram of the reaction between **1**+**2b** catalysed by **P1@C1** overtime [**1**] = [**2b**] = 500 µM in DMEM+10% FBS, [**C1**] = 50 µM, performed at 37 °C, [**P1**]:[**C1**] = 1:5, [P] = ~ 1 mg/mL. [a]mass of 239 added to the SIM channel.

The next substrate investigated was diazo compound **2c**, which can form bioactive cytotoxic compound **3c** as previously described (Figure 12A). **P1@C1** showed complete consumption of **2c** and formation of **3c** in 24 h in PBS, DMEM and DMEM+FBS. In case of **C4**, the reaction did not go to completion and a significant amount of **2c** remained in the reaction mixture (Figure 12B,C). In short, **P1@C1** is not only efficient, but is also a versatile catalyst that can promote NH insertion in different diazo substrates. In addition, the hydrophilic nature of diazo compounds did not hinder metal carbene formation or slowed down the reaction as full conversion was obtained within 24 h.

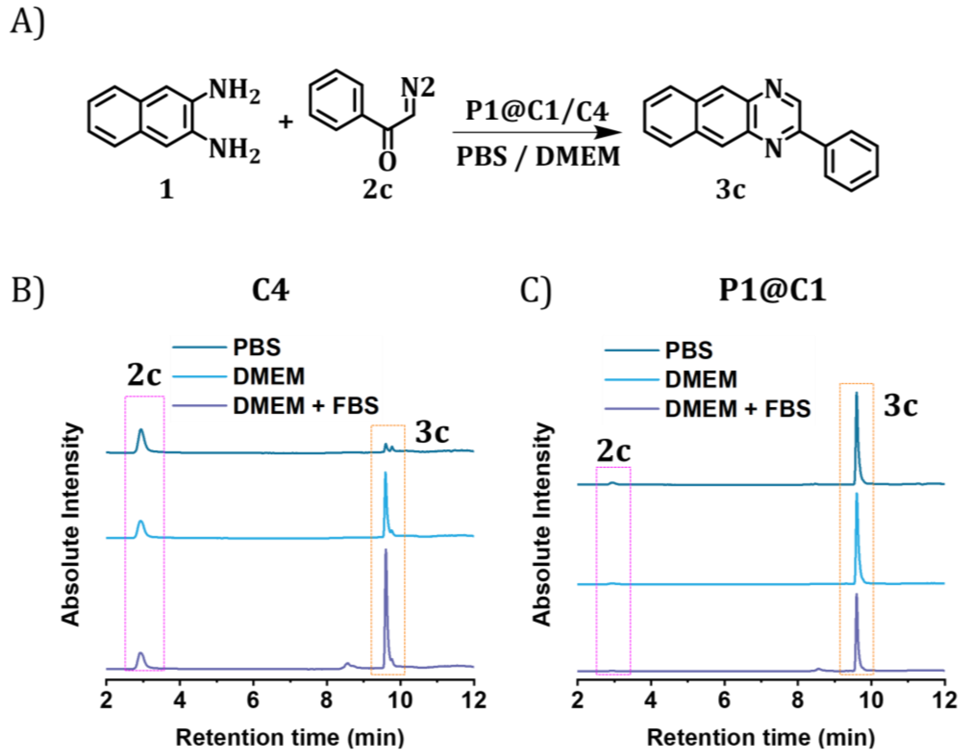

Figure 12: A) Formation of benzoquinoxaline **3c** when **1** and **2c** were reacted with **P1@C1** or **C4**; B) HPLC-MS chromatogram of the same reaction catalysed by **C4**; C) and by **P1@C1** after 24 h, monitored at 279 nm. [**1**] = [**2c**] = 500 µM in PBS, DMEM and DMEM+10% FBS, [**C1**] = 50 µM, all reactions performed at 37 °C, [**P1**]:[**C1**] = 1:5 (molar ratio); [**P1**] = ~ 10 µM (~ 1 mg/mL).

4.7 Investigating the formation of side products

The most common side products during metal carbene reactions as reported in literature are diazo carbene dimer and OH insertion product. To elucidate if these side reactions occur, we did several control experiments.

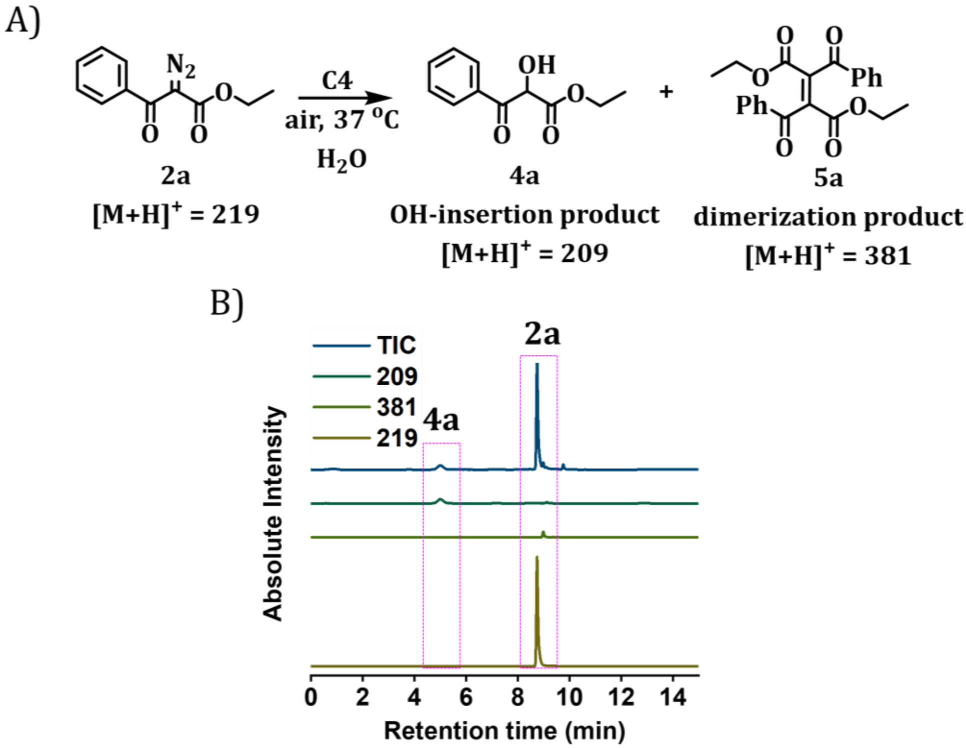

Figure 13: A) Formation of side products by OH insertion to product **4a** and dimerization to **5a** from **2a** in the presence of **C4**; B) HPLC-MS chromatogram of the reaction of **2a** in the presence of **C4** in water after 24 h. Each side product mass was added to SIM channel, reaction conditions [**2a**] = 500 µM in water [**C4**] = 50 µM, performed at 37 °C.

Hereto, diazo substrate **2a** was treated with catalyst **C4** using the same reaction conditions as described before in water. With the help of SIM (selective ion monitoring) channels, we looked specifically at the OH insertion product **4a** and dimer **5a** (Figure 13), as this allows high degree of sensitivity. Even after 49 h of reaction, diazo substrate **2a** remained in the reaction mixture. However, small amounts of the OH insertion product **4a** and dimer **5a** were found (Figure 13B). As these peaks are not significantly visible during catalytic reactions performed, we ruled out their formation when using **P1@C1** as the catalyst.

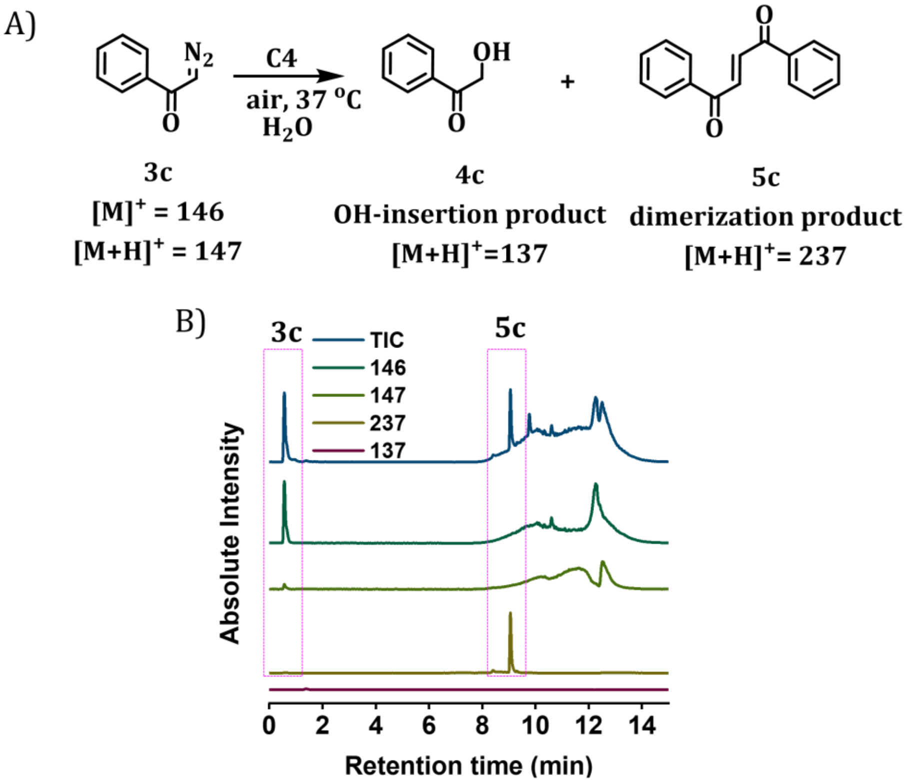

Figure 14: A) Formation of side products by OH insertion to product **4c** and dimerization to **5c** from **2c** in the presence of **C4**; B) HPLC-MS chromatogram of the reaction of **2c** in the presence of **C4** in water after 24 h. Each side product mass was added to SIM channel, reaction conditions [**2c**] = 500 µM in water [**C4**] = 50 µM, performed at 37 °C.

All reactions performed for evaluation of side products was performed in the presence of hydrophilic catalyst **C4**. In case of substrate **2b**, no major side products were observed as well. But in case of substrate **2c**, a significantly higher amount of dimer **5c** was formed while no OH insertion product **4c** was observed (Figure 14). The dimer formation could be due to the high reactivity of diazo substrate **2c** compared to **2a** and **2b**. **2a** and **2b** have two electron withdrawing substituents making them less reactive and less prone to decomposition when compared to **2c**, which only has one. But, when the reaction is catalysed by **P1@C1**, only the peak corresponding to product **2c** was observed as major peak. This allowed us to conclude that the **P1@C1** catalysed NH insertion reaction is highly selective towards the formation of the quinoxaline products and hence meet the criteria to be exported into biological environments.

4.8 Exporting reactions to living cells

The reactions in cell culture medium such as DMEM and DMEM+FBS confirmed that **P1@C1** is an efficient catalyst and stays catalytically active for prolonged period of times in competitive environments. Furthermore, the fact that only a low catalyst loading is required for complete product conversion made it a promising system to be tested in the presence of living cells. The reaction between **1** and **2a** was chosen as a model reaction as it forms fluorescent benzoquinoxaline **3a** that allows visual monitoring of reaction in living cells.

The first step towards this was to test the biocompatibility of the catalysts, substrates and products. To test that, we performed cytotoxicity assays where HeLa cells were incubated with **P1@C1**, **1**, **2a** and **3a** for 24 h. Concentration of substrates **1** and **2a** was varied from 25 µM to 200 µM. The CCK8 cell viability assay after an incubation time of 24 h showed that both of them did not show any significant cytotoxicity (Figure 15). However, reduced cell viability of approximately 70% was observed in case of **1** from 50 µM onwards. This was in contrast to the results reported by Mascareñas and co-workers, as they observed 90 –100% viability up to a concentration of 100 µM for **1**, **2a** and **3a** in HeLa, MCF7 and HEK293 cell lines. In their case, the incubation time was only 18 h. Therefore, we decreased the incubation time to 14 h in case of **1**, which increased cell viability to 98% (Figure 15A). In the case of **3a**, a reduced cell viability was observed from 15 µM onwards (Figure 15C), which is also in contrast to the observation of Mascareñas and co-workers. Visual inspection of the wells indicated the presence of crystals which could be the reason for cell death. We anticipated that catalytic reactions when performed in the presence of amphiphilic polymeric nanoparticles can solubilize and diffuse the products better, thereby preventing crystal formation. For the most important part, cells incubated with **P1@C1** from concentrations 5 – 15 µM for 24 h displayed good cell viability (Figure 15D).

The first control experiments were performed in which HeLa cells were incubated with only **1+2a**, **1+P1@C1** and **2a+P1@C1**, using 100 µM of **1** and **2a** and 2 µM of **P1@C1**. Cells were visualised under a confocal microscope at an excitation wavelength of 405 nm. Confocal images of cells incubated with **1+2a** and **1+P1@C1** showed a low fluorescence signal arising from **1** as it is weakly fluorescent when excited at 405 nm (Figure 16). It is clear that **2a+P1@C1** did not contribute to any fluorescence. To perform catalytic reactions, cells were at first incubated with 100 µM **1** and **2a** for 1.5 h, 3 h and 5 h, together with 2 µM of **P1@C1** (P1:C1 = 1:5).

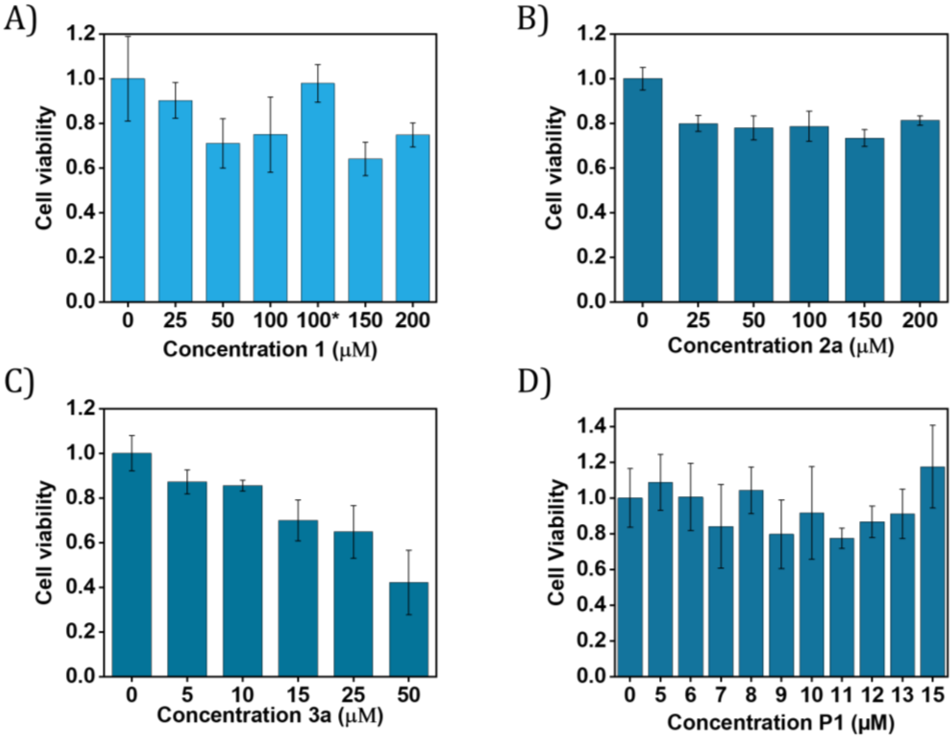

Figure 15: HeLa cells CCK8 cell viability assays when incubated with A) **1** (25 – 200 µM) B) **2a** (25 – 200 µM) C) **3a** (5 – 50 µM)and D) **P1@C1** (5 – 15 µM), all for 24 h. *Incubation time 14 h. The results are average of 3 wells.

Confocal microscopy images of the catalytic reactions revealed intracellular fluorescence buildup, indicating that product **3a** is formed, notably within 1.5 h at a catalyst loading of 10 mol% (Figure 16). An increase in fluorescence intensity is observed when incubation time is increased to 5 h, indicating the continuation of product formation. Previous research in our group on the internalisation of polymeric nanoparticles indicated that nanoparticles can be taken up by cells via endocytosis, leading to their accumulation in lysosomes 24 h after incubation.[9,49] Therefore, we performed reactions using **P1@C1**, by using shorter incubation time of up to 5 h which is expected to promote extracellular reactions. While we hypothesize that product **3a** was formed extracellularly, it is likely to penetrate the cell wall. As this neutral compound has a small size, low molecular weight and lipophilic nature (Log P = 4.5), it can diffuse through the lipid bilayer to the interior of cells. This can also be inferred from the homogeneous distribution of the product inside the cytoplasm. Although, quantification of the amount of product formed inside the HeLa cells was not performed, it is clear from these experiments that **P1@C1** is catalytically active in mammalian cell environments.

Our next goal was to elicit biological effects in mammalian cells, for which we performed the reaction to form cytotoxic product **3c** from **1** and **2c**. Compound **3c** belongs to a class of molecules known as Tyrphostins (Tyrosin phosphorylation inhibitors), which have distinct biological profiles due to their tyrosine kinase inhibitory activity. Compound **3c** is called Tyrphostin AG1385 and induces cell apoptosis. By looking at the toxicity profile of substrate **2c**, the CCK8 cell viability assay showed that it was innocuous to cells even up to 200 μM concentration (Figure 17A). While **3c** promoted a decrease in cell viability of 40% after 24 h from 25 μM concentration, the viability did not increase further with increasing concentration (Figure 17B). This observation is in line with the results reported in literature[25] where Gutiérrez *et al.* hypothesized that this could be due to the tendency of the highly hydrophobic drug (Log P = 4.3) to aggregate and precipitate, hindering biological effects. In order to test if **3c** can be synthesized *in situ* in cells by **P1@C1**, we incubated **1+2c+P1@C1** and determined the cell viability using CCK-8 assay. Using a low incubation time of 5 h and a low catalyst loading of 10 mol% did not show any significant differences in cell viability. Therefore, a substrate concentration of 100 and 200 μM with a catalyst loading of 25 and 50 mol% were used. Reactions performed with 100 μM substrates also did not show any pronounced decrease in cell viability (Figure 17C). However, with 25 and 50 mol% catalyst loading, the cell viability decreased to less than 40% at 200 µM substrate concentration (Figure 17C).

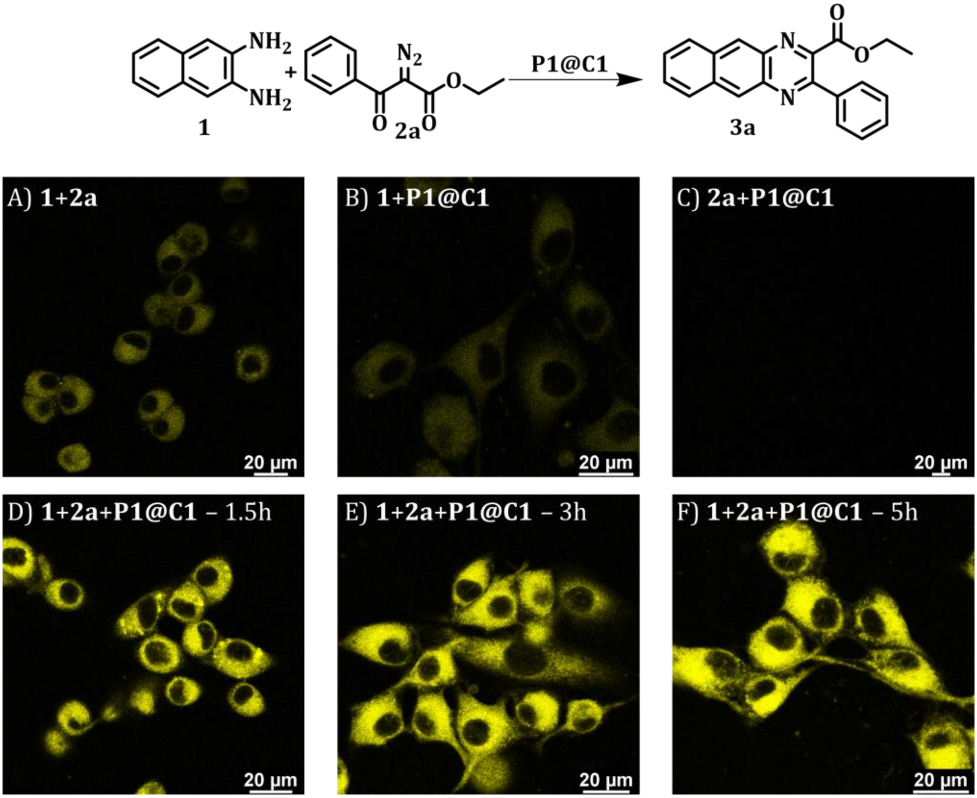

Figure 16: Confocal microscopy images of HeLa cells incubated with A) **1**+**2a** for 5 h B) **1**+**P1@C1** for 5 h C) **2a**+**P1@C1** for 5 h D) **1**+**2a**+**P1@C1** for 1.5 h E) **1**+**2a**+**P1@C1** for 3 h F) **1**+**2a**+**P1@C1** for 5 h, λ_{ex} = 405 nm, λ_{em} = 579-639 nm, [**1**] = [**2a**] = 100 µM and [**C1**] = 10 µM, [**P1**] = 2 µM, T = 37 °C.

When comparing the results obtained here to the results reported by Gutiérrez *et al.* using copper catalysts, our system is slightly less effective in inducing cell death as they observed decreased cell viability of 40% at 100 µM substrate concentration and 50 mol% catalyst loading.[25] We attribute this reduced efficiency tentatively to the hydrophobic nature of the product **3c**. Hydrophobic **3c** may accumulate in the hydrophobic pocket of polymeric nanoparticles, limiting the rate of mass transfer by slow diffusion, and leading to a reduced bioavailability. The copper catalysts used by Gutiérrez *et al.* was

$Cu(OAc)_2$ salt, which does not have hydrophobic regions to reduce the bioavailability. We also performed control experiments with only **1**+**2c**, **1**+**P1@C1** and **2c**+**P1@C1** at 100 μM of substrates and 2 μM of **P1@C1**. The combination **1**+**2c** and **1**+**P1@C1** when incubated with cells did not decrease the cell viability as expected. Unexpectedly, the combination **2c**+**P1@C1** induced cell death with a cell viability of only 14%, which is even less than what is observed for **3c** (Figure 17 D). It is reported in recent studies that some metal carbenes within paramagnetic metal catalysts such as Co(II), Rh(II) and Ir(II) are not closed shell metal carbenes as imagined but metal-carbene radicals, and even the metal-diazo-adduct precursor is presumed to have radical character.[50] Because of the vigorous N_2 evolution and high efficiency of NH insertion reactions, such radicals are often less studied, however, **2c** is reported to form metal-diazo radical when complexed to $[RhCl(cod)]_2$.[50]

In our case, in the absence of diamine **1**, the metal carbene radicals may have formed between **2c** and **C1** which induced the generation of harmful ROS (reactive oxygen species) triggering cell death.[51] As the cells incubated at the same concentration of **2c**+**P1@C1** in the presence of diamine **1** exhibited good cell viability, formation of these ROS during NH insertion reactions can be ruled out (Figure 17D). All in all, **P1@C1** proved to be catalytically active in the presence of living mammalian cells with high efficiency leading to the formation of benzoquinoxalines within short reaction times. Therefore, it has the potential to be developed as a promising catalyst for biomedical applications as quinoxaline scaffolds are present in many biorelevant compounds.

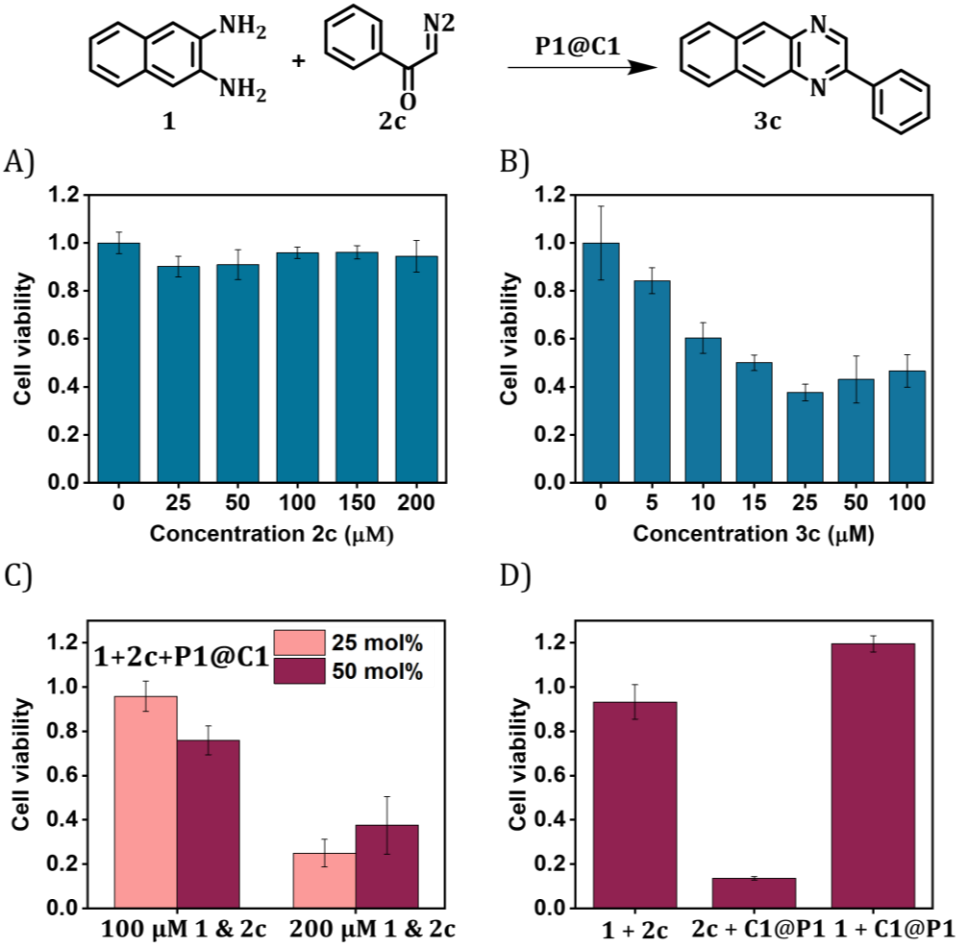

Figure 17: HeLa cells CCK8 cell viability assays when incubated with A) **2c** for 24 h (25 – 200 μM) B) **3c** for 24 h (5 – 100 μM) C) Catalytic reaction **1**+**2c** (100 & 200 μM) using **P1@C1** (25 % 50 mol%) in HeLa cells after 14 h D) Control reactions in HeLa cells with **1**+**2c**, **2c**+**P1@C1** and **1**+**P1@C1**, [**1**] = [**2c**] = 100 μM, [**C1**] = 10 μM, [**P1**] = 2 μM, incubated 14 h. The results are the average of 3 wells.

4.9 Role of polymer scaffolds in bioorthogonal catalysis – a comparison

Polymeric micelles also possess a hydrophobic space for catalysts and reactants, hereby providing protection for catalysts from surrounding environment and boost the reaction rate even when the substrate concentration is low (Figure 18).[52] All in all, they offer the same advantages as that of single-chain polymeric nanoparticles in aqueous solutions, with the difference that they are larger in size with a larger hydrophobic pocket.

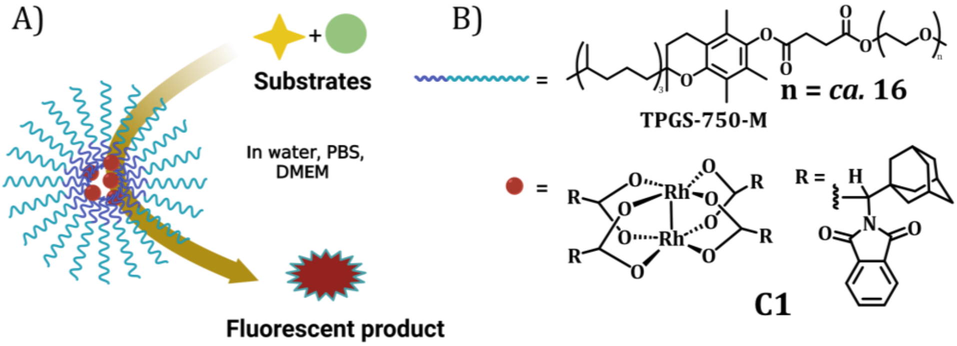

Figure 18: A) Representation of reaction involving two substrates using micellar system M@C1 B) Structure of surfactant **TPGS-750-M** and catalyst **C1** used to prepare **M1@C1**.

Lipshutz and co-workers have made significant contributions towards the development of polymeric surfactants that have been used as catalysts carriers for a variety of metal-catalysed cross-coupling reactions in water at room temperature.[53,54] Various 'designer' surfactants were developed, and the results showed that the makeup of the surfactant matters for metal-catalysed reactions as it directly influences the interior of micelles.[55] In addition, the size and particle shape of the micelles affected the efficiency of reactions, with larger particles often showing better-quality cross-couplings. They speculated this was a result of larger particles better accommodating the different components of the reactions.[55]

As discussed in Chapter 1, there are multiple carrier materials available to perform bioorthogonal catalysis, and all of them have significant potential to advance nanomedicine. A comparative evaluation of the different platforms is crucial for a thorough understanding and optimization of their applications, but this is currently still lacking. We were curious to know, how well the polymeric micelles developed by Lipshutz *et al* are as catalysts carriers when compared to polymeric nanoparticles in aqueous solutions of varying complexity.[72] Therefore, we chose the commercially available surfactant TPGS-750-M (Figure

18B), which is one of the best carrier systems developed by Lipshutz *et al.* TPGS-750-M forms micelles with an average size of 50 nm (observed by DLS and TEM),[55] and the critical micelle concentration (CMC) of this surfactant in cell culture medium is 0.007 wt%, making it suitable for reactions under diluted conditions.[56]

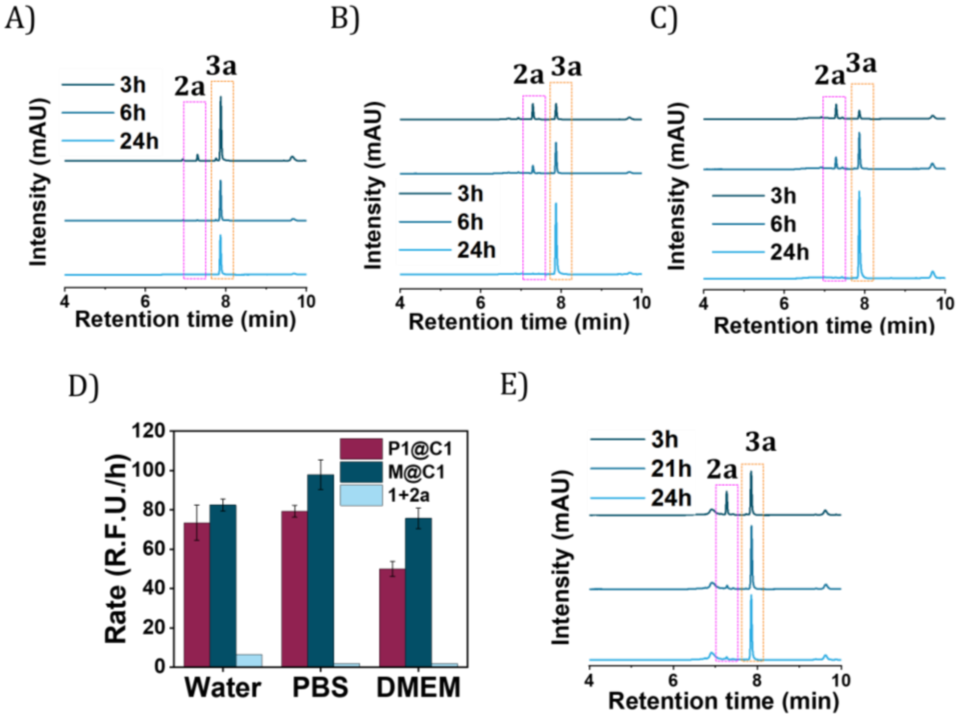

Figure 19: HPLC-UV chromatogram of reaction progress of **1** and **2a** over time catalysed by **M@C1**, monitored at 279 nm wavelength after 24 h, A) [**1**] = [**2a**] = 500 µM, [**C1**] = 50 µM, 0.1 wt% TPGS in water B) [**1**] = [**2a**] = 100 µM, [**C1**] = 10 µM, 0.02 wt% TPGS in water C) [**1**] = [**2a**] = 50 µM, [**C1**] = 5 µM, 0.01 wt% TPGS in water D) Comparison of reaction rate catalysed by **P1@C1** and **M@C1** (t_0 = 10 min and t_F = 180 min) determined using fluorescence kinetics experiment; substrates **1** and **2a** without catalyst was used as control; λ_{ex} = 330 nm and λ_{em} = 386 nm. Reaction conditions: [**1**] = [**2a**] = 500 µM, [**C1**] = 50 µM, 0.1 wt% of surfactant and **P1** in reaction medium, T = 37 °C in water, PBS and DMEM; The results are average of three independent measurements E) HPLC-UV chromatogram of reaction catalysed by **M@C1** in DMEM+FBS, [**1**] = [**2a**] = 500 µM, [**C1**] = 50 µM, 0.1 wt% TPGS in DMEM+10% FBS, T = 37 °C.

Dirhodium carboxylate catalyst **C1** was encapsulated in polymer micelles, where the wt% of the surfactant in water was kept the same as that of amphiphilic polymer **P1** wt% for comparison. The sample preparation was performed similar to that of polymeric nanoparticles: surfactant and hydrophobic catalyst were co-dissolved in trichloroethylene and the solvent was slowly evaporated under vacuum. Micelles were formulated by the addition of deionized water and vigorous stirring for 3 h to form **M@C1**. Even though Lipshutz and co-workers reported that they directly mix the surfactant and catalysts in aqueous solutions vigorously, we observed that our protocol ensured better encapsulation of catalysts and faster kinetics.

First, the reaction between **1** and **2a** was analysed in water, at 500 µM of substrate concentration and 10 mol% catalyst loading, corresponding to 0.1 wt% of surfactant. Almost full conversion of **2a** to **3a** was observed within 6 h in this case (Figure 19A).The reactions were further performed in dilute conditions, *i.e* at 100 and 50 µM substrate concentrations, where 10 mol% catalyst loading (0.02 wt% and 0.01 wt% of surfactant) was used. In both cases, the reactions reached full conversion in 24 h (Figure 19B,C). The micellar catalysis is equally efficient at lower substrate concentrations compared to **P1@C1,** even when its concentration is very close to CMC.

In order to compare the efficiency of **P1@C1** and **M@C1**, we looked at the rate of reaction determined by the decrease in the fluorescence intensity of diamine **1**. From the results, it is clear that they follow the same trend in activity in different reaction media and **M@C1** performed slightly better than **P1@C1** (Figure 19D). This could be due to the more dynamic nature of micelles and larger hydrophobic pocket that may permit better accumulation and faster diffusion of reactants and products when compared to polymeric nanoparticles. As the last step, we also investigated if micelles can remain catalytically active in more complex media such as in the presence of serum proteins, even in this case full conversion to products was observed without any side product formation (Figure 19E). Therefore, **M@C1** also proved to be a highly efficient catalyst suitable for bioorthogonal reactions.

4.10 Discussion and Conclusions

Dirhodium carboxylates are very stable and reactive catalysts, satisfying the major requirements for a bioorthogonal catalyst to work in biological media. Encapsulation of these catalysts employing hydrophobic interactions in the amphiphilic polymeric nanoparticles proved to be very efficient for catalysts that are hydrophobic (Log P > 10). To the best of our knowledge, this is the first time highly hydrophobic rhodium catalysts **C1-C2** are utilized to perform NH carbene insertion reaction in homogeneous aqueous solution or in the presence of living cells. Although, **C3** and **C4** are already reported to catalyse the same reaction in water, those were done at very high substrate concentrations (100 mM) and heterogeneous conditions albeit with a reasonable yield of 72% and 38%, respectively.[25] The very first report on using NH insertions for synthesis of bioactive agents *in situ* in living cells utilized $Cu(OAc)_2$ salt as catalyst. However, inherent toxicity of copper is problematic when considering further applications. Also, Cu complexes are susceptible to fast deactivation by nucleophiles in complex media, although they gave a satisfactory yield of 50-80% in biologically relevant media at millimolar concentration of substrate and 10 mol% $Cu(OAc)_2$.

Screening of stable dirhodium(II) carboxylate catalysts revealed that **C1** and **C3** (Log P ~ 10) perform to their fullest potential in water when encapsulated in polymeric nanoparticles. But the potential of catalyst **C2** (Log P = 27) at **P1**:**C1** (1:5) ratio was diminished. In this case, 1:5 incorporation ratio may have led to saturation of the hydrophobic domains, with no space left to accommodate substrates. This could be altered by decreasing catalyst incorporation.

P1@C1 performed the best and met all the requirements required for an efficient bioorthogonal catalyst. For the application of **P1@C1** in living cells, we aimed at performing extracellular catalysis because of two reasons. First, synthesizing lipophilic substrates that comply with Lipinski's rule[57] outside the cell membrane is more efficient to allow their permeation into the cytoplasm. The diazo substrate may not permeate the membrane as efficiently by itself. Second, the Jeffamine M-1000-functionalised polymeric nanoparticles are generally taken up by cells via endocytosis over a time period of several hours, and end up in lysosomes making it difficult to perform intracellular catalysis. We believe coupling reactions work best for extracellular catalysis and are the future for biomedical applications. One downside to these reactions is that hydrophobic substrates formed can get accumulated in the hydrophobic domain of polymeric nanoparticles, limiting their catalytic efficiency and compromising the bioavailability of the product formed. This is in line with the observation that **3c** showed poorer biological effects in our case than what is reported in the literature for same concentration using $Cu(OAc)_2$ catalyst.[25] Among the three reactions tested, the reaction between **1** and **2b** forming the product **3b** which spontaneously hydrolysed to **3b'** suggests a solution to this problem. Substrate modification with handles for tandem reactions in complex media may enhance product diffusion. Also, this an excellent example to indicate that polymeric nanoparticles can work in tandem with other enzymes.

The comparison of catalytic efficiency between micellar and polymeric nanoparticle-based systems suggests that a larger hydrophobic domain may further enhance the efficiency. But the advantages of the nanoparticle-based system from an application point of view outweigh this slight enhancement in activity. They can benefit more from their small size which allows tissue permeability and renal clearance (if the size can be carefully optimized). Further, they also allow ease of functionalisation with targeting moieties or fluorescent markers helping in targeted therapy.

All in all, our study showed the potential of exporting hydrophobic dirhodium carboxylate catalysts to living cells to perform NH carbene insertion reactions with the help of both amphiphilic polymeric nanoparticles as well as polymeric micelles. The encapsulation of the dirhodium catalysts in the amphiphilic systems is excellent (97-99% for polymeric micelles towards hydrophobic catalysts with Log P>10). In addition, the efficiency of selected catalysts to perform NH carbene insertion reactions was high even at low catalyst loading and at low substrate concentrations. Importantly, the best-performing polymeric nanoparticle catalyst **P1@C1** was exported to HeLa cells where it catalysed the NH insertion reaction to produce photophysically and biologically active products with high efficiency. To highlight this efficiency, the reactions performed in cells were really 'catalytic' with catalytic loadings as low as 10 mol%, which is rarely attained in the case of TMC-catalysed bioorthogonal reactions. In future, the repertoire of efficient bioorthogonal reactions can also be expanded using the catalysts used in this work. Also, we anticipate that these studies will drive further advancements in the field, allowing to export new and stable hydrophobic catalysts and reactions to biological environments, leading to new breakthroughs.

4.11 Experimental section

Instrumentation

All NMR measurements were recorded on a Bruker 400 MHz spectrometer or Varian Mercury Vx 400 MHz (^{1}H at 400 MHz, ^{13}C at 100 MHz and ^{19}F at 376 MHz) at ambient temperature. The ^{1}H NMR chemical shifts (*d*) are reported in ppm downfield from tetramethylsilane (TMS). The resonance of the deuterated solvent was used as an internal standard for reporting ^{13}C NMR chemical shifts (*d*). Peak multiplicities are abbreviated as: singlet (s), doublet (d), triplet (t), quartet (q), multiplet (m) and broad (br). Downfield ^{13}C NMR chemical shifts are reported using the resonance of the deuterated solvent as an internal standard. Br = broad, d = doublet, dd = double doublet, m = multiplet, p = pentet, s = singlet, t = triplet, and q = quartet are the abbreviations used. Shimadzu Prominencei LC2030C 3D equipped with a Shimadzu RID20A refractive index detector was used to perform SEC measurements. The elution solvent used was THF containing 10 mM LiBr (flow = 1 mL/min). A mixed C and mixed D column combined in series with an exclusion limit = 2.000.000 g mol-1, 7.5 mm i.d. 300 mm previously calibrated with poly(styrene) from Polymer Laboratories was used. DMF-SEC measurements were carried out on a PLGPC50 plus (Varian) equipped with a refractive index detector. Dimethylformamide containing 10 mM LiBr (flow = 1 mL min^{-1}) was used as eluent in combination with a Shodex GPCKD804 column (exclusion limit = 400.000 Da; 0.8 cm i.d. 300 mm). This column was calibrated with poly(ethylene glycol from Polymer Laboratories. Dialysis was carried out with the help of a Spectra/Por Dialysis Membrane with a Molecular Weight CutOff of 6-8 kDa. Malvern Zetasizer with 830 nm laser at 90° was used for dynamic light scattering experiments and samples were filtered over a 0.2 μm PVDF filter prior to measurements to remove any dust particles from hindering the measurements. Inductively coupled plasma-optical emission spectroscopy (ICP-OES) measurements were performed on a SpectroBlue Ametek after calibration using rhodium standard solution at different concentrations. Grace Reveleris X2 was utilized for automated column chromatography where Büchi prepacked silica columns were used to load sample (liquid loading/dry loading as specified). High Performance Liquid chromatography LC-UV was performed using Shimadzu UFLC-XR with PDA detector. Eluents used were A: water + 0.1% formic acid and B: ACN + 0.1% formic acid. The column used was a Kinetex column EVO C18, with length 50 mm and internal diameter 2.1 mm. It has a pore size of 100 Å and particle size 5 μm. Optimised HPLC method is as follows: A/B (90:10) isocratic 5 min, followed by gradient A/B (90:10) to A/B (0:100) in 2 min, A/B (0:100) isocratic 2 min, A/B (0:100) to A/B (90:10) gradient in 2 min. The flow rate was kept constant at 0.2 mL/min and measurements were performed at room temperature. High Performance Liquid Chromatography

– HPLC-UV/MS was performed on a SHIMADZU Nexera-I LC-2040C 3D coupled with LC-MS 2020 for detection. Eluents, column and HPLC method for separation was the same as that used for HPLC-UV, except that the flow rate was kept constant at 0.15 mL/min and the column temperature was maintained at 40 °C. For cell experiments, analysis of the microplate was performed using a Tecan MC-SPARK. Agilent Cary Eclipse fluorescence spectrophotometer coupled with a temperature controller was used fluorescence kinetic experiments. Confocal microscopy images of HeLa cells were obtained with a Leica SP5 confocal microscope with a HyD2 detector. Identical conditions were followed throughout all measurements. Leica software and ImageJ was used for processing images. Amicon® Ultra-15 Centrifugal Filter Units were used for filtering polymers from catalysts. Rhodium ICP standard solution was purchased from Sigma Aldrich and was diluted in deionized water to prepare respective concentration ranges.

Materials

All commercial reagents were purchased from Sigma Aldrich or TCI and were used without further purification. Dulbecco's Modified Eagle's Medium (DMEM) and fetal bovine serum (FBS) were purchased from Thermofisher Scientific. CCK8 viability assay kit was purchased from Sigma-Aldrich. All bulk solvents were purchased from Biosolve. All the deuterated solvents were purchased from Cambridge Isotopes Laboratories. Dry solvents were obtained from an MBRAUN Solvent Purification System (MBSPS). Jeffamine M1000 polyetheramine was kindly provided by Huntsman. Amphiphilic polymer **P1** was synthesized according to the protocol of similar polymer as described in chapter 2 and has molecular weight $M_{n,\mathrm{cal}}$ = 98.0 g/mol and polydispersity of 1.21 as determined from GPC-SEC$_{\mathrm{DMF}}$. All catalysts and surfactant TPGS-M-750 were commercially available and used as it is. Diazo substrates **2a-c** and corresponding products **3a-c** were synthesized according to the reported protocol.[25,46]

Experimental Procedures

General procedure for the encapsulation of dirhodium-based catalyst in amphiphilic polymer

Depending on the encapsulation ratio (**P**:**C**) or variability in the experiment, the required amounts of polymer and catalyst were co-dissolved in trichloroethylene and transferred to a glass vial. Trichloroethylene was gently allowed to evaporate by nitrogen or argon flow to form a thin film on glass, and this film was dried completely under vacuum at 60 °C overnight. To this vial, deionized water was added, vortexed, and sonicated for 45 min. After sonication, solution was placed in a pre-heated oven at 80 °C for 45 min. The solution was then suspended in air overnight to equilibrate to room temperature.

Procedure for determining the encapsulation efficiency

10 mL of catalyst-encapsulated polymeric nanoparticles P1@C1-C4 were prepared according to the protocol described above, with polymer:catalyst ratio = 1:5, such that the solution has 10 μM

P1 and 50 µM C1-C4. Rhodium calibration curves were created using rhodium standard solution from a series of concentrations 0.1 – 0.5 mg/mL and 2-10 mg/mL separately. Calibration curves at these two concentration regimes were created each time before quantification for better accuracy. Catalyst-encapsulated nanoparticles P1@C1-C4 were added to centrifugal filters with a molecular weight cutoff of 50 kD and were centrifuged for 15 min at 3000 RPM. The filtrate solution was then analysed using ICP-OES to determine the concentration of palladium leached out from polymeric nanoparticles into water.

Synthesis of diazo substrates 2a-c and benzoquinoxalines 3a-c

*Synthesis of 2-diazo-3-oxo-3-phenylpropanoate (**2a**)*

p-Acetamidobenzenesulfonyl azide (*p*-ABSA, 0.75 g, 3.12 mmol, 1.2 eq.) was dissolved in dry ACN (5 mL) in a dry round bottom Schenk flask at 0 °C under argon atmosphere. To this solution ethyl benzoylacetate (0.45 mL, 2.6 mmol, 1.0 eq.) was added slowly. To this mixture, diazabicyclo[5.4.0]undec-7-ene (DBU, 0.47 mL, 3.12 mmol, 1.2 eq) was added dropwise which resulted in a clear yellow solution. This reaction mixture was then stirred for 5h and removed from ice bath to slowly bring it to room temperature. The reaction mixture was then quenched with water (6 mL) and extracted with ethyl acetate (3 x 6 mL). The combined organic phases were dried over sodium sulfate, filtered and concentrated under reduced pressure. The product was purified by flash column chromatography using heptane/ethyl acetate (95/5) as eluent on silica, the pure product was obtained as a yellow oil. Yield: 76% (431.00 mg, 1.98 mmol) ^{1}H NMR (400 MHz, $CDCl_3$): δ 7.70 – 7.57 (m, 2H), 7.57 – 7.47 (m, 1H), 7.47 – 7.35 (m, 2H), 4.25 (q, J = 7.1 Hz, 2H), 1.26 (t, J = 7.1 Hz, 3H).^{1}H NMR is in accordance with the literature.[25]

*Synthesis of ethyl 2-diazo-3-oxobutanoate (**2b**)*

To a solution of *p*-acetamidobenzenesulfonyl azide (*p*-ABSA, 0.75 g, 3.13 mmol, 1.2 eq.) in dry ACN (5.4 mL) in dry round bottom Schlenk flask under argon atmosphere at 0 °C, ethyl acetoacetate (0.34 mL, 2.7 mmol, 1.0 eq.) was added slowly. To this mixture, 1,8-diazabicyclo[5.4.0]undec-7-ene (DBU, 0.48 mL, 3.13 mmol, 1.2 eq) was added dropwise and the solution turned to a yellow thick paste. To solubilize the components better an additional 0.5 mL of dry ACN was added which resulted in a clear orange reaction mixture and this solution was stirred for 6h. The reaction was monitored by TLC, the reaction mixture was then slowly brought to room temperature. Afterwards, the mixture was quenched with water (6 mL) and extracted with ethyl acetate (3 x 6 mL). The combined organic phases as then dried over magnesium sulfate, filtered and concentrated under reduced pressure. The product was purified by flash column chromatography using heptane/ethyl acetate (9/1) as eluent on silica, and the pure product was obtained as a yellow oil. Yield: 65% (272 mg, 1.74 mmol) ^{1}H NMR (400 MHz, $CDCl_3$): δ 4.31 (q, J = 7.1 Hz, 2H), 2.48 (s, 3H), 1.34 (t, J = 7.1 Hz, 3H). ^{1}H NMR is in accordance with the literature.[25]

*Synthesis of 2-diazo-acetophenone (**2c**)*

To a solution of *p*-acetamidobenzenesulfonyl azide (p-ABSA, 0.75 g, 3.12 mmol, 1.0 eq.) and benzoylacetone (0.51 g, 3.12 mmol, 1.0 eq.) in ethanol (3.2 mL) in a round bottom flask, methylamine (40% in MeOH, 0.29 mL, 2.83 mmol, 0.9 eq.) was added dropwise. The solution turned orange thick paste, which was diluted by adding 10 mL of ethanol. This resulted in a yellow solution which was stirred for 2 h at room temperature under argon atmosphere. The reaction was monitored by TLC, and upon completion, the reaction mixture was concentrated under reduced pressure. The pure product was purified by flash column chromatography with heptane/ethyl acetate (9/1) as eluent on silica and the product was obtained as an orange solid. Yield: 70% (317 mg, 2.17 mmol). ^{1}H NMR (400 MHz, $CDCl_3$) δ 7.81 – 7.70 (m, 2H), 7.59 – 7.50 (m, 1H), 7.45 (dd, J = 8.3, 6.8 Hz, 2H), 5.90 (s, 1H). ^{1}H NMR is in accordance with the literature.[25]

*Synthesis of 3-phenylbenzo[g]quinoxaline-2-carboxylate (**3a**)*

Diazo compound **2a** (22.1 mg, 0.1 mmol, 1.0 eq.) was added to a 4 mL glass vial, and to this, a solution of $Rh_2(esp)_2$ (10 mol%) in Milli-Q water (250 µL) was added. To ensure the complete transfer of the heterogeneous catalyst $Rh_2(esp)_2$, the vial was washed again 3 times with 250 µL of Milli-Q water and added to the reaction mixture. To this solution, 2,3-diaminonaphthalene **1** (15.6 mg, 0.1 mmol, 1.0 eq.) was added. The reaction mixture was heterogeneous and was placed in a pre-heated oil bath (40 °C) and stirred for 24 h, open to the air. After, the reaction mixture was transferred to a larger vial of 16 mL and was then extracted with ethyl acetate (4x 3 mL). The organic phases were combined and dried over magnesium sulfate, filtered, and was dried under reduced pressure. The pure product was obtained by automated column chromatography using the Grace Column (12 g, 20 µm Silica), where heptane/EtOAc (9:1) was used as eluent. Due to the homoeopathic scale of reaction, yield could not be calculated. Pure product obtained was used to calibrate HPLC-UV. ^{1}H NMR (400 MHz, $CDCl_3$): δ 8.81 (s, 1H), 8.77 (s, 1H), 8.21 – 8.08 (m, 2H), 7.88 – 7.75 (m, 2H), 7.70 – 7.58 (m, 2H), 7.54 (dd, J = 5.1, 1.9 Hz, 3H), 4.37 (q, J = 7.2 Hz, 2H), 1.21 (t, J = 7.1 Hz, 3H). ^{1}H NMR is in accordance with literature.[25]

*Synthesis of 3-methylbenzo[g]quinoxaline-2-carboxylate (**3b**)*

Diazo compound **2b** (15.70 mg, 100 µmol, 1.0 eq.) was added to a 4 mL glass vial, followed by the addition of a solution of $Rh_2(OAc)_4$ (10 mol%) in Milli-Q water (1.0 mL) was added. To this mixture, 2,3-diaminonaphthalene **1** (15.70 mg, 100 µmol, 1.0 eq.) was added and placed in a pre-heated oil-bath at 40 °C. The reaction mixture was stirred for 24 h open to air. After that, the reaction mixture was transferred to a bigger vial and was washed with 1.5 mL of Milli-Q water and was extracted with ethyl acetate (3x 5 mL). The combined organic phases were then dried over magnesium sulfate, filtered, and concentrated under reduced pressure. The pure product was then obtained by automated column chromatography on the Grace Column (4 g, 20 µm Silica) using heptane/ethyl acetate (8/2) as eluent. Due to the homoeopathic scale of reaction, yield could not be calculated. The pure product obtained was used to calibrate HPLC-UV. ^{1}H NMR (400

MHz, $CDCl_3$): δ 8.78 (s, 1H), 8.61 (s, 1H), 8.12 (dd, J = 7.8, 1.9 Hz, 2H), 7.72 – 7.47 (m, 2H), 4.59 (q, J = 7.2 Hz, 2H), 2.99 (s, 3H), 1.52 (t, J = 7.1 Hz, 3H). ^{1}H NMR is in accordance with the literature.[25]

*Synthesis of Tyrphostin AG1385 (**3c**)*

2,3-Diaminonaphthalene **1** (16.0 mg, 101 μmol, 1.0 eq.) was taken in a 16 mL vial, to which $Rh_2(OAc)_4$ (10 mol%) was added. Followingly, 0.8 mL of Milli-Q water was added and the vial was placed in a pre-heated oil bath at 40 °C and was stirred open to air. Diazo compound **3c** (14.8 mg, 101 μmol, 1.0 eq.) was then dissolved in 0.2 mL acetonitrile and was added slowly to this reaction mixture over 4 h using a syringe pump. After stirring for 24 h, 1.5 mL of Milli-Q water was further added and the reaction mixture was extracted with ethyl acetate (4x 5 mL). The combined organic phases was then dried over magnesium sulfate, filtered, and concentrated under reduced pressure. The pure product was obtained by automated column chromatography on the Grace Column (4 g, 20 μm Silica) using a gradient from heptane to heptane/ethyl acetate (9:1) as eluent. Due to the homoeopathic scale of reaction, yield could not be calculated. The pure product obtained was used to calibrate HPLC-UV. ^{1}H NMR (400 MHz, $CDCl_3$) δ 9.41 (s, 1H), 8.72 (d, J = 16.2 Hz, 2H), 8.34 – 8.19 (m, 2H), 8.20 – 8.09 (m, 2H), 7.67 – 7.51 (m, 5H). ^{1}H NMR is in accordance with the literature.[25]

NH carbene insertion reactions in aqueous solutions

*General procedure for catalytic NH-insertion reactions in presence of **P1:***

Water or PBS as reaction medium: To a solution of catalyst-encapsulated nanoparticles **P1@C1-C3** (10 μM **P1**, **P1**:**C** = 1:5), which was prepared in 992 μL Milli-Q water/PBS, 4 μL diamine **1** (0.5 μmol, 1.0 eq.) was added from a stock solution in DMSO (125 mM). The reaction mixture was stirred briefly before the addition of **2a** (4 μL, 0.5 μmol, 1.0 eq) from a stock solution in DMSO (125 mM). The reaction mixture was placed in a pre-heated oil bath (37 °C) and vigorously stirred for 24 h, open to air. After each required time point, a sample aliquot was taken. 10 μL aliquot was added to a vial to which 40 μL Milli-Q water and 50 μL acetonitrile was added. The sample was vortexed and then injected into HPLC-UV/MS. Although this procedure is for reactions with 500 μM substrate concentration, for other reactions where substrate and catalyst concentrations were varied, the same protocol was followed.

DMEM or DMEM+FBS: same procedure as above was followed except that **P1@C1** was prepared at a very high concentration of 500 μM in Milli-Q water and then diluted to reach desired concentration in DMEM or DMEM+FBS.

*General procedure for catalytic NH-insertion reactions in absence of **P1:***

Water or PBS or DMEM or DMEM+FBS as reaction medium: 988 μL corresponding medium was added to a glass vial, followed by the addition of **1** and **2a** (from corresponding stock solution), same concentration as mentioned above. Water soluble catalyst **C4** was added to this mixture from a stock solution of 12.5 mM in THF in such a way that the final concentration of the catalyst is 50 μM and substrates are 500 μM in water/PBS. The reaction mixture was placed in a preheated oil bath at 37 °C and was vigorously stirred for 24 h. During the reaction, at different time points, aliquots were taken and diluted in water and acetonitrile as mentioned above. This solution was then injected into HPLC-UV/MS for monitoring the reaction progress.

General procedure for fluorescence kinetic experiments:

The reactions were performed in a fluorescence cuvette in 3 mL total volume following the same procedure as mentioned above, in the presence or absence of **P1**. The fluorescence intensity of diamine **1** was followed overtime λ_{exc} = 330 nm and λ_{emm} = 386 nm.

NH carbene insertion reactions in HeLa cells

Assessment of cell viability: HeLa cells were cultured and seeded in Dulbecco's modified Eagle's medium (DMEM) supplemented with 10% fetal bovine serum (FBS) and phenol red. Cytotoxicity of substrates (**1**, **2a** and **2c)**, products (**3a** and **3c**) and **C1@P1** was studied using the cell counting kit-8 (CCK8) assay. A 96-well plate was used seed HeLa cells. Wells were filled with 100 μL of cell suspension containing 8000 cells. The plate was then placed in an oven at 37 °C with 5% CO_2 flow for 24 h. Then, the required compound to be tested was added to the cells. Substrates **1**, **2a**, **2c** were added at concentrations of 25, 50, 100, 150 and 200 μM, **3a** at concentrations of 5, 10, 15, 25 and 50 μM and **3c** at concentrations of 5, 10, 15, 25, 50 and 100 μM. Compounds were added from freshly prepared DMSO stock solutions. Not more than 0.5 μL DMSO was added to cells, so the stock solutions were prepared accordingly. Cytotoxicity of **C1@P1** was tested at concentrations of 5, 6, 7, 8, 9, 10, 11, 12, 13 and 15 μM. **C1@P1** stock solution (100 μM) was prepared in live cell imaging solution. The amount of stock solution volume to be added was first removed from the well to keep concentrations constant. Followingly, the plate was placed in the oven. After 24 h, the medium was removed and 100 μL DMEM with 10% CCK8 were added to each well. The plate was then placed back in the oven at 37 °C for 2 to 4 h. The absorbance of each well containing cells was measured at 450 nm at the microplate reader. Cell viability was determined as a fold change of the absorbance with respect to untreated cells. Error bars represent the standard deviation of 3 different wells.

Procedure for NH carbene insertion reactions in Hela cells

*Formation of **3a**:* Cultured HeLa cells were seeded in a μ-Slide 18 well from Ibidi. Wells were filled with 100 μL of cell suspension containing 8000 cells. Cells were incubated with **C1@P1**, **1** and **2a** for the incubation time as mentioned. **C1@P1**, **1** and **2a** were mixed briefly together in the correct composition before addition to the cells. **C1@P1** was added from a freshly prepared stock solution (100 μM) in live cell imaging solution and **2a** was added from DMSO stock solution (5 μL). Later, the μ-Slide was placed back in the oven. The cells were then monitored in a confocal microscope.

*Formation of **3c**:* The procedure was followed as explained above for substrates **1** and **2c**. After the indicated reaction times the compound containing medium was removed and 100 µL DMEM with 10% CCK8 was added to each well. The plate was then placed back in the oven at 37 °C for 2 to 4 h. The absorbance of each well containing the cells was measured at 450 nm at the microplate reader. Cell viability was determined as explained before.

4.12 References

(1) van de L'Isle, M. O. N.; Ortega-Liebana, M. C.; Unciti-Broceta, A. *Transition Metal Catalysts for the Bioorthogonal Synthesis of Bioactive Agents*; Elsevier Current Trends, 2021; Vol. 61, pp 32–42. https://doi.org/10.1016/J.CBPA.2020.10.001.

(2) Miller, M. A.; Askevold, B.; Mikula, H.; Kohler, R. H.; Pirovich, D.; Weissleder, R. Nano-Palladium Is a Cellular Catalyst for *in vivo* Chemistry. *Nat Commun* **2017**, *8* (1), 1–13. https://doi.org/10.1038/ncomms15906.

(3) Miller, M. A.; Mikula, H.; Luthria, G.; Li, R.; Kronister, S.; Prytyskach, M.; Kohler, R. H.; Mitchison, T.; Weissleder, R. Modular Nanoparticulate Prodrug Design Enables Efficient Treatment of Solid Tumors Using Bioorthogonal Activation. *ACS Nano* **2018**, *12* (12), 12814–12826. https://doi.org/10.1021/ACSNANO.8B07954/SUPPL_FILE/NN8B07954_SI_002.PDF.

(4) Pérez-López, A. M.; Rubio-Ruiz, B.; Sebastián, V.; Hamilton, L.; Adam, C.; Bray, T. L.; Irusta, S.; Brennan, P. M.; Lloyd-Jones, G. C.; Sieger, D.; Santamaría, J.; Unciti-Broceta, A. Gold-Triggered Uncaging Chemistry in Living Systems. *Angewandte Chemie* **2017**, *129* (41), 12722–12726. https://doi.org/10.1002/ange.201705609.

(5) Yusop, R. M.; Unciti-Broceta, A.; Johansson, E. M. V.; Sánchez-Martín, R. M.; Bradley, M. Palladium-Mediated Intracellular Chemistry. *Nat Chem* **2011**, *3* (3), 239–243. https://doi.org/10.1038/nchem.981.

(6) Chen, J.; Wang, J.; Li, K.; Wang, Y.; Gruebele, M.; Ferguson, A. L.; Zimmerman, S. C. Polymeric "Clickase" Accelerates the Copper Click Reaction of Small Molecules, Proteins, and Cells. *J Am Chem Soc* **2019**, *141* (24), 9693–9700. https://doi.org/10.1021/jacs.9b04181.

(7) Chen, J.; Wang, J.; Bai, Y.; Li, K.; Garcia, E. S.; Ferguson, A. L.; Zimmerman, S. C. Enzyme-like Click Catalysis by a Copper-Containing Single-Chain Nanoparticle. *J Am Chem Soc* **2018**, *140* (42), 13695–13702. https://doi.org/10.1021/jacs.8b06875.

(8) Bai, Y.; Feng, X.; Xing, H.; Xu, Y.; Kim, B. K.; Baig, N.; Zhou, T.; Gewirth, A. A.; Lu, Y.; Oldfield, E.; Zimmerman, S. C. A Highly Efficient Single-Chain Metal-Organic Nanoparticle Catalyst for Alkyne-Azide "Click" Reactions in Water and in Cells. *J Am Chem Soc* **2016**, *138* (35), 11077–11080. https://doi.org/10.1021/JACS.6B04477/ASSET/IMAGES/LARGE/JA-2016-04477X_0002.JPEG.

(9) Liu, Y.; Pujals, S.; Stals, P. J. M.; Paulöhrl, T.; Presolski, S. I.; Meijer, E. W.; Albertazzi, L.; Palmans, A. R. A. Catalytically Active Single-Chain Polymeric Nanoparticles: Exploring Their Functions in Complex Biological Media. *J Am Chem Soc* **2018**, *140* (9), 3423–3433.

(10) Tsubokura, K.; Vong, K. K. H.; Pradipta, A. R.; Ogura, A.; Urano, S.; Tahara, T.; Nozaki, S.; Onoe, H.; Nakao, Y.; Sibgatullina, R.; Kurbangalieva, A.; Watanabe, Y.; Tanaka, K. *In vivo* Gold Complex Catalysis within Live Mice. *Angewandte Chemie International Edition* **2017**, *56* (13), 3579–3584. https://doi.org/10.1002/ANIE.201610273.

(11) Learte-Aymamí, S.; Vidal, C.; Gutiérrez-González, A.; Mascareñas, J. L. Intracellular Reactions Promoted by Bis(Histidine) Miniproteins Stapled Using Palladium(II) Complexes. *Angewandte Chemie International Edition* **2020**, *59* (23), 9149–9154. https://doi.org/10.1002/ANIE.202002032.

(12) Konč, J.; Sabatino, V.; Jiménez-Moreno, E.; Latocheski, E.; Pérez, L. R.; Day, J.; Domingos, J. B.; Bernardes, G. J. L. Controlled In-Cell Generation of Active Palladium(0) Species for Bioorthogonal Decaging. *Angewandte Chemie - International Edition* **2022**, *61* (8). https://doi.org/10.1002/anie.202113519.

(13) Bai, Y.; Chen, J.; Zimmerman, S. C. *Designed Transition Metal Catalysts for Intracellular Organic Synthesis*; Royal Society of Chemistry, 2018; Vol. 47, pp 1811–1821.

https://pubs.rsc.org/en/content/articlehtml/2018/cs/c7cs00447h (accessed 2020-06-04).

(14) Rebelein, J. G.; Ward, T. R. *In vivo* Catalyzed New-to-Nature Reactions. *Curr Opin Biotechnol* **2018**, *53*, 106–114. https://doi.org/10.1016/J.COPBIO.2017.12.008.

(15) Völker, T.; Meggers, E. Chemical Activation in Blood Serum and Human Cell Culture: Improved Ruthenium Complex for Catalytic Uncaging of Alloc-Protected Amines. *ChemBioChem* **2017**, *18* (12), 1083–1086. https://doi.org/10.1002/CBIC.201700168.

(16) Völker, T.; Dempwolff, F.; Graumann, P. L.; Meggers, E. Progress towards Bioorthogonal Catalysis with Organometallic Compounds. *Angew Chem Int Ed Engl* **2014**, *53* (39), 10536–10540. https://doi.org/10.1002/anie.201404547.

(17) Pérez-López, A. M.; Rubio-Ruiz, B.; Sebastián, V.; Hamilton, L.; Adam, C.; Bray, T. L.; Irusta, S.; Brennan, P. M.; Lloyd-Jones, G. C.; Sieger, D.; Santamaría, J.; Unciti-Broceta, A. Gold-Triggered Uncaging Chemistry in Living Systems. *Angewandte Chemie International Edition* **2017**, *56* (41), 12548–12552. https://doi.org/10.1002/ANIE.201705609.

(18) Destito, P.; Sousa-Castillo, A.; Couceiro, J. R.; López, F.; Correa-Duarte, M. A.; Mascareñas, J. L. Hollow Nanoreactors for Pd-Catalyzed Suzuki-Miyaura Coupling and O-Propargyl Cleavage Reactions in Bio-Relevant Aqueous Media. *Chem Sci* **2019**, *10* (9), 2598–2603. https://doi.org/10.1039/C8SC04390F.

(19) Unciti-Broceta, A.; Johansson, E. M. V.; Yusop, R. M.; Sánchez-Martín, R. M.; Bradley, M. Synthesis of Polystyrene Microspheres and Functionalisation with Pd0 Nanoparticles to Perform Bioorthogonal Organometallic Chemistry in Living Cells. *Nat Protoc* **2012**, *7* (6), 1207–1218. https://doi.org/10.1038/nprot.2012.052.

(20) Rajagopalan, T. G.; Stein, W. H.; Moore, S. The Inactivation of Pepsin by Diazoacetylnorleucine Methyl Ester. *Journal of Biological Chemistry* **1966**, *241* (18), 4295–4297. https://doi.org/10.1016/S0021-9258(18)99785-1.

(21) Carminati, D. M.; Fasan, R. Stereoselective Cyclopropanation of Electron-Deficient Olefins with a Cofactor Redesigned Carbene Transferase Featuring Radical Reactivity. *ACS Catal* **2019**, *9* (10), 9683–9697. https://doi.org/10.1021/ACSCATAL.9B02272/ASSET/IMAGES/MEDIUM/CS9B02272_M002.GIF.

(22) van Oers, M. C. M.; Abdelmohsen, L. K. E. A.; Rutjes, F. P. J. T.; van Hest, J. C. M. Aqueous Asymmetric Cyclopropanation Reactions in Polymersome Membranes. *Chemical Communications* **2014**, *50* (31), 4040–4043. https://doi.org/10.1039/C3CC48865A.

(23) Mix, K. A.; Aronoff, M. R.; Raines, R. T. Diazo Compounds: Versatile Tools for Chemical Biology. *ACS Chem Biol* **2016**, *11* (12), 3233–3244. https://doi.org/10.1021/ACSCHEMBIO.6B00810/ASSET/IMAGES/MEDIUM/CB-2016-008105_0006.GIF.

(24) Andersen, K. A.; Aronoff, M. R.; McGrath, N. A.; Raines, R. T. Diazo Groups Endure Metabolism and Enable Chemoselectivity in Cellulo. *J Am Chem Soc* **2015**, *137* (7), 2412–2415. https://doi.org/10.1021/JA5095815/SUPPL_FILE/JA5095815_SI_001.PDF.

(25) Gutiérrez, S.; Tomás-Gamasa, M.; Mascareñas, J. L. Exporting Metal-Carbene Chemistry to Live Mammalian Cells: Copper-Catalyzed Intracellular Synthesis of Quinoxalines Enabled by N−H Carbene Insertions. *Angewandte Chemie* **2021**. https://doi.org/10.1002/ANGE.202108899.

(26) Sletten, E. M.; Bertozzi, C. R. Bioorthogonal Chemistry: Fishing for Selectivity in a Sea of Functionality. *Angewandte Chemie - International Edition*. September 7, 2009, pp 6974–6998. https://doi.org/10.1002/anie.200900942.

(27) Ramakrishna, K.; Sivasankar, C. Iridium Catalyzed Acceptor/Acceptor Carbene Insertion into N-H Bonds in Water. *Org Biomol Chem* **2017**, *15* (11), 2392–2396. https://doi.org/10.1039/c7ob00177k.

(28) Gillingham, D.; Fei, N. Catalytic X-H Insertion Reactions Based on Carbenoids. *Chem. Soc. Rev* **2013**, *42*, 4918. https://doi.org/10.1039/c3cs35496b.

(29) Anding, B. J.; Woo, L. K. Iridium Porphyrin Catalyzed N-H Insertion Reactions: Scope and Mechanism. *Organometallics* **2013**, *32* (9), 2599–2607. https://doi.org/10.1021/OM400098V/SUPPL_FILE/OM400098V_SI_001.PDF.

(30) Rioz-Martínez, A.; Oelerich, J.; Ségaud, N.; Roelfes, G. DNA-Accelerated Catalysis of Carbene-Transfer Reactions by a DNA/Cationic Iron Porphyrin Hybrid. *Angewandte Chemie International Edition* **2016**, *55* (45), 14136–14140.

https://doi.org/10.1002/ANIE.201608121.

(31) Srour, H. F.; Maux, P. Le; Chevance, S.; Carrié, D.; Yondre, N. Le; Simonneaux, G. Diazo Ester Insertion in NH Bonds of Amino Acid Derivatives and Insulin Catalyzed by Water-Soluble Iron and Ruthenium Porphyrin Complexes (FeTSPPCl) as Application of Carbenoid Transfer in Aqueous Media. *J Mol Catal A Chem* **2015**, *407*, 194–203. https://doi.org/10.1016/J.MOLCATA.2015.06.028.

(32) Abu-Elfotoh, A. M. NH Insertion Reactions Catalyzed by Reusable Water-Soluble Ruthenium(II)-Hm-Phenyloxazoline Complex. *Tetrahedron Lett* **2017**, *58* (51), 4750–4754. https://doi.org/10.1016/J.TETLET.2017.10.062.

(33) Minus, M. B.; Kang, M. K.; Knudsen, S. E.; Liu, W.; Krueger, M. J.; Smith, M. L.; Redell, M. S.; Ball, Z. T. Assessing the Intracellular Fate of Rhodium(II) Complexes. *Chemical Communications* **2016**, *52* (78), 11685–11688. https://doi.org/10.1039/C6CC05192H.

(34) Antos, J. M.; Mcfarland, J. M.; Iavarone, A. T.; Francis, M. B. Chemoselective Tryptophan Labeling with Rhodium Carbenoids at Mild PH. https://doi.org/10.1021/ja900094h.

(35) Antos, J. M.; Francis, M. B. Selective Tryptophan Modification with Rhodium Carbenoids in Aqueous Solution Scheme 1. Covalent Modification of Tryptophan Residues on Proteins Using Metallocarbenes Scheme 2. Modification of 3-Methylindole with Metallocarbenes in Aqueous Media. *J. AM. CHEM. SOC* **2004**, *126*, 10256–10257. https://doi.org/10.1021/ja047272c.

(36) Tishinov, K.; Schmidt, K.; Häussinger, D.; Gillingham, D. G. Structure-Selective Catalytic Alkylation of DNA and RNA. *Angewandte Chemie - International Edition* **2012**, *51* (48), 12000–12004. https://doi.org/10.1002/ANIE.201205201.

(37) Snyder, J. P.; Padwa, A.; Stengel, T. A Stable Dirhodium Tetracarboxylate Carbenoid: Crystal Structure, Bonding Analysis, and Catalysis [15]. *J Am Chem Soc* **2001**, *123* (45), 11318–11319. https://doi.org/10.1021/JA016928O/SUPPL_FILE/JA016928O_S1.PDF.

(38) Nicolas, I.; Le Maux, P.; Simonneaux, G. Asymmetric Catalytic Cyclopropanation Reactions in Water. *Coord Chem Rev* **2008**, *252* (5–7), 727–735. https://doi.org/10.1016/j.ccr.2007.09.003.

(39) Wynne, D. C.; Olmstead, M. M.; Jessop, P. G. Supercritical and Liquid Solvent Effects on the Enantioselectivity of Asymmetric Cyclopropanation with Tetrakis[1-[(4-Tert-Butylphenyl)-Sulfonyl]-(2S)-Pyrrolidinecarbox Ylate]Dirhodium(II). *J Am Chem Soc* **2000**, *122* (32), 7638–7647. https://doi.org/10.1021/JA000894N/SUPPL_FILE/JA000894N_S.PDF.

(40) Wurz, R. P.; Charette, A. B. Transition Metal-Catalyzed Cyclopropanation of Alkenes in Water: Catalyst Efficiency and *in situ* Generation of the Diazo Reagent. *Org Lett* **2002**, *4* (25), 4531–4533. https://doi.org/10.1021/ol0270879.

(41) Barberis, M.; Pérez-Prieto, J.; Herbst, K.; Lahuerta, P. Chiral Dirhodium(II) Catalysts with Ortho-Metalated Arylphosphine Ligands: Synthesis and Application to the Enantioselective Cyclopropanation of α-Diazo Ketones. *Organometallics* **2002**, *21* (8), 1667–1673. https://doi.org/10.1021/OM0110437/ASSET/IMAGES/LARGE/OM0110437H00002.JPEG.

(42) Adly, F. G. On the Structure of Chiral Dirhodium(II) Carboxylate Catalysts: Stereoselectivity Relevance and Insights. *Catalysts 2017, Vol. 7, Page 347* **2017**, *7* (11), 347. https://doi.org/10.3390/CATAL7110347.

(43) Doyle, M. P. Perspective on Dirhodium Carboxamidates as Catalysts. *Journal of Organic Chemistry* **2006**, *71* (25), 9253–9260. https://doi.org/10.1021/JO061411M/ASSET/IMAGES/LARGE/JO061411MF10.JPEG.

(44) Melillo, D. G.; Shinkai, I.; Liu, T.; Ryan, K.; Sletzinger, M. A Practical Synthesis of (±)-Thienamycin. *Tetrahedron Lett* **1980**, *21* (29), 2783–2786. https://doi.org/10.1016/S0040-4039(00)78606-0.

(45) Ter Huurne, G. M.; De Windt, L. N. J.; Liu, Y.; Meijer, E. W.; Voets, I. K.; Palmans, A. R. A. Improving the Folding of Supramolecular Copolymers by Controlling the Assembly Pathway Complexity. *Macromolecules* **2017**, *50* (21), 8562–8569. https://doi.org/10.1021/acs.macromol.7b01769.

(46) Pandit, R. P.; Kim, S. H.; Lee, Y. R. Iron-Catalyzed Annulation of 1,2-Diamines and Diazodicarbonyls for Diverse and Polyfunctionalized Quinoxalines, Pyrazines, and Benzoquinoxalines in Water. *Adv Synth Catal* **2016**, *358* (22), 3586–3599. https://doi.org/10.1002/ADSC.201600503.

(47) Gutiérrez, S.; Tomás-Gamasa, M.; Mascareñas, J. L. Exporting Metal-Carbene Chemistry to Live

Mammalian Cells: Copper-Catalyzed Intracellular Synthesis of Quinoxalines Enabled by N–H Carbene Insertions. *Angewandte Chemie* **2021**, *133* (40), 22188–22196. https://doi.org/10.1002/ange.202108899.

(48) Blevins, D. J.; Nazir, R.; Hossein Dabiri, S. M.; Akbari, M.; Wulff, J. E. The Effects of Cell Culture Conditions on Premature Hydrolysis of Traceless Ester-Linked Disulfide Linkers. *J Drug Deliv Sci Technol* **2022**, *78*, 103950. https://doi.org/10.1016/J.JDDST.2022.103950.

(49) Deng, L.; Albertazzi, L.; Palmans, A. R. A. Elucidating the Stability of Single-Chain Polymeric Nanoparticles in Biological Media and Living Cells. *Biomacromolecules* **2022**, *23* (1), 326–338. https://doi.org/10.1021/acs.biomac.1c01291.

(50) Li, F.; Xiao, L.; Liu, L. Metal-Diazo Radicals of α-Carbonyl Diazomethanes. *Scientific Reports 2016 6:1* **2016**, *6* (1), 1–8. https://doi.org/10.1038/srep22876.

(51) Sun, Z.; Chen, Y.; Yao, S.; Yuan, H.; Song, D.; Guo, Z.; He, W. Photoinduced Carbene for Effective Photodynamic Therapy Against Hypoxic Cancer Cells. *CCS Chemistry* **2022**, 1–10. https://doi.org/10.31635/CCSCHEM.022.202202324.

(52) Zhang, X.; Huang, R.; Gopalakrishnan, S.; Cao-Milán, R.; Rotello, V. M. Bioorthogonal Nanozymes: Progress towards Therapeutic Applications. *Trends in Chemistry*. Cell Press April 1, 2019, pp 90–98. https://doi.org/10.1016/j.trechm.2019.02.006.

(53) Lipshutz, B. H.; Ghoraib, S. "Designer"-Surfactant-Enabled Cross-Couplings in Water at Room Temperature. *Aldrichimica Acta* **2012**, *45* (1), 3.

(54) Lipshutz, B. H.; Ghorai, S. Transitioning Organic Synthesis from Organic Solvents to Water. What's Your E Factor? *Green Chemistry* **2014**, *16* (8), 3660–3679. https://doi.org/10.1039/C4GC00503A.

(55) Lipshutz, B. H.; Ghorai, S.; Abela, A. R.; Moser, R.; Nishikata, T.; Duplais, C.; Krasovskiy, A.; Gaston, R. D.; Gadwood, R. C. TPGS-750-M: A Second-Generation Amphiphile for Metal-Catalyzed Cross-Couplings in Water at Room Temperature. *Journal of Organic Chemistry* **2011**, *76* (11), 4379–4391. https://doi.org/10.1021/JO101974U/SUPPL_FILE/JO101974U_SI_001.PDF.

(56) Wallace, S.; Balskus, E. P. Designer Micelles Accelerate Flux Through Engineered Metabolism in E. Coli and Support Biocompatible Chemistry. *Angewandte Chemie International Edition* **2016**, *55* (20), 6023–6027. https://doi.org/10.1002/ANIE.201600966.

(57) Lipinski, C. A.; Lombardo, F.; Dominy, B. W.; Feeney, P. J. Experimental and Computational Approaches to Estimate Solubility and Permeability in Drug Discovery and Development Settings. *Adv Drug Deliv Rev* **2001**, *46* (1–3), 3–26. https://doi.org/10.1016/S0169-409X(00)00129-0.

Chapter 5

Cu(I) amphiphilic polymeric nanoparticles: from ensemble to single-particle catalysis

Abstract: In this work, the diversity of reactivity of catalytic Cu(I) SCPNs is evaluated at the single-particle level using single-molecule fluorescence microscopy. To this end, amphiphilic polymers functionalised with Cu-binding ligand, biotin, hydrophobic and hydrophilic grafts were developed to perform depropargylation and azide-alkyne click reactions in water with high efficiency. Dimethylpropargyl-protected pro-dyes based on rhodamine and resorufin were developed as substrates for depropargylation reactions and the most suitable substrate was identified for single-molecule studies. The catalytic behaviour of these SCPNs was first evaluated at the ensemble level which revealed enzyme-like kinetics and simplified the determination of their turnover frequency. Further, single-molecule kinetic studies were performed, which for the first time revealed the diversity in reactivity of individual SCPNs within the same batch during depropargylation reactions in water. The amphiphilic polymers with different hydrophobic pendant groups behaved similarly, exhibiting the same average turnover frequency during single-molecule studies, which was consistent with ensemble measurements. But, the turnover frequencies determined from single-molecule kinetic studies were significantly lower than those from the ensemble. The initial findings from single-molecule SCPN catalysis appear to be promising, as they have the potential to reveal differences in reactivity that may be attributed to structural heterogeneity.

This work has been performed in close collaboration with Emmanouil Archontakis (microscopy measurements and analysis).

5.1 Introduction

Enzymes are Nature's macromolecular biological catalysts and show remarkable activity, selectivity, and specificity, which have been fine-tuned through millions of years of natural selection.[1] Their intricate three-dimensional structures and precise positioning of catalysts for specific substrate binding have made them an ideal template for the design of synthetic catalysts. Chemists have long sought to mimic them, one such approach being the folding of synthetic polymer chains around metal catalysts to form catalytic single-chain polymeric nanoparticles (SCPNs), which loosely resemble the folded polypeptide structure of metalloenzymes.[2,3] With the advances in the field, there are few reports where catalytic SCPNs have shown enzyme-like kinetics, substrate binding, high reaction rate and selectivity during the last few years.[3–6] Although significant progress has been made in their development, their catalytic performance lags significantly behind that of enzymes. Unlike enzymes, catalytic SCPNs possess inherent structural heterogeneity that arises from the stochastic incorporation of the different monomers and catalytic moieties, as well as the varying molar mass of the copolymers. As a consequence, each SCPN is expected to exhibit unique catalytic activity and selectivity, owing to the non-uniform distribution of catalytic sites in different microenvironments.[2] Quantitative analysis of the catalytic activity of SCPNs at the ensemble level only provides an average value of their catalytic activity, which limits our understanding of the diversity of catalytic potential at the single-polymer level. Therefore, developing a technique to directly monitor the catalytic activity of individual SCPNs is required to gain insights into the effect of structural heterogeneities on its catalytic performance in future.[2]

Single-molecule fluorescence microscopy (SMFM) is a valuable tool that has already been utilized to study the kinetic behavior of individual immobilised enzymes at single turnover resolution. When non-fluorescent substrates are converted to fluorescent products that diffuse out of the confocal volume, fluorescent bursts can be visualised using a super-resolution microscope. These burst can be used to determine the catalytic activity of individual enzymes.[7] The pioneering work of Michaelis and Menten[8] or the subsequent works for the analysis of the enzyme kinetics were based on the assumption that all individual enzymes in a solution are identical.[7] Xie and co-workers were the first to report single-molecule enzyme kinetics in 1988.[9] They revisited the Michael-Menten kinetics in a single-molecule context, and concluded that single-molecule enzyme catalysis also showed saturation kinetics similar to ensemble measurements but new microscopic interpretations were given to the Michaelis-Menten equation (vide infra, section 5.5.1).[10,11] The single molecule studies have revealed that the catalytic rates in a population of enzymes are heterogeneous resulting in a distribution of rate constants due to their static and dynamic heterogeneity.[12] Enzymes are susceptible to structural variations during their expression and storage, which can affect their intrinsic catalytic properties leading to static heterogeneity. Temporal fluctuations in the catalytic activity of enzymes are also observed that arise due to the changes in the conformation of the enzymes over time leading to differences in their catalytic activity. This is the cause of dynamic heterogeneity.[12] Even in enzymes that are monodisperse and structurally homogeneous, minor fluctuations in catalytic activity can be probed by single-molecule catalysis, especially temporal fluctuations which are impossible to track during ensemble measurements.[1] Therefore, it is clear that SMFM measurements help to look at the activity of individual catalysts with spatiotemporal resolution. Single-molecule approaches for single-enzyme studies have now been employed in studying nano and microscale heterogeneous catalysts.[13–17] In the pioneering work of Chen and co-workers, they investigated the heterogeneous reactivity of Au nanoparticles at the single-molecule level. Their study also revealed activity fluctuations over time due to both catalysis-induced and spontaneous surface restructuring of the catalysts.[13]

When it comes to SCPNs, single-molecule approaches will be highly beneficial to probe the intrinsic and temporal heterogeneity in their catalytic activity. This requires the development of catalysts with high turnover frequency to obtain good statistics for a reliable interpretation of the data. Despite the challenges in attaining sufficiently high turnover frequencies in synthetic systems, it is worthwhile to start taking crucial first step so that we can gain a deeper understanding of the heterogeneity in synthetic compartmentalised catalysts. Recently, the single-particle polarity of SCPNs has been successfully probed by Archontakis *et al.* using Nile Red-based spectral point accumulation for imaging in nanoscale topography (NR-sPAINT) super-resolution fluorescence technique. This unveiled the heterogeneity in polarity within the individual nanoparticles in the same batch (intraparticle heterogeneity) and across different polymer designs (interparticle heterogeneity).[18] Therefore, this study emphasizes the possibility of establishing a technique to study heterogeneity in the catalytic function of SCPNs at single-particle level.

In our group, Liu *et al.* have previously taken first steps to evaluate the single-particle kinetics of SCPNs using confocal microscopy. Catalytic Cu-SCPNs were successfully immobilised on the surface of glass coverslips, and were found to retain their catalytic activity. However, issues such as low TOF of the catalyst and low signal-to-noise ratio in measurements were encountered.[2] To overcome the above-mentioned challenges, in this work, we aim to use super-resolution microscopy to study SCPN kinetics at the single-particle level. Towards this, we developed highly efficient and fast Cu(I) SCPNs that exhibited high turnover frequencies towards depropargylation and azide-alkyne click reaction (CuAAC). We attempted to improve the signal-to-noise ratio by developing dimethylpropargyl-protected substrates based on resorufin and rhodamine activable by Cu(I) SCPNs. The enzyme-like catalytic behavior of SCPNs was evaluated to determine the turnover frequency at the ensemble level. Finally, catalytic SCPNs were immobilised on coverslips and conditions were optimized to study their activation kinetics at the single-particle level. The preliminary results of single-molecule catalysis revealed the heterogeneity in catalytic activity between different nanoparticles within the same batch.

5.2 Design and synthesis of fluorogenic substrates

The design of proper fluorogenic substrates is a crucial factor for single-molecule and ensemble kinetic analysis of SCPN catalysis. The ideal pro-fluorophores should be non-fluorescent and should not contribute to any background fluorescence. In this study, we chose Cu(I) catalysed reactions such as depropargylation and click reactions owing to their fast kinetics towards the catalytic formation of fluorophores. Both click and depropargylation reactions were initially studied at the ensemble level to assess their performance. However, depropargylation was finally selected for single-molecule studies due to its simpler one-substrate system, which facilitates analysis with less complexity. Also, it has the following additional advantages: (i) the protecting group on the substrates directly affects their reactivity and hereby the turnover frequency of Cu(I) SCPNs can be tuned; (ii) hydrophobic substrates partition preferably into the hydrophobic catalytic domains of the SCPNs, but the formation of products that are more hydrophilic will allow product diffusion to the solution at nanomolar/picomolar concentration.

CuAAC reactions were performed on commercially available azide and alkyne substrates to check the efficiency of the Cu(I) SCPNs. For the depropargylation, substrates were designed with dimethyl propargyl as the protecting group to render the fluorophores non-fluorescent. Single-molecule studies demand fluorophores with high brightness for a good signal-to-noise ratio and they also require good photostability. We selected rhodamine 110 and resorufin, which were previously used for single-molecule enzyme and heterogeneous catalysis studies[13,19](Scheme 1). Pro-res **1** and **2** have dimethyl propargylic carbonate and an ether protection, respectively (Scheme 1A). Pro-rho **3** has dimethyl propargylic carbamate protection based on morpholine carbonyl rhodamine 110 (McRh110) **5** (Scheme 1A,B).

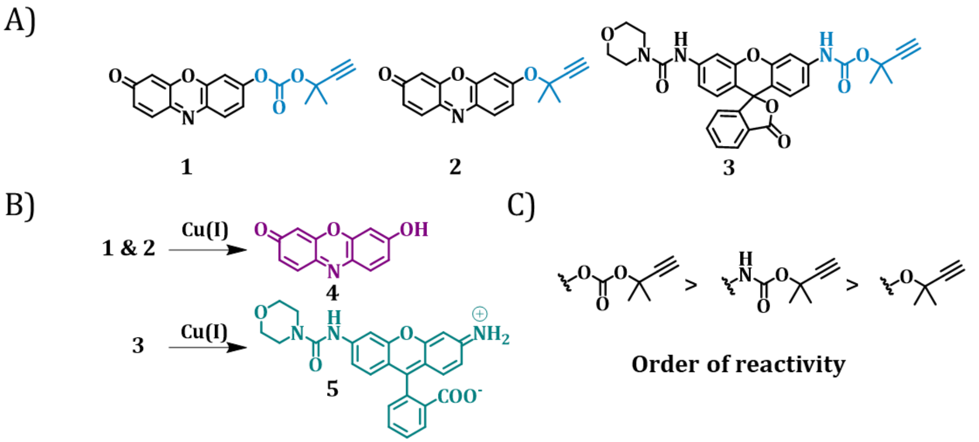

Scheme 1: A) Chemical structures of dimethylpropargyl masked pro-dyes of resorufin and McRh110 B) Chemical structure of fluorophores after activation of pro-dyes using Cu(I) in water C) Decreasing order of reactivity of protecting group towards depropargylation reaction catalysed by Cu(I) catalyst.

McRh110 **5** was used to ensure that there is only one cleavable group. This simplifies the interpretation of results since fluorescent reaction intermediates with different fluorescence properties will complicate the analysis. The three protecting groups *O*-carbonyl propargyl, *N*-carbamate propargyl and *O*-propargyl show a decrease in the activity towards depropargylation by Cu(I) (Scheme 1C) and will help to identify the best substrate for single-molecule studies. The synthesis protocol of the newly developed pro-dyes pro-res **1** and pro-res **2** can be found in the experimental section. Pro-rho **3** was synthesized according to a previously reported protocol.[2]

5.3 Synthesis and characterization of Cu(I) based amphiphilic polymeric nanoparticles

In order to observe the turnover of substrates to products in a reasonable timescale during single-molecule kinetic studies, it is crucial for the reactions to be fast, although it is not possible to match the efficiency of enzymes. The first step towards achieving high turnover frequencies is the selection of appropriate ligands for the Cu catalyst that can enhance the reaction rate of depropargylation or click reactions. In previous work, our group has investigated the performance of bimpy (mono(benzimidazoylmethyl)-bis(pyridylmethyl)) and phenanthroline-based SCPNs, where bimpy-based SCPNs were observed to be faster towards click reactions in water.[20] Here, we aimed to explore the potential of alternative ligands with higher efficiency than that of bimpy.

Copper-binding proteins occurring in nature predominantly employ amino acids glycine and histidine as chelating ligands. The strong binding properties of histidine and its analogous triazole group have already been studied and they are used as building blocks for CuAAC ligands.[21] Glycine derivative ligand **6** (gly) has recently been reported to enhance the reaction rate of copper-catalysed click reactions while having excellent biocompatibility.[21] We, therefore, envisaged this ligand will show the same rate acceleration when applied in a depropargylation reaction. The gly **6** ligand was synthesized from glycine methyl ester according to the reported protocol.[21] In addition, DTE ligand **7** functionalised with the oxazoline group was found to serve as an accelerating ligand towards CuAAC by Presolski's group (unpublished results) and was obtained from them for comparison. DTE is a thermally irreversible photochromic scaffold, that can be toggled between a flexible “open” and more rigid “closed” form with distinct steric and electronic properties. [22,23] When DTE is functionalised with oxazoline group, the open and closed conformation can have a different binding affinity towards copper.[22,23] This can also help to tune reaction kinetics providing spatiotemporal control and was therefore interesting to look at. The two new ligands were compared with the previously used bimpy **8** to investigate the rate acceleration in Cu-catalysed depropargylation reactions. In all cases, we used pro-rho **3** as the substrate for the depropargylation reactions in water at a 1:1 ligand-to-copper ratio. The appropriate ligands was mixed with $CuSO_4$, which was reduced *in situ* to Cu(I) using sodium ascorbate before the start of the reaction. Then, the pro-rho **3** was added, and the formation of the product McRh110 **5** was monitored using fluorescence spectroscopy over time. The results showed that gly **6** was found to catalyse the reaction faster when compared and DTE performed the least (Figure 1B). Therefore, gly **6** was chosen for incorporation into the polymer backbone.

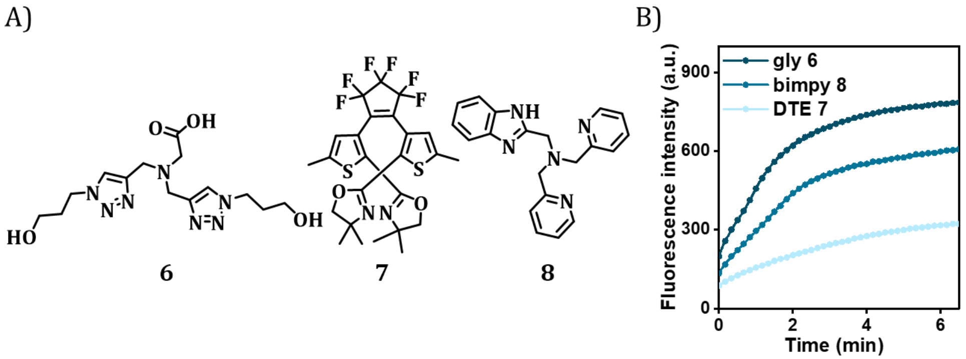

Figure 1: A) Chemical structures of Cu(I) binding ligands gly **6**, DTE **7** and bimpy **8**, which were all screened for depropargylation reactions in water. B) Fluorescence kinetic profiles for the activation of pro-rho **3** using **6-8** as ligands for Cu(I) in water, [pro-rho **3**] = 30 µM, [**6-8**] = 30 µM, [$CuSO_4$] = 30 µM, [NaAsc] = 2 mM, T = 37 °C. λ_{ex}= 485 nm and λ_{em} = 520 nm.

To incorporate the gly ligand **6** into the amphiphilic polymer backbone, a covalent crosslinking strategy was used as previously reported by Zimmerman and co-workers[4] (Scheme 2). This strategy allows facile incorporation of ligand

6, leaving the carboxylate anion free to give additional stabilization for the Cu(I) ion. At first, the poly(pentafluorophenyl acrylate) homopolymer ***p*PFPA$_{180}$** was synthesized with a degree of polymerisation, DP = 180 and molar mass dispersity (*Đ*) of 1.19), which is similar as polymers reported in earlier chapters. This polymer backbone was further functionalised with pendant groups to make polymer precursors **P1$_a$-P5$_a$** with the following pendant groups: (i) biotin for immobilising catalytic SCPN on streptavidin functionalised coverslips for the single-molecule studies, (ii) dodecyl azide to allow intramolecular crosslinking with diyne **4** via CuAAC to install the gly **6** ligand into the polymer, (iii) *n*-dodecyl for additional hydrophobicity, (iv) BTAs for a structured hydrophobic interior and (v) Jeffamine M-1000 for imparting hydrophilicity. Amphiphilic polymers **P1$_a$-P5$_a$** were designed with varying degrees of pendant groups (Scheme 2). Table 1 summarizes the details of the polymer composition. We aimed for an incorporation of around 3% biotin and ~20% dodecyl azide (except **P5$_a$** which has ~40% dodecyl azide). **P1$_a$-P3$_a$** were designed to have varying amounts of the hydrophobic grafts, where **P1$_a$** has only dodecyl azide for hydrophobicity, **P2$_a$** has an additional ~5% BTA for a more structured hydrophobic interior and **P3$_a$** has ~15% dodecyl instead of BTA (Table 1, Scheme 2). We wanted to investigate if the changes in the hydrophobic interior affect the kinetics of the reaction both at the ensemble as well as the single-particle level. **P4$_a$** has ~20% BTA and was aimed to promote intermolecular aggregation for the formation of multichain aggregates. It has been previously established that an incorporation of more than 10% BTA pendant groups induces intermolecular aggregation via hydrogen bonds.[24] In **P5$_a$**, ~40% dodecyl azide units were incorporated to promote interchain covalent crosslinking to form aggregates. Both types of aggregates may show a different reactivity and are therefore interesting to evaluate.

Amphiphilic polymers **P1$_a$-P3$_a$** were first formulated to SCPNs in water (20 mg/mL) and were then intramolecularly crosslinked using diyne **4** by CuAAC reaction according to a reported protocol.[4] After the reaction, copper was removed using a Chelex resin and the polymers were dialyzed in water for 5 days to obtain **P1-P3**. The presence of copper hindered the characterization of polymers afterwards and also its removal allowed more precise control over the amount of copper used for catalysis measurements. The complete removal of copper was therefore confirmed using MP-AES spectroscopy for **P1** and further using control experiments during catalysis. The incorporation of the ligand was confirmed by IR spectroscopy by the disappearance of the peak 2096 cm^{-1} corresponding to the azide group (Figure 12A). **P4$_a$-P5$_a$** were used to form aggregated particles **P4-P5**, therefore the above protocol was performed in a mixture of THF/water and at a higher concentration (50 mg/mL), where THF promoted the solubility of these polymers, enhancing intermolecular crosslinking.[25]

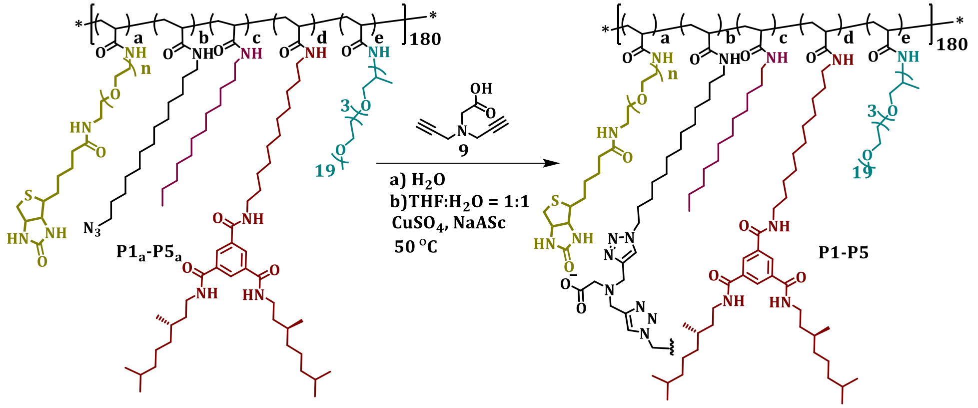

Scheme 2: Chemical structure of amphiphilic polymers functionalised with biotin, dodecyl azide, dodecyl, BTA and Jeffamine M-1000 **P1$_a$-P5$_a$** and the subsequent incorporation of diyne **9** to obtain ligand-functionalised amphiphilic polymers **P1-P5** by CuAAC reaction (details in experimental section). Reaction medium: **P1-P3** in H_2O, **P4-P5** in THF: H_2O (1:1).

The size of the polymeric nanoparticles before and after the incorporation of the ligand was monitored using dynamic light scattering experiments (DLS). All polymer precursors **P1$_a$-P3$_a$** and **P5$_a$** formed nanoparticles with hydrodynamic radius (R_H) of 4-5 nm. **P4$_a$** formed particles of R_H = 9.2 nm, similar to the observations reported by ter Huurne *et al.,* suggesting BTA-induced aggregates of 2 or more chains.[24] After incorporation of gly **6** ligand, **P1-P3** showed the same or slightly smaller hydrodynamic radii of 3-5 nm confirming the formation of intramolecularly crosslinked SCPNs (Table 1). While **P4-P5** exhibited R_H of 50 nm indicating the formation of intermolecular aggregates. Size exclusion chromatography (SEC) of the polymer precursors **P1$_a$-P5$_a$** in DMF, indicated all polymers have similar polydispersity (*Đ*) of 1.2. After ligand incorporation, SEC was performed in PBS. **P1-P3** were again found to have similar dispersity (*Đ*) as that of their precursors (*Đ* =1.3) while **P5** has a dispersity of 1.98, with a shorter retention time (6.5 min) than that of **P1-P3** (8.5 min) confirming the presence of large aggregated particles (Figure 2B). An overview of R_H and polydispersity (*Đ*) of all polymers can be found in Table 1.

Table 1: Overview of the copolymer composition, number-average molecular weight (M_n) and molar mass dispersity (*Đ*) of ***p*PFP$_{180}$** and **P1-P5**. Hydrodynamic radius (R_H) of nanoparticles before (**P1$_a$-P5$_a$**) and after incorporation of the ligand (**P1**-**P5**)in H_2O.

Polymer	a	b	c	d	e	*Đ*	$M_{n,\,SEC}$ (kD)	$M_{n,\,theoretical}$ (kD)	R_H (nm)
***p*PFPA$_{180}$**						1.19[a]	30.2[a]	42	-
P1$_a$	3	18	-	-	71	1.21[b]	59.1[b]	161	4.3
P2$_a$	3	18	-	5	69	1.20[b]	44.3[b]	158	5.0
P3$_a$	3	18	12	-	67	1.25[b]	47.5[b]	165	5.0
P4$_a$	3	17	-	17	53	1.26[b]	44.4[b]	155	9.2
P5$_a$	3	36	-	-	59	1.25[b]	50.3[b]	153	5.4
P1	3	18	-	-	71	1.38[c]	15.5[c]	164	3.4
P2	3	18	-	5	69	1.35[c]	23.4[c]	161	4.9
P3	3	18	12	-	67	1.35[c]	16.3[c]	168	4.8
P4	3	17	-	17	53	n.d.[#]	n.d.[#]	-	51
P5	3	36	-	-	59	1.98[c]	77.5[c]	-	53
P6	-	-	20	-	80	1.16[b]	24.4[b]	181.0	6.0

a-e were determined by ^{19}F NMR. M_n and *Đ* were measured by SEC in [a]THF, relative to poly(styrene) standards, in [b] DMF with 10 mM LiBr, relative to poly(ethylene oxide) standards and [c]in H_2O, relative to poly(ethylene oxide) standards. Hydrolysis of pentafluorophenylacrylate backbone was observed during post-functionalisation with amines **P1$_a$** = 8%, **P2$_a$** = 5%, **P4$_a$** = 10% **P5$_a$** = 2%.[#]not determined as polymeric nanoparticles did not elute out of the column.

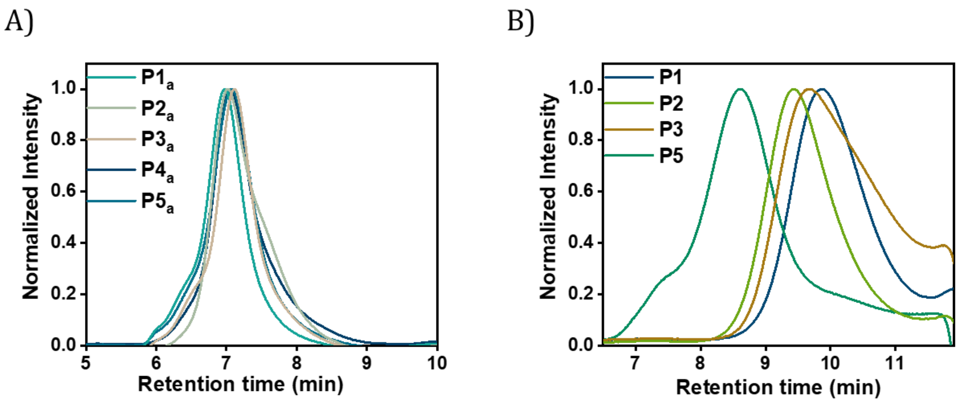

Figure 2: A) Normalised SEC traces in DMF of polymer precursors **P1ₐ-P5ₐ** (1 mg/mL). B) Normalised SEC traces in PBS of **P1-P5** after incorporation of ligand (1 mg/mL).

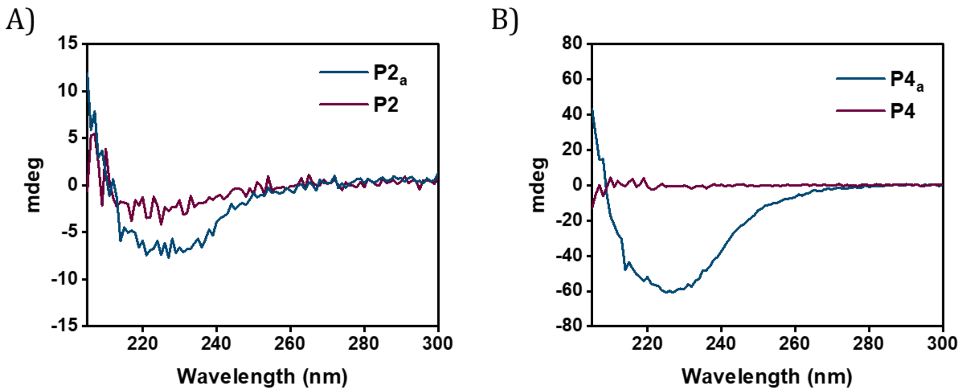

Figure 3: Circular dichroism spectra of polymeric nanoparticles A) **P2ₐ** and **P2** after intramolecular crosslinking B) **P4ₐ** and **P4** after intermolecular crosslinking. [**P**] = 0.5 mg/mL, T = 20 °C, in H_2O. Crosslinking of **P2ₐ** was performed at 20 mg/mL polymer concentration in H_2O. **P4ₐ** was performed at 50 mg/mL polymer concentration in H_2O: THF (1:1 v/v).

The self-assembly of BTA grafts before and after the incorporation of ligands was monitored using circular dichroism (CD spectroscopy). CD spectra of **P2ₐ** showed a negative CD signal centred around $\lambda = 225$ nm indicating the presence of left-handed (*M*) helical BTA stacks. However, the incorporation of the ligand reduced the size of the CD effect, indicating that BTA self-assembly is negatively affected in **P2** (Figure 3A). Polymer precursor **P4ₐ** also indicated the presence of BTA helical stacks. However, after intermolecular crosslinking in THF, a solvent that competes with hydrogen bonds, at very high concentrations of the polymer (50 mg/mL), the self-assembly was disrupted completely (Figure 3B).

5.4 Investigating catalytic efficiency of nanoparticles – click reactions on hydrophobic substrates

To check the efficiency of the developed SCPNs towards CuAAC reactions, coumarin azide was chosen as the substrate to react with various hydrophilic and hydrophobic alkynes (Scheme 3) to help us gain insights into the substrate scope of SCPNs in water. All SCPNs **P1-P3** have an average of 17 crosslinked ligand **6**, and therefore the same number of copper binding sites. At first, **P1-P3** were formulated to SCPNs in water and mixed with $CuSO_4$ in a 1:1 ligand:copper ratio to form **P1-P3@Cu(II)**. This ligand: copper ratio (1:1) was used as it is known that triazoles are weak binders of Cu(I) (advantageous for CuAAC) and multidentate interactions (from triazoles and central donor nitrogen atom) are therefore required to have a high overall affinity for the metal which is additionally stabilized by the carboxylate group.[26] The rate of the reaction between azide **10** and hydrophilic alkyne **11a** was first studied when Cu(II) was reduced before the start of the reaction using 2 mM sodium ascorbate to form **P1-P3@Cu(I)**. At 10 mol% Cu(I) concentration, the reactions with **P1-P3@Cu(I)** SCPNs were completed in 30 min, and exhibited similar kinetics despite the differences in polymer structure (Figure 4A). On the other hand, control experiments using polymer **P6@Cu(I)** without ligands or only **Cu(I)** did not proceed. The product formed was monitored using HPLC-UV. In this case, after the CuAAC reaction, the formed product **12a** is more hydrophilic than coumarin azide **10**, and eluted earlier from the column (Figure 4B).

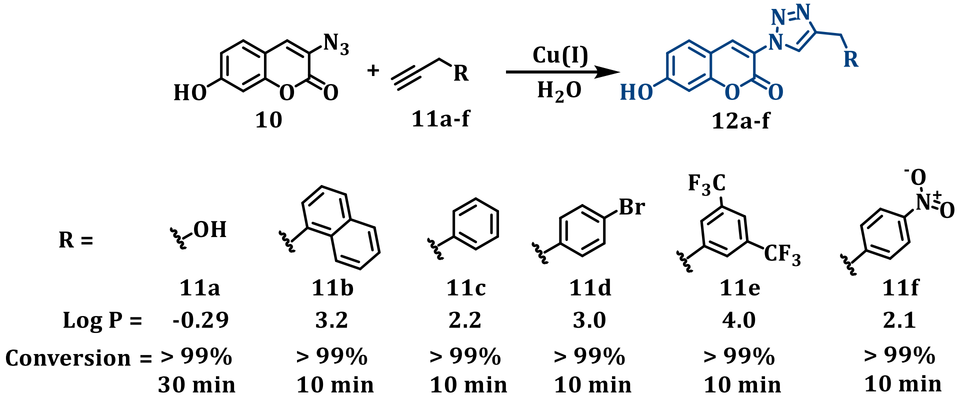

Scheme 3: Structures of coumarin azide **10** and alkynes **11a-f** to form fluorescent clicked products **12a-f**.

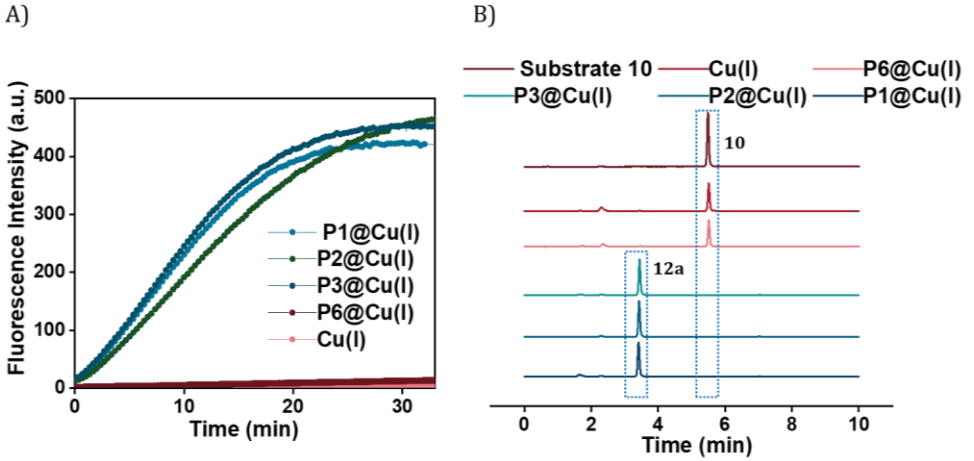

Figure 4: A) Fluorescence kinetic profile of CuAAC reaction between **10** and **11a** to form **12a** using **P1-P3@Cu(I)**, **P6@Cu(I)** and **Cu(I)**, in H_2O, [**Cu(I)**] = 10 µM, [**10**] = 100 µM, [**11a**] = 400 µM, [NaAsc] = 2 mM, [**P**] = ~600 nM, at room temperature, λ_{ex} = 340 nm and λ_{em} = 470 nm. B) HPLC-UV chromatogram after 35 min, showing complete disappearance of **10** and formation of **12a** in case of **P1-P3@Cu(I)**, monitored at λ = 340 nm.

Further, **P1@Cu(I)** was used to catalyse click reaction with a series of more hydrophobic alkynes **11a-f**. In all cases, the reaction was completed within 10 min, owing to the high hydrophobicity of the alkynes that ensure accumulation near the catalytic active site in the hydrophobic domain. Upon completion of the reactions, the resulting hydrophobic products **12b-f** (longer retention time in chromatogram compared to coumarin azide **10**, Figure 5) precipitated, leading to an inhomogeneous mixture. The results clearly show the crosslinked polymers are highly effective for click reactions. However, the right combination of substrates to form a hydrophilic product after the click reaction as is to case for **12a** is crucial to keep the reactions homogeneous.

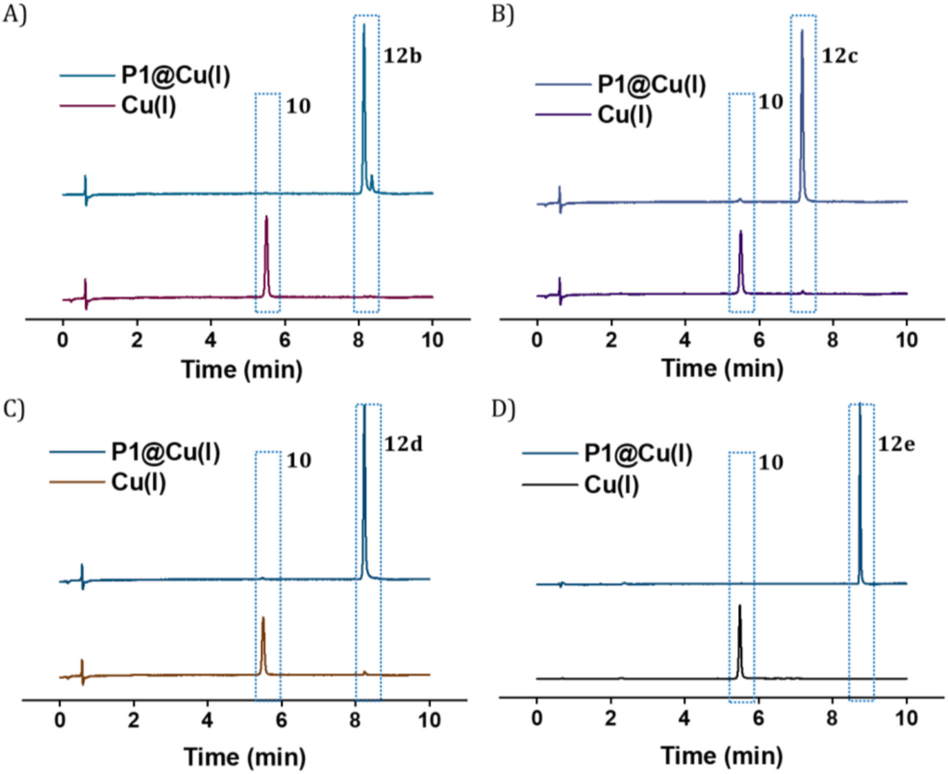

Figure 5: HPLC-UV chromatogram after CuAAC reaction between **10** and **11b-e** to form **12b-e** using **P1@Cu(I)** and **Cu(I)**, monitored after 10 min, at λ = 340 nm. Reaction conditions: in H_2O, [**Cu(I)**] = 10 µM, [**10**] = 100 µM, [**11b-e**] = 400 µM, [NaAsc] = 2 mM, [**P**] = ~600 nM, at room temperature.

5.5 Selection of the optimal substrate for single-particle catalysis

Crosslinked polymers are highly effective for the click reactions, which presents opportunities for investigating dual-substrate systems in single-molecule kinetic studies. However, we focus on one-substrate reactions because it simplifies the analysis for the initial optimisation of the system. To identify the optimal substrate that combines high reactivity in the presence of Cu(I) with the formation of a hydrophilic product that diffuses out of the hydrophobic pocket, we evaluated the efficacy of Cu(I) SCPNs in catalysing the depropargylation of substrates **1-3**. The rate of pro-dye activation was monitored using fluorescence spectroscopy over time. Catalytically active polymer **P1@Cu(I)**, control polymer **P6@Cu(I)** and free **Cu(I)** were compared in each case to see the effect of the ligand on rate acceleration. For reliable analysis of the heterogeneity in SCPN catalysis, functionalised polymers must exhibit high efficiency compared to free copper catalysts or copper catalysts in the presence of ligand-free polymers. Catalysis was performed at nanomolar concentrations of polymers (~120 nM, 0.02 mg/mL) in water and 30 μM substrate concentration, to assess their compatibility for single-molecule studies. At first, the activation of the highly reactive substrate pro-res **1** was monitored. The fluorescence kinetic curves indicated that the reaction proceeded fast and the fluorescence intensity saturated within 10 min for all **P1@Cu(I)**, **P6@Cu(I)** and **Cu(I)** (Figure 6A). Therefore, the presence of the covalently attached ligand is not required for fast turnover of the substrate. Also, substrate hydrolysis was observed in the presence of sodium ascorbate over a prolonged period of time (1 day). This implicated that pro-res **1** is not a good substrate for single-molecule studies as it cannot clearly bring out the heterogeneities in catalysis and can also get auto-hydrolysed to the product.

Secondly, the most stable substrate pro-res **2** was tested, under similar conditions and catalysts. The results indicated that **P1@Cu(I)** catalysed the reaction and exhibited a higher reaction rate than **P6@Cu(I)** and **Cu(I)** confirming the accelerating role of the ligand in depropargylation (Figure 6B). The reactions were then performed with **P1-P3@Cu(I)**, and all catalysed the reaction. However, full conversion of the product was only obtained after 4 h in each case (Figure 15B). This suggested that pro-res **2** may not be the most suitable substrate, as a long measurement time will be required for single molecule studies to see turnovers per particle.

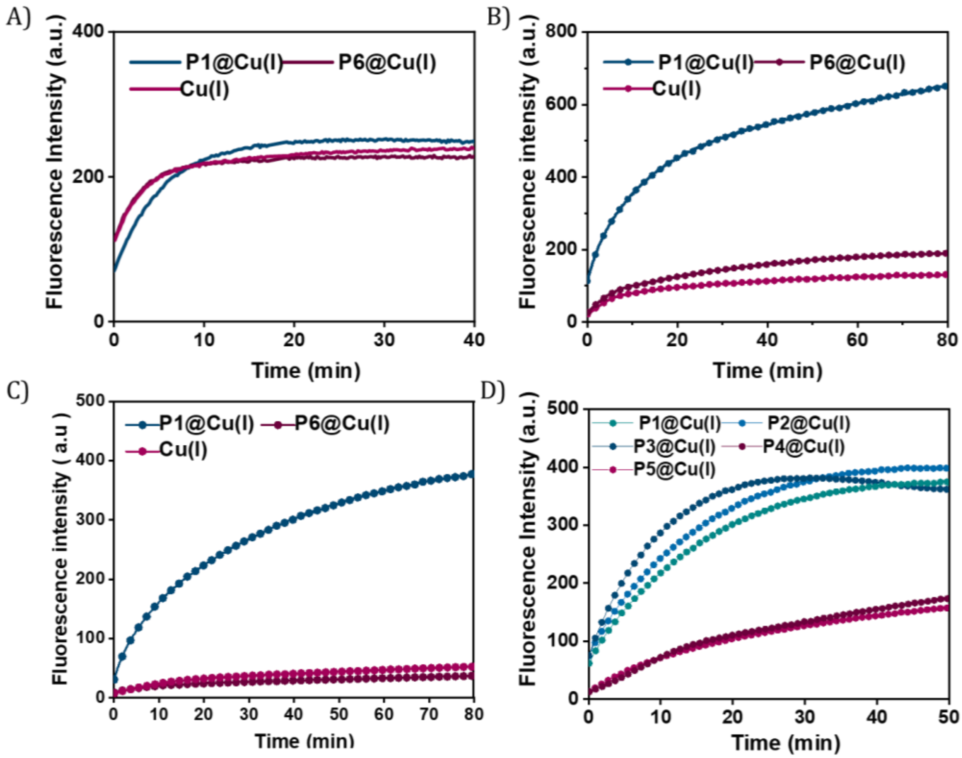

Figure 6: Fluorescence kinetic profile of depropargylation reaction of substrates **1**-**3** using **P1@Cu(I)**, **P6@Cu(I)** and **Cu(I)** in H_2O A) Activation of pro-res **1**, T = 20 °C B) Activation of pro-res **2**, T = 20 °C C) Activation of pro-rho **3**, T = 20 °C D) Activation of pro-rho **3** using **P1-P5@Cu(I)**, T = 37 °C. In all cases, [**Cu(I)**] = 2 μM, [**1-3**] = 30 μM, [NaAsc] = 2 mM, [**P**] = ~120 nM. A, B: λ_{ex} = 532 nm and λ_{em} = 587 nm. C, D: λ_{ex} = 485 nm and λ_{em} = 520 nm.

Thirdly, pro-rho **3** was tested, and the results were similar to that of pro-res **2**, where **P1@Cu(I)** catalysed the product formation faster than **P6@Cu(I)** and **Cu(I)** (Figure 6C). Near quantitative conversion was obtained within 80 min at 30 μM substrate concentration (Figure 15C). The complete consumption of the substrate was only observed at a higher temperature (37 °C) or at room temperature when substrate and catalyst concentrations were increased to 100 μM and 10 μM respectively (Figure 15C, D). Therefore, we chose to perform further studies at 37 °C.

A comparison of reaction kinetics at the ensemble level between all Cu(I) nanoparticles **P1-P5@Cu(I)** was then performed using pro-rho **3** as substrate. For **P1-P3@Cu(I)** SCPNs, the differences in the polymer microstructure did not show significant effects on their catalytic activity. However, intermolecularly cross-linked particles **P4-P5@Cu(I)** performed significantly poorer (Figure 6D). This may be caused by the absence of a well-defined hydrophobic catalytic domain as the ligands are formed by interchain crosslinking and therefore exposed in the hydrophilic region of particles. The substrates might have partitioned to the hydrophobic core of the large aggregates resulting in a slower reaction rate. In conclusion, pro-res **2** and pro-rho **3** seemed to be the most promising for single-particle kinetics.

5.6 Towards the optimization of single-particle kinetic studies

5.6.1 Insights into single-particle enzyme kinetics

Single-particle fluorescent microscopic techniques detect the formation of fluorescent products from non-fluorescent substrates catalysed by the immobilised nanocatalysts or enzymes on a coverslip. When excited with a laser beam of the required excitation wavelength of the product, product formation can be visualised as a sudden increase in fluorescence intensity. Similarly, when the product dissociates, a sudden decrease in intensity is followed. The dissociated product molecules move out of confocal volume and are undetectable due to their fast diffusion. These sudden intensity rise and fall or so-called fluorescent bursts are stochastic and can be recorded for individual nanocatalysts over time using a total internal reflection fluorescence microscope to get a time trajectory of fluorescence intensity (Figure 7A). Each on-off cycle consists of waiting times τ_{off} and τ_{on} and corresponds to the single turnover of the product formation and product dissociation, respectively. The reaction kinetics and corresponding kinetic parameters of individual nanoparticles can be studied using the statistical properties of stochastic τ_{off} such as their probability distributions and averages.[27,28]

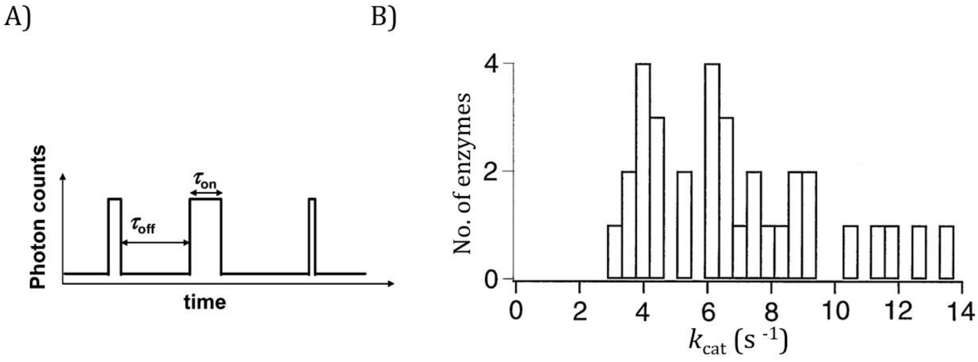

Figure 7: A) Schematic of single-molecule turnover trajectory showing off-on bursts of product formation[29] B) Distribution of k_{cat} from individual enzyme molecules in the same sample (Cholesterol Oxidase), from the work of Xie and co-workers. [30,31]

$$\mathrm{E + S} \underset{k_{-1}'}{\overset{k_1'}{\rightleftharpoons}} \mathrm{ES} \xrightarrow{k_{\text{cat}}} \mathrm{EP} \xrightarrow{\text{fast}} \mathrm{E + P} \qquad \textbf{(1)}$$

Equation 1: Elementary steps of the Michaelis-Menten model for enzyme catalysis[8,30] where E = enzyme, S = substrate, P = product, ES = enzyme-substrate complex, EP = enzyme-product complex.

$$V = \frac{V_{\text{max}}\,[\mathrm{S}]}{[\mathrm{S}] + K_{\mathrm{M}}} \qquad \textbf{(2)}$$

Equation 2: Ensemble MM equation[8,30] where [S] = substrate concentration, V = velocity of reaction, V_{max} = maximum velocity achieved by system, K_{m} = Michaelis constant.

$$<\tau>^{-1} = \frac{k_{\text{cat}}\,[\mathrm{S}]}{[\mathrm{S}] + K_{\mathrm{M}}} \qquad \textbf{(3)}$$

Equation 3: Single-molecule MM equation[10,30] where τ = waiting time before each product generation, [S] = substrate concentration, K_{m} = Michaelis constant, k_{cat} = turnover number of enzymes or turnover frequency of nanoparticles.

The kinetic behavior of the majority of the biocatalysts can be described using Michaelis-Menten (MM) model at the ensemble level. The mechanism is mainly one catalytic site and one substrate kinetic model, where an enzyme **E** binds to a substrate **S** to form enzyme-substrate complex **ES**, which transforms into enzyme product complex **EP**, which can release the product **P** to regenerate the enzyme **E** for the next catalytic cycle (1). The classic MM equation (2) describes the substrate concentration dependence of ensemble product formation rate, where the product formation rate v increases with the increase in the substrate concentration which eventually saturates to maximum rate v_{max}. $v_{\mathrm{max}} = k_{\mathrm{cat}}[\mathrm{E}]$ (Equation 4), where [E] is the total enzyme concentration and k_{cat} is the turnover number. Xie and co-workers found that single-molecule enzyme kinetics also show saturation kinetics similar to the ensemble measurements and provided a microscopic interpretation of MM equation (2) to yield single-molecule MM equation (3), where τ is the waiting time between each product generation (τ_{off} in Figure 7A). If we compare equation (2) with equation (3), it is clear that enzymatic velocity measured in ensemble measurement is related to mean waiting time in single-molecule measurement by $1/\langle\tau\rangle = V/[\mathrm{E}]$, this is from the equivalence between averaging over single-molecule time trace and averaging of a large ensemble of identical molecules.[8,10] In short, the inverse of the waiting time of product formation represents the rate of product formation in single-molecule studies.[29,30]

Single-chain polymeric nanoparticles are reminiscent of enzymes and share similar properties, although they cannot match their efficiency yet. But, the approach to single-molecule enzyme kinetics can be adapted for SCPNs due to their similarities. As described in the introduction section, static disorder and dynamic disorder in enzymes have already been probed by single-molecule catalysis. In the scope of this study, we are interested in heterogeneity in catalytic function of SCPNs at single-particle level and therefore a comparison to the behaviour of enzymes is essential. The static heterogeneity in catalytic activity in the enzyme Cholesterol Oxidase was probed by the distribution of on and off waiting times from time trajectories by Xie and co-workers, from which the distribution of k_{cat} from many enzyme molecules in the same sample was obtained (Figure 7B).[30,31] The causes of this heterogeneity in activity in enzymes and nanoparticles can be compared, as the structure of catalysts can govern their intrinsic catalytic properties. Therefore, we decided to probe the heterogeneity in SCPN catalysis using the same approach. The Michaelis-Menten mechanism is based on one-catalytic site and one-substrate kinetic model as applicable for the majority of the enzymes.[32] On the other hand, SCPNs have several catalytically active sites but in this work, we consider each SCPN as a single catalyst as we look at the turnover frequency of individual SCPN at single-molecule level.

5.7 Determination of k_{cat} at ensemble level – Michaelis-Menten model

In enzymology, k_{cat} or turnover number of enzymes is the maximum number of substrate molecules converted to products per enzyme molecule per second. In the case of organometallic catalysis, the turnover number is determined as number of moles of reactant that a mole of catalyst converts before it is deactivated, whereas the turnover frequency (TOF) is turnover per unit time and holds the same meaning as that of k_{cat} in enzyme catalysis.[30] This turnover frequency can often vary depending on substrate concentrations and often lead to discrepancies if exact reaction conditions are not reported.[33] In this study, for pro-rho **3** activation, at 30 μM substrate and 2 μM catalyst concentration (~120 nM polymer concentration, at 37 °C, reaction completed in 80 min), the turnover frequency of polymeric nanoparticles was found to be 180 h^{-1}. At room temperature, at high concentrations of substrate and catalyst (100 μM and 10 μM Cu(I)) it was found to be 120 h^{-1}. Although this gave a ballpark idea of the approximate turnover frequency of our Cu-SCPNs, the behaviour can be completely different at concentrations where single-molecule studies are performed (nanomolar to picomolar concentrations).

Although SCPNs show enzyme-like kinetics following the Michaelis-Menten model as reported earlier, we need to ensure that the Cu(I) SCPNs developed in this study also exhibit similar behaviour under dilute conditions. For this, pro-rho **3** activation was monitored over time using **P1@Cu(I)** at 37 °C at 5 nM concentration of polymer. The substrate concentration was increased from 100 to 800 nM, but no sign of saturation was observed. Upon further increasing the concentrations to micromolar concentration, the reaction rate started to saturate (Figure 8A). The saturation curve followed the Michaelis-Menten model and $V_{\max}$ was found to be 41.5 nM/min. Considering each particle as a single catalyst (although multiple Cu centres may be present per particle), the equation $v_{\max} = k_{\text{cat}}[E]$ (here [E] = [P] = 5 nM) affords k_{cat} of 498 h^{-1}. Details and the Michaelis Menten plot along with the error bar are given in the experimental section (Figure 15A). To assess if there are significant differences between the different polymer designs, **P3@Cu(I)** was also studied at substrate concentrations from 1 – 18 μM, and the same behaviour was observed (Figure 8B). The k_{cat} was determined to be 433 h^{-1} for **P3@Cu(I)**. The results fitted to the Lineweaver-Burk plot showed a linear relation between $1/V$ vs $1/[S]$ (V = velocity or reaction rate, S = substrate concentration) (Figure 15B). From this study, it is clear that SCPNs follow the one substrate MM model, making it easier to export the system to single-molecule studies.

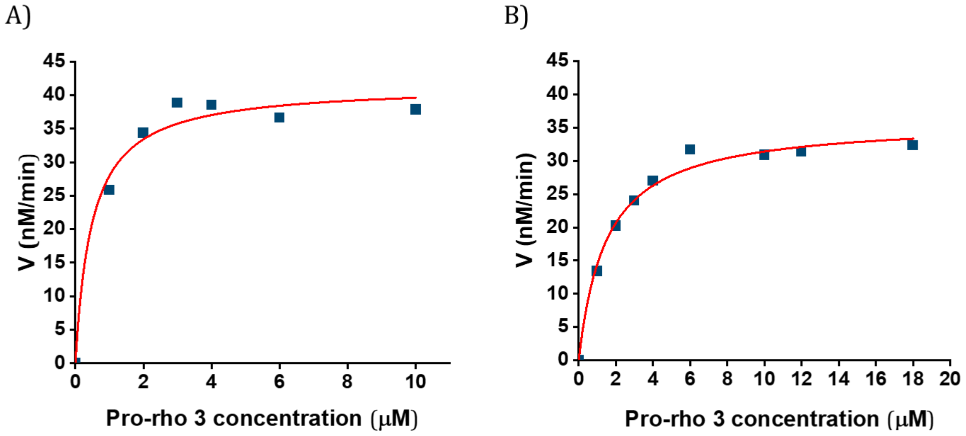

Figure 8: Michael-Menten fitting (y = ($V_{\max}$ × x)/(K_m + x) of reaction kinetics of pro-rho **3** activation by A) **P1@Cu(I)**, values obtained for $V_{\max}$ = 41.51 ± 1.92 nM/min and K_m = 0.48 ± 0.14 μM, R^2 = 0.97. B) **P3@Cu(I)**, values obtained for $V_{\max}$ = 36.09 ± 1.11 nM/min and K_m = 1.49 ± 0.19 μM, R^2 = 0.98. T = 37 °C, rate monitored using fluorescence kinetic experiment (t_0 = 0 min and t_f = 10 min) and concentration of product determined from the calibration curve of rho **5**, [**P**] = 5 nM, in H_2O.

5.7.1 Optimization of single-particle SCPN catalysis

Biotin-functionalised catalytic Cu(I) SCPNs were immobilised on a plasma-treated coverslip according to the already reported protocol (Figure 9A).[18] For this, **P1-P3@Cu(II)** prepared in fresh MilliQ water was first mixed with streptavidin, which was then immobilised on a biotinylated BSA-covered coverslip. The coverslip was placed on a glass slide to create a capillary chamber of volume 30 µL. Substrates selected for single-molecule studies were pro-res **2** and pro-rho **3**. Pro-res **2** showed high background fluorescence leading to visually bright patterns probably due to unspecific binding to the surface. This is also previously observed for similar substrates for enzyme catalysis, where they photobleached these areas to overcome it.[10] In our case, the low reaction rate of **P1-P3@Cu(I)** towards this substrate posed further challenges and therefore was not used for further studies. Therefore, pro-rho **3** was chosen as the substrate for kinetic measurements.

At first, the catalytic activity of immobilised catalytic SCPNs was assessed. This was performed by increasing concentrations of **P1@Cu(II)** nanoparticles from 5 nM, 100 nM and 2500 nM at 1 µM pro-rho **3** concentration. In order to reduce **P1@Cu(II)** to **P1@Cu(I)**, two protocols were tested. In the first case, we washed the immobilised SCPNs with 1 mM sodium ascorbate (NaASc) solution, followed by the addition of 1 µM pro-rho **3**. But in this case, proper localisations of fluorescent bursts were not observed probably because the immobilised SCPNs were washed away along with the ascorbate solution. In the second case, pro-rho **3** and sodium ascorbate solution were mixed to reach a final concentration of 1 µM: 1mM (pro-rho **3**: NaAsc) in MilliQ water, which was added to the chamber just before catalysis studies. In the second protocol, localised fluorescent bursts were visualised and localisations were increased with increasing nanoparticle concentration (Figure 16). This confirmed that immobilised SCPNs retained their catalytic activity and are suitable for single-molecule kinetic experiments. Pro-rho **3** is prone to autohydrolysis and non-specific fluorescent bursts were observed on BSA-covered coverslips. Freshly purified pro-rho **3** was therefore used for further experiments to minimize this.

In order to perform the kinetic experiments, the nanoparticle and substrate concentration were further optimized to achieve a good signal-to-noise ratio and statistics. Keeping the concentration of nanoparticles at 5 nM, the pro-rho **3** concentration was decreased to 100 nM and localisations were compared to coverslip and control nanoparticles **P7** (Figure 9B). **P7** is a biotin-functionalised control polymer with BTA, dodecyl and Jeffamine M-1000 grafts without the ligand obtained from Linlin Deng, which was previously used for

NR-sPAINT single-molecule experiments.[18] Significant increase in localisations was observed in the case of 5 nM **P3@Cu(I)** compared to controls experiments (Figure 9). A further increase in localisations was achieved by increasing both the nanoparticle's concentration (in this case 12.5 nM) or the substrate concentration (1 μM).

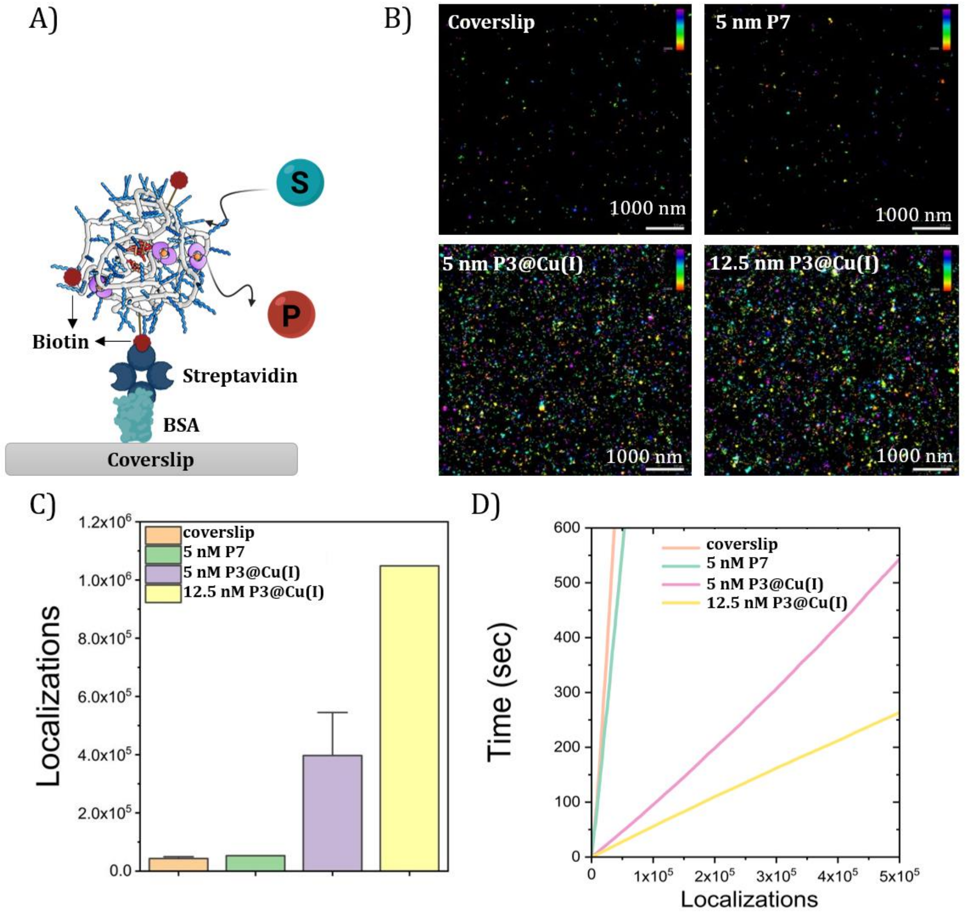

Figure 9: A) Schematic of immobilisation of catalytic SCPNs to coverslip using BSA and streptavidin. B) Time-sequence single-molecule catalysis mapping – control coverslip, control **P7** and **P3@Cu(I)**. Different colours indicate the different portions of product molecules formed sequentially in time (blue to red) after 30k frames C) Localisations of product molecules after catalysis measurements - controls and **P3 @Cu(I)** D) Localisation of product molecules overtime - controls and **P3@Cu(I)**. a) [pro-rho **3**] = 100 nM, [NaAsc] = 1 mM when [**P**] = 5 nM. b) [pro-rho **3**] = 1 μM, [NaAsc] = 1 mM when [**P**] = 12.5 nM.

To increase the TOF and thereby attain good statistics while keeping the signal-to-noise ratio high, further optimizations were performed varying the concentration of substrate and amount of copper in SCPNs. Finally, a concentration of 1 nM **P1-P3@Cu(I)** with 400 nM of pro-rho **3** and 1 mM sodium ascorbate was found to be most suitable for kinetic measurements. To capture enough turnovers from catalysts, each single-molecule measurement was performed for 30 min (60000 frames) in triplicates for kinetics studies at 37 °C.

5.7.2 Determination of k_{cat} at the single-particle level

With the optimized conditions as described in the previous section, single-particle kinetic studies were performed for catalytic nanoparticles **P1-P3@Cu(I)**. Stochastic fluorescent bursts were recorded over time, which showed the localised formation of the product over time indicating single-particle catalysis (Figure 10A). The fluorescent time trajectory of these localised fluorescent bursts was recorded to obtain the waiting time τ_{off} between product formations. The single-molecule kinetic data analysis was performed by Emmanouil Archontakis. The distribution of the waiting time τ_{off} of individual nanoparticles was obtained from the kinetic measurements. All catalytic SCPNs **P1-P3@Cu(I)** evidently showed heterogeneity in catalysis at the single-particle level as observed from intraparticle turnover dispersity (Figure 10B-C). Individual nanoparticles with high turnover as well as low turnover were detected in the same batch.

The heterogeneity in catalytic function of SCPNs at single-particle level can arise due to several factors such as molar mass dispersity of polymers and differences in the polarity of the hydrophobic domain, microenvironment of Cu(I) catalysts, three-dimensional conformation of polymers etc. Although it is not possible to accurately map these contributing factors, the effect of molar mass dispersity and polarity of the hydrophobic domain can be explained as follows. Using the computational drift program developed by Xu and co-workers[34], it is possible to visualise the monomer composition of random heteropolymers. As a representative example we used **P2** (Figure 11), which helps to visualise the differences in the number of Cu(I) catalysts present per polymer chain (same as Cu-ligand) and its microenvironment due to the dispersity in the degree of polymerisation and positioning of the different pendant groups along the polymer backbone (Figure 11B).

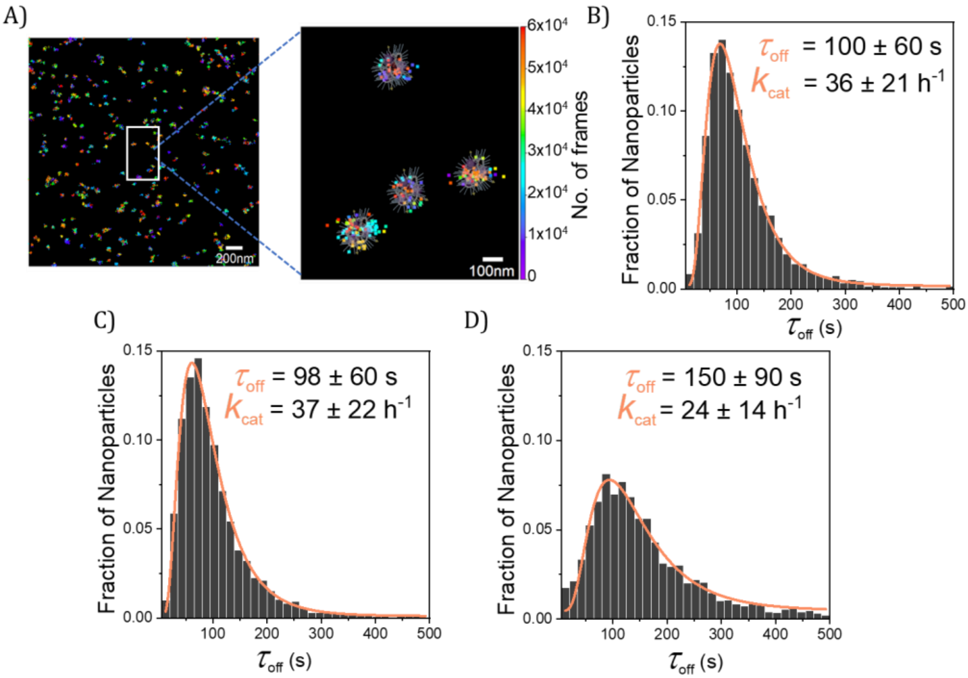

Figure 10: A) Time-sequence single-molecule catalysis mapping of rho **5** formation by catalytic SCPNs, different colours indicate the different portions of product molecules formed sequentially in time (blue to red) after 30k frames. Localised fluorescent bursts can be observed in zoomed-in image, where the SCPN schematic is not to scale, but represents the probability of products formed from individual SCPNs, after filtration of sparse localisations. B) Distribution of τ_{off} of **P1@Cu(I)** C) Distribution of τ_{off} of **P2@Cu(I)** D) Distribution of τ_{off} of **P3@Cu(I)**. [**P**] = 1 nM, [pro-rho **3**] = 400 nM, [NaAsc] = 1 mM, T = 37 °C.

Archontakis *et al.* have previously mapped the polarity of individual SCPNs of similar polymer designs (except the Cu-binding ligand) using NR-sPAINT super-resolution technique. It was revealed that within a single batch of polymers, particles with higher or lower amounts of hydrophobic groups exist.[18] The particles with a higher amount of hydrophobic grafts might exhibit a higher turnover number as they can accommodate the hydrophobic substrate pro-rho **3**. However, this can only be corroborated by combining NR-sPAINT with kinetic measurements on the same batch of catalytic SCPNs in future.

To further compare different polymer designs, the distribution of τ_{off} was used to obtain the average τ_{off} value of each catalytic system **P1-P3@Cu(I)**. The inverse of the average τ_{off} was taken to obtain k_{cat} (Figure 10B-D). All SCPNs despite the differences in polymer microstructure had similar k_{cat}, ranging between 24 – 37 h^{-1}. This could be due to the fact that the water is not involved in the rate-determining step of depropargylation reactions and therefore the concentration of water or its diffusion to hydrophobic pocket does not affect the rate of reaction. Consequently, the small differences in the hydrophobic domain of different polymer designs may not contribute to significant differences in their catalytic activity. This was also as inferred from ensemble kinetic studies of pro-rho **3** activation (Figure 6D). The k_{cat} derived from single molecule studies (~ 30 h^{-1}), is less compared to that of at the ensemble level (~ 400 h^{-1}). Most likely, the immobilisation of particles affect their dynamic nature partially. Aggregated particles **P4-P5@Cu(I)** were not tested due to their low catalytic efficiency.

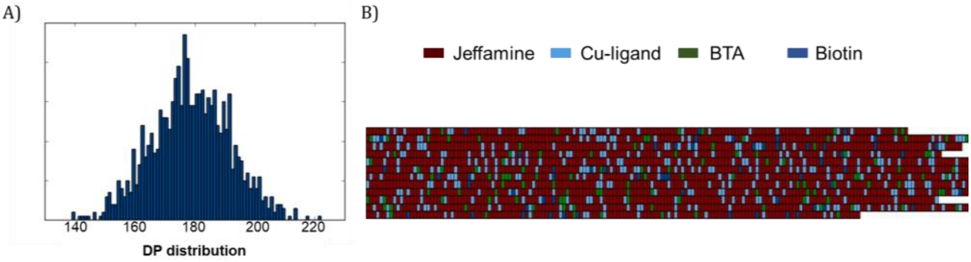

Figure 11: Compositional drift program[34] output for **P2** A) Normalised DP distribution B) Rows representative of individual polymer compositions, each row denotes one polymer and each colour indicates the corresponding monomer incorporation. (Reactivity of all monomers was assigned as 1, DP =178, 4 monomers with percentages mentioned in Table 1 for **P2**), predicted dispersity index = 1.006.

5.8 Conclusions and Outlook

Although there have been advances in the development of catalytic SCPNs for bioorthogonal catalysis in biological settings, the heterogeneity in catalytic activity of SCPNs at single-particle level has never been probed. This understanding is very valuable for the rational design of amphiphilic polymers that show high efficiency for future biomedical applications. To this end, we developed efficient catalytic Cu(I) SCPNs that can promote fast click and depropargylation reactions in water. We also designed and synthesized fluorogenic probes based on resorufin and rhodamine to tune the activity of catalytic SCPNs and the best substrate pro-rho **3** was used for single-particle catalysis studies. We evaluated the catalytic behaviour of SCPNs and found that they showed enzyme-like kinetics following the Michaelis-Menten model. This helped to calculate k_{cat} at the ensemble level which was found to be ~ 400 h^{-1}. By careful optimisation of reaction conditions, we observed catalytic turnovers of individual particles by single-molecule kinetic measurements. The intraparticle turnover dispersity was clearly evident from the distribution of the waiting time τ_{off}. There were no significant differences between different polymer designs, which can be attributed to the similarity in the hydrophobic domain sufficient enough to accommodate the hydrophobic substrates. The effect of polymer microstructure on catalytic activity is not pronounced in Cu(I) catalysed reactions, as the turnover solely relies on the presence of Cu(I) in the vicinity of the chelating ligand, which is the same in all polymer designs. The turnover number (k_{cat}) of all catalytic SCPNs **P1-P3@Cu(I)** during single-molecule kinetic experiments was found to be between 24-37 h^{-1}, which is low compared to the values of around 400 h^{-1} obtained in ensemble measurements. Despite the low turnover numbers, we observed diversity in the reactivity of individual SCPNs for the first time. Although preliminary, our studies have laid a foundation for single-molecule SCPN kinetics which can be useful to probe changes in reactivity over time or in the presence of other biomolecules. In future, this approach can also be utilized for two substrate systems where click reactions can be performed for the generation of CalFluors (Click Activated Luminogenic Fluorophores).[35]

It is also important to consider the limitations of this approach during the discussed interpretations as there is the presence of a small fraction of autohydrolysed products and also the possibility of products diffusing back to the hydrophobic pocket. Further improvements in signal-to-noise ratio by developing more efficient catalytic systems with high turnovers similar to that of enzymes and better substrates can offer more reliable statistics.

Furthermore, it is currently unknown how the diversity in reactivity relates to primary structure and 3D conformation of the polymers. The current work is a small step towards unveiling the diversity of reactivity of individual catalytic SCPNs which are hidden in ensemble measurements. In future, this can help in the rational design of polymers by finding the relation between their defined three-dimensional structure and catalytic efficiency to attain enzyme-like selectivity and activity.

5.9 Experimental section

Materials and characterization methods

All chemicals were purchased either from Merck or TCI chemicals. Poly(ethylene glycol) 2-aminoethyl ether biotin (average Mn = 2,300 g/mol) was purchased from Sigma Aldrich. Deuterated solvents were purchased from Cambridge isotope laboratories. The dialysis membrane was regenerated cellulose tubing purchased from Spectra/Por® with a molecular weight cut-off of 6-8 kDa. All solvents were purchased from Biosolve. ***p*PFPA$_{180}$** was synthesized according to the protocol described in first chapter, in this case with a degree of polymerisation 180 and dispersity 1.19. BTA amine was previously synthesized in our lab according to the reported protocol.[24] Starting material 2-(12-Bromododecyl)isoindoline-1,3-dione was obtained from Jolanda Spiering, DTE **7** was obtained from Stanislav Presolski, bimpy **8** was obtained from Bas de Waal. Pro-res **1** and pro-rho **3** were synthesized by Jolanda Spiering. ^{1}H and ^{13}C measurements were recorded on Bruker 400 MHz spectrometer at ambient temperature, and chemical shifts were recorded concerning TMS as the internal standard for ^{1}H and ^{13}C spectra. Fluorescence measurements were performed on an Agilent Cary Eclipse fluorescence spectrophotometer using 1 cm × 1 cm pathlength quartz cuvettes. CD measurements were performed on Jasco J-815 spectropolarimeter using 0.5 cm pathlength quartz cuvettes. Liquid chromatography - UV was performed using Shimadzu UFLC-XR with PDA detector with water + 0.1% formic acid and ACN + 0.1% formic acid as eluents on Kinetex column C18 5 mm EVO 100 Å. HPLC Method 1 for pro-dyes **1** - **3**: eluent A: water (0.1% formic acid); eluent B: acetonitrile (0.1% formic acid); and A/B = 90:10 isocratic 2 min, 90:10 to 0:100 in 2 min, isocratic 2 min, 0:100 to 90:0 in 2 min, and isocratic 2.0 min (flow = 0.2 mL/min). Size exclusion chromatography (SEC) measurements of poly(pentafluorophenyl)acrylate were recorded using Shimadzu LC-2030C 3D with RID-20 refractive index detector and PDA detector at a flow rate of 1 mL min^{-1} with THF as eluent with Agilent mixed-C and mixed-D column in series at 40 °C. Exclusion limit = 2.000.000 g mol^{-1}, 7.5 mm i.d. × 300 mm. Calibration was performed using polystyrene standards from polymer laboratories. DMF-SEC measurements of functionalised polymers were performed using PL-GPC-50 plus (Varian Inc. Company) equipped with a refractive index detector. DMF with 10 mM LiBr was used as eluent at a flow rate of 1 mL min^{-1} on the Shodex GPC-KD-804 column at 50 °C. Exclusion limit = 100.000 Da, 0.8 cm i.d. × 300 mm calibrated using poly (ethylene oxide) from polymer laboratories. SEC measurements in PBS (pH = 7.4) were carried out on a Shimadzu

CBM-20A System at 20 °C equipped with a Shimadzu RID-10A RI detector, SIL-20A autosampler, and 2 LC-20AD pumps on a Shodex OHpak SB-804 HQ column (exclusion limit = 1000 kDa, i.d. = 0.8 cm, L = 300 mm) with a TSKgel SWXL type guard column (i.d. = 0.6 cm, L = 40 mm), with PBS as an eluent at a constant flow rate of 0.8 mL min-1. The column was calibrated against poly(ethylene oxide) (PEO) (Polymer Laboratories). Copper quantification was performed on Agilent MP-AES 4200 (Microwave plasma atomic emission spectrometer) elemental analyser calibrated using Palladium Standard for ICP. Dynamic light scattering experiments were performed using Malvern Zetasizer with 830 nm laser and an angle of scattering 90°. Single-molecule images were obtained in an Oxford Nanoimager microscope (ONI, Oxford, UK).

Synthesis

Methyl bis(3-(trimethylsilyl)prop-2-yn-1-yl)glycinate[21]

Glycine methyl ester hydrochloride (8 mmol, 1 g) and trimethylsilylacetylene (20 mmol, 1.9 g) was added to a 100 mL round bottom flask under the argon atmosphere. To this, 37% formaldehyde (20 mmol, 1.6 g) solution was added followed by sodium bicarbonate (8 mmol, 668 mg) and CuCl (0.796 mmol, 78.8 mg). The reaction mixture was stirred overnight at 35 °C and the reaction progress was monitored by TLC. Then, the solution was extracted using dichloromethane (3 × 75 mL), filtered through celite and dried over sodium sulfate. Finally, the solvent was evaporated to obtain the crude mixture as an oil. This crude mixture was then purified by Grace Reveleris flash column chromatography over silica gel (EtOAc/Hexane – 0/100 to 50/50, v/v) to yield the product as a colourless oil. Yield = 1.7 g, 70%. ^{1}H NMR (400 MHz, $CDCl_3$) δ 3.72 (s, 3H), 3.52 (s, 4H), 3.44 (s, 2H), 0.15 (s, 18H).

Methyl di(prop-2-yn-1-yl)glycinate[21]

Methyl bis(3-(trimethylsilyl)prop-2-yn-1-yl)glycinate (4.8 mmol, 1.5 g) was dissolved in 20 mL methanol in a round bottom flask. Potassium carbonate (15 mmol, 2 g) was added to this solution and stirred for 3 h. After monitoring the completion of the reaction by TLC, methanol was removed by evaporation. Followingly, water (20 mL) was added to the flask and the product was extracted using EtOAc (3 ×10 mL), the combined organic phase was washed with saturated NaCl solution (1 × 10 mL) and dried over anhydrous $MgSO_4$. After the solvent was removed under vacuum and the crude product was purified by Grace Reveleris flash column chromatography over silica gel (Heptane/EtOAc – 50/50, v/v) to obtain pure product as a colourless oil. Yield = 396 mg, 50%. ^{1}H NMR (400 MHz, $CDCl_3$) δ 3.73 (s, 3H), 3.56 (s, 4H), 3.47 (s, 2H), 2.26 (t, J = 2.4 Hz, 2H).

*Diyne **9**: di(prop-2-yn-1-yl)glycine*[21]

Methyl di(prop-2-yn-1-yl)glycinate (1.8 mmol, 300 mg) was dissolved in 5 mL methanol in a 25 mL round bottom flask, followed by the addition of lithium hydroxide monohydrate (18 mmol, 756 mg). This mixture was sonicated for 5 min and was allowed to stir for 4 h at room temperature. The completion of the reaction was monitored by TLC. After the competition of the reaction, methanol was evaporated and the residue was acidified to reach approximately pH = 3, then the product was extracted using DCM/methanol (9/1, v/v) (3×10 mL). The organic phase was allowed to stand undisturbed for 3 days and the product precipitated as a colourless solid. Yield = 135 mg, 50%. ^{1}H NMR (400 MHz, D_2O) δ 4.25 (dt, *J* = 2.5, 1.1 Hz, 4H), 3.95 (t, *J* = 1.2 Hz, 2H), 3.12 (dt, *J* = 3.3, 2.1 Hz, 2H). ^{13}C NMR (100 MHz, D_2O) δ 169.83, 79.86, 71.66, 54.65, 43.21.

Bis((1-(3-hydroxypropyl)-1H-1,2,3-triazol-4-yl)methyl)glycine[21]

Di(prop-2-yn-1-yl)glycine (0.7 mmol, 108 mg) was dissolved in 3 mL acetonitrile, followed by the addition 3-azidopropan-1-ol (1.5 mmol, 158 mg). To this mixture, DIPEA (N,N-diisopropylethylamine) (1.7 mmol, 220 mg) and CuI (0.06 mmol, 11.4 mg) were added. The reaction mixture was then stirred overnight. The completion of the reaction was monitored by TLC and after the completion, the solvent was passed through celite and evaporated under reduced pressure. To this crude mixture, 50 mL diethyl ether was added and the precipitate was collected after 24 h. The precipitate was then washed with diethyl ether and vacuum dried to obtain the pure product as a white solid. Yield = 197 mg, 80%. ^{1}H NMR (400 MHz, D_2O) δ 7.95 (s, 2H), 4.51 (t, *J* = 7.0 Hz, 4H), 3.88 (s, 4H), 3.58 (t, *J* = 6.2 Hz, 4H), 3.13 (s, 2H), 2.14 (p, *J* = 6.6 Hz, 4H).

2-(12-Azidododecyl)isoindoline-1,3-dione[36]

2-(12-bromododecyl)isoindoline-1,3-dione (1.5 g, 3.8 mmol) was dissolved in 5 mL DMF under dry conditions and argon atmosphere, followed by the addition sodium azide (11 mmol, 744 mg). The reaction mixture was allowed to stir at room temperature overnight. Subsequently, water (20 mL) was added to the reaction mixture, and the product was extracted using dichloromethane (3×10 mL) and organic phase was dried over sodium sulfate and evaporated under vacuum to get crude product. This was purified by column chromatography on silica gel (Heptane/EtOAc – 92/8, v/v) to obtain pure product as white solid. Yield = 1.2 g, 90%. ^{1}H NMR (400 MHz, $CDCl_3$) δ 7.83 (dq, *J* = 6.5, 3.2 Hz, 2H), 7.70 (dt, *J* = 5.1, 2.2 Hz, 2H), 3.67 (t, *J* = 7.4 Hz, 2H), 3.25 (t, *J* = 7.1 Hz, 4H), 1.67 (t, *J* = 7.1 Hz, 2H), 1.27 (m, *J* = 8.5 Hz, 16H). FT-IR (ATR): ν(cm^{-1}) 2925.72, 2854.55, 2091.5, 1773.05, 1712.74, 1681.99, 1615.84, 1466.82, 1437.25, 1395.1, 1368.02, 1256.41, 1188.04, 1171.79, 1087.19, 1053.03, 890.40, 792.89, 755.76, 718.98, 693.06, 658.80, 622.97, 556. 74, 529.69.

12-Azidododecan-1-amine[36]

2-(12-azidododecyl)isoindoline-1,3-dione (1.2 g, 3.3 mmol) was dissolved in 7 mL THF, followed by the addition of hydrazine monohydrate (10 mmol, 0.3 mL). The reaction mixture was allowed to stir overnight at 60 °C. Subsequently, the solvent was removed under reduced pressure and chloroform (15 mL) was added to the residue. This solution was washed with 1 M NaOH solution

(3×10 mL). The organic phase was then dried over anhydrous sodium sulfate and solvent was removed under vacuum. The crude product was then purified by column chromatography on silica gel (EtOAc to EtOAc/isopropylamine 90/10 v/v) to obtain pure product as oil that solidifies when stored in fridge. Yield = 357 mg, 48%. ^{1}H NMR (400 MHz, $CDCl_3$) δ 3.25 (t, *J* = 7.0 Hz, 2H), 2.67 (t, *J* = 7.0 Hz, 2H), 1.59 (p, *J* = 7.0 Hz, 2H), 1.44 – 1.21 (m, 20H). FT-IR (ATR): *ν*(cm^{-1}) 3313.39, 2922.89, 2852.77, 2092.31, 1586.6, 1465.64, 1348.88, 1257.42, 1071.49, 818.05, 721.92, 638.04, 557.47. MALDI-TOF-MS: m/z calc: 226; found: 227 $[M+H]^+$

Pro-res **1**: *2-methylbut-3-yn-2-yl (3-oxo-3H-phenoxazin-7-yl) carbonate*

Triphosgene (445 mg, 1.5 mmol) was dissolved in 2 mL DCM under argon atmosphere and was cooled on ice bath. 2-Methylbut-3-yn-2-ol (290 µL, 3 mmol) and pyridine (266 µL, 3.3 mmol) was added dropwise to the above solution of triphosgene which resulted in a white precipitate. The mixture was allowed to stir for 1.5 h on ice bath, followed by the evaporation of DCM under argon flow. To this crude mixture, 3 mL DMF was added resulting in a clear solution. This solution was added dropwise into another flask containing resorufin (160 mg, 0.7 mmol) and triethylamine (200 µL, 1.5 mmol) dissolved in 16 mL DMF under the argon atmosphere on ice bath. After the addition, the mixture was allowed to stir on ice bath for 15 min and then at room temperature for 2 h. After monitoring the reaction by TLC, the mixture was decanted to remove unreacted resorufin. To the mixture 200 mL water was added and then was extracted using DCM (4×20 mL). The combined organic phase was washed with brine solution and dried over sodium sulfate and DCM was evaporated under reduced pressure at room temperature. The product was then dried under vacuum and purified by column chromatography on silica gel (EtOAc/Heptane - 30/70 v/v) to obtain the pure product as brownish powder. Yield = 15 mg, 6%. ^{1}H NMR (400 MHz, $CDCl_3$) δ 7.80 (d, *J* = 8.7 Hz, 1H), 7.43 (d, *J* = 9.8 Hz, 1H), 7.29 (s, 1H), 7.23 (d, *J* = 2.5 Hz, 1H), 6.87 (dd, *J* = 9.8, 2.0 Hz, 1H), 6.33 (d, *J* = 2.0 Hz, 1H), 2.65 (s, 1H), 1.82 (s, 6H). ^{13}C NMR (100 MHz, $CDCl_3$) δ 144.34, 135.22, 134.80, 131.15, 118.64, 109.13, 107.30, 83.07, 77.21, 76.05, 73.92, 28.65.

FT-IR (ATR): *ν*(cm^{-1}) 3290, 3048, 2994, 1772, 1623, 1608, 1572, 1515, 1246, 1220, 1196, 1129, 885, 848, 772, 667. MALDI-TOF-MS: m/z calc: 323.0; found: 323 $[M]^-$, deprotected product resorufin 212 $[M-H]^-$.

Pro-res **2**: *7-((2-methylbut-3-yn-2-yl)oxy)-3H-phenoxazin-3-one*

Resorufin sodium salt (500 mg, 2.13 mmol) was dissolved in 20 mL DCM under argon atmosphere in a round bottom flask. To this solution, potassium carbonate (587 mg, 4.2 mmol) and potassium iodide (70 mg, 0.4 mmol) was added. Subsequently, 3-chloro-3-methylbut-1-yne (459 µL, 4.2 mmol) was added and the reaction was allowed to stir overnight at room temperature. The solvent was decanted to remove the unreacted resorufin and was evaporated under vacuum. Water (30 mL) was added to the residue and the product was extracted using DCM (5×10 mL). The combined organic phase was washed with brine solution, dried over sodium sulfate and evaporated to get the crude product. The crude product was purified using column chromatography on silica gel (EtOAc/Heptane – 0/100 to 30/70 v/v) to obtain the pure product as a bright orange powder. Yield = 41 mg, 7%. ^{1}H NMR (400 MHz, CDCl$_3$) δ 7.69 (d, *J* = 8.9 Hz, 1H), 7.43 (d, *J* = 9.8 Hz, 1H), 7.29 (d, *J* = 2.6 Hz, 1H), 7.15 (dd, *J* = 8.9, 2.6 Hz, 1H), 6.84 (dd, *J* = 9.8, 2.0 Hz, 1H), 6.33 (d, *J* = 2.0 Hz, 1H), 2.73 (s, 1H), 1.76 (s, 6H). ^{13}C NMR (100 MHz, Chloroform-*d*) δ 186.50, 160.17, 150.01, 146.19, 145.02, 134.86, 134.52, 131.15, 129.02, 118.01, 106.88, 105.63, 84.60, 77.36, 77.16, 76.84, 75.77, 73.41, 29.67. FT-IR (ATR): *v*(cm^{-1}) 3213, 3059, 2108, 1648, 1609, 1590, 1565, 1499, 1483, 1394, 132, 1339, 1319, 1258, 1235, 1218, 1182, 1136, 1113, 1102, 980, 951, 912, 888, 867, 835, 819, 746, 716, 706, 649, 642, 619, 609, 566, 543, 506, 492, 467. MALDI-TOF-MS: m/z calc: 279.0; found: 302 [M+Na]$^+$, 281 [M+2ACN+2H]$^{2+}$.

McRh110 **5***: 2-(3-Iminio-6-(morpholine-4-carboxamido)-3H-xanthen-9-yl)benzoate*[2]

Rhodamine 110 chloride (600 mg, 1.6 mmol) was added to the dried round bottom flask under the argon atmosphere and was dissolved in dry DMF (48 mL). NaH (60% dispersion in oil) (144 mg, 2.2 mmol) was added portion wise and the flask was covered with aluminium foil. The reaction mixture was stirred for 2 h. 4-Morpholine carbonyl chloride (210 µL, 1.8 mmol) dissolved in 2 mL DMF was added dropwise to the above reaction mixture. The reaction was then stirred overnight under argon wrapped in aluminium foil at room temperature. The solvent was evaporated under the vacuum at room temperature to obtain the crude product. The pure product was obtained by column chromatography on silica gel. At first, EtOAc/Heptane (5/95) was used as eluent. To remove the leftover impurity after the first column, purification was performed again on silica gel using EtOAc as eluent to obtain the pure product as a bright orange powder. Yield = 145 mg, 21%. ^{1}H NMR (400 MHz, CDCl$_3$) δ 7.98 (d, *J* = 7.5 Hz, 1H), 7.69 – 7.55 (m, 2H), 7.50 (d, *J* = 2.2 Hz, 1H), 7.15 (d, *J* = 7.5 Hz, 1H), 6.81 (dd, *J* = 8.6, 2.2 Hz, 1H), 6.68 (s, 1H), 6.59 (d, *J* = 8.6 Hz, 1H), 6.57 – 6.47 (m, 2H), 6.33 (dd, *J* = 8.5, 2.4 Hz, 1H), 3.91 (s, 2H), 3.72 (t, *J* = 4.9 Hz, 4H), 3.48 (t, *J* = 4.9 Hz, 4H). ^{13}C NMR (100 MHz, CDCl$_3$) δ 154.59, 153.26, 152.62, 151.96, 148.83, 140.93, 134.98, 129.56, 129.05, 128.33, 126.79, 124.84, 124.09, 115.05, 113.39, 111.55, 108.42, 107.45, 101.51, 84.02, 66.48, 44.27.

Pro-rho **3**: *2-methylbut-3-yn-2-yl (3'-(morpholine-4-carboxamido)-3-oxo-3H-spiro[isobenzofuran-1,9'-xanthen]-6'-yl)carbamate*[2]

Triphosgene (842 mg, 2.8 mmol) was dissolved in 2 mL acetonitrile and 1 mL chloroform under argon atmosphere. This mixture was then cooled under ice bath. In another flask, McRh110 **5** (155 mg, 0.3 mmol) was dissolved in 2 mL acetonitrile and 0.5 mL pyridine. This clear solution was added dropwise into the previous solution. The mixture was allowed to stir for 15 min on ice bath and was then brought to room temperature, stirring for 1 h. Then, distilled 2-methylbut-3-yn-2-ol (2.37 mL, 24.5 mmol) dissolved in 2 mL pyridine was added dropwise over a period of 15 min to the reaction mixture while cooling on ice bath. After addition, the mixture was stirred on ice bath for an additional 10 min and then was brought to room temperature. This mixture was again left for stirring for another 2.5 h under room temperature. The reaction was monitored by TLC. To the reaction mixture, 40 mL of chloroform was added and then washed with 1M HCl (2×30 mL), followed by saturated sodium bicarbonate solution (1×30 mL) and finally with brine solution (30 mL). The organic phase was then dried over sodium sulfate and was evaporated to dryness. The crude product was purified by column chromatography on silica gel (EtOAc/Heptane – 40/60 v/v) to obtain the pure product as orange powder. Yield = 52 mg, 27%. Prior to single-molecule studies, the dye was freshly purified again. ^{1}H NMR (400 MHz, $CDCl_3$) δ 8.00 (d, *J* = 7.4 Hz, 1H), 7.71 – 7.56 (m, 2H), 7.51 (d, *J* = 2.2 Hz, 1H), 7.41 (d, *J* = 2.2 Hz, 1H), 7.10 (d, *J* = 7.4 Hz, 1H), 6.94 (ddd, *J* = 8.5, 6.0, 2.2 Hz, 2H), 6.78 (s, 1H), 6.72 – 6.61 (m, 3H), 3.74 (t, *J* = 4.8 Hz, 4H), 3.50 (t, *J* = 4.8 Hz, 4H), 2.59 (s, 1H), 1.75 (s, 6H). ^{13}C NMR (100 MHz, $CDCl_3$) δ 169.70, 154.55, 153.31, 151.91, 151.71, 151.31, 141.09, 139.99, 135.14, 129.75, 128.56, 128.36, 126.31, 125.00, 123.99, 115.48, 114.11, 113.50, 113.13, 107.46, 106.37, 84.62, 82.88, 72.73, 72.66, 66.48, 44.30, 29.19, 29.16, 28.93. MALDI-TOF-MS: m/z calc: 553.1; found: 554.2 $[M+H]^+$.

*Post functionalisation of **p-PFPA$_{180}$** to **P1$_a$-P5$_a$***

P1$_a$: ***p*-PFPA$_{180}$** (172 mg, 1 eq, 0,0040 mmol) was dissolved in dry THF in a Schlenk flask and was kept in a preheated oil bath at 50 °C. To this solution, 12-azidododecan-1-amine (32 mg, 36 eq, 0,14 mmol) was added and stirred for 2 h. Incorporation was followed by ^{19}F NMR by comparing the peaks of free pentafluorophenol with those in the polymer backbone. Afterwards, biotinylated PEG amine (55 mg, 6 eq, 0.024 mmol) was added to the mixture and stirred for 2 h, and incorporation was monitored. Finally, pre-dried Jeffamine M-1000 (800 mg, 212 eq, 0.8 mmol) was added. The reaction mixture was then left overnight under argon and the completion of the reaction was again monitored using ^{19}F NMR. Then, the reaction mixture was purified by dialysis (1 x 1 L methanol, 2 x 1 L THF) for 3 days. After dialysis, THF was reduced to ~ 3 mL using rotary evaporator and the polymer was precipitated into ice-cold pentane (800 mL). The polymer was dried under vacuum overnight at 50 °C to yield a colourless solid and was stored at -19 °C. Yield: 380 mg, $M_{\text{theoretical}}$ = 161 kD, $M_{\text{n, SEC-DMF}}$ = 59.1 kD, $Đ$ = 1.21. ^{1}H NMR (400 MHz, $CDCl_3$) δ 6.92 – 6.01 (br), 4.15 – 3.90 (br), 3.84 – 3.14 (m), 1.90 – 1.82 (br), 1.72 – 1.52 (s), 1.41 – 0.93 (m). FT-IR (ATR): ν(cm^{-1}) 3520.56, 2865.86, 2096.31, 1650.15, 1544.45, 1454.07, 1348.63, 1325.4, 1296.42, 1249.42, 1096.62, 947.46, 848.32, 522.91. $M_{\text{theoretical}}$ = 161 kD, $M_{\text{n, SEC-DMF}}$ = 59.1 kD, $Đ$ = 1.21.

Same protocol was followed for all polymers with varying ligands as specified below:

P2$_a$: ***p*-PFPA$_{180}$** (180 mg, 1 eq, 0,0042 mmol), 12-azidododecan-1-amine (34 mg, 36 eq, 0,15 mmol), BTA amine (25 mg, 9 eq, 0.037 mmol), biotinylated PEG amine (57 mg, 6 eq, 0.025 mmol) and Jeffamine M-1000 (890 mg, 212 eq, 0.8 mmol). The polymer was dried under vacuum at 50 °C to yield a colourless solid and was stored at -19 °C. ^{1}H NMR (400 MHz, $CDCl_3$) δ 8.51 – 8.39 (br), 6.86 – 6.32 (br), 4.18 – 3.13 (m), 1.91 – 1.51 (m), 1.41 – 1.04 (m). FT-IR (ATR): ν(cm^{-1}) 3519.56, 2866.02, 2096.51, 1650.73, 1543.94, 1454.53, 1348.76, 1325.35, 1294.99, 1249.98, 1094.69, 947.35, 848.13, 523.42. $M_{\text{theoretical}}$ = 158 kD, $M_{\text{n, SEC-DMF}}$ = 44.3 kD, $Đ$ = 1.20.

P3$_a$: ***p*-PFPA$_{180}$** (150 mg, 1 eq, 0,0031 mmol), 12-azidododecan-1-amine (25 mg, 36 eq, 0,11 mmol), dodecyl amine (15.4 mg, 27 eq, 0.083 mmol), biotinylated PEG amine (47 mg, 6 eq, 0.018

mmol) and Jeffamine M-1000 (657 mg, 212 eq, 0.65 mmol). The polymer was dried under vacuum at 50 °C to yield a colourless solid and was stored at -19 °C. ^1H NMR (400 MHz, $CDCl_3$) δ 6.86 – 6.13 (br), 4.27 – 3.95 (br), 3.87 – 3.13 (m), 1.94 – 0.82 (m). FT-IR (ATR): ν(cm^{-1}): 3301.87, 2863.67, 2096.15, 1649.47, 1540.03, 1454.47, 1346.79, 1324.91, 1295.06, 1249.38, 1199.43, 1098.22, 1039.84, 947.47, 845.32, 522.96. $M_{\text{theoretical}}$ = 165 kD, $M_{\text{n, SEC-DMF}}$ = 47.5 kD, $Đ$ = 1.25.

P4$_a$: ***p*-PFPA$_{180}$** (108 mg, 1 eq, 0,0025 mmol), 12-azidododecan-1-amine (21 mg, 36 eq, 0,09 mmol), BTA amine (59 mg, 36 eq, 0.090 mmol), biotinylated PEG amine (35 mg, 6 eq, 0.015 mmol) and Jeffamine M-1000 (530 mg, 212 eq, 0.53 mmol). The polymer was dried under vacuum at 50 °C to yield a colourless solid and was stored at -19 °C. ^1H NMR (400 MHz, $CDCl_3$) δ 8.63 – 8.26 (br), 6.81 – 6.22 (br), 4.08 – 2.98 (m), 1.92 – 0.55 (m). FT-IR (ATR): ν(cm^{-1}): 3301.82, 2865.4, 2096.44, 1643.59, 1536.7, 1465.27, 1344.28, 1281.06, 1242.58, 1101.66, 962.31, 842.98, 691.52, 526.93. $M_{\text{theoretical}}$ = 155 kD, $M_{\text{n, SEC-DMF}}$ = 44.4 kD, $Đ$ = 1.26.

P5$_a$: ***p*-PFPA$_{180}$** (100 mg, 1 eq, 0,0023 mmol), 12-azidododecan-1-amine (38 mg, 72 eq, 0,16 mmol), biotinylated PEG amine (32 mg, 6 eq, 0.013 mmol) and Jeffamine M-1000 (487 mg, 212 eq, 0.48 mmol). The polymer was dried under vacuum at 50 °C to yield a colourless solid and was stored at -19 °C. ^1H NMR (400 MHz, $CDCl_3$) δ 7.00 – 5.89 (br), 4.14 – 3.14 (m), 1.92 – 0.93 (m). FT-IR (ATR): ν(cm^{-1}): 3313.89, 2863.61, 2095.93, 1649.86, 1543.46, 1465.8, 1344.17, 1280.38, 1242.12, 1102.47, 962.9, 842.55, 527.8. $M_{\text{theoretical}}$ = 153 kD, $M_{\text{n, SEC-DMF}}$ = 50.3 kD, $Đ$ = 1.25.

*General procedure for the incorporation of the diyne **9** into the polymer backbone*

Synthesis of **P1**-**P3**: Diyne **9** was incorporated into the polymeric backbone according to the modified 'folding and cross-linking' strategy reported by Zimmerman and co-workers.[4] In a 25 mL round bottom flask, **P1$_a$** (100 mg, 0.00062 mmol, 1 eq) was dissolved in 5 mL water. The solution was sonicated for 1 h. The azide pendant groups in the polymer backbone are present in 30 eq (considering the incorporation ratio monitored from ^{19}F NMR). Therefore, diyne **9** (1.7 mg, 0.011 mmol, 18 eq (with 15 eq azide was still left, equivalence optimized by the stepwise increase of diyne **9**) was added to this solution of nanoparticles in water, followed by the addition of $CuSO_4$ (1 mg, 0.006 mmol, 10 eq) and sodium ascorbate (20 mg, 0.10 mmol, 161 eq). The reaction mixture was then allowed to stir overnight under argon. Afterwards, 1 g Chelex resin was added to the reaction mixture to remove copper and was allowed to stir for another 24 h. Followingly, the resin was removed by filtration and the solution was dialyzed in deionized water (5 x 1 L) for 5 days. Afterwards, water was slowly and carefully removed using the rotary evaporator and the polymer was dried under vacuum overnight at 50 °C to obtain a pale yellow solid in all cases. Yield = 20-30 mg. The same procedure with the same amounts was followed for **P2** and **P3**.

P1: ^1H NMR (400 MHz, D_2O) δ 8.45 – 8.40 (br), 8.22 – 8.16 (m), 4.85 – 4.81 (d), 3.91 – 3.27 (m), 2.12 – 1.76 (s), 1.27 – 0.95 (br). FT-IR (ATR): ν(cm^{-1}): 3504.07, 2866.26, 1648.32, 1542.17, 1453.42, 1348.53, 1297.19, 1249.3, 1094.89, 946.76, 845.98. $M_{\text{theoretical}}$ = 164 kD, $M_{\text{n, SEC-PBS}}$ = 15.5 kD, $Đ$ = 1.38.

P2: ^{1}H NMR (400 MHz, D_2O) δ 8.47 – 8.43 (br), 8.23 – 8.14 (m), 4.85 – 4.81 (s), 3.81 – 3.29 (m), 1.31 – 0.99 (br). FT-IR (ATR): ν(cm^{-1}): 3437.19, 2867.07, 1647.18, 1544.54, 1452.73, 1348.65, 1294.81, 1249.96, 1094.27, 947.04, 846.59, 521.88. $M_{\text{theoretical}}$ = 161 kD, $M_{\text{n, SEC-PBS}}$ = 23.4 kD, $Đ$ = 1.35.

P3: ^{1}H NMR (400 MHz, D_2O) δ 8.41 – 8.37 (br), 8.22 – 8.16 (m), 4.85 – 4.81 (s), 4.53 – 4.35 (s), 3.92 – 3.27 (m), 1.36 – 1.12 (br). FT-IR (ATR): ν(cm^{-1}): 3436.86, 2869.53, 1646.34, 1548.24, 1454.48, 1348.8, 1296.07, 1250.18, 1091.99, 947.74, 844.89, 805.17, 523.09. $M_{\text{theoretical}}$ = 168 kD, $M_{\text{n, SEC-PBS}}$ = 16.3 kD, $Đ$ = 1.35.

Synthesis of **P4**: In a 25 mL round bottom flask, **P4$_a$** (100 mg, 0.00064 mmol, 1 eq) was dissolved in 2 mL THF: water (1:1) v/v by vortexing to form a hazy solution. Diyne **9** (1.7 mg, 0.011 mmol, 18 eq) was added to this solution, followed by the addition of $CuSO_4$ (1 mg, 0.006 mmol, 10 eq) and sodium ascorbate (20 mg, 0.10 mmol, 161 eq). The reaction mixture was then allowed to stir overnight under argon. Afterwards, 1 g Chelex resin was added to the reaction mixture to remove copper and was allowed to stir for another 24 h. Followingly, the resin was removed by filtration and the solution was dialyzed in deionized water (5 x 1 L) for 5 days. Afterwards, water was slowly and carefully removed using the rotary evaporator and the polymer was dried under vacuum overnight at 50 °C to obtain a pale yellow solid. Yield = 36 mg. ^{1}H NMR (400 MHz, D_2O) δ 8.48 – 8.44 (s), 8.23 – 8.16 (m), 4.86 – 4.81 (s), 3.78 – 3.61 (br), 1.36 – 1.01 (br). FT-IR (ATR): 3384.97, 2920.94, 1619.34, 1492.07, 1451.51, 1389.65, 1098.96, 947.73, 905.4, 802.35, 699.53, 521.96. SEC-PBS: polymer did not elute out of the column.

Synthesis of **P5**: Same procedure as above was followed with **P5$_a$** (100 mg, 0.00064 mmol, 1 eq), diyne **9** (3.4 mg, 0.022 mmol, 36 eq), $CuSO_4$ (1 mg, 0.006 mmol, 10 eq) and sodium ascorbate (20 mg, 0.10 mmol, 161 eq). Yield = 22 mg^{1}H NMR (400 MHz, D_2O) δ 8.39 – 8.34 (s), 8.14 – 8.06 (m), 5.64 – 3.49 (s). FT-IR (ATR): 3301.67, 2921.97, 2865.28, 1633.64, 1538.84, 1492.34, 1451.92, 1386.5, 1348.82, 1258.23, 1100.13, 948, 906.56, 848.94, 802.65, 700.01, 535.61. $M_{\text{n, SEC-PBS}}$ = 77.5 kD, $Đ$ = 1.98.

Dynamic light scattering measurements: All polymers were dissolved in MilliQ water at 1 mg/mL concentration and was sonicated for 1 h. Samples were allowed to rest for another hour and were taken for measurements.

Circular dichroism measurements: The same sample preparation as above was followed, where 0.5 mg/mL concentration of polymers was prepared in MilliQ water.

MP-AES measurements: ICP standard solution for copper was used to create a calibration curve for copper from 1 ppm -10 ppm concentration (Figure 12B). 1 mg/mL of **P1** solution in MilliQ water was then analysed for detection of the presence of any residual copper used for the incorporation of the catalyst. The concentration from calibration curve was found to be -0.01 ppm (negative value could be due to instrumental error and can be considered as 0 ppm).

Ensemble catalysis measurements

Click reactions: All substrate stock solutions were prepared in DMSO. Coumarin azide **10** at 100 mM, all alkynes **11a-f** at 400 mM concentration. Sodium ascorbate stock solution was prepared in MilliQ water at 200 mM and $CuSO_4$ also in MilliQ water at 10 mM concentration. **P1-P3** was prepared by dissolving 1 mg polymer in 991 µL MilliQ water by sonicating for 1 h. The samples were allowed to rest for 1 h and then, 9 µL of $CuSO_4$ stock solution was added into the solution was stirred for 15 min to reach a final concentration of ~ 6 µM of **P1-P3@Cu(II)** and 90 µM **Cu(II)** concentration in the sample (ligand:Cu molar ratio = 1:1).

For CuAAC reactions with polymers, 333.3 µL of **P1-P3@Cu(II)** stock solution (as prepared above) was added to a 10 mm fluorescence cuvette, followed by the addition of 2630.7 µL of MilliQ water. To this solution, 3 µL of coumarin azide **10** stock solution and 3 µL of alkyne stock solution (depending on each reaction) was added. Finally, 30 µL of sodium ascorbate stock solution was added just before the start of reaction to reduce Cu(II) to Cu(I) and the reaction was monitored by fluorescence spectroscopy at λ_{ex} = 340 nm and λ_{em} = 470 nm over time with stirring. For hydrophilic alkyne **11a**, the progress of the reaction was followed by an increase in fluorescence intensity of the product formed over time. After 30 min, when fluorescence intensity reached a plateau, aliquot was taken from the reaction mixture and injected to HPLC-UV. For hydrophobic alkynes **11b-f**, the fluorescence intensity increased up to 3 min after which it started decreasing. In case of hydrophobic alkynes, the product formed was more hydrophobic making the solution non-homogeneous making it difficult to track the reaction progress using fluorescence spectroscopy. Therefore, aliquots from the reaction mixture were dissolved in acetonitrile to reach water:ACN ratio 1:1 and this was injected to HPLC-UV. In all cases, products **12b-f** was found to be the major fraction but the complete conversion was only obtained in 10 min. For CuAAC control reactions, the same procedure as above was followed where at first 90 µM of $CuSO_4$ solution was prepared without polymers.

Depropargylation reactions: All substrate stock solutions **1**-**3** were prepared in DMSO at 30 mM concentration. Sodium ascorbate stock solution was prepared in MilliQ water at 200 mM and $CuSO_4$ also in MilliQ water at 10 mM concentration. **P1**-**P3** and **P6** was prepared by dissolving 1 mg polymer in 991 µL MilliQ water by sonicating for 1 h. **P4**-**P5** was prepared by dissolving 1 mg polymer in 991 µL MilliQ water by sonicating for 2 h. The samples were allowed to rest for 1 h and then, 9 µL of $CuSO_4$ stock solution was added into the solution was stirred for 15 min to reach a final concentration of ~ 6 µM of **P1**-**P5@Cu(II)** and 90 µM **Cu(II)** concentration in the sample (ligand:Cu molar ratio = 1:1).

For depropargylation reaction at 30 µM substrate concentration, 66.6 µL of **P1-P6@Cu(II)** stock solution was added to a 10 mm fluorescence cuvette, followed by the addition of 2900.4 µL of MilliQ water. To this solution, 3 µL of substrate **1**-**3** stock solution was added. Finally, 30 µL of sodium ascorbate stock solution was added just before the start of reaction to reduce Cu(II) to Cu(I) and the reaction was monitored by fluorescence spectroscopy at λ_{ex} = 532 nm and λ_{em} = 587 nm for substrates **1** and **2**, and λ_{ex} = 485 nm and λ_{em} = 520 nm for substrate **3**. Aliquots from reaction mixture was taken at specified time intervals and diluted with acetonitrile (water:ACN = 1:1 v/v) and injected HPLC-UV to confirm the formation of products. The reactions were performed either at room temperature or at 37 °C as specified.

For depropargylation reaction at 100 µM substrate pro-rho **3** concentration, 100 mM stock solution of **3** was made in DMSO. 333.3 µL of **P1@Cu(II)** stock solution was added to a 10 mm fluorescence cuvette, followed by the addition of 2633.7 µL of MilliQ water. To this solution, 3 µL of substrate **3** stock solution was added. Finally, 30 µL of sodium ascorbate stock solution was added just before the start of reaction to reduce Cu(II) to Cu(I) and the reaction was monitored by fluorescence spectroscopy λ_{ex} = 485 nm and λ_{em} = 520 nm. Aliquots from reaction mixture was taken at specified time intervals and diluted with acetonitrile (water:ACN = 1:1 v/v) and injected to HPLC-UV to confirm the formation of products. For control reactions, the same procedure as above was followed where at first 90 µM of $CuSO_4$ solution was prepared without polymers.

Comparison of ligand **6-8** efficiency: Pro-rho **3** was prepared at 30 mM stock solution, 30 mM stock solution of ligands **6-8** was also prepared in DMSO**.** $CuSO_4$ and sodium ascorbate stock at 10 mM and 200 mM respectively in MilliQ water. For catalysis, all stock solutions were diluted to reach final concentration as specified in 3 mL water in 10 mm fluorescence cuvette and reaction was monitored using fluorescence spectroscopy over time (Figure 12A).

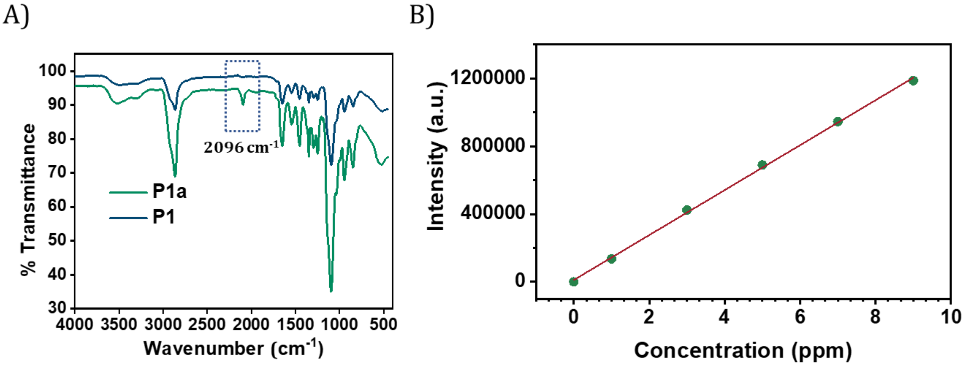

Figure 12: A) Infrared spectra of amphiphilic polymer of **P1**$_a$ and **P1**: before and after incorporation of diyne **9** confirming the disappearance of azide peak at 2096 cm^{-1}. B) MP-AES calibration curve of Cu using ICP Cu standard solution from 0-10 ppm in H_2O.

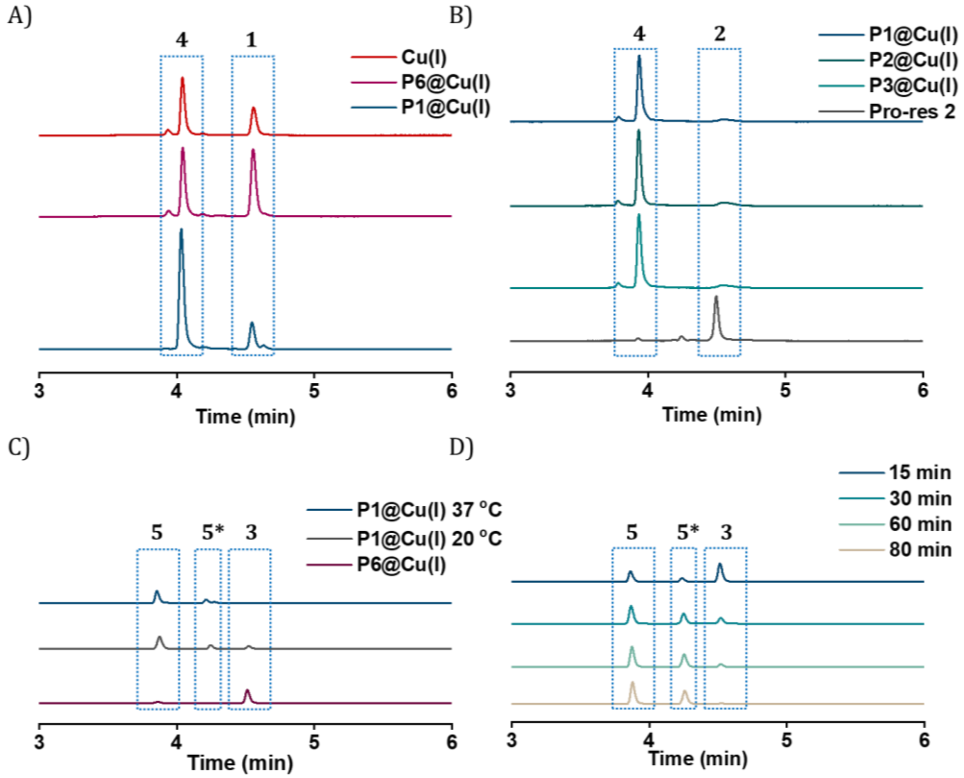

Figure 13: HPLC-UV chromatogram A) pro-res **1** activation using **P1@Cu(I), P6@Cu(I)** and **Cu(I)**, T = 20 °C B) pro-res **2** activation using **P1-P3@Cu(I)** and **Cu(I))**, T = 20 °C C) pro-rho **3** activation using **P1@Cu(I)**, T = 20 °C and 37 °C and **P6@Cu(I)**, T = 20 °C. A,B,C: Reaction conditions = in H_2O, [**Cu(I)**] = 2 μM, [**1-3**] = 30 μM, [NaAsc] = 2 mM, [**P**] = ~120 nM. D) pro-rho **3** activation using **P1@Cu(I)** over time, reaction conditions = in H_2O, [**Cu(I)**] = 10 μM, [**1-3**] = 100 μM, [NaAsc] = 2 mM, [**P**] = ~600 nM. **5*** formed during pro-rho activation was also monitored using HPLC-MS, but was not detected as sharply as seen in UV, with $[M+H]^+$ = 510 and is expected to be the intermediate after depropargylation before the release of CO_2 stabilised by Na^+ from sodium ascorbate.

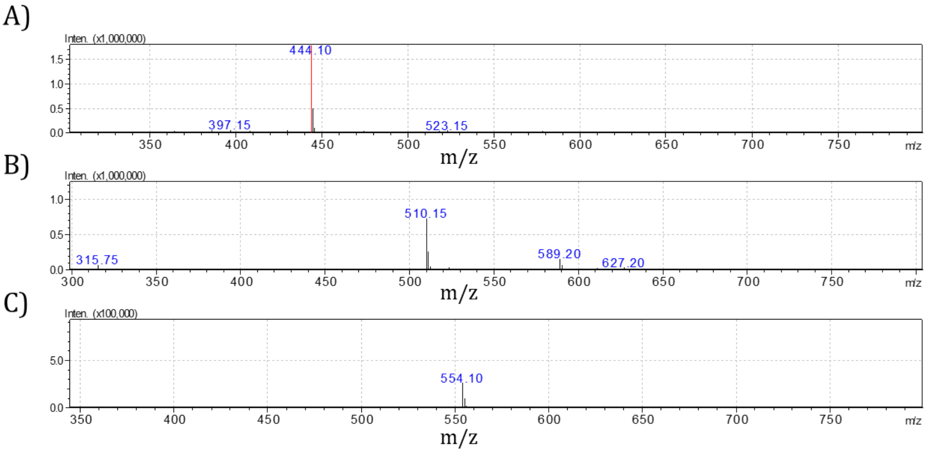

Figure 14: Mass spectrum obtained from HPLC of A) rho **5** B) **5*** C) pro-rho **6** after 30 min of pro-rho 3 activation using **P1@Cu(I)**, reaction conditions = in H_2O, [**Cu(I)**] = 10 µM, [**1-3**] = 100 µM, [NaAsc] = 2 mM, [**P**] = ~600 nM, T = 20 °C.

Ensemble kinetic studies

Determination of k_{cat}:

Calibration of rho **5**: The product rho **5** calibration curve was prepared from 100 – 600 nM of **5** concentration at λ_{ex} = 485 nm and λ_{em} = 520 nm using the fluorescence spectrophotometer. For this, 100 µM stock solution of rho **5** was prepared in MilliQ water to minimise the presence of DMSO in the reaction mixture. From the calibration curve, the concentration of product formed in the reaction mixture overtime was interpolated.

Sample preparation: **P1-P3@Cu(II)** stock solution was prepared by dissolving 1 mg **P1**-**P3** in 982 µL MilliQ water by sonicating for 1 h. The samples were allowed to rest for 1 h, followed by the addition of 18 µL $CuSO_4$ stock solution and stirred for 15 min. The ligand:Cu ratio was 1:2 in this case, in order to compare the k_{cat} with single-molecule kinetic studies where the above-mentioned ration was required to obtain sufficient turnovers. This leads to a final concentration of polymer ~ 6 µM and 180 µM Cu(II) in the sample. 100 µM pro-rho **3** stock solution was freshly prepared in MilliQ water by diluting from 10 mM DMSO stock solution(1 v/v% DMSO in water), to minimize the amount of DMSO in the reaction mixture while ensuring the solubility of pro-rho **3** in water. 200 mM stock solution of sodium ascorbate was used.

Kinetic studies of **P1@Cu(I)**: 3 µL of **P1@Cu(I)** stock solution was added to 10 mm fluorescence cuvette, followed by the addition of MilliQ water (2979 µL – 2442 µL, depending on the increasing amount of substrate concentration keeping total volume 3 mL). To this solution, 3 µL – 540 µL of pro-rho **3** stock solution (100 μM in water) was added. After mixing, the fluorescence cuvette was placed in the spectrophotometer with stirring on. Just before the start of kinetic measurements, 15 μL of sodium ascorbate stock solution was added (to reach 1 mM concentration in the reaction mixture to keep it the same as used for single-molecule studies). The initial rate of reaction was monitored by the change in fluorescent intensity in the first 10 min after the start of the experiment. The rate of change in concentration was calculated back from the calibration curve of rho **6**. The rate of change in concentration was then plotted with change in substrate concentration, where the rate was found to saturate with increasing substrate concentration following the Michaelis-Menten model, which was fitted to obtain the maximum velocity or rate V_{max}. From the V_{max}, the k_{cat} was found by following the equation, $V_{max} = k_{cat}[E]$, where [E] is the enzyme concentration, in this case, polymer concentration is approximately 5 nM. Therefore, from the Michaelis-Menten model fitted for **P1@Cu(I)** kinetics, we found that V_{max} = 41.5 nM/min and corresponding k_{cat} was calculated to be 8.3 min^{-1} or 498 h^{-1}(V_{max} /[P = 5nM]).

For **P1@Cu(I)**, the rate of reaction is the average of 4 independent measurements (Figure 15A). 1/[S] vs 1/V was plotted to obtain the Lineweaver-Burk plot which confirmed the linear relationship (Figure 15B).

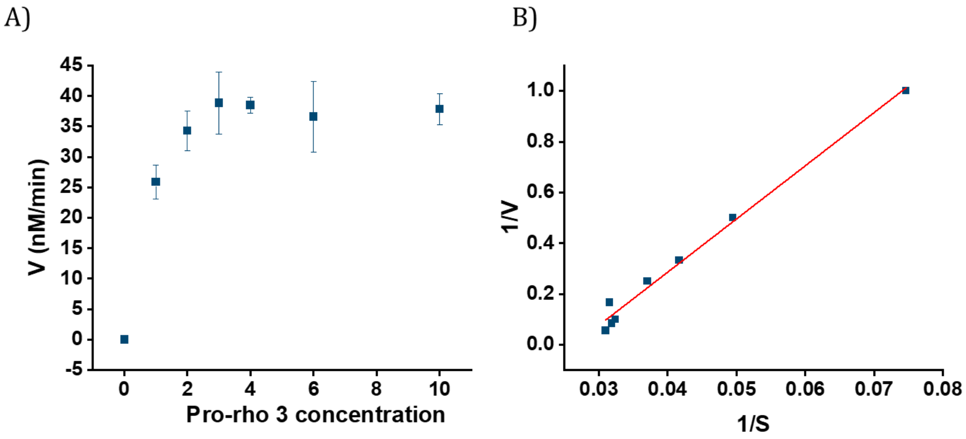

Figure 15: A) Change in the initial reaction rate of the depropargylation reaction of pro-rho **3** with the increase in substrate concentration using **P1@Cu(I)**, error calculated from three independent measurements. B) Lineweaver-Burk plot of reaction kinetics of the same reaction catalysed by **P3@Cu(I)**, rate monitored using fluorescence kinetic experiment (t_0 = 0 min and t_f = 10 min) and concentration of product determined from the calibration curve of rho **5**, [**P**] = 5 nM, in H_2O, T = 37 °C, pro-rho **3** concentration as indicated, Equation : $1/V = (K_m/V_{max} \times 1/[S]) + (1/V_{max})$, in the plot y = 1/V and x = 1/[S], $R^2 = 0.98$.

Single-particle kinetic studies

Immobilisation on coverslips and catalysis measurements: Coverslips (24×24 mm^2) immersed in methanol were kept in the ultrasound sonication bath for 15 min. Followingly, they were dried with nitrogen flow and plasma treated for 1 min. The coverslip was kept over the glass slide using two strips of double-sided tape to form a capillary chamber with an inner volume of ~30 µL. Then, 30 µL of 0.1 mg/ml biotinylated bovine serum albumin dissolved in buffer A (10 mM TRIS-HCl, 50 nM NaCl, pH 8.0) was introduced into the chamber and incubated for 1 h. Afterwards, the unbound BSA were washed away by flushing the chamber with 200 µL Buffer A solution. 5 µM of **P1-P3@Cu(II)** biotinylated SCPNs were mixed with 0.03 mg/mL streptavidin. This solution was then shaken at 300 rps at room temperature for 45 min. This solution was then diluted to reach desired concentration (5 nM – 12.5 nM) as specified for each measurement. Diluted SCPNs were then introduced into the chamber and incubated for 45 min. The unbound particles were then washed again using 100 µL of MilliQ water.

A 100 µM stock solution of substrate rho **3** was prepared in MilliQ water by diluting from 10 mM stock solution in DMSO. 200 mM stock solution of sodium ascorbate was also prepared. For catalysis studies, substrate pro-rho **3** and sodium ascorbate were mixed together to reach the specified concentration for each experiment. For the final kinetic studies, 400 nM substrate to 1 mM sodium ascorbate was used. To reach this, 100 µM stock solution was first diluted to 10 µM concentration in water. 40 µL of 10 µM pro-rho **3** stock solution was added to 955 µL MilliQ water, followed by the addition of 5 µL of 200 mM sodium ascorbate stock solution (similarly for other concentrations). The pro-dye was freshly purified before single-molecule catalysis studies and sample preparation was performed just before single-molecule measurements to minimize the presence of autohydrolysed product.

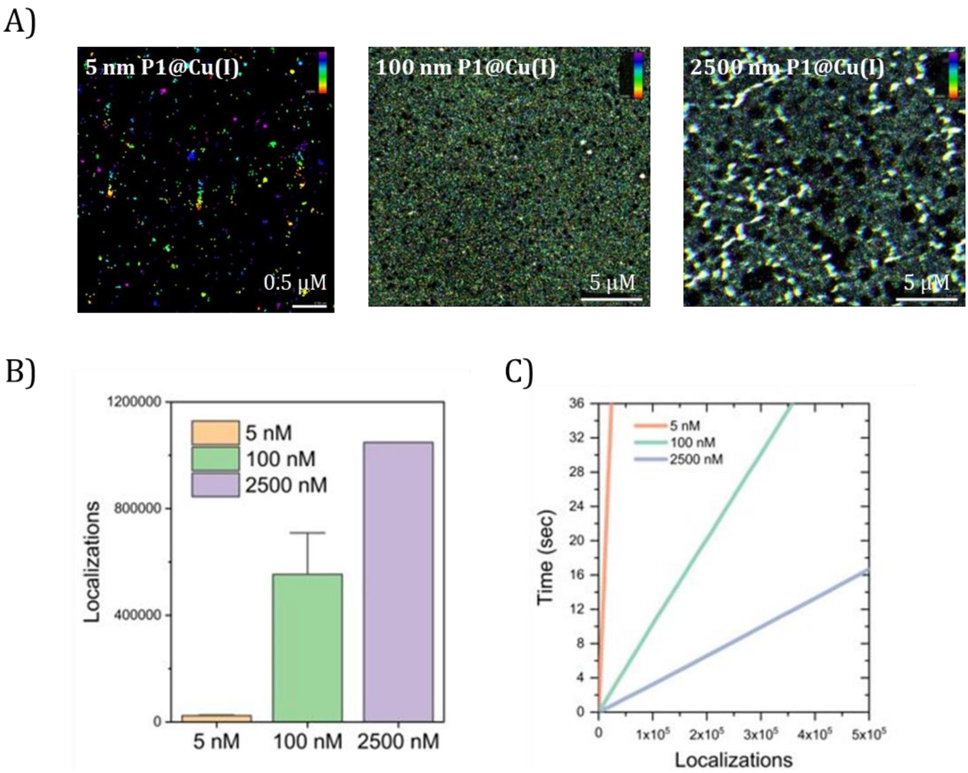

Figure 16: A) Time-sequence catalysis mapping using TIRF microscope monitoring the activation of pro-rho **3** by immobilised **P1@Cu(I)** in increasing concentrations B) Localisations of product molecules after catalysis measurements at different concentrations of **P1@Cu(I)** D) Localisation of product molecules overtime at different concentrations of **P1@Cu(I)**, [pro-rho **3**] = 1 µM, [NaAsc] = 1 mM, [**P**] = 5, 100 and 2500 nM.

The 30 µL of the prepared substrate-ascorbate solution was then introduced into the chamber and the glass slide was introduced ONI microscope with temperature pre-set at 37 °C. The sample was illuminated with a 480 nm laser, using total internal reflection fluorescence (TIRF) for 60000 frames, and dye fluorescence was recorded using a 100×, 1.4 NA oil immersion objective, passed through a beam splitter. Images were acquired onto a 427 × 520 pixel region (pixel size 0.117 µm) of a sCMOS camera, with an exposure time of 20 ms. Images were reconstructed using the ONI Nimos software in order to identify and fit the point spread functions and obtain the super-resolved position of the target molecule.

5.10 References

(1) Janssen, K. P. F.; de Cremer, G.; Neely, R. K.; Kubarev, A. v.; van Loon, J.; Martens, J. A.; de Vos, D. E.; Roeffaers, M. B. J.; Hofkens, J. Single Molecule Methods for the Study of Catalysis: From Enzymes to Heterogeneous Catalysts. Chem Soc Rev 2014, 43 (4), 990–1006.

(2) Liu, Y.; Turunen, P.; De Waal, B. F. M.; Blank, K. G.; Rowan, A. E.; Palmans, A. R. A.; Meijer, E. W. Catalytic Single-Chain Polymeric Nanoparticles at Work: From Ensemble towards Single-Particle Kinetics. Mol Syst Des Eng 2018, 3 (4), 609–618.

(3) Chen, J.; Wang, J.; Bai, Y.; Li, K.; Garcia, E. S.; Ferguson, A. L.; Zimmerman, S. C. Enzyme-like Click Catalysis by a Copper-Containing Single-Chain Nanoparticle. J Am Chem Soc 2018, 140 (42), 13695–13702.

(4) Chen, J.; Wang, J.; Li, K.; Wang, Y.; Gruebele, M.; Ferguson, A. L.; Zimmerman, S. C. Polymeric “Clickase” Accelerates the Copper Click Reaction of Small Molecules, Proteins, and Cells. J Am Chem Soc 2019, 141 (24), 9693–9700.

(5) Cole, J. P.; Hanlon, A. M.; Rodriguez, K. J.; Berda, E. B. Protein-like Structure and Activity in Synthetic Polymers. J Polym Sci A Polym Chem 2017, 55 (2), 191–206.

(6) Huerta, E.; Stals, P. J. M.; Meijer, E. W.; Palmans, A. R. A. Consequences of Folding a Water-Soluble Polymer Around an Organocatalyst. Angewandte Chemie 2013, 125 (10), 2978–2982.

(7) Wang, Y. A Plasmonic Nanotorch: Pushing Plasmon-Enhanced Fluorescence for Applications in Single-Molecule Enzymology, Eindhoven University of Technology, 2020.

(8) Michaelis, L.; Menten, M. M. L. The Kinetics of Invertin Action. FEBS Lett 2013, 587 (17), 2712–2720.

(9) Lu, H. P. Single-Molecule Enzymatic Dynamics. Science (1979) 1998, 282 (5395), 1877–1882.

(10) English, B. P.; Min, W.; van Oijen, A. M.; Kang, T. L.; Luo, G.; Sun, H.; Cherayil, B. J.; Kou, S. C.; Xie, X. S. Ever-Fluctuating Single Enzyme Molecules: Michaelis-Menten Equation Revisited. Nature Chemical Biology 2006 2:2 2005, 2 (2), 87–94.

(11) Ye, R.; Mao, X.; Sun, X.; Chen, P. Analogy between Enzyme and Nanoparticle Catalysis: A Single-Molecule Perspective. ACS Catal 2019, 9 (3), 1985–1992.

(12) Ye, R.; Mao, X.; Sun, X.; Chen, P. Analogy between Enzyme and Nanoparticle Catalysis: A Single-Molecule Perspective. ACS Catal 2019, 9 (3), 1985–1992.

(13) Xu, W.; Kong, J. S.; Yeh, Y. T. E.; Chen, P. Single-Molecule Nanocatalysis Reveals Heterogeneous Reaction Pathways and Catalytic Dynamics. Nature Materials 2008 7:12 2008, 7 (12), 992–996.

(14) Zhou, X.; Xu, W.; Liu, G.; Panda, D.; Chen, P. Size-Dependent Catalytic Activity and Dynamics of Gold Nanoparticles at the Single-Molecule Level. J Am Chem Soc 2010, 132 (1), 138–146.

(15) Zhou, X.; Andoy, N. M.; Liu, G.; Choudhary, E.; Han, K. S.; Shen, H.; Chen, P. Quantitative Super-Resolution Imaging Uncovers Reactivity Patterns on Single Nanocatalysts. Nature Nanotechnology 2012 7:4 2012, 7 (4), 237–241. https://doi.org/10.1038/nnano.2012.18.

(16) Chen, T.; Dong, B.; Chen, K.; Zhao, F.; Cheng, X.; Ma, C.; Lee, S.; Zhang, P.; Kang, S. H.; Ha, J. W.; Xu, W.; Fang, N. Optical Super-Resolution Imaging of Surface Reactions. Chem Rev 2017, 117 (11), 7510–7537.

(17) Chen, T.; Zhang, Y.; Xu, W. Single-Molecule Nanocatalysis Reveals Catalytic Activation Energy of Single Nanocatalysts. J Am Chem Soc 2016, 138 (38), 12414–12421.

(18) Archontakis, E.; Deng, L.; Zijlstra, P.; Palmans, A. R. A.; Albertazzi, L. Spectrally PAINTing a Single Chain Polymeric Nanoparticle at Super-Resolution. J Am Chem Soc 2022, 144 (51), 23698–23707.

(19) Turunen, P.; Rowan, A. E.; Blank, K. Single-Enzyme Kinetics with Fluorogenic Substrates: Lessons Learnt and Future Directions. FEBS Lett 2014, 588 (19), 3553–3563.

(20) Liu, Y.; Pauloehrl, T.; Presolski, S. I.; Albertazzi, L.; Palmans, A. R. A. A.; Meijer, E. W. Modular Synthetic Platform for the Construction of Functional Single-Chain Polymeric Nanoparticles: From Aqueous Catalysis to Photosensitization. J Am Chem Soc 2015, 137 (40), 13096–13106.

(21) Guo, Y. Y.; Zhang, B.; Wang, L.; Huang, S.; Wang, S.; You, Y.; Zhu, G.; Zhu, A.; Geng, M.; Li, L. An Efficient and Easily-Accessible Ligand for Cu(I)-Catalyzed Azide–Alkyne Cycloaddition Bioconjugation. Chemical Communications 2020, 56 (92), 14401–14403.

(22) Sud, D.; Norsten, T. B.; Branda, N. R. Photoswitching of Stereoselectivity in Catalysis Using a

Copper Dithienylethene Complex. Angewandte Chemie - International Edition 2005, 44 (13), 2019–2021.

(23) Majee, D.; Presolski, S. Dithienylethene-Based Photoswitchable Catalysts: State of the Art and Future Perspectives. ACS Catal 2021, 11 (4), 2244–2252.

(24) Ter Huurne, G. M.; De Windt, L. N. J.; Liu, Y.; Meijer, E. W.; Voets, I. K.; Palmans, A. R. A. Improving the Folding of Supramolecular Copolymers by Controlling the Assembly Pathway Complexity. Macromolecules 2017, 50 (21), 8562–8569.

(25) Wijker, S.; Deng, L.; Eisenreich, F.; Voets, I. K.; Palmans, A. R. A. En Route to Stabilized Compact Conformations of Single-Chain Polymeric Nanoparticles in Complex Media. Macromolecules 2022, 55 (14), 6220–6230.

(26) Rodionov, V. O.; Presolski, S. I.; Díaz, D. D.; Fokin, V. V.; Finn, M. G. Ligand-Accelerated Cu-Catalyzed Azide-Alkyne Cycloaddition: A Mechanistic Report. J Am Chem Soc 2007, 129 (42).

(27) Xiao, Y.; Xu, W. Single-Molecule Fluorescence Imaging of Nanocatalysis. Chin J Chem 2021, 39 (6), 1459–1470.

(28) Xu, W.; Kong, J. S.; Chen, P. Single-Molecule Kinetic Theory of Heterogeneous and Enzyme Catalysis. Journal of Physical Chemistry C 2009, 113 (6), 2393–2404.

(29) Xu, W.; Kong, J. S.; Chen, P. Single-Molecule Kinetic Theory of Heterogeneous and Enzyme Catalysis. Journal of Physical Chemistry C 2009, 113 (6), 2393–2404.

(30) Ye, R.; Mao, X.; Sun, X.; Chen, P. Analogy between Enzyme and Nanoparticle Catalysis: A Single-Molecule Perspective. ACS Catal 2019, 9 (3), 1985–1992.

(31) Lu, H. P. Single-Molecule Enzymatic Dynamics. Science (1979) 1998, 282 (5395), 1877–1882.

(32) Xu, W.; Shen, H.; Liu, G.; Chen, P. Single-Molecule Kinetics of Nanoparticle Catalysis. Nano Res 2009, 2 (12), 911–922.

(33) Kozuch, S.; Martin, J. M. L. “Turning over” Definitions in Catalytic Cycles. ACS Catal 2012, 2 (12), 2787–2794.

(34) Smith, A. A. A.; Hall, A.; Wu, V.; Xu, T. Practical Prediction of Heteropolymer Composition and Drift. ACS Macro Lett 2019, 8 (1), 36–40.

(35) Shieh, P.; Dien, V. T.; Beahm, B. J.; Castellano, J. M.; Wyss-Coray, T.; Bertozzi, C. R. CalFluors: A Universal Motif for Fluorogenic Azide Probes across the Visible Spectrum. J Am Chem Soc 2015, 137 (22), 7145–7151.

(36) Leenders, C. M. A.; Jansen, G.; Frissen, M. M. M.; Lafleur, R. P. M.; Voets, I. K.; Palmans, A. R. A.; Meijer, E. W. Monosaccharides as Versatile Units for Water-Soluble Supramolecular Polymers. Chemistry - A European Journal 2016, 22 (13), 4608–4615.

Summary

The recent development of bioorthogonal chemistry has caused a paradigm shift in chemical biology opening doors to biomedical applications. From studying biomolecules in their native environment to using the same chemistry to release toxic drugs in human cancer patients, bio-orthogonal chemistry has flourished in the past decade. Bioorthogonal catalysis using transition metals is even more fascinating as it offers the possibility of recurrent reactions at the site of interest. However, the use of transition metal-catalysed bioorthogonal reactions in living systems is still in the early stages. This is primarily because, developing stable, biocompatible, and highly active bio-orthogonal catalysts to function in a complex living environment is challenging. Inspired by nature's design of metalloenzymes, our single-chain polymeric nanoparticles form a versatile and biocompatible platform for bioorthogonal catalysis when incorporated with transition metal catalysts. SCPNs with well-defined hydrophobic domains can act as a protective shield to these catalysts and carry them to the site of interest to activate pro-drugs or synthesize bioactive agents in situ. Therefore, developing highly stable and active catalytic SCPNs with properties similar to metalloenzymes can bring us a step closer to their therapeutic applications. In this thesis, we investigated ways to improve the catalytic efficiency of single-chain polymeric nanoparticles to function in complex biological media and to export them to living cells.

After a literature overview on bioorthogonal catalysis in Chapter 1, the thesis focuses on the development of catalytic SCPNs based on Pd(II), Pd(0), Rh(II) and Cu(I) catalysts. In Chapter 2, we evaluated different aspects of the Pd(II)-SCPN based catalytic system to improve its performance in complex media. For this, we developed amphiphilic polymers with polyacrylamide backbone and functionalised them with the Pd(II)-binding ligands triphenylphosphine and bipyridine. We systematically evaluated the effect of polymer microstructure, ligand–metal complex, and substrate hydrophobicity on the catalytic activity of the nanoparticles for depropargylation reactions in water, PBS or DMEM. The results showed that the catalytic activity of nanoparticles is primarily impacted by the ligand–metal complex while polymer microstructure only has a minor influence. Moreover, the rate of reaction is increased for hydrophobic substrates. Triphenylphosphine-based Pd(II) SCPN was then used to activate anti-cancer pro-drugs based on 5-FU, paclitaxel, and doxorubicin in complex media. In Chapter 3, the developed Pd(II) catalysts were reduced to Pd(0) inside SCPNs using a mild reduction treatment with CO, which significantly improved its catalytic efficiency in complex media. Pd(0) SCPNs were then used for

depropargylation of pro-rhodamine and activation of a newly developed prodrug of 5-fluorouracil in complex media. We expanded the repertoire of reactions that Pd(0) SCPNs can carry out to Heck and Suzuki-Miyaura coupling reactions in water.

In Chapter 4, we prepared Rh-SCPNs using a non-covalent strategy where hydrophobic interactions were employed to encapsulate catalysts in the hydrophobic pocket of SCPNs. Highly stable and active hydrophobic rhodium catalysts were encapsulated in the hydrophobic pocket of SCPNs. They catalyzed NH insertion reactions to promote the annulation of alpha-keto diazocarbenes with ortho-amino arylamines, to form fluorescent benzoquinoxaline and a bioactive agent. The reactions were truly catalytic in nature and were exported to complex media without any loss in catalytic efficiency thus expanding the toolset of bioorthogonal chemistry.

In Chapter 5, we developed highly active Cu-SCPNs varying polymer microstructures that perform both depropargylation and click reactions to map the heterogeneity in catalysis at the single-particle level using single-molecule fluorescence microscopy (SMFM) studies. The Cu-SCPNs showed enzyme-like behaviour as observed from Michaelis–Menten kinetics. The differences in polymer microstructure did not influence the catalytic activity as observed both at the ensemble and single-particle level. But, intraparticle turnover dispersity in catalysis was observed during SMFM studies within each catalytic system which could be attributed to the dispersity in the polymers and differences in the microenvironment of Cu(I) catalysts.

Curriculum Vitae

Anjana Sathyan was born on March 17th, 1994 in Kuzhuppilly, Kerala, India. She completed her secondary education at Jnanodaya Central School, Kalady in 2010 and her higher secondary education at Viswajyoti Public School, Angamaly in 2012. Afterwards, she joined for integrated BS-MS dual degree program at Indian Institute of Science Education and Research, Pune with DST Inspire Scholarship from Government of India in 2013. During her bachelor studies, she worked on the synthesis and development of hydrogen sulfide releasing pro-drugs in the research group of Prof. Harinath Chakrapani. Later, during her master studies, she worked on the development of sulfonamide based synthetic anion transporters in the research group of Prof. Pinaki Talukdar. She continued in the same group for her graduation project where she worked on stimuli-responsive small molecule anion transporters. After that, she started her PhD in the group of Supramolecular Chemistry and Catalysis under the guidance of Prof.dr.Ir. Anja Palmans in 2019. Her PhD was a part of Marie Skłodowska-Curie European Training Network, THERACAT on the topic 'Bioorthogonal catalysis for cancer therapy'. During her PhD, she worked on the development of single-chain polymeric nanoparticles as bioorthogonal catalysts for pro-drug activation in cells aimed at side-effect-free cancer therapies. The most important results are discussed in this thesis.

List of Publications

Sathyan, A.; Croke, S.; Pérez-López, A. M.; de Waal, B. F. M.; Unciti-Broceta, A.; Palmans, A. R. A. Developing Pd(II) based amphiphilic polymeric nanoparticles for pro-drug activation in complex media. *Mol. Syst. Des. Eng.* **2022,** *7*, 1736-1748.

Sathyan, A.; Deng, L.; Loman, T.; and Palmans, A.R.A. Bio-orthogonal catalysis in complex media: Consequences of using polymeric scaffold materials on catalyst stability and activity. *Catalysis Today,* **2023**, *418*, 114116.

Sathyan, A.; Loman, T.; Deng, L.; and Palmans, A.R.A. Amphiphilic Polymeric Nanoparticles Enable Homogenous Rhodium-Catalysed NH Insertion Reactions in Living Cells. *Nanoscale*, submitted.

Deng, L.; **Sathyan, A.**; Adam, C.; Unciti-Broceta, A.; Sebastian, V.; and Palmans, A.R.A. Pd(0) based SCPNs as efficient bio-orthogonal catalysts for pro-drug activation in living cells, in preparation.

Acknowledgments

It has been a little more than four years since I took my flight from Kochi, Kerala, and flew three and a half time zones away, landing in Amsterdam on a cold winter day in December. My PhD journey, like any other, was challenging with ups and downs, but just like the different seasons unfold, it was exciting and colorful over time. Now, as I write the final and most important part of my thesis, I cannot wrap up without thanking many amazing and kind people whom I have met during my time here, as well as those who were already a part of my life. Without all of you, I could not have made this happen.

First and foremost, I would like to thank two people who are the reason I found the strength to stay in Eindhoven and finish my PhD! Shaneesh and Rashija. I cannot thank you both enough for making me a part of the family and giving me a place to stay when I had nowhere to go, even when you didn't know me. Thank you for being there for me when I was most scared and completely lost. You both are the most incredible people I have ever met, and I will forever be grateful for your kindness. I wish you both all the great things in the years to come, and may you always stay happy.

Now, to the most important person in my PhD journey and the driving force behind who I am now and what I have accomplished in the last four years, my promoter, Anja. I don't have enough words to thank you! First, for offering me this position and introducing me to the exciting field of bioorthogonal chemistry. I was so lucky to have a mentor like you. Despite all the challenges, you always taught me to look at the positive side of everything. Thank you for being patient and supporting me both professionally and personally whenever I needed it. I admire your constant positive energy, which motivates and brings happiness to everyone around you. I will certainly miss hearing all the stories from your holidays around the world. I wish you and Sjef the opportunity to visit all the places in the world you both desire, and hopefully, one day you can make it to Kerala.

Next to my co-promoter, Asier, I am very happy to have met you. I still remember your first lecture during the initial THERACAT training at Eindhoven; your excitement for the pro-5FU prodrug was contagious. All of your lectures have been a huge inspiration to me. I greatly admire your passion for developing new drugs and BOOM chemistry. Thank you for the collaborations; without the prodrugs you sent us, I would not have been able to make progress with my projects. Additionally, I want to express my gratitude for your valuable feedback on the paper. I would also like to extend my thanks to Ana, Stephen, and Catherine for synthesizing the prodrugs and generously sharing them with me.

Lorenzo, thank you for your valuable feedback during our joint meetings. Although the SMFM studies did not give amazing results as we expected, it was an exciting project and a valuable learning experience for me. I would also like to express my gratitude to my committee members: Luc, Rint, Yiliu, and Bert for accepting to be a part of my thesis committee and for dedicating time to read and evaluate my thesis.

Victor, the very first email I sent you was to inform you that I might not be able to attend my presentation at UCRA due to a delayed visa, and you were chairing the session. Little did I know then what the future held or that we would be working on an amazing collaboration for an exciting project. I want to thank you for suggesting the idea for reducing my Pd(II) catalysts and offering to carry it out in Spain.

To my paranymphs, Linlin and Stefan: You guys were an important part of my PhD; thank you for always being there for me when I needed help and for always being such cheerful officemates. Thank you, Linlin, for our collaborations; I learned a lot from you. I enjoyed all of our OGO teaching sessions, late-night and weekend experiments, dinners, and shopping trips. Thank you for introducing me to some of the best Chinese cuisine. Stefan, thank you for translating Dutch for me whenever need and explaining the most fascinating dutch traditions. I learned a lot from our discussions, and it was always exciting to work together to solve problems. I have many memorable moments with both of you, especially our road trip to Grenoble and hiking after 24 hours of continuous experiments. I wish you both the best of luck in your final year, and once again, thank you for being my paranymphs.

Manos, you are an amazing friend and collaborator. It was an incredible learning experience exploring SMFM studies on SCPNs with you. I wish you all the best in your new job and hope you continue to pursue your passion for new travel adventures. Prakash, although I have known you for only a short time, I am really happy that you joined our group. I am sure your vast knowledge in organometallic chemistry will fuel some amazing projects. It is a pity that my time here is coming to an end; I could have learned a lot working together with you. Thank you for correcting my thesis down to the tiniest detail. Tessa, I admire your passion, enthusiasm, and determination to see things through to the end. It was a pleasure working together with you, and I want to thank you for uncovering the impact of Rh-SCPNs. I wish you all the best for your PhD; I am sure you will do great! Marle, thank you for always being ready to help whenever I was in need. I wish you all the best as you finalize your thesis.

Martina, thank you so much for all the help during the last four years. Without you, I couldn't have even had the date fixed for my defense. To me, you are a superwoman. Carla, you are like a spring flower, spreading happiness to everyone around you. Thank you for all the help over the past years. Jolanda, during my first year, I was always so scared of you and thought you were not very friendly. But with time, I realized you are a very sweet and caring person. You are the heart of Lab 2, and in fact, all SMO labs, keeping them up and running. I can't thank you enough for all your efforts during the Covid time that helped everyone do lab work in a safe environment. Also, thank you for synthesizing resorufin and rhodamine pro-dyes. No synthesis is impossible for you. Thanks for your constant support, not just to me, but to everyone around you. The words "you can do it" can sometimes do wonders, as they did when I was too stressed finishing up my thesis.

Bas, thank you for helping me synthesize the rhodamine pro-dye. I learned a lot from you. It was fun working with you and Linlin, and also enjoyed our discussions during the lockdown. Joost, I want to thank you for allowing me to use the HPLC despite the fact that my HPLC samples were problematic and arranging new column for analyzing 5-FU. Lou, without you, I could not have finished my projects, as most of my experiments involved using either one of the HPLC machines. Thank you for helping me set up everything, from changing columns whenever needed to unblocking it when my polymers mess it up. You always had a smiling face and I was always relieved to do my measurements when you were around. Sebastian, thank you for lending me the hypercarb column and providing further explanations about it. Roy, thank you for sharing the coumarin precursor with me.

Ramkrishna and Sanjukta, I enjoyed the time when both of you were in Eindhoven, our trips, conversations, and the delicious food you both cooked. Thank you for also making my mom feel at home when she visited Eindhoven. I wish you both the very best in the coming years and hope to see you soon in India. Shikha, I'm happy to have met you. Thank you for trying to make me go to the SSC (although it didn't last long) and for understanding me so well that you almost know what I'm going to say every time we plan something. I hope you achieve everything you dream of and have fun in Mainz. Kripa, you were a bit more successful in motivating me to go to SSC than Shikha. I enjoyed our badminton sessions together with Prakash and Anurag. Thank you for all the motivation while I was writing my thesis, and I wish you all the best with your postdoc. Fang, you are very sweet, and I wish I had met you sooner and gone on many more trips together. Fan, Hailin, and Du, thank you for introducing me to Chinese cuisine, sharing stories about China, and always being kind. Hailin, I will always remember the mooncake story. Souma, Muhabbat, Hui, Diederik, you were all my first office mates. Thanks to all of you for being very welcoming to me. Muhabbat, I still remember that I had my very first coffee in TU/e with you. Since then, you have always been a good friend, supportive, and motivating. Souma, the same goes for you. It's always nice to talk about the worries of writing and finishing the PhD. Thank you both for being weekend partners and caring about me. Yunfei, I want to thank you for helping me finalize my thesis printing, giving suggestions about the cover design, and clearing all my doubts in the final stage. I wish all of you the very best after the PhD. Shahzad, thank you for assuring me that the writing would go well and for all the thoughtful conversations. I wish you and your family a very happy and wonderful time ahead.

Simone, I didn't know you well when I joined my PhD, just that I had to take your spot when you left. But when you came back to the very same office, I got to know you better. I am so grateful for that, as you understand me so well. You have the charm of making the office lively and cheerful every time. I enjoyed our conversations, office dinners, and hearing your stories from different places around the world. Thank you for believing in me and giving me confidence when I struggled with writing my first paper. I wish you could continue exploring the world and be as happy as always.

Julian, thank you for helping me get acquainted with the new lab environment when I first joined and teaching me how to do polymerization. Christian, thank you for lending a helping hand when I initially started my lab work. Lafayette, thank you for showing me how to do sample preparation perfectly. Thank you to all the new and old members of SMO: Stephen, Bart, David, Freek, Joost, Laura, Magda, Marco, Stef, Giulia, Osamu, Esmee, Roy, Ghislaine, Fabian, Tobias, Lu, Chidambar, Silvia, Gijs, Jesus, Pongphak, Andreas, Martin, Sandra, Patricia, Annelore, Elisabeth, Brigitte, Mathijs, Marcin, and Beatrice for a pleasant work atmosphere. To all the OGO students, Lieke, Roy, Luc, Tom, Rico, Carla, Izzy, Frank, and Ji Hye, it was great working with all of you. Ji Hye, thank you for keeping me company while I was writing my thesis.

Merin, Vishnu, and Nithin, thank you all for being my TU/e support system. Thank you for listening to my endless complaints about oxidized phosphine polymers and trying to cheer me up. Also, thank you for valuable discussions and suggestions whenever I faced problems. Alma, Jesil, Jazleena, Jithin, and Swathi, thank you for being my online support system, especially for keeping me sane during the Covid times. I guess if it weren't for our video calls every day, I couldn't have survived those days. Jazleena, thank you for being my critical reader for papers and presentations. Your feedback has always helped me improve my work. Jesil, thank you for being there for me when I felt lost and alone after being scammed by the housing agency. Alma, thank you for being patient when I kept canceling plans to visit Uppsala, blaming one thing or another. I'm happy that I could at least make it to your defense. And most importantly thank you for the support all this time.

Anurag, a lot has happened in the last four years, and I want to thank you for always being there for me and helping me stay strong. I am eagerly waiting for the day when you will also finish your PhD so that we can start our adventures together. लखनऊ मम्मी और पापा, जब मैं थीसिस लिख रहा था, तब आप दोनों का समर्थन के लिए धन्यवाद। Thank you Lincy chechi, Lisha chechi, Nisha chechi, Dasettan, Seena aunty and Bose valyacha for keeping me in your prayers and always believing in me. To my loving teachers in Jnanodaya and Sr. Agnus Claire, thank you for the love all this time and for giving me the courage to chase my dreams, it all started right there. Jolly Ma’am, I can’t wait to show you what I have written.

Amma, I am here today because of you. I can't even begin to put into words what I want to say. And I hope you know it, so I am keeping it short, I love you! I am truly blessed to be your daughter.

Anjana

“Do your little bit of good where you are; its those little bits of good put together that overwhelm the world” – Desmond Tutu